Local Signature of Kondo Interaction Probed by XMCD in Rare Earths Intermetallic Compounds.

Weibin Li

▶ **To cite this version:**

Weibin Li. Local Signature of Kondo Interaction Probed by XMCD in Rare Earths Intermetallic Compounds.. Materials Science [cond-mat.mtrl-sci]. Sorbonne Université, 2022. English. NNT : 2022SORUS094 . tel-03773619

HAL Id: tel-03773619

https://theses.hal.science/tel-03773619v1

Submitted on 9 Sep 2022

HAL is a multi-disciplinary open access archive for the deposit and dissemination of scientific research documents, whether they are published or not. The documents may come from teaching and research institutions in France or abroad, or from public or private research centers.

L'archive ouverte pluridisciplinaire **HAL**, est destinée au dépôt et à la diffusion de documents scientifiques de niveau recherche, publiés ou non, émanant des établissements d'enseignement et de recherche français ou étrangers, des laboratoires publics ou privés.

SORBONNE UNIVERSITÉ

ÉCOLE DOCTORALE 397

PHYSIQUE ET CHIMIE DES MATÉRIAUX

Institut de Minéralogie, de Physique des Matériaux et de Cosmochimie

Synchrotron SOLEIL

THÈSE DE DOCTORAT DE PHYSIQUE

Local Signature of Kondo Interaction Probed by XMCD in Rare Earths Intermetallic Compounds

par

Weibin LI

Présentée et soutenue publiquement le 4 avril 2022

Devant un jury composé de:

M. Franck VIDAL Institut des NanoSciences de Paris	Prof. Sorbonne Université	Président
Mme. Valérie PAUL-BONCOUR Institut de Chimie et des Matériaux Paris-Est	DR CNRS	Rapportrice
M. Richard MATTANA Unité Mixte de Physique CNRS/Thales	CR CNRS	Rapporteur
M. Fabrice SCHEURER Institut de Physique et de Chimie des Matériaux de Strasbourg	CR CNRS	Examinateur
M. Philippe SAINCTAVIT Institut de Minéralogie, de Physique des Matériaux et de Cosmochimie	DR CNRS	Directeur de thèse
Mme. Edwige OTERO Synchrotron SOLEIL	Scientifique de Ligne	Co-encadrante de thèse
M. Jean-Paul KAPPLER Institut de Minéralogie, de Physique des Matériaux et de Cosmochimie	Chercheur Invité	Invité

Local Signature of Kondo Interaction Probed by XMCD in Rare Earths Intermetallic Compounds

Abstract

This doctoral thesis studies the Kondo effect of rare earth compounds measured by X-ray absorption spectroscopy (XAS). Two diluted intermetallic systems: A non-Kondo system $Er_{0.025}Pd_{0.975}$ and a Kondo system $Yb_{0.005}Au_{0.995}$ have been measured by XAS with circular polarized X-ray under strong magnetic field and weak magnetic field for temperatures from 0.2 K to 300 K. X-ray Magnetic Circular Dichroism (XMCD) spectra and X-ray Magnetic Linear Dichroism (XMLD) spectra have been extracted. The magnetic moment of the spin and of the orbit of the diluted impurity atom are obtained by applying the magneto-optical sum rules. Calculations by Ligand Field Multiplet (LFM) theory are performed to simulate the magnetic properties. The comparison between the Kondo system and the non-Kondo system, as well as the experimental measurements and the simulations allows the discovery of the local Kondo signature around the critical Kondo temperature T_K for the Kondo system $Yb_{0.005}Au_{0.995}$.

To achieve the experimental objective, part of this thesis has been devoted to instrumental developments. Hence a new $^3He - ^4He$ dilution insert, named DICHRO50 which is able to cool the sample down to 180 mK, has been installed in the cryomagnet of DEIMOS beamline at Synchrotron SOLEIL; it is aimed to soft X-ray XAS-XMCD measurements. Moreover, a former dilution insert hosted in so-called TBT-mK cryomagnet has been upgraded to be installed on ID12 beamline at ESRF; it is aimed for hard X-ray XAS-XMCD measurements.

Signature Locale de L'effet Kondo Révélée par XMCD dans des Intermétalliques de Terres Rares

Résumé

Cette thèse doctorale étudie l'effet Kondo des composés de terre rare par spectroscopie d'absorption des rayons X (XAS). Deux systèmes intermétalliques dilués : un système non-Kondo d'$Er_{0.025}Pd_{0.975}$ et un système Kondo d'$Yb_{0.005}Au_{0.995}$ ont été mesurés par XAS avec des rayons X polarisés circulairement sous champ magnétique fort et aussi en champ magnétique faible pour une température variant de 0.2 K à 300 K. Les signaux de dichroïsme circulaire magnétique de rayons X (XMCD) et les spectres de dichroïsme linéaire magnétique de rayons X (XMLD) ont été extraits. Les moments magnétiques de spin et d'orbite ont été obtenus par application des règles de somme magnéto-optiques. Des calculs dans le cadre de la théorie des multiplets en champ de ligands (LFM) ont été faits pour simuler les signaux expérimentaux et ainsi remonter aux propriétés magnétiques. Dans le système Kondo, celui de l'ytterbium dans l'or, on observe pour des champs magnétiques $\leq$ 0.5 T et des températures inférieures à 1 K une différence prononcée entre l'aimantation attendue pour un atome isolé et celle observée expérimentalement : c'est le signe de l'effet Kondo.

Pour arriver aux objectifs expérimentaux, une partie de travail de cette thèse a été consacrée à des développements instrumentaux. Un nouvel insert DICHRO50 qui fonctionne avec la dilution d'$^3He-^4He$ a été installé dans le cryo-aimant de la ligne DEIMOS du Synchrotron SOLEIL. Cet instrument est développé pour des mesures de XAS, de XMCD ou des XMLD dans le domaine des rayons X mous. Il permet de refroidir un échantillon jusqu'à 180 mK. Un autre cryo-aimant, le TBT-mK, a été installé sur la ligne ID12 à l'ESRF où j'ai participé à des mesures de XMCD dans le domaine des rayons X durs.

献给妈妈

Remerciements

Je tiens à remercier Philippe Sainctavit, mon directeur de thèse, qui m'a accordé la confiance pour réaliser ce projet de thèse, m'a guidé tout au long de ma thèse, et m'a apporté nombreux conseils scientifiques précieux. Je remercie Edwige Otero, mon encadrante de thèse, pour sa gentillesse, sa disponibilité et pour m'avoir donné beaucoup de conseils expérimentaux très pratiques afin de réussir mes différents projets expérimentaux. J'aimerais remercier Jean-Paul Kappler pour m'avoir donné des conseils d'un point de vue d'expert hors pair et m'avoir transmis sa passion ainsi que sa culture en science et en technologie pendant nos nombreuses discussions fructueuses.

Je voudrais remercie Franck Vidal qui a présidé mon jury de thèse. J'aimerais remercier Valérie Paul-Boncour et Richard Mattana qui m'ont fait l'honneur d'être rapportrice et rapporteur de ma thèse et m'ont apporté des commentaires instructifs. Je remercie Fabrice Scheurer qui a accepté de participer à mon jury de thèse, m'a apporté des échanges et des commentaires constructifs et je le remercie également pour m'avoir invité à participer à certains de ses projets qui sont proches de mon sujet de recherche.

Je remercie sincèrement Philippe Ohresser, responsable de DEIMOS à Synchrotron SOLEIL, qui a assuré un très bon management de la ligne et une organisation excellente des projets d'expérience. Je remercie chaleureusement Florian Leduc, assistant ingénieur de DEIMOS, pour sa sympathie, sa gentillesse, sa disponibilité et son talent incomparable pour résoudre des problèmes techniques concrets.

J'aimerais remercier les autres personnes et les équipes avec qui j'ai eu l'honneur de collaborer pendant ma thèse : Guy Schmerber de l'IPCMS qui a magnifiquement fabriqué exclusivement pour ma thèse des échantillons d'erbium et d'ytterbium de très bonne qualité et a réalisé des mesures de diffraction et de SQUID, Wolfgang Felsch de l'Université Georg-August de Göttingen qui nous a donné ces merveilleux composés de cérium pour nos projets. Je remercie Benoît Baptiste et Marie-Anne Arrio de l'IMPMC, Andrei Rogalev, Fabrice Wilhelm et Pascal Voisin de la linge ID12 à l'ESRF, Elsa Lhotel de l'Institut Néel. Loïc Joly de I'IPCMS. Merci à Massine Kelaï ainsi que l'équipe d'Amandine Bellec et Vincent Repin de MPQ, Luqiong Zhang ainsi que l'équipe de Talal Mallah de l'ICMMO, l'équipe de Matteo Mannini de l'Université de Florence et l'équipe de Rodolphe Clérac de CRPP.

Cette thèse a été réalisée au sein de l'IMPMC en associant la ligne DEIMOS à Synchrotron SOLEIL. Pour l'IMPMC, je remercie mes collègues de bureau : Alexis Amouretti, Steven Delhommaye, Florian Lahrouch, pour la très bonne ambiance de travail, pour des discussions très intéressantes, détentes et parfois marrantes et pour nombreux moments inoubliables qu'on a partagés ensemble. Je remercie également Clémence Besançon et Mathieu Moog qui ont installé dans notre bureau plus tard pour une très bonne ambiance de travail et pour diverses discussions très intéressantes entre nous. Je tiens à remercier les autres doctorants du couloir 23/24 au 4e étage : Théo Caroff, Cécile Noirot, Malika Khelfallah, Ali Aarab, Julia Jourdan, Déa Jais et Léa Gardie pour des activités "afterwork" inédites et très conviviales. Pour Synchrotron SOLEIL, je remercie mes collègues et des personnes que j'ai rencontrés très souvent : Fadi Choueikani, Danilo Longo, Benoît Gobaut, Dominique Prieur, Sylvain Brochet, Gilles Cauchon, Stéphane Morand, Thierry Moreno, Blandine Capitanio, Muriel Thomasset, James Ablett et Mathieu Silly pour avoir partagé leurs expériences professionnelles et de la vie quotidienne, créant ainsi un excellent environnement convivial de travail.

Je remercie l'École Doctoral 397 de Sorbonne Université qui a financé mon projet de thèse et je remercie Synchrotron SOLEIL pour m'avoir financé l'inscription à des formations, des conférences et des séminaires, en France et à l'étranger, qui sont très importants pour la communauté de recherche ainsi que pour moi.

Je salue tous les efforts qui ont été réalisés par Sorbonne Université, l'École Doctorale 397, l'IMPMC et Synchrotron SOLEIL pour supporter et accompagner des doctorants pendant la pandémie de COVID-19.

A la fin, je remercie ma famille et en particulier, merci infiniment à ma mère.

谢谢妈妈的养育之恩和一直以来对我的支持！

Contents

List of Figures

List of Tables

Chapter 1

Introduction

1.1 Investigation of magnetism by X-ray

Since the discovery of an unknown radiation named X-ray in 1895 by Wilhelm Röntgen [1], the X-ray based technique has become one of the most important methods for matter investigation. Here are some milestones of the X-ray dichroism technique development in history [2, 3]. Barkla proved in 1905 that X-rays could be polarized by scattering [4]. He also proved that it is possible to produce a linearly polarized X-ray beam with a polarization rate close to 100% [5]. The polarization of X-ray gives an important key for investigating the magnetic properties of matter.

In the first half of twentieth century, numerous researches have been dedicated to the measurement of dichroic signals [6, 7, 8, 9, 10, 11, 12, 13, 14, 15]. Although some of them could be measured, the signals remained quite small so that it was too early to use the dichroism for the investigation of the magnetic properties of matter.

Erskine and Stern predicted by calculation in 1975 that the magnetic properties can be extracted by the absorption of circularly polarized X-ray at core-to-valence transitions [16]. Despite some experimental efforts, they could not measured dichroic X-ray absorption at Ni $M_{2,3}$ edges. It was not before 1983 that Schütz *et al.* recorded the difference of circular polarized XAS[1] under magnetic field on L edges of oriented iridium isotopes though the sensibility was still not enough [17].

The magnetic linear dichroism was predicted by calculations done on rare earths $M_{4,5}$ edges by Thole *et al.* in 1985 [18]. In 1986, van der Laan *et al.* performed the experiments with polarized synchrotron radiation at LURE[2] and obtained the first strong magnetic X-ray dichroism in the $M_{4,5}$ absorption spectra of magnetically ordered rare-

[1] X-ray absorption spectroscopy

[2] Laboratoire d'Utilisation du Rayonnement Électromagnétique, 1972-2003, Orsay, France

earth materials and observed for the first time XMLD[3] [19]. In 1987, XMCD[4] has also been observed by Schütz *et al.* at Fe-*K* edge in DESY[5] [20].

In 1992 and 1993, Theo Thole who had already worked on sum rules in connection with X-ray absorption made a breakthrough and proposed the famous magneto-optical sum rules that makes XMCD a unique method to obtain the spin [21] and orbit [22] magnetic moments of the absorbing atom. Sum rules are performed by calculating simple integrals of the experimental XAS and XMCD signals. The validity of the sum rules were later experimentally confirmed by Chen *et al.* who measured the $L_{2,3}$ edges of Fe and Co [23].

In 1993, Brouder [24] showed how it was possible to extract ground state quantities such as $\langle J_z \rangle$ and $\langle J_z^2 \rangle$ where J_z is the projection of the total angular momentum $\boldsymbol{J}$. The brakets $\langle\rangle$ stand for an average over the occupied multielectronic levels. This concept will be largely used in this thesis.

With the development of third and fourth generation synchrotrons which dramatically improve the performance of the beam and its polarization, XMCD has become one of the most successful technique to investigate magnetic properties of different materials. Nowadays, more than 50 synchrotron beamlines in the world are dedicated to XMCD measurements [25]. On the other hand, XMLD remains a bit confidential and rather few measurements exist. The interpretation of XMLD has even been the subject of an animated scientific controversy and the reader should refer to one of the papers by Gerrit van der Laan to address this question [26, 27, 28, 29, 30].

1.2 Ultra-low temperature devices for synchrotron XAS experiments

The interest to perform the XAS experiments at ultra-low temperature will be presented in the next chapter. Here we would like to track the historical development of ultra-low temperature devices for synchrotron based XAS experiments.

To our knowledge, Stephen Cramer has been the first scientist to develop a cryomagnet suited for XAS and XMCD measurements below 1 K. A couple of experiments were performed in 1986 by his post-doctoral fellows and PhD students among which Marie-Anne Arrio, Lisa M. Miller, Corie Ralston, and Jason J. Christiansen. Whether the actual temperature of the sample was indeed below 1K was not obvious. In 1998, the second variable temperature insert was built and installed on SU22 beamline at Super-ACO in LURE. This insert was built around a ^{3}He$-^4$He dilution refrigerator

[3] X-ray magnetic linear dichroism
[4] X-ray magnetic circular dichroism
[5] Deutsches Elektronen-Synchrotron, Hambourg, Germany

[31]. It was the first ultra-low temperature device in the world for XMCD which allowed to cool down the sample below 1 K. This device received the name TBT-mK. It was in use on SU22@Super-ACO and SU23@Super-ACO beamlines until the end of LURE laboratory, in 2003. TBT-mK was then moved to other European beamlines such as BACH@ELETTRA (2003-2005)[6], EU46@BESSY II (2004-2007)[7], and finally SIM@SLS[8] from 2005 till 2017. During these migrations significant results have been collected [32, 33]. In 2018, the cryomagnet has been installed on the ID12@ESRF[9] for a new scientific adventure. A part of my PhD work has been dedicated to the installation of TBT-mK on ID12 where I contributed to the first XMCD experiments in the hard X-ray range in the sub-kelvin range.

In 2017, an endstation called TTXMCD was installed at P04, PETRA III, DESY for XMCD measurements which allows to obtain 100 mK with an external magnetic field of 7 T [34, 35] but unfortunately I am not aware that any further scientific results have ever been published so far from this beamline.

In 2018, another insert DICHRO50 with a ^{3}He – ^{4}He dilution refrigerator was made and installed in the cryomagnet on DEIMOS beamline at Synchrotron SOLEIL[10]. The instrumental development and the installation of this VTI has been part of my PhD thesis. Compared to TBT-mK, this version integrates the most advanced cryogenics technology with a great improvement on a user-friendly control [36]. The details of DICHRO50 will be presented in the next chapter.

Although the ^{3}He – ^{4}He dilution refrigerator was invented in 1965 [37, 38] and well developed later, it is still a great challenge to make it work on a synchrotron beamline. This is mainly due to a complex experimental geometry, general UHV environment, requirements for Total Electron Yield detection (insulation of the sample but for a wire connection at 300 K at one of its extremity). Today, there are only two ultra-low temperature ($T < 1$ K) devices for XMCD on synchrotrons, that are TBT-mK at ESRF and DICHRO50 at SOLEIL.

1.3 Kondo effect

The electrical resistivity of a superconductor drops to zero when the temperature is lower than a certain critical temperature T_C. For a normal metal, the simplest theories state that the electrical resistivity varies linearly with temperature and so that it tends to zero for $T = 0$ K. In the real life, a non zero residual resistance is due to the scattering

[6] ELETTRA Sincrotrone, Trieste, Italy
[7] Berliner Elektronenspeicherring-Gesellschaft für Synchrotronstrahlung, Berlin, Germany
[8] Swiss Light Source, Villigen, Switzerland
[9] European Synchrotron Radiation Facility
[10] Source Optimisée de Lumière d'Énergie Intermédiaire du LURE

of the electrons (electron-electron, electron-lattice vibrations) at low temperature. The non-zero residual resistance is related to defects in the crystal [39].

However, in 1934 de Haas *et al.* found at low temperature, a minimum of electrical resistivity at a critical, finite temperature for gold when magnetic impurities are present. At the difference of what is expected theoretically for a pure metal and experimentally for a common metal, when the temperature is lowered below this critical temperature, the electrical resistivity increases [40]. The anomaly was also found in other diluted systems [41]. Further experiments proved that the appearance of the minimum of resistivity depends on the concentration of impurities [42].

In 1964 Jun Kondo interested in the measurements by Sarachik *et al.* of diluted Fe in a series of Nb−Mo alloys [43] and gave an explanation based on the so-called $s-d$ model, which includes the coupling between the spin magnetic moment of a local impurity and the conduction electrons of the matrix [44]. It was the first significant explanation for the anomaly that received the name of Kondo effect. Kondo stated "*when a resistance minimum is found, we invariably find some evidence of localized moments, and inversely when localized moments are revealed, we usually observe a minimum in resistivity. This conclusion indicates that the resistance minimum is a direct consequence of the interaction between spins of the localized impurity and conduction electrons ...*" [44] Kondo used a third order perturbation theory to calculate the scattering of conduction electrons by the impurity potential in the first Born approximation to yield an expression for the resistivity [44, 45]. Here we show only the final results and details of the calculation can be found in references [44, 45, 46, 47]. The impurity resistivity is given by [45]

$$R_{\text{imp}} = \frac{3\pi m \mathscr{J}^2 S(S+1)}{2e^2\hbar\epsilon_F}\left[1+4\mathscr{J}\rho_0 \ln\left(\frac{k_B T}{D}\right)\right] = R_{\text{m}}\left[1+4\mathscr{J}\rho_0 \ln\left(\frac{k_B T}{D}\right)\right] \quad (1.1)$$

where $\mathscr{J}$ is an exchange coupling parameter, m the electron mass, e the electron charge, ϵ_F is the Fermi energy, ρ_0 is the density of states of the conduction band at the Fermi energy ϵ_F and D is the bandwidth of the conduction band. We assume that $k_B T \ll D$. The total resistivity can be written as

$$R = aT^5 + cR_A + cR_{\text{imp}} = aT^5 + cR_A + cR_{\text{m}}\left[1+4\mathscr{J}\rho_0 \ln\left(\frac{k_B T}{D}\right)\right]. \quad (1.2)$$

where a is a constant, and c the impurity concentration. R_{m} is obviously defined from (Eq.1.1). The first term is due to the phononic vibrations that dominate at high temperature. It predicts the classical behavior of normal metals. The second term is a term of non-magnetic, potential scattering where R_A does not depend on temperature. The third term is the Kondo contribution whose sign depends on $\mathscr{J}$. When $\mathscr{J} > 0$ the ferromagnetic type interaction makes the resistivity a monotonic function of the

temperature that decreases with a decreasing temperature. For $\mathscr{J} < 0$, the antiferromagnetic type gives a minimum of resistivity at

$$T_{\min} = \left(\frac{4|\mathscr{J}|\rho_0 R_{\mathrm{m}}}{5a} \right)^{\frac{1}{5}} c^{\frac{1}{5}}. \tag{1.3}$$

Historically this minimum temperature was often taken as the Kondo temperature [48]. But this minimum temperature depends on R_{m} and the characteristic of the phonon scattering so that this definition is imperfect. Although the $s-d$ model explains qualitatively the resistivity minimum and its divergence as $T \to 0$, later studies considering higher scattering processes by Abrikosov showed that the higher order terms yield an even stronger divergence for $T \to 0$ [49]. By summing the most divergent terms, Abrikosov obtained the expression for the resistance

$$R = \frac{cR_{\mathrm{m}}}{\left[1 - 2\mathscr{J}\rho_0 \ln\left(\frac{k_B T}{D}\right)\right]^2}. \tag{1.4}$$

For $\mathscr{J} > 0$, R decreases monotonically and converges as $T \to 0$ but diverges as $\mathscr{J} < 0$. The Kondo temperature T_K is defined as the finite temperature at which the resistance diverges, which is

$$k_B T_K \sim D \exp\left(-\frac{1}{2|\mathscr{J}|\rho_0}\right). \tag{1.5}$$

With the definition of the Kondo temperature above, the model proposed by Kondo is applicable down to T_K but it does not work for $T < T_K$. Eliminating the divergence at $T \to 0$ became the so-called Kondo problem and that proved to be a great theoretical challenge during the 1960s and 1970s.

In the late of 1960s, Anderson tried to solve this problem by introducing the idea of scaling [50, 51]. He named humorously this scaling method "Poor Man's Scaling". The term "poor man" refers to the fact that the bandwidth is not rescaled to its original size after each progressive renormalization [48]. For an antiferromagnetic interaction, the effective coupling between the local moment and the conduction electrons increases. However for this antiferromagnetic case, D can only be reduced to the order of $k_B T$, which is the only energy scale that characterizes the low-temperature (strong-coupling) physics of the Kondo model [52]. Passing this limit makes the perturbative approach not valid any more. Nevertheless, Anderson *et al.* assumed that the process could be continued down to the lowest energy scales by $|\mathscr{J}| \to \infty$ [53]. That implies the formation with an infinite coupling on ground state and the impurity is bound by forming a singlet.

In 1970s, a great contribution was made by Wilson who treated this problem with the non-perturbative numerical renormalization group approach. The assumption of

Anderson is confirmed by Wilson [54, 55]. For the first time, Wilson succeeded to calculate the spin-1/2 Kondo model for the whole temperature range [55, 56, 57, 58].

With the models presented above, the physical picture for an impurity is the following (Figure 1.1): when the impurity is diluted, increasing $|\mathscr{J}|$ couples the impurity spin to the spin of a conduction electron. The ground state is a many particle state. The local moment of the impurity is screened by forming a spin singlet so that the impurity appears to be a non magnetic impurity. The singlet is formed below T_K and can be destroyed by thermal fluctuations for high temperature. At the Fermi energy level for $T < T_K$, the magnetic scattering processes give rise to another important phenomenon which is the so-called Kondo resonance or the Abrikosov-Suhl resonance in the impurity spectral density with a bandwidth of $k_B T_K$ [59].

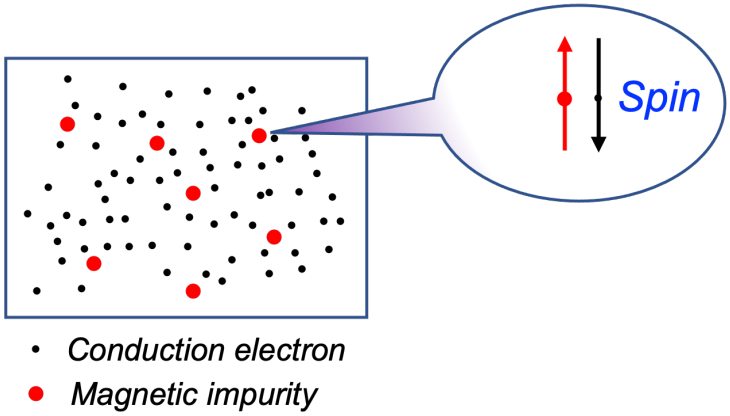

Figure 1.1: Magnetic impurities diluted in a pure metal. A magnetic impurity is coupled with a spin of a conduction electron and forms a singlet which is similar to a non magnetic impurity.

The Kondo singlet can also be destroyed by external magnetic fields. Costi found that for an impurity with $S = 1/2$, the Kondo singlet exists if the Zeeman energy roughly satisfies $g_J \mu_B |B| \leq 0.5\, k_B T_K$ or $|B| \leq k_B T_K/(2 g_J \mu_B)$ where g_J is the Landé g factor [60]. When $|B| > k_B T_K/(2 g_J \mu_B)$, the Kondo singlet is destroyed and the Kondo effect disappears.[11]

1.4 Experimental progress

The first major experiments dealing with the Kondo effect were resistivity, conductivity or susceptibility measurements in macroscopic samples. These measurements played an important role in the historical understanding of the Kondo effect but were

[11] The Zeeman energy can be compensated by applying an electric field. The Kondo resonance can then be restored but is split into 2 peaks [61, 62, 63, 64].

far from providing a complete overview of the electronic structure of the impurity. The first difficulty was to separate the electronic structure of the impurity and from the electronic structure of the matrix. The second obstacle was to separate spin and orbit magnetic moments; indeed, in most models the orbit magnetic moment was considered as zero. X-ray magnetic circular dichroism (XMCD) can probe easily a specific chemical element thanks to its excellent chemical selectivity and it is also a way to measure separately the spin magnetic moment and the orbital magnetic moment and their temperature dependence. Recently, the Kondo effect has been explored by XAS-XMCD measurements by Joly *et al.* who investigated for the first time Fe diluted in a Cu matrix and showed the evidence of the Kondo screening [33] down to $T = 2\,\mathrm{K}$. They obtained the variation of the spin and orbit magnetic moments as a function of temperature. Other interesting investigations of the Kondo effect performed by XMCD at low temperature have been published elsewhere [65, 66, 67, 68, 69]. The main difficulty for this kind of experiment is the necessity for extremely advanced cryogenics instrumentation adapted to synchrotron measurements.

1.5 Objectives of the present work

The installation of the DICHRO50 ^{3}He$-^4$He dilution variable temperature insert on the soft X-ray DEIMOS beamline at SOLEIL in February 2018 and the installation of the TBT-mK cryomagnet on hard X-ray ID12 beamline at ESRF in October 2018 made it possible to perform the XAS-XMCD measurements in the whole temperature range from the room temperature down to about 200 mK.

Chapter 2 presents the physics of the cryogenic systems that have been developed for XAS and XMCD measurements. Although a large part of the information exists in the literature, there is no general overview of the general requirement necessary for XAS, XMCD, XMLD measurements below 1 K. In addition, I provide in this chapter many information concerning specific instrumental developments and explain in details the specificity of a dilution refrigerator working in a UHV environment. I want to stress that this chapter that concerns more than 50% of my activity during this 3-year PhD thesis is certainly not a plain gathering of the existing literature but contains many additional information and gathers many instrumental information that proved to be essential for recording XAS data below 1 K.

Chapter 3 is a basic presentation of XAS, XMCD and XMLD spectroscopies that is intended to provide a general framework necessary to the self-consistency of this manuscript. The reader familiar with XAS, XMCD and XMLD can easily skip this chapter.

Chapter 4 is a presentation of the various calculations that I have been perform-

ing. All the necessary ingredients are presented with special care to the treatment of a $(2J+1)$-fold degenerate ground state in spherical symmetry with both spin-orbit coupling and Zeeman interactions. This approach is fully applicable to rare-earths where in most cases the ground state at room temperature (and below) is well described by a $J(L,S)$ multiplet. Then the crystal field is considered within the $(2J+1)$-fold degenerate ground state and the connection is made between the crystal-field split ground state and the spin and orbit magnetic moments or other operators such as J_z^2.

Chapter 5 deals with a non Kondo $Er_{0.025}Pd_{0.975}$ intermetallic alloy. We measured the XAS-XMCD spectra from 300 K down to 200 mK with an external magnetic field of ± 6.5 T. By applying the sum rules, we access the magnetic moment of the spin and of the orbit. A series of SQUID measurements has been performed from 200 mK to 4.2 K. By comparing the XMCD and the SQUID measurements, we deduce the magnetic polarization of palladium due to the erbium impurity. Comparing the experimental XMLD variation to the calculated ones, we have been able to deduce the crystal field parameters for this intermetallic alloy. I then present ligand field multiplet calculations with crystal field splitting and Zeeman splitting that yield the variation of the magnetic moment as a function of temperature and the variation of the XMLD signal as a function of temperature. Since there is no Kondo interaction, we estimate that the experimental magnetization will be close to the one calculated for an isolated atom.

Chapter 6 deals with the $Yb_{0.005}Au_{0.995}$ intermetallic alloy that is a Kondo system. We measured the XAS-XMCD spectra between 300 K and 200 mK with an external magnetic field between $+6.5$ T and -6.5 T. By applying the sum rules, we accessed to the magnetic moment of the spin and of the orbit. The ligand field multiplet calculations with crystal field splitting and Zeeman splitting yielded the variation of the magnetic moment as a function of temperature and the variation of the XMLD signal as a function of temperature. The ligand field multiplet calculations with no consideration of the conduction band is supposed to be valid when there is no Kondo interaction. We expect to observe a fair agreement between calculations and experiments at high temperature well above the Kondo temperature and a difference at low temperature side that could be interpreted as a sign of the Kondo interaction. With the formation of Kondo singlet at low temperature and the screening of the magnetic moment of the impurity, the experimental magnetic moment of ytterbium is expected to be smaller than that of the calculation. We then mimicked the Kondo screening with the model developed by K. D. Schotte and U. Schotte [70]. Additional information from the temperature dependence of the XMLD signals is also analyzed.

Chapter 2

Cryogenics Principles and Applications

Although the present chapter might look like a bibliography presentation of the cryogenic systems on which I have been working, I want to stress that it is not the case and for me it has been a full time scientific adventure. During the last 3 years, I have myself assembled most of the equipments, either on DEIMOS@SOLEIL or on ID12@ESRF. I contributed to the definition of the commissioning experiments that had to be performed. I performed the commissioning and elaborated the technico-scientific analysis. This work is extremely time consuming, not so much rewarding as for publications but it is mandatory and beneficial to the whole community when such complicated devices are developed. I also want to say that when you are that much involved in developing advanced, cryogenic prototypes, the reward stands mainly in the deep understanding of the instruments.

2.1 Motivations of the ultra-low temperature

The ultra-low temperature ($T < 1\,\mathrm{K}$) is essential for the research on magnetic properties. According to Curie's law, the paramagnetic properties of the paramagnetic materials follow the relation

$$\mathbf{M} = C\,\frac{\mathbf{B}}{T}, \tag{2.1}$$

where $\mathbf{M}$ is the magnetization, C is the Curie constant of the material, $\mathbf{B}$ is the magnetic field, T is the temperature. First, at the current stage, it is very difficult to increase the magnetic field because of the technical limit and the expensive cost. Thus, if one wants to make the magnetization $\mathbf{M}$ vary in a large range, one has to think about a better way which is changing the temperature. Although one has also to make a great effort to reach the temperature below 1 K, changing the temperature remains easier than changing the magnetic field. For example, at present, the maximal magnetic field that can be created on DEIMOS beamline at Synchrotron SOLEIL is 7 T [71] and

according to the present technique, this value can be hardly increased by a factor of 3. On the other hand, from 4.2 K, which is near the boiling point of ^{4}He at atmospheric pressure, to 200 mK, which is the actual minimal temperature on DEIMOS beamline, a factor of 20 in magnetization is obtained effectively. Moreover, this performance can still be improved if we update the temperature shielding system which allows to achieve a lower limit of temperature.

Second, the matter approaches his fundamental state when the temperature gets close to the absolute zero. For many systems, the separation energy of the ground state and the first excited state is less than 1 meV. The measurements at ultra-low temperature allow separating the contributions of the ground state and that of the excited states. With the energy-temperature conversion (if $T = 300\,\mathrm{K}$, $k_B T \simeq 25\,\mathrm{meV}$), one knows that the temperature below 1 K is essential.

Third, for the magnetic phenomena such as spin transition, metal-insolator transition, magnetic ordering, relaxation of the metastable state, superconductivity, and Kondo effect, in many cases the critical temperatures are below 1 K. Here is an example of the relaxation of the metastable state (Figure 2.1). The magnetization curves of the Fe_4 monolayer molecules are measured by XMCD at a temperature between 350 mK and 900 mK. One can easily notice the impact of temperature with the fact that the magnetization curves highly depend on temperature between 500 mK and 900 mK, so that the ultra-low temperature is necessary and important for the measurements of magnetic properties of such systems.

2.2 Cryogenics principles

2.2.1 Properties of ^{4}He and ^{3}He at ultra-low temperature

To access the ultra-low temperature, the properties of cryoliquids are radically important. Helium is used in all refrigeration methods for $T < 10\,\mathrm{K}$ as an intermediate or final refrigeration stage [72]. ^{4}He has a unique stable isotope: ^{3}He. Helium gas is one of the gases which are most difficult to liquefy since under atmospheric pressure, the boiling point of ^{4}He is 4.2 K and that of ^{3}He is 3.19 K. These two isotopes of helium cannot be solidified under their own vapor pressure even at the absolute zero. ^{4}He becomes superfluid below 2.1768 K and ^{3}He becomes superfluid below 2.5 mK [72].

The "CroMag" cryomagnet on DEIMOS beamline works with two cooling modes: the ^{4}He pumping cooling mode and the ^{3}He – ^{4}He dilution mode. The following section presents the cryogenic principles of these the two cooling modes.

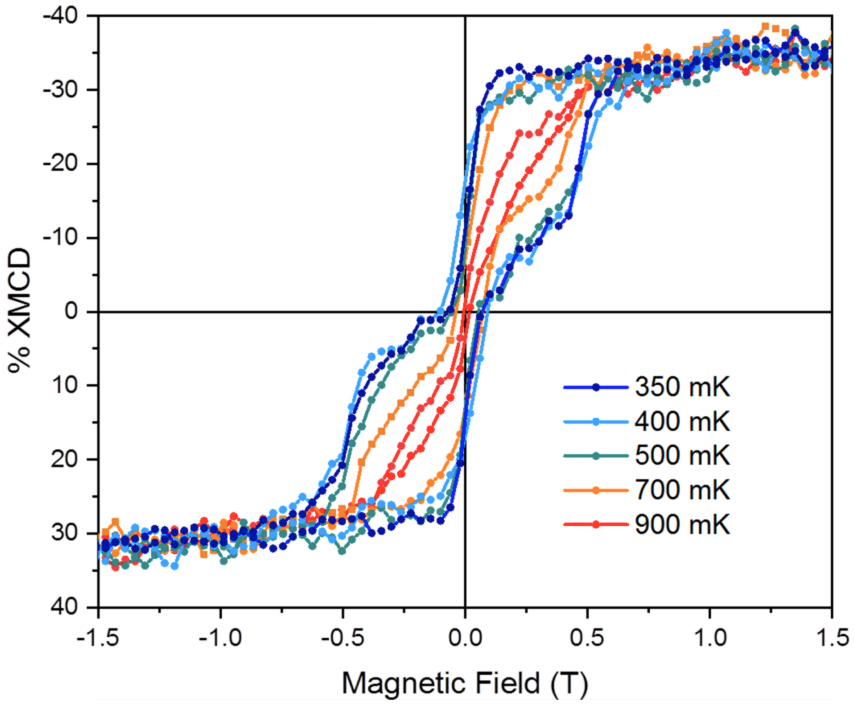

Figure 2.1: XMCD-detected magnetization curves of a monolayer of Fe_4 molecules in the 350-900 mK range. [36]

2.2.2 The pumping cooling mode

The sum of the enthalpy and the latent heat of evaporation of ^{4}He vary considerably with temperature. This makes the cooling performance with ^{4}He very powerful. In quantitative terms, the enthalpy variation of 1 kg of ^{4}He between the liquid phase at 4.2 K and the gaseous phase at 300 K is 1571 kJ which consist of 21 kJ of evaporation latent heat at 4.2 K and 1550 kJ of enthalpy variation between the gaz phase at 4.2 K and the gaseous phase at 300 K.

On the other hand, the latent heat of ^{4}He at low temperature is very small and quasi independent of temperature between 0 K and 4.2 K (Figure 2.2) which means the liquid ^{4}He is quite easy to evaporate. The dip in the ^{4}He latent heat curve is due to the transition between the normal fluid (denoted ^{4}He I) and the superfluid (denoted ^{4}He II) at 2.1768 K. The Clausius-Clapeyron equation is

$$\frac{\mathrm{d}P}{\mathrm{d}T} = \frac{S_{\mathrm{gas}} - S_{\mathrm{liq}}}{V_{\mathrm{gas}} - V_{\mathrm{liq}}}, \tag{2.2}$$

where P is the saturated vapor pressure, T the temperature of ^{4}He vapor, S the entropy and V the molar volume. With the approximation $V_{\mathrm{gas}} \gg V_{\mathrm{liq}}$ we have $V_{\mathrm{gas}} - V_{\mathrm{liq}} \approx V_{\mathrm{gas}}$. With the consideration of reversible process of entropy at constant pressure, we

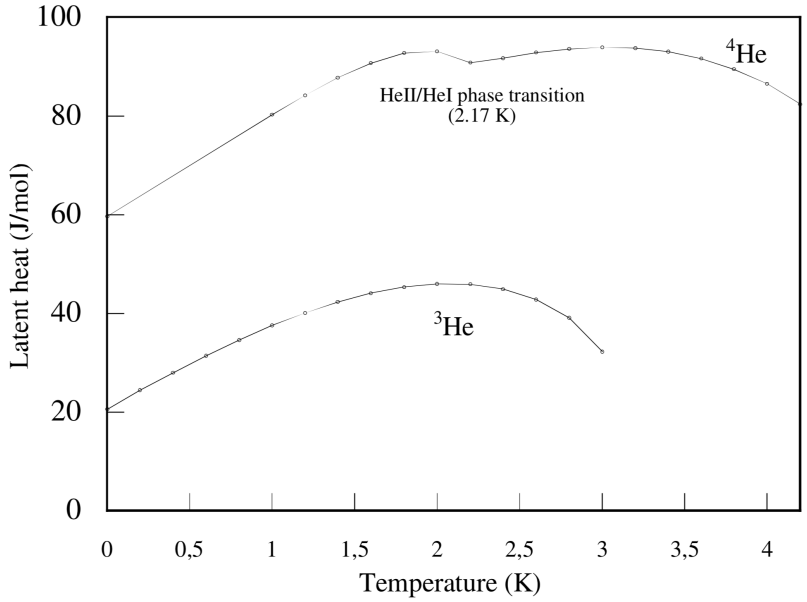

Figure 2.2: Variation of the latent heat of ^{4}He and ^{3}He at low temperature. [73]

have $S_{\text{gas}} - S_{\text{liq}} = L/T$, where L is the latent heat. If we consider ^{4}He gas as an ideal gas, with the ideal gas equation $V_{\text{gas}} \approx RT/P$, we deduce

$$\frac{\mathrm{d}P}{\mathrm{d}T} = \frac{S_{\text{gas}} - S_{\text{liq}}}{V_{\text{gas}} - V_{\text{liq}}} = \frac{LP}{RT^2} \tag{2.3}$$

where $R = 8.314\,46\,\mathrm{J \cdot mol^{-1} \cdot K^{-1}}$ is the ideal gas constant. Since the latent heat of evaporation is quasi independent between 0 K and 4.2 K, we can approximate the latent heat by an average value L_{av} which is 88 J/mol or 22 kJ/kg which is very close to the value of that at 4.2 K: 21 kJ/kg. With this approximation, the integral of (Eq.2.3) gives

$$\frac{P}{P_0} \simeq \exp\left[\frac{L_{\text{av}}}{R}\left(\frac{1}{T_0} - \frac{1}{T}\right)\right]. \tag{2.4}$$

Equation 2.4) shows that the lower the pressure on the ^{4}He bath, the lower the temperature. Theoretically, one can access a temperature as close as wanted to the absolute zero by pumping ^{4}He. But in reality, the technical limit of pressure that one can apply on ^{4}He is in the range of milibar. With the relation between the vapor pressure and the temperature (Figure 2.3), the lowest temperature that one can obtain with this cooling mode is between 1 K and 1.5 K according to the pumping performances. This cooling mode is a very efficient method to reach temperatures between 4.2 K and 1 K.

According to the relation between the vapor pressure and the temperature (Figure 2.3), the cooling performance can be improved if one uses ^{3}He liquid as the cryoliquid

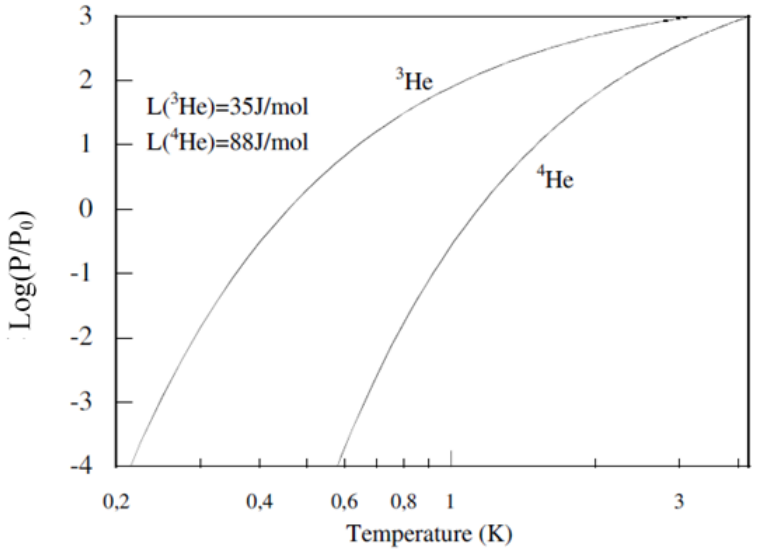

Figure 2.3: Vapor pressure as a function of temperature for liquid ^{4}He and liquid ^{3}He at low temperature. $P_0 = 1$ mbar. [73]

instead of ^{4}He liquid. The temperature limit can reach 0.3 K with ^{3}He. However, the isotropic abundance of ^{3}He is only 2×10^{-6} [74] so that ^{3}He costs a huge amount. For example, ^{3}He costs $\approx 100\,000$ € per mole while ^{4}He costs less than 0.4 € per mole. The little abundance of ^{3}He is a serious problem for the continuous research on ultra-low temperature. Several cryostats working with ^{3}He pre-cooled by a ^{4}He bath [75, 76, 77, 78] have been made, and this cooling mode was used quite frequently until the 1960s. However it is common today to use a ^{3}He – ^{4}He dilution refrigerator, which will be the subject of next part, since the ^{3}He – ^{4}He dilution refrigerator does not lose ^{3}He (^{3}He is recycled) and in principle, a lower temperature can be obtained with such a cryostat.

2.2.3 The ^{3}He – ^{4}He dilution cooling mode

The ^{3}He – ^{4}He mixture

The ^{3}He – ^{4}He dilution cooling mode is made for accessing temperatures below 1 K. The phase diagram (Figure 2.4) shows the thermodynamic properties of the ^{3}He – ^{4}He mixture below 1 K. We define x the mole fraction of ^{3}He by

$$x = \frac{n_3}{n_3 + n_4}, \tag{2.5}$$

where n_3, n_4 are the number of moles of ^{3}He and ^{4}He. The point at $x = 0.669$, $T = 0.827$ K separates two phases :

- If $T > 0.827\,\mathrm{K}$, either in the superfluid ^{3}He$-^4$He phase or in the normal fluid ^{3}He$-^4$He phase, there is only one phase of mixture ^{3}He$-^4$He for any mole fraction of ^{3}He and ^{4}He in the mixture.

- If $T < 0.827\,\mathrm{K}$ and the mole fraction of ^{3}He x is smaller than 6.4%[1], there is only one phase of ^{3}He$-^4$He mixture and the concentration of ^{3}He x is below 6.4%. However if the mole fraction of ^{3}He is larger than 6.4%, there is always a separation of two phases: one phase rich in ^{3}He that is almost pure ^{3}He for $T \leq 0.2\,\mathrm{K}$. One phase poor in ^{3}He but for which the ^{3}He concentration is always larger than 6.4% even at the absolute zero. This phenomena is an important property for the ^{3}He$-^4$He dilution process.

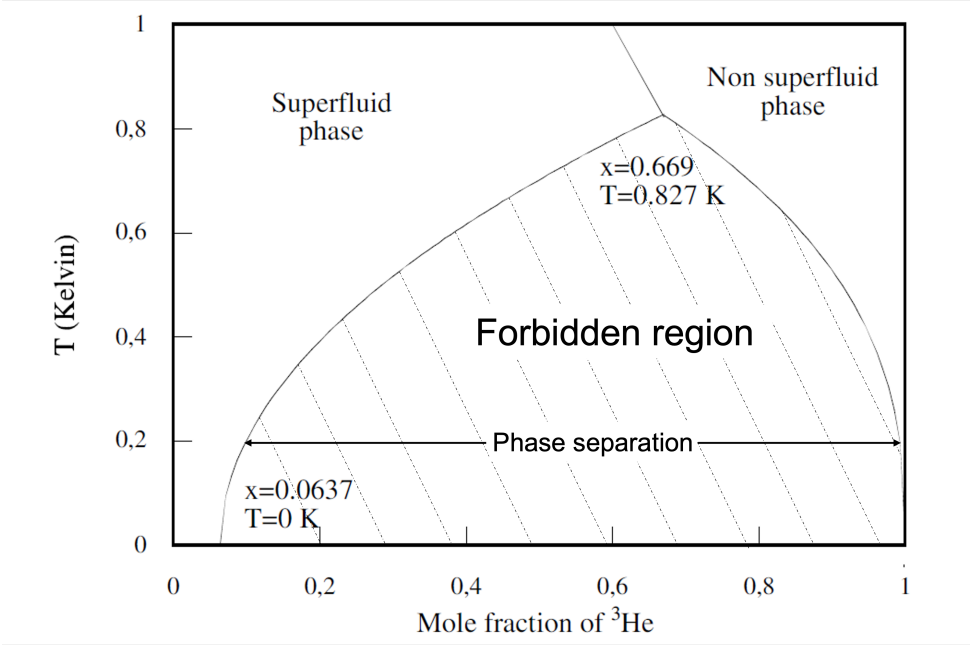

Figure 2.4: Phase diagram of ^{3}He$-^4$He mixture below 1 K. [73]

This phenomena can be explained by two facts: the van der Waals forces and the zero point energy. For the van der Waals interactions, ^{3}He and ^{4}He isotopes have the same atomic number hence the same electronic configuration. The complete-filled 1s-shell makes the polarisability of ^{3}He and ^{4}He very small. For comparison, the van der Waals interaction of hydrogen is very weak, but that of helium is even more than ten times weaker. For the zero point energy, we consider that the helium isotope atoms are confined in the radius of a sphere $a = \sqrt[3]{V_\mathrm{m}/\mathcal{N}_0}$, where V_m is the molar volume and $\mathcal{N}_0 = 6.022 \times 10^{23}\,\mathrm{atom/mol}$ is the Avogadro number. With the one-dimension box model, the zero point energy of the isotope is $E_0 = h^2/(8ma^2)$, where m is the mass of isotope. At the absolute zero, the molar volumes of ^{3}He and that of ^{4}He are

[1]This value varies between different experiments from 6.4% to 6.8% [37, 79, 80]. Here we make $x = 6.4\%$ [81] as reference value.

36.84 cm^3/mol and 27.58 cm^3/mol which lead to a difference of 10% between these helium isotopes. The zero point energy of ^{3}He is larger than that of ^{4}He so that the interaction of ^{3}He – ^{4}He atoms is weaker than that of ^{4}He – ^{4}He. This makes it easier for the ^{3}He atom to locate among the ^{4}He atoms rather than among the ^{3}He atoms.

For the following discussion, we denote "3" for the pure ^{3}He, "3c" for the concentrated phase of ^{3}He and "3d" for the dilute phase of ^{3}He in the index notations. Specifically at $T = 0$, we denote $L_{3c}(0) = L_3(0)$ for the latent heat of ^{3}He. The chemical potential of ^{3}He is given by $\mu_{3c} = -L_3$. To remove a ^{3}He atom from the concentrated phase into vacuum, the amount of energy required is $L_3(0)/\mathcal{N}_0$.

For the dilute phase, the binding energy of a ^{3}He atom in ^{4}He liquid with mole fraction of ^{3}He $x \to 0$ is

$$\frac{\mu_{3d}(0)}{\mathcal{N}_0} = -\epsilon_{3d}(0). \tag{2.6}$$

With the discussion above, the facts that a ^{3}He atom has more stability in the ^{4}He than in ^{3}He can be written by $L_3(0) < \epsilon_{3d}(0)$ as we can see in Figure 2.5.

However, the dissolution of ^{3}He atoms cannot be unlimited. Firstly, the attractive magnetic interaction between the ^{3}He atoms and the density effect of the ^{3}He atoms in the ^{4}He liquid tend to assemble the ^{3}He atoms in the ^{4}He liquid. The origin of the density effect is that the zero-point energy of the ^{3}He atom is larger than that of the ^{4}He so that the liquid near to a ^{3}He atom is more dilute than that near to a ^{4}He atom. Two ^{3}He atoms tend to combine together since they remain more stable than when each one of them surrounded by ^{4}He atoms. Consequently, the binding energy of ^{3}He decreases with more and more ^{3}He atoms diluted in ^{4}He liquid which satisfies the inequality $-\epsilon_{3d}(x) < -\epsilon_{3d}(0)$.

Secondly, a ^{3}He atom is a fermion and it must obey Pauli exclusion principle. The same energy state can only be occupied by two ^{3}He atoms at maximum which means μ_{3d} should be with the consideration of the Fermi energy $E_F = k_B T_F(x)$. At equilibrium, the chemical potential should satisfy the relation

$$\mu_{3c} = \mu_{3d}, \tag{2.7}$$

and this equality leads to

$$\frac{\mu_{3d}(x)}{\mathcal{N}_0} = -\epsilon_{3d}(x) + k_B T_F(x_d). \tag{2.8}$$

For a unity of volume $(2\pi)^3/\mathcal{V}$, the quantity of ^{3}He atoms n_3 in a sphere volume of $4\pi k_F^3/3$ is

$$n_3 = 2\,\frac{4\pi k_F^3}{3}\,\frac{\mathcal{V}}{(2\pi)^3} \tag{2.9}$$

where the prefactor 2 signifies two ^{3}He atoms in the same transitional state with the consideration of Pauli's exclusion principle. With (Eq.2.9) and the relation $p = \hbar k$ and $\mathscr{V} = \frac{(n_3+n_4)}{\mathscr{N}_0} V_m$, the Fermi energy is

$$E_F = k_B T_F(x) = \frac{p_F^2}{2m_3^*} = \frac{\hbar^2}{2m_3^*}\left(\frac{3\pi^2 n_3}{\mathscr{V}}\right)^{2/3} = \frac{\hbar^2}{2m_3^*}\left(\frac{3\pi^2 x \mathscr{N}_0}{V_m}\right)^{2/3}. \tag{2.10}$$

where m_3^* is the effective mass of ^{3}He atoms. The (Eq.2.8) becomes

$$\frac{\mu_{3d}(x)}{\mathscr{N}_0} = -\epsilon_{3d}(x) + \frac{\hbar^2}{2m_3^*}\left(\frac{3\pi^2 x \mathscr{N}_0}{V_m}\right)^{2/3}. \tag{2.11}$$

Regardless of V_m and m_3^* which depend only weakly on x, we have $k_B T_F(x_d) \propto x^{2/3}$. $m_3^*/m_3 = 2.28$ at $x \to 0$ and $m_3^*/m_3 = 2.4$ at $x \to 0.064$ [82]. The term $\epsilon_{3d}(x)$ should be obtained from the experimental measurement or from a theoretical calculation. The detail of the calculation and the experimental data can be found in references [83, 84, 85, 86, 87, 88, 81]. Figure 2.5 shows that at $T = 0$ and $x = 6.4\%$, the chemical potentials of ^{3}He and ^{4}He reach the equilibrium. On the other hand, since ^{4}He atom is a boson and the binding energy does not decrease with augmentation of the quantity of ^{4}He atoms, the solubility of ^{4}He in ^{3}He tends to zero in ultra-low temperature. Consequently, if one mixes pure ^{3}He and ^{4}He, when the mole fraction of ^{3}He is larger than 6.4%, ^{3}He dilutes into ^{4}He so that the solubility of ^{3}He in ^{4}He is never vanishing.

Isenthalpic decompression

In order to work with the ^{3}He – ^{4}He dilution mode, one has to obtain the separation of the ^{3}He concentrated phase and the ^{3}He dilute phase in ^{4}He phase. The principle we use here is the Joule-Thomson effect of the isenthalpic decompression. The ^{3}He – ^{4}He mixture is compressed to about 3 bar and cooled down to 4.2 K, followed by a decompression. In such a case, the variation of the enthalpy is

$$\mathrm{d}H = T\mathrm{d}S + V\mathrm{d}P = T\left(\frac{\partial S}{\partial T}\right)_P \mathrm{d}T + \left[V + T\left(\frac{\partial S}{\partial P}\right)_T\right]\mathrm{d}P. \tag{2.12}$$

With the definition of the volumetric coefficient of thermal expansion

$$\alpha = \frac{1}{V}\left(\frac{\partial V}{\partial T}\right)_P \tag{2.13}$$

and the isobaric heat capacity

$$C_P = T\left(\frac{\partial S}{\partial T}\right)_P \tag{2.14}$$

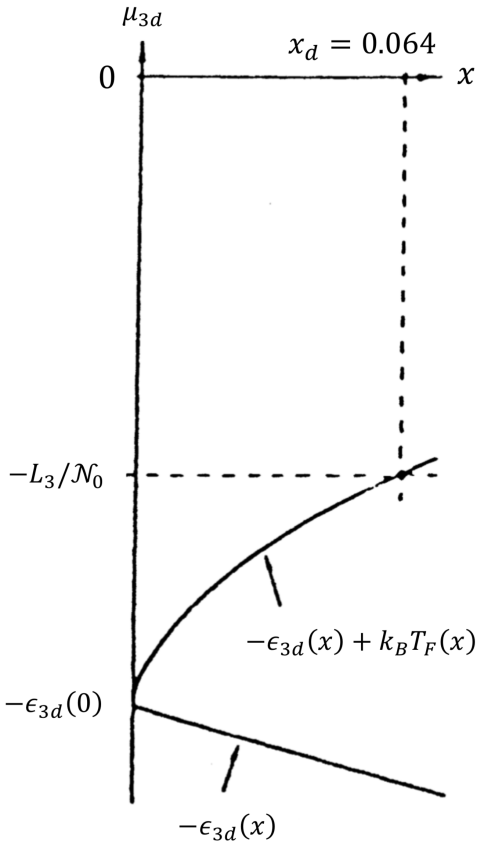

Figure 2.5: Variation of the chemical potential μ_{3d} as a function of the ^{3}He mole fraction x at $T = 0\,\mathrm{K}$. [89]

and with one of Maxwell's relations in thermodynamic

$$-\left(\frac{\partial S}{\partial P}\right)_T = \left(\frac{\partial V}{\partial T}\right)_P = \alpha V, \tag{2.15}$$

for $\mathrm{d}H = 0$, we have the isenthalpic decompression for the so-called Joule-Thomson coefficient μ_{JT} :

$$\mu_{JT} = \left(\frac{\partial T}{\partial P}\right)_H = \frac{V}{C_P}\left(\alpha T - 1\right). \tag{2.16}$$

From the preceding equation, we know that when $\alpha T - 1 > 0$, $\mu_{JT} > 0$ and the decompression leads to a decrease of temperature. This temperature is the inversion temperature which is about 50 K for ^{4}He [90]. With this method we cool down the mixture to obtain the separation of the two phases and we can also cool down the mixture below 1 K by using this method.

Osmotic pressure

Since the ^{3}He concentrated phase and the ^{3}He – ^{4}He mixture phase have different volumetric mass density and the concentrated phase of ^{3}He is lighter than the ^{3}He – ^{4}He mixture phase, the ^{3}He phase floats above the ^{3}He – ^{4}He mixture phase.

These two phases coexist in a chamber that is called the mixing chamber where we find the ^{3}He concentrated phase above the ^{3}He – ^{4}He mixture phase. The transfer of the ^{3}He atoms from the ^{3}He concentrated phase to the ^{3}He – ^{4}He mixture phase is endothermic.

An important property of the ^{3}He – ^{4}He mixture is the variation of the osmotic pressure for the different concentrations of the ^{3}He in the mixture. The liquid mixture can be considered as an ideal solution for $T \gtrsim 0.15\,\mathrm{K}$ and the mole fraction of ^{3}He $x \lesssim 0.03$ so that the osmotic pressure is described by van't Hoff's law

$$\Pi V_{3d} \simeq RT. \tag{2.17}$$

where Π is the osmotic pressure, $V_{3d} = V_4/x$ is ratio of the molar volume of the ^{4}He liquid V_4 and the concentration of ^{3}He x. This equation shows that for a fixed volume of the ^{3}He – ^{4}He mixture, the variation of the concentration of the ^{3}He in the mixture transforms to a variation of the temperature.

Notice that the van't Hoff law can describe the osmotic pressure in the still but in the mixing chamber (see Section 2.2.3), the temperature is too low compared to T_F so that van't Hoff law is no more applicable and the osmotic pressure should be obtained from measurements [37]. As it is mentioned above, when $T \simeq 0.7\,\mathrm{K}$ at the still and $T \simeq 0.1\,\mathrm{K}$ at the mixing chamber, there is an equilibrium with a concentration of 6.4% of ^{3}He in the dilute phase and the concentration of ^{3}He with $T = 0.7\,\mathrm{K}$ in the still can be deduced by

$$x_{\mathrm{st}} = x_{\mathrm{mc}} \frac{T_{\mathrm{mc}}}{T_{\mathrm{st}}} \simeq 1\% \tag{2.18}$$

where "st" is short for still and "mc" is short for mixing chamber.

Here is the mechanism of the production of the osmotic pressure: if one pumps ^{3}He from the still, the quantity of ^{3}He decreases so that a difference of osmotic pressure $\Pi_{\mathrm{mc}} - \Pi_{\mathrm{st}}$ appears. Consequently, it causes that the ^{3}He atoms move from the mixing chamber to the still. As a result, the ^{3}He atoms from the ^{3}He concentrated phase penetrate into the ^{3}He dilute phase. The movement of the ^{3}He atoms from the concentrated phase to the dilute phase leads to a variation of enthalpy so that the cooling power appears.

Cooling power

The specific heat in the concentrated phase below 40 mK can be easily deduced from references [91, 92], which is $C_3 \simeq 22T\,\mathrm{J}\cdot\mathrm{mol}^{-1}\cdot\mathrm{K}^{-1}$. The enthalpy can be calculated by

$$H_3(T) = H_3(0) + \int_0^{T'} C_3(T')\mathrm{d}T' = H_3(0) + 11T^2. \tag{2.19}$$

In the dilute phase, the liquid can be considered as a non interacting Fermi liquid with $T \ll T_F$. In fact, for $x = 6.4\%$, $T_F = 0.38\,\mathrm{K}$. For $T = 40\,\mathrm{mK}$, $T \ll T_F$ can be considered as satisfied. In this case, the specific heat is given by

$$C_{3d} = \mathscr{N}_0 k_B \frac{\pi^2}{2}\frac{T}{T_F} = \mathscr{N}_0 k_B \frac{\pi^2}{2}\frac{2m_3^* k_B}{\hbar^2}\left(\frac{V_M}{3\pi^2 x \mathscr{N}_0}\right)^{2/3} T. \tag{2.20}$$

With $m_3^*/m_3 = 2.4$ for $x = 6.4\%$ and the numerical application, we have

$$C_{3d} \simeq 106T\,\mathrm{J}\cdot\mathrm{mol}^{-1}\cdot\mathrm{K}^{-1}. \tag{2.21}$$

For the dilute phase, we have

$$\begin{aligned} H_{3d}(T) &= H_3(T) + T[S_{3d}(T) - S_3(T)] \\ &= H_3(0) + 11T^2 + T\left(\int_0^T \frac{C_{3d}}{T'}\mathrm{d}T' - \int_0^T \frac{C_3}{T'}\mathrm{d}T'\right) = H_3(0) + 95T^2 \end{aligned} \tag{2.22}$$

Since the enthalpy of the dilute phase of ^{3}He is larger than that of the concentrated phase of ^{3}He, when an atom of ^{3}He passes from the concentrated phase to the dilute phase, the increase of enthalpy is compensated by a quantity of heat Q taken away from the system so that one observes a cooling effect of the system. For one mole of ^{3}He, the heat or the enthalpy variation is:

$$Q = \Delta H = H_{3d}(T) - H_3(T) = 84T^2, \tag{2.23}$$

where Q is expressed in Joule and T in Kelvin. Comparing (Eq.2.19) and (Eq.2.22), If we define $\dot{n}$ the mole quantity of ^{3}He per second that passes from the concentrated phase to the dilute phase, we have

$$\dot{Q} = \dot{n}Q = 84\dot{n}T^2. \tag{2.24}$$

The preceding equation shows a quadratic relation between the temperature and the cooling power. For instance, if the temperature decreases by 10%, the efficiency of the cooling system decreases by 20%. The minimal temperature of the dilution is limited

by the construction, and it becomes very difficult to attain temperatures below 10 mK.

Mechanism of the ^{3}He – ^{4}He dilution in the still and in the mixing chamber

The ^{3}He – ^{4}He dilution is illustrated by Figure 2.6. Figure 2.7 is the photo of this part on the VTI of DICHRO50.

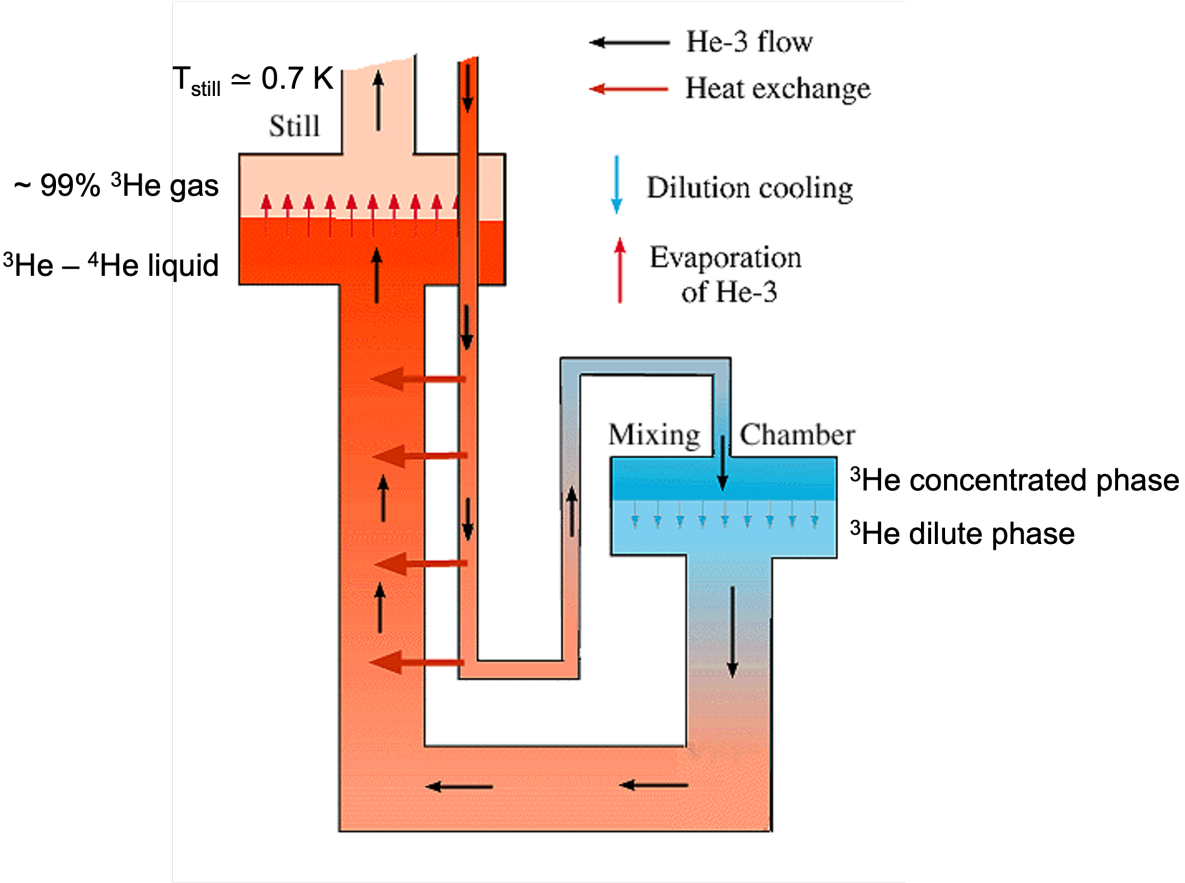

Figure 2.6: Scheme of the concepts of the dilution refrigerator. The blue color indicates the coldest zone and the red color indicates the warmest zone. In the still, there is mixture of the gaseous and liquid phase and there is only the liquid phases anywhere else [93].

The system works in a closed circuit in order not to lose any ^{3}He. In the still, the temperature is about 0.7 K and there is an equilibrium between the liquid and the gaseous phase of the ^{3}He – ^{4}He mixture. At 0.7 K, the vapor pressure of ^{3}He is larger than that of ^{4}He with nearly 99% of the vapor phase consisting of ^{3}He. One recovers mainly ^{3}He by pumping the still and consequently, the concentration of the ^{3}He in the liquid phase in the still decreases. The liquid phase in the still is at thermodynamic equilibrium with the dilute liquid phase in the mixing chamber. The decrease of the concentration of ^{3}He in the still causes the decrease of the concentration of ^{3}He

in the dilute phase in the mixing chamber. This variation of the concentration of ^{3}He in the dilute phase in the mixing chamber breaks the equilibrium of the osmotic pressure between the ^{3}He concentrated phase and the ^{3}He dilute phase. The difference of the osmotic pressure between these two phases makes the ^{3}He atoms cross the interface between the two phases and pass from the concentrated phase into the ^{3}He dilute phase and the variation of the enthalpy cools down the mixing chamber.

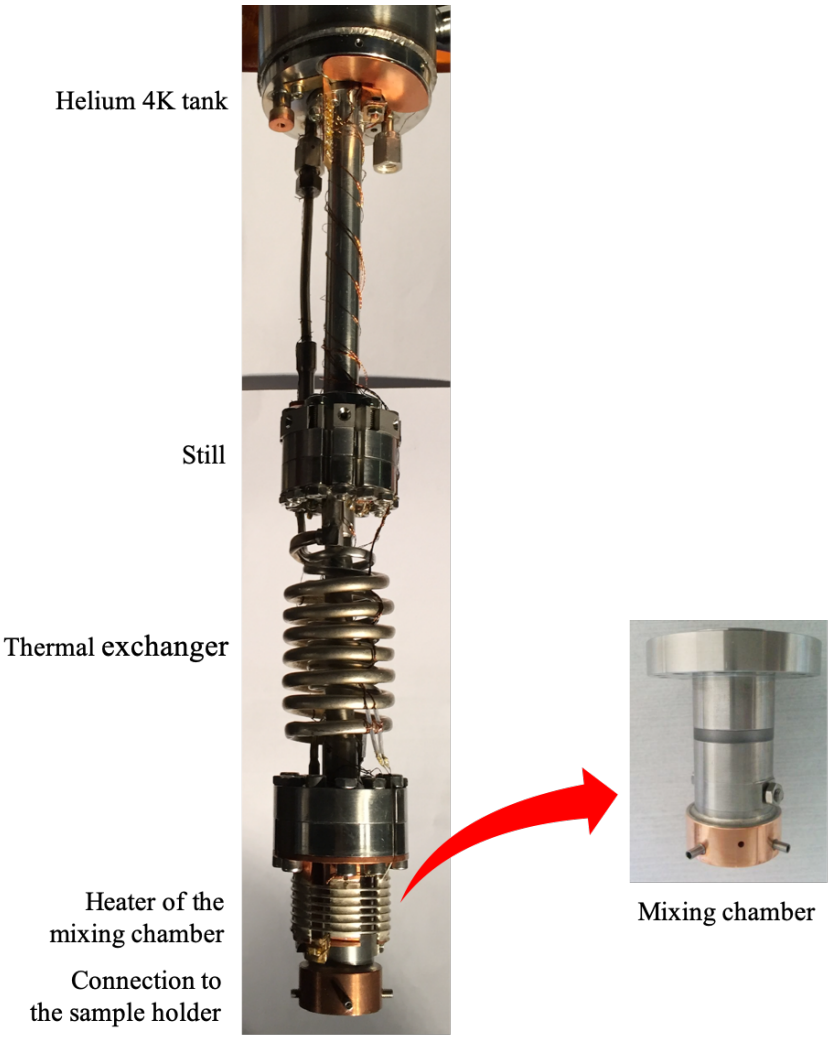

Figure 2.7: Photo of the different parts of the dilution system. The mixing chamber is equipped with a heater which controls the temperature between 0.2 K and 300 K.

The vapor exiting the still is recovered, pumped, and reinjected into the mixing chamber so that the circulation of the dilution works continuously. The mechanism of the recovery and of the pumping will be presented in the following sections.

2.3 Cryomagnet endstation on DEIMOS beamline

The present section gives a general description of the CroMag cryomagnet on DEIMOS beamline. Figure 2.8 shows the CroMag cryomagnet on DEIMOS beamline and a scheme of the CroMag cryomagnet.

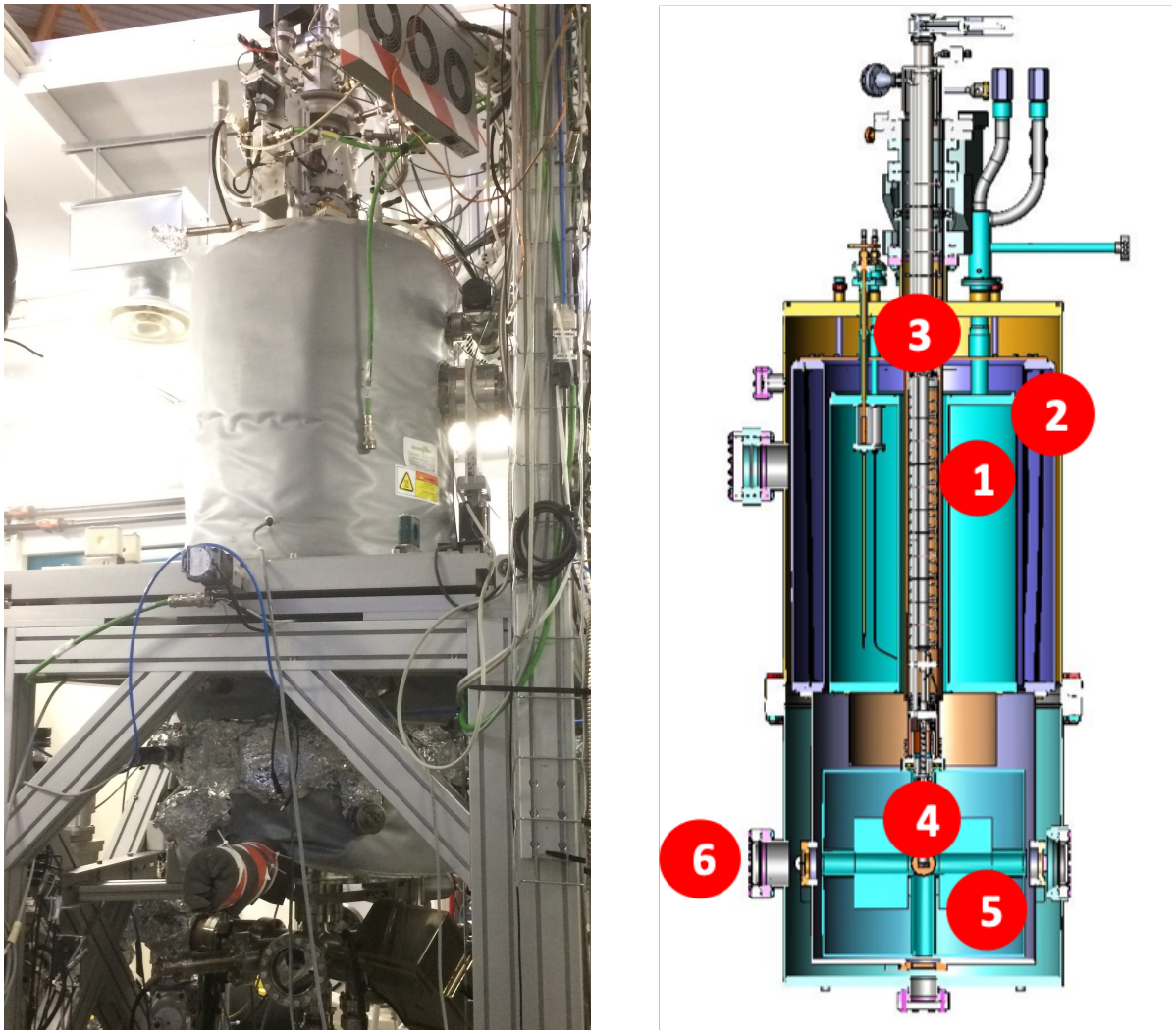

Figure 2.8: (Left) The CroMag cryomagnet on endstation of DEIMOS beamline. (Right) Scheme of the CroMag croymagnet. (1) Main reservoir of ^{4}He liquid. (2) Anti-cryostat of liquid nitrogen. (3) Dilution VTI. (4) Still, mixing chamber and sample holder. (5) Superconducting magnet. (6) Entrance of the X-ray. (DEIMOS - Synchrotron SOLEIL)

The CroMag cryomagnet consists of two parts: a superconducting magnet and a variable temperature insert (VTI). The superconducting magnet is in the 60-liter-main reservoir of liquid ^{4}He which is surrounded by a 60-liter-anti-cryostat of liquid nitrogen. The main ^{4}He reservoir provides ^{4}He for the cooling system and for thermalisation of the superconducting magnet. The anti-cryostat of liquid nitrogen is built for

primary cooling of the whole cryomagnet and for the thermal insulation between the external wall at room temperature and the ^{4}He reservoir. There are two split superconducting coils mounted on a 6 flange cross. The first magnet, the longitudinal magnet, delivers a magnetic field up to $\pm 7\,\mathrm{T}$ along the X-ray beam direction and a second one, the transverse magnet, a $\pm 2\,\mathrm{T}$ horizontal field perpendicular to the X-ray beam direction. The maximal sweeping rate of the magnetic field is $0.05\,\mathrm{T/s}$.

The lower parts of the dilution refrigerator, the still and the mixing chamber are located at the bottom of the VTI and the sample holder is screwed on the mixing chamber so that it is at the intersection of the two superconducting magnets. The dilution refrigerator is presented in 2.2.3.

The whole CryoMag chamber is maintained in a UHV environment with a typical base pressure in the low 10^{-10} mbar range. Thanks to the efficient cryogenic pumping due to the large cold surface of the 60 liters of nitrogen and the 60 liters of ^{4}He, there is no need for additional mechanical pumping that might be a source of noise, perturbing the measurements.

The CroMag cryomagnet is equipped with three types of detectors:

(i) a device for measuring the currents of the total electron yield (TEY),

(ii) a diode working in integrating mode for the total fluorescence yield (TFY)

(iii) a diode working in integrating mode for the transmitted flux for transparent samples.

The maximum flux of X-ray that arrives on the sample is in the range of 10^{12} photons/s at 750 eV. By playing with the undulator, the beam source, the monochromator, the various mirrors, and the exit slits, the flux of X-ray can be modulated from 10^7 to 10^{12} photons/s. At 750 eV, the average spectral resolution $E/\Delta E$ is about 7000 and it can be varied between 6000 and 10000 over the whole energy range.

2.4 The specificity of DICHRO50 VTI

The DICHRO50 is based on the general principles discussed at the beginning of the present chapter. However the DICHRO50 VTI has its own unique, remarkable properties. The following section presents how the ^{3}He – ^{4}He dilution principles are realized on the DICHRO50 VTI.

2.4.1 DICHRO50 VTI in the cryomagnet

Before 2018, the CroMag cryomagnet was equipped with a VTI based on the ^{4}He pumping mode which allowed cooling down to $T = 1.5\,\mathrm{K}$ (see Section 2.5). In 2013, the DICHRO50 project was launched in collaboration with ten European laboratories.

The main goal of this project was to construct a new VTI based on a ^{3}He – ^{4}He dilution principle under UHV conditions. The new DICHRO50 VTI was supposed to replace the ancient 1.5 K-VTI in the CroMag cryomagnet with significant gain in performance compared to TBT-mk that was a first version of a dilution fridge developed in 1998.

The DICHRO50 VTI was manufactured by CryoConcept and expected to achieve ultra-low temperature (50 mK) on the mixing chamber. The DICHRO50 VTI has two cooling modes: the ^{4}He pumping mode and the ^{3}He – ^{4}He dilution mode. The ^{4}He pumping mode can cool down the mixing chamber down to 1 K. In the ^{3}He – ^{4}He dilution mode, the DICHRO50 VTI could reach 180 mK after optimization of the thermal shielding, reducing eddy currents, with no X-ray beam light on the sample. In normal measurements conditions (*i.e.* with X-ray beam), the minimal temperature T_{lim} is 200 mK.

2.4.2 General layout of the dilution mode of the DICHRO50 VTI

The ^{3}He – ^{4}He dilution works in a closed cycle. We start the description of the closed cycle at the entrance of the pumping unit. The mixture is first pumped by a turbomolecular pump (PTM), supplemented by a primary pump (PPM). During the normal operation of the dilution mode, the pressure at the entrance of the PTM is in the range of 10^{-1} mbar. After exiting the PPM, the pressure of the mixture is between 500 and 100 mbar and it is compressed by a compressor above 1 bar. The compressed mixture flows through a nitrogen cold trap. It is a filter cooled by liquid nitrogen that separates eventual impurities, such as water, carbon dioxide, and oxygen that might be present in the ^{3}He – ^{4}He mixture. The purification process of the ^{3}He – ^{4}He mixture is necessary to prevent condensation of impurities that would block the extremely thin capillaries of the dilution refrigerator at temperatures lower than 4.2 K.

The compressed mixture at 300 K is first cooled by various heat exchangers down to around 4.2 K. The cooling power of the heat exchanger comes from a ^{4}He reservoir, labeled the 4K-tank. Inside of the 4K-tank, various probes measure the temperature of the tank and the helium level. The 4K-tank is alimented by the ^{4}He reservoir of the superconducting coils. Then the mixture, cooled down to around 4.2 K goes through Joule-Thompson isenthalpic decompression devices that further cool the mixture down to 1 K or 2 K (see Section 2.2.3). Then the mixture flows through the heat exchanger inside the still so that at the exit of the still exchanger, the mixture is at the temperature of the still (generally around 0.8 K). Then it flows through a continuous heat exchanger located between the still and the mixing chamber where the mixture is further cooled down to the temperature of the mixing chamber.

Then the ^{3}He – ^{4}He dilution process starts as described in Section 2.2.3. In the mixing chamber, there are two separated phases, the dilute and the concentrated ^{3}He

phases. Since the dilute phase of ^{3}He is heavier than the concentrated one, the concentrated phase floats above the dilute phase. The dilution of ^{3}He atoms from the concentrated into the dilute phase is endothermic and then cools the mixing chamber. The liquid in the dilute phase is connected to the still and because of the difference of temperature and ^{3}He concentration in the dilute phase present in the mixing chamber and the still, an osmotic pressure drives the ^{3}He molecules into the still. Between the mixing chamber and the still, the dilute phase flows through the continuous exchanger and is warmed up as it is cooling down the concentrated mixture incoming into the mixing chamber. The still temperature is around 0.8 K and 1.2 K so that the diluted mixture boils in the still : there are two phases, a liquid one and a gaseous one. The liquid phase is a dilute phase, with a small concentration of ^{3}He but since the equilibrium vapor pressure of ^{3}He is much larger than the equilibrium vapor pressure of ^{4}He, the vapor in the still mainly contains ^{3}He molecules. The gaz is then pumped by the PTM and when exiting from the dilution fridge, the cold, gaseous vapor of mainly ^{3}He molecules flows through various heat exchangers which cool the injected mixture. When entering the PTM, the mixture temperature is 300 K.

2.4.3 Pre-cooling mode of the refrigerator

One of the most important novelties for DICHRO50 is that it is equipped with a fast pre-cooling circuit provided by a double still circuitry that cools the whole system (still, continuous exchanger, mixing chamber) well below 50 K. Since the dilution VTI works under ultra-high vacuum, it cannot be pre-cooled by a cold exchange gas as it is commonly done for most applications. The pre-cooling procedure is achieved by a secondary ^{3}He – ^{4}He mixture circuit bypassing the Joule-Thomson thermal impedances. The concept of the pre-cooling mode and that of the dilution mode is presented in Figure 2.9. About 10% of the ^{3}He – ^{4}He mixture is injected into the bypass circuit, cooled down by the 4K-tank and injected directly to the mixing chamber. This pre-cooling is switched off when the temperature of the still, the continuous exchanger, and the mixing chamber is around 4.2 K.

This pre-cooling procedure is fast, 45 minutes between 300 K to 4.2 K and it is necessary any time the sample is changed since changing the sample requires to warm-up the mixing chamber to 300 K. The dilution mode starts after the pre-cooling is done (Figure 2.10).

2.4.4 Sample transfer procedure

In order to prevent the blockage between the sample holder and the mixing chamber due to the difference of the temperature, the sample should be transfered at room

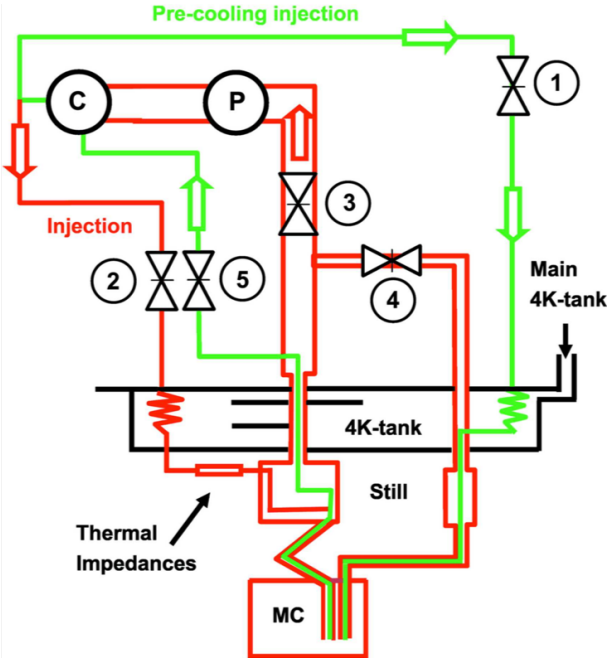

Figure 2.9: Scheme of the refrigerator circuits (Courtesy of CryoConcept). Green: pre-cooling mode. Red: dilution mode. C = compressor, P = pump and MC = mixing chamber. Black: 4 K-tank of the refrigerator, fed by the ^{4}He main reservoir. During the pre-cooling mode, the valve positions are: (1) and (5) = open; (2), (3) and (4) = closed; P = off and C = on. For the dilution mode, the valve positions are: (1) and (5) = closed; (2) and (3) = open; P = on, C = on; and (4) = open only for the pre-cooling circuit purging. [36]

temperature ($\sim$ 300 K). In other words, the mixing chamber should be warmed up to about 300 K. A heater manufactured by Thermocoax, and fixed to the mixing chamber heats it and allows to attain the higher experimental temperature for the measurements or the room temperature for the sample transfer. The principle of the heating is the Joule heating effect. The sum of the heating resistance and the resistance of the conducting wire is 63 Ω. The heater is piloted by software.

The system has a good performance for stabilizing any temperature between 200 mK to 350 K. For example, at ultra-low temperature below 1 K, the accuracy of the measure is about $\pm$25 mK. However, in the range between 1.2 K and 4.2 K, the temperature presents fluctuations because this range of temperature is above the dilution mode and below a conventional 4K-tank mode. Except for this very range, the temperature can be set to any arbitrary temperature between 4.2 K and 300 K and the stability is excellent over more than one day. Moreover, this temperature remains stable during helium refill of the main helium reservoir. Figure 2.1 shows one of the first series of measurements. The magnetic relaxation of the Fe_4 molecule has dynamic properties and strongly depends on the temperature, so that the shape of the magnetization curves are

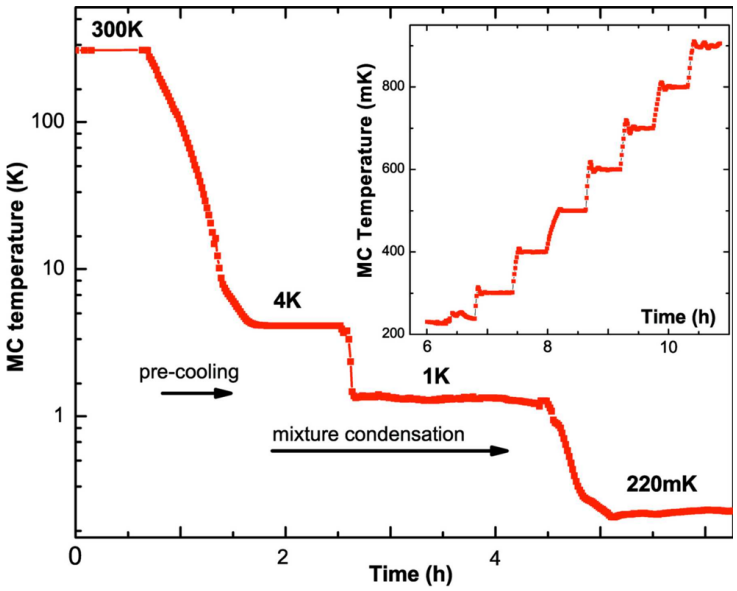

Figure 2.10: Evolution of the temperature in the mixing chamber on a logarithmic scale as a function of time during the pre-cooling and mixture-condensation procedures. Starting from 300 K, about 4 h are required to reach T_{lim}. The inset illustrates the temperature stabilization at various set points, from 200 mK to 900 mK, every 100 mK. [36]

a good indication of the temperature as can be seen for temperatures between 350 mK and 900 mK.

When the sample needs to be changed, a heating procedure starts between 4.2 K to 300 K and it lasts typically 90 minutes. When a new sample is mounted at 300 K, around three hours are needed to cool it down to ultra-low temperature, *i.e.* 0.2 K (Figure 2.10).

2.4.5 Temperature measurement in the mixing chamber

The temperature in the mixing chamber is measured with a full range thermometer sensor made by CryoConcept: it is made of a RuO_2 type resistor diode mounted in series with a silicon resistor diode. The silicon resistor measures the temperature between 4 K and 350 K. The measurement below 4 K is read by the RuO_2 resistor. In fact, the resistance of RuO_2 remains in the same range for the temperature above 4 K but it varies considerably more below 4 K especially below 100 mK as shown in Figure 2.11. This property is very favorable for the thermometry in the millikevin range. The full-range thermometer has a high sensitivity between 10 mK and 300 K and it is installed in the mixing chamber to have $T_{\text{mixing chamber}} \approx T_{\text{sample holder}}$. The precision of the thermal sensor is better than 1 mK and the uncertainty on the sample temperature depends mainly on the thermal connections between the sample and the sample

holder and on the nature of the sample itself.

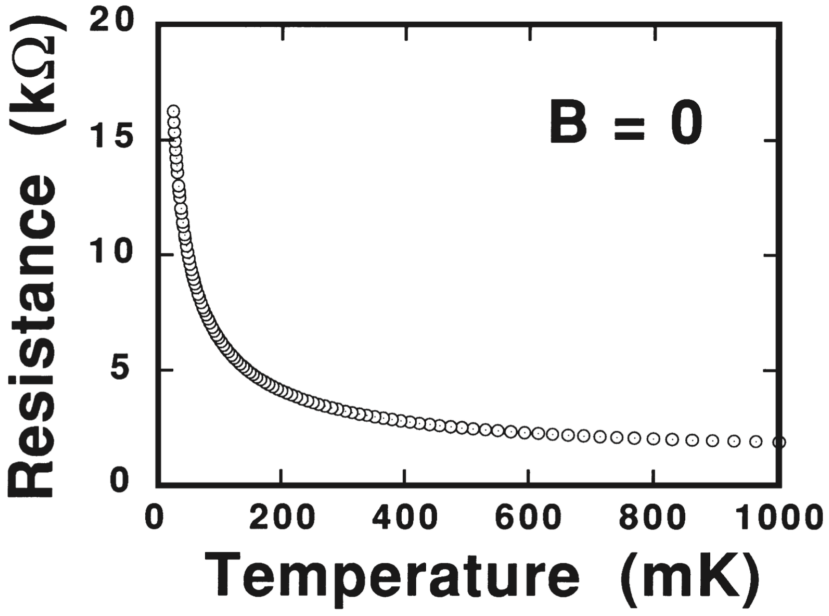

Figure 2.11: Typical resistance of RuO_2 as a function of temperature from 25 to 100 mK [94].

An additional silicon thermometer is mounted on the outside of the mixing chamber to assuring the temperature measurement. A second RuO_2 resistor measures the temperature of the still and a silicon diode measures the temperature of the 4 K-tank.

2.4.6 Cooling power of the ^{3}He – ^{4}He refrigerator and the radiation shielding

Before installation of the dilution VTI into the cryomagnet, the VTI was installed in a closed cryostat and a minimal temperature of 60 mK could be obtained in the mixing chamber. The measured cooling power was 50 μW at 100 mK and 170 μW at 200 mK. After installation in the CroMag cryomagnet, the minimal temperature was about 180 mK. The difference of performance is due to the parasite IR radiations mostly coming from the various view-ports.

Since the superconducting coils split, there are six open bores around the sample. Different thermal shields are placed in the open bores of the cryomagnet:

- A 4 K thermalized high-purity aluminum foil of 0.7 mm thickness is placed at the entrance of the X-ray beam which allows to cut the infra-red flux of the ring and also to reduce the photon flux by a factor of ten. This foil can be removed by a manipulator if one wants to avoid the transmission signals of the aluminum.

- The bore along the transfer and the back bore are closed by two retractable infrared radiation copper shields, which are thermalized the 77 K nitrogen and the 4 K helium reservoirs of the cryomagnet.

- The two bores which are perpendicular to the beam axis in the horizontal plane are made for observation of the sample during the sample transfer procedure. These bores should be shielded during the measurements. In fact, they are first shielded by a sapphire disk placed on the liquid nitrogen 77 K reservoir, and another low-pass infrared Schott filter followed by a second sapphire disk fixed on the 4 K canister (Figure 2.12). To make more protection for TEY measurements, before starting the measurements, each of these bores is covered by two black plastic lid and aluminum foil film from the outside.

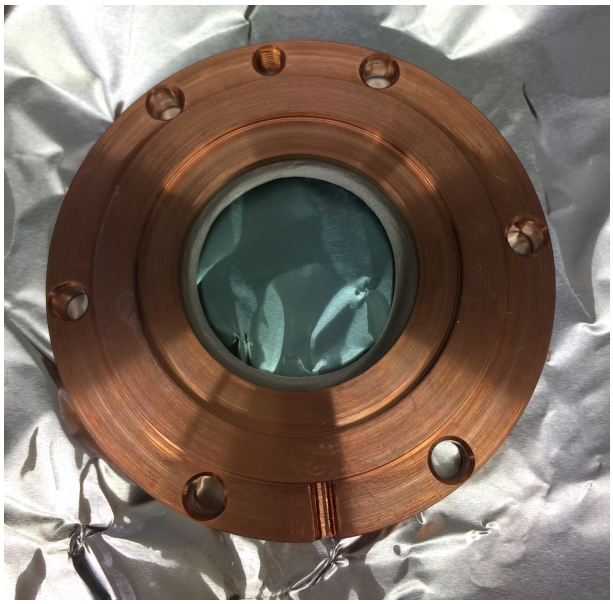

Figure 2.12: Shielding screen for the perpendicular bores with low-pass IR filter (with some green color) and sapphire disk.

Black body radiation at 300 K

For the perpendicular and horizontal bores, the thermal parasite radiation is the radiation at 300 K emitted either by the view-ports or transmitted by the view-ports. We assume that these radiations are emitted by a black body at 300 K. We can apply Planck's law:

$$B_\lambda(\lambda, T) = \frac{2hc^2}{\lambda^5} \frac{1}{e^{\frac{hc}{\lambda k_B T}} - 1}, \tag{2.25}$$

and we can obtain the distribution of the spectral radiation of the black body $B_\lambda(\lambda)$ at 300 K. Figure 2.13 shows this distribution.

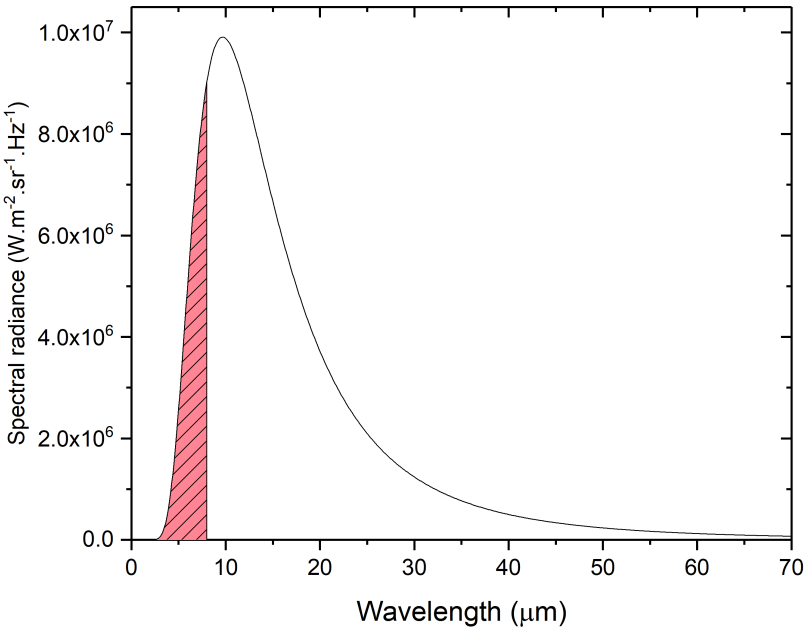

Figure 2.13: Distribution of the spectral radiance of black body at 300 K. The red part is the energy of emission by black body at 300 K that cannot be shielded by the sapphire disk.

One can calculate the derivative to obtain the wavelength for the maximal $B_\lambda(\lambda)$. Without calculating the derivative, one can also apply Wien's law:

$$\lambda_{\max} = \frac{b}{T} \tag{2.26}$$

where $b = 2.898 \times 10^{-3}$ m.K is the Wien constant. The maximum intensity is found at $\lambda = 9.6\,\mu$m which proves that the radiations are in the infra-red range.

In fact, the transmission rate of the sapphire is about 80% for $\lambda < 8\,\mu$m and about 60% for $\lambda > 90\,\mu$m. The transmission rate is almost 0 for wavelengths between $8\,\mu$m and $90\,\mu$m so that infra-red contributions are stopped. For the radiations outside the range from $8\,\mu$m to $90\,\mu$m, the infra-red Schott filter stops sensitively the infra-red radiations with wavelengths smaller than $\lambda < 8\,\mu$m or larger than $\lambda > 90\,\mu$m.

All bores, except for the upper vertical bore of the cryomagnet, are equipped with black-painted copper tubes which are very efficient in reducing the reflection of the infra-red radiations.

2.4.7 Eddy current effects

During the measurements, when the magnetic field is changing, one observes an evidence of the augmentation of the temperature as it is shown in the Figure 2.14. The reason is that the mixing chamber, the sample holder and maybe the sample itself are metallic and electric conductors which produce an electromotive force in a varying magnetic field, the so-called eddy current effect. The electromotive force generates the eddy currents on the surface of the conductor, hence the thermal energy. Eddy currents are inevitable, however, we can define experimentally an appropriate sweeping rate of the magnetic field to avoid the high increase of the temperature. The heating power is related to the magnetic field sweeping rate, the electrical conductance and some geometrical factors.

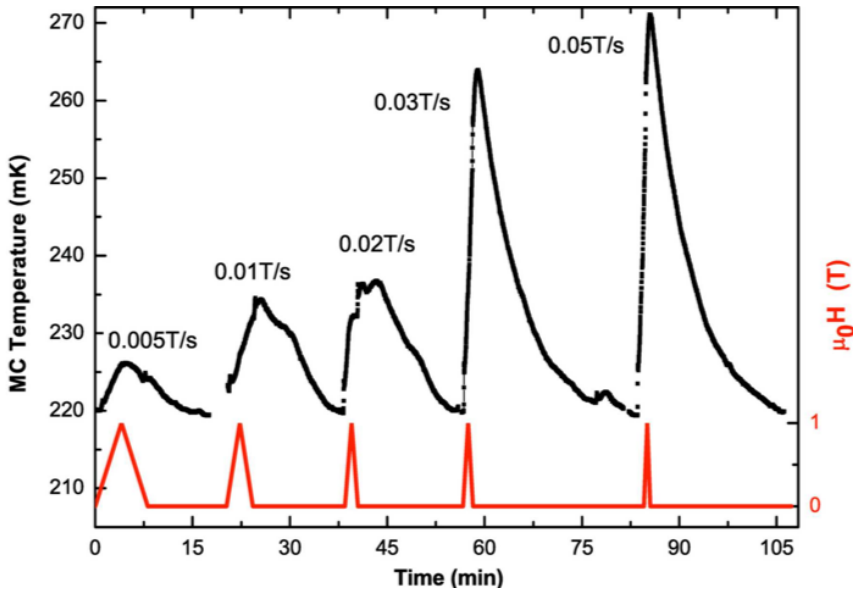

Figure 2.14: Evolution of the mixing chamber temperature for different sweeping rates of the magnetic field. For each rate, the field varies continuously from 0 T to 1 T and back to 0 T.

To minimize this effect, the sample holder and the mixing chamber are built out of a CuBe alloy (2*at*.% of Be in Cu) that reduces the conductance in the ultra-low temperature regime and correlatively, the heating power of the eddy currents, at least by a factor of ten with respect to pure cooper. The CuBe sample holder is better suited for the measurements at ultra-low temperature. Figure 2.14 shows experimental measurements of the temperature variation due to the eddy currents. For each rate, the field was varied continuously from 0 T to 1 T and back to 0 T (Figure 2.14). For $0.02\,\mathrm{T\,s^{-1}}$ sweeping rate, the temperature increase is below 20 mK, with a return to the initial temperature in 15 minutes. As we know from induction, the heating power increases

with increasing magnetic field sweeping rate. For the continuous magnetic field variations when measuring XMCD-detected magnetization curves, the sweeping rate is fixed to $0.01\,\mathrm{T\,s^{-1}}$, leading to a temperature increase of about 50 mK in the case of a magnetic loop amplitude of ± 3 T.

2.4.8 Electrical insulation

The principal detection mode is TEY (Total Electron Yield). The low-noise TEY detection requires an electrical insulation of the sample holder larger than 100 $G\Omega$. Using the experience of our previous version, we built the mixing chamber as an assembly of a top and a lower metal part, separated by a sapphire ring which ensures a quasi-perfect electrical insulation (R > 200 $G\Omega$, in the teraohm range) of the lower part of the mixing chamber, and, correlatively, a high sensitivity of the sample current measurement (a fraction of fA). This technique provides a perfect electrical insulation whatever the temperature, with a He leak rate lower than 3×10^{-10} mbar L s^{-1}. The sapphire ring also ensures an excellent thermal conduction since the hole through the sapphire permits direct contact of the cooling He mixture with the bottom of the mixing chamber where the sample holder is screwed.

2.5 The 2K VTI on DEIMOS beamline

Besides the DICHRO50 VTI, another VTI, labelled 2K VTI, can be mounted inside the CroMag cryomagnet of DEIMOS. This VTI, which works with liquid ^{4}He, provides an alternative solution to achieve the full range of the temperature from 1.8 K, the temperature of the pumped liquid helium, to room temperature. As explained in Section 2.2.2, we can achieve temperatures below 4.2 K by pumping over a liquid ^{4}He bath.

Figure 2.15 shows the extremity of the 2K VTI. The ^{4}He tank is fed by the main reservoir of liquid ^{4}He thanks to a capillary pipe controlled by a needle valve. Through a copper sample holder connector, the liquid ^{4}He cools the sample down to 4.2 K. On DEIMOS beamline, we use a primary helium pump to pump over the ^{4}He tank. A standard primary pump is able to obtain a vacuum in the range of 20 mbar, from Figure 2.3 with a simple calculation, we can obtain a temperature below 2 K in the helium bath.

A pumped ^{4}He cryostat is a rapid way to reach temperatures around 2 K. Figure 2.16 shows the time necessary to warm-up and cool-down the sample. We need about one hour and a half to cool down the sample holder from 300 K to 4.2 K and about one hour from 4.2 K to about 1.7 K. The pumping power is not easy to adjust so that the lowest temperature defined by the pumping power of the primary helium pump is

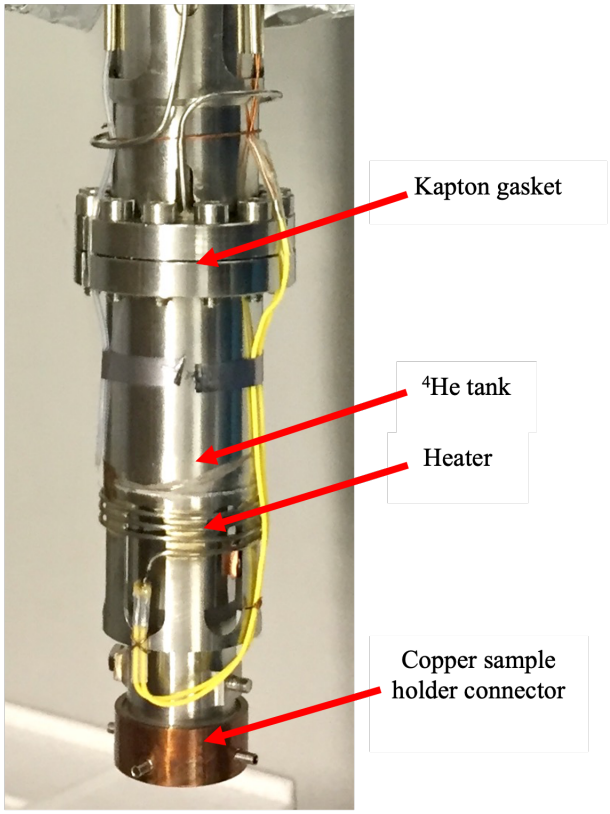

Figure 2.15: The extremity of the 2K VTI

the only really stable temperature: around 1.8 K. For temperatures between 1.8 K and 4.2 K, variations of pressure inside the 4K-tank or inside the ^{4}He magnet reservoir tend to make it difficult to stabilise the temperature.

In order to warm up the helium bath from 2 K to 4.2 K, one needs to stop the helium pumping so that the pressure inside the 4K-tank reaches atmospheric pressure. The helium bath is warmed up by its surrounding environment and the incoming liquid ^{4}He from the main helium reservoir. During this process, one can easily observe that the temperature of the helium liquid and the pressure above the liquid increase very slowly up to a certain value and then drastically increase passed this value. This value is the so-called λ point between the normal fluid and the superfluid. On DEIMOS, one observes this value at around 2.177 K, which is very close to the common value 2.168 K in the reference [72]. This proves the excellent calibration of the DT600 silicon diode temperature sensor. From the evolution of the temperature recorded as a function of time, Figure 2.17 shows the different variations of speed around the λ point. With a zoom around the λ point, we notice the different behavior of the variations of the temperature and the pressure for $T < \lambda$ and $T > \lambda$. This behavior can be also clearly visualized by tracing the pressure as a function of the temperature (Figure 2.17 - Bottom). Note that the data is recorded during the warming up process. To reach

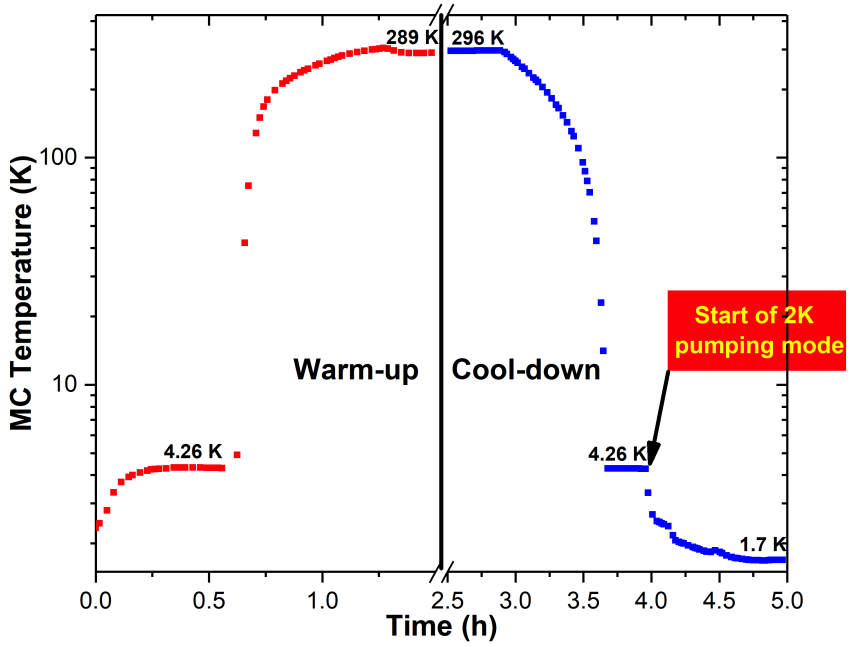

Figure 2.16: Typical evolution of the temperature as a function of time during warm-up and cool-down process.

temperatures above 4.2 K, one turns on the helium tank heater (Figure 2.15) so that the temperature can be set between 4.2 K and 300 K. It takes around 1.5 hours to warm-up a sample from 1.8 K to 300 K.

It is delicate to find a set of balanced values of the needle valve opening controlling the ^{4}He incoming debit and the heating power. On one hand, one needs to maintain a stable temperature, on the other hand, one wants to limit the ^{4}He consumption. For example, at around 2 K, if the needle valve between the ^{4}He reservoir of the coils and the 4K-tank is too much open, the "warm" liquid at 4.2 K will heat up the helium bath. If the needle valve is too much closed, the 4K-tank will get empty and the temperature will increase.

As another example, at 20 K, one can get the goal temperature by two different settings: one can fully open the needle valve and set the heater to high power or an optimised opening of the needle valve with an intermediate power of the heater. The former setting is easy to set but consumes much more liquid ^{4}He and freezes the exit pipes of the helium tank so that water condensation tends to appear at the top of the CryoMag. The latter, optimised setting is to be looked for although it can be quite tricky to find. In addition, the settings have different values from one experimental condition to another, so that the precise setting can only be determined during the experiment. Table 2.1 is an example of a series of values found during the experiments for the project N°20191826 which took place in September 2020.

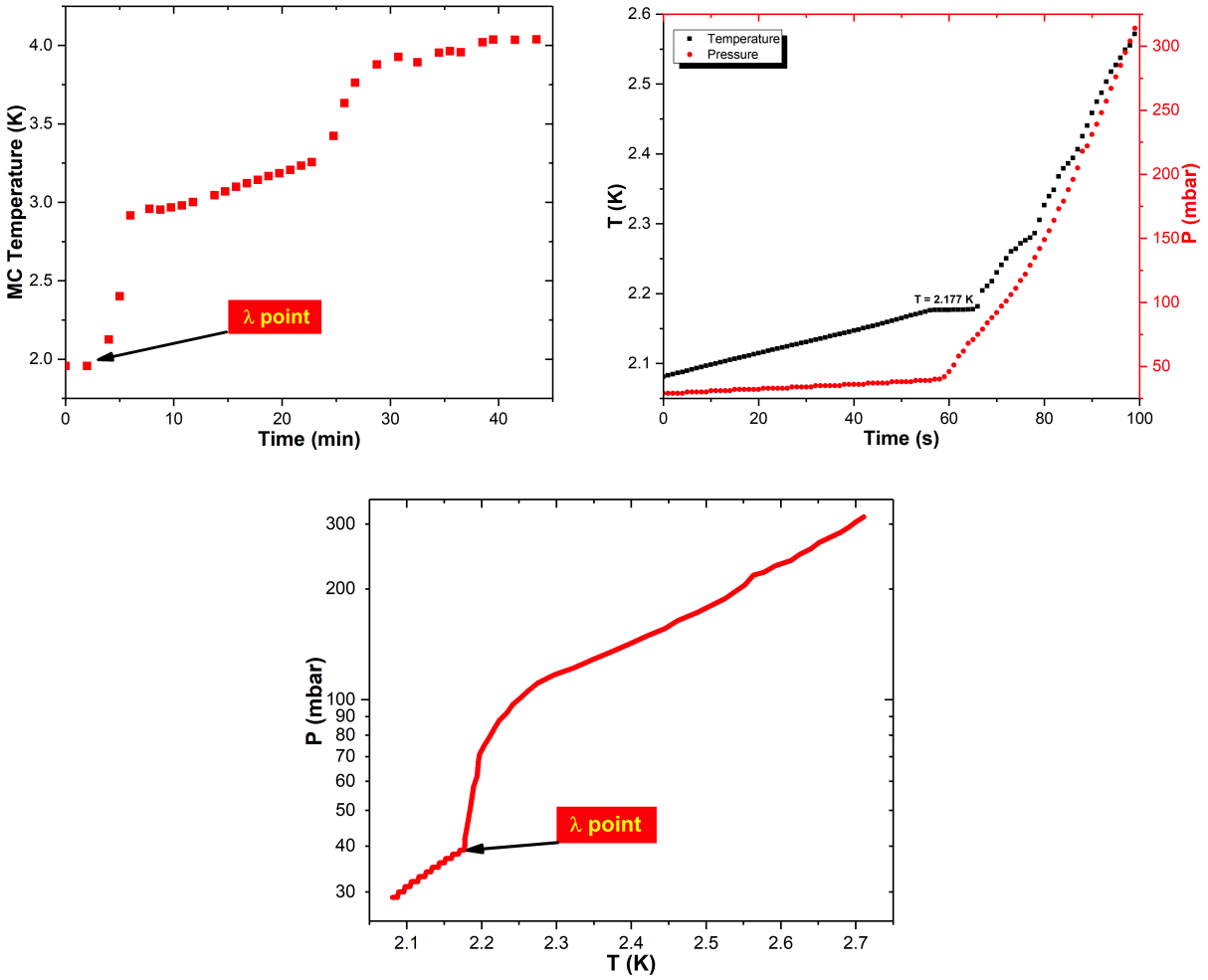

Figure 2.17: (Top-Left) Evolution of the temperature during the warm-up process. The different regimes can be seen around the λ point. (Top-Right) Zoom around the λ point with the pressure measured above the liquid ^{4}He. The λ point is measured for 2.177 K. (Bottom) Evolution of the pressure above the liquid ^{4}He as a function of the temperature.

T	$\leq$ 2 K	4 K	10 K	20 K	30 K	50 K	100 K	150 K	200 K	300 K
Opening turns	1.6	1.6	1.8	1.7	1.8	1.9	1.8	2	1.8	1.8

Table 2.1: Values of the needle valve opening (1 units of turns *i.e.* 360°, 0 is the closed position) for different temperatures when equilibrium is insured between a stable temperature, a high collection data quality for XAS, and minimal helium consumption.

Both TEY (Total Electron Yield) and TFY (Total Fluorescence Yield) detection modes have been installed on the 2K VTI. Although the main detection mode I have used for my PhD work was the TEY mode, the TFY detection mode was always present and gave complementary information.

2.6 TBT-mK cryomagnet on ID12 beamline at ESRF

Another cryomagnet called TBT-mK was developped in the 1998 by Kappler and Sainctavit [73, 31]. It was the first device in the world that allowed to cool a sample below 300 mK for XMCD measurements on a synchrotron.

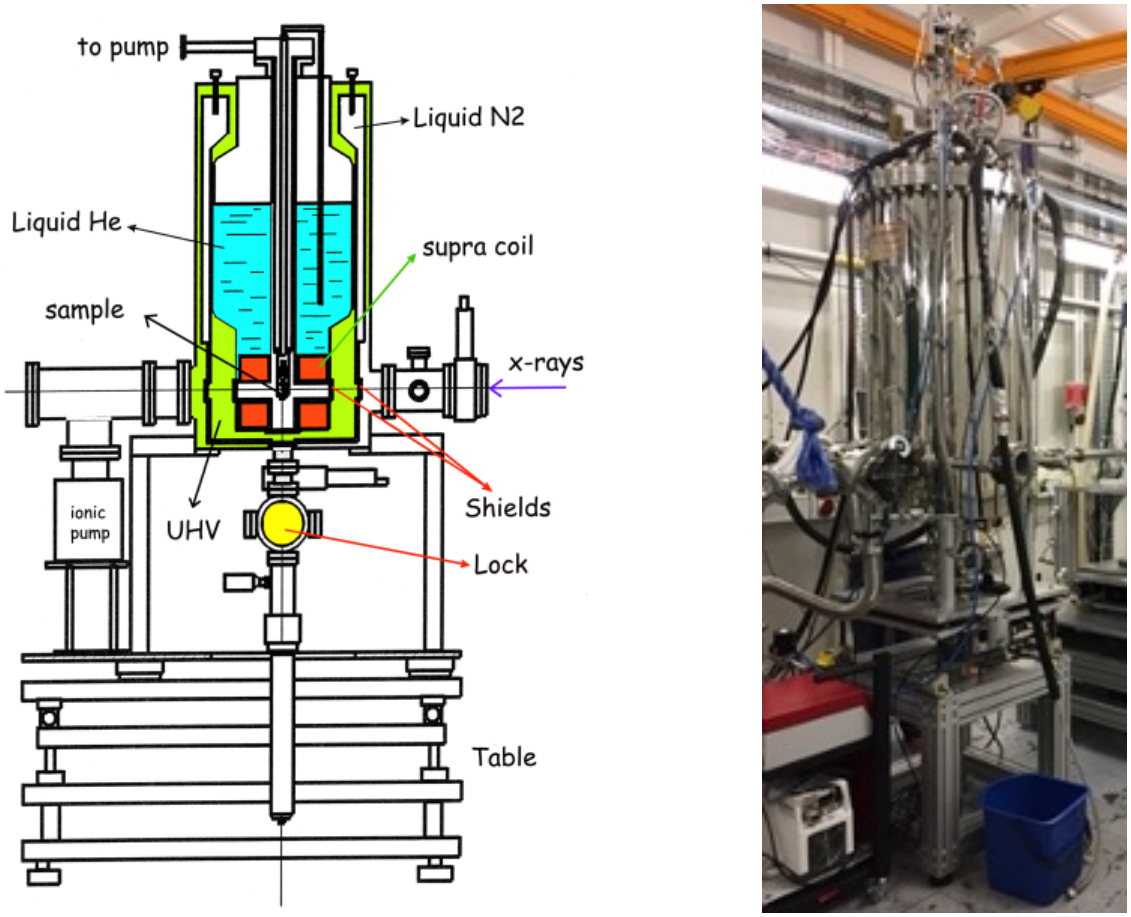

Figure 2.18: (Left) Inner structure of the TBT-mK. (Right) TBT-mK installed on the ID12 beamline at ESRF.

The TBT-mK cryomagnet is a $^3He-^4He$ dilution refrigerator that inspired the concept of DICHRO50 for DEIMOS beamline. The scheme on the left of Figure 2.18 shows the inner structure of the cryomagnet. The main difference for DICHRO50 is the connection with the helium reservoir and the 4K-tank. The TBT-mK is equipped a U-shaped helium transfer rod that connects the reservoir to the 4K-tank at the difference of DICHRO50 where the connection is ensured by a capillary circulating in the UHV chamber. The TBT-mK transfer rod can be easily dismounted so that mechanical intervention on the dilution VTI can be fast and easy to perform. The TBT-mK provides an experimental environment where the sample is sitting in 10^{-10} mbar UHV conditions with stable temperature between 260 mK and 4.2 K. Using TBT-mK for tem-

peratures below 4.2 K is absolutely optimal and other devices should be used when $4.2\,\mathrm{K} < T < 300\,\mathrm{K}$.

2.6.1 Installation on ID12 beamline and the temperature tests of the TBT-mK

First, we have adapted the TBT-mK to the ID12 configuration. The energy range of the ID12 beamline at ESRF is from 2 keV to 15 keV. For radioprotection, all measurements are performed in a hutch so that all the motors of this 20-year-old instrument have been developed to be piloted from the outside. Pascal Voisin has been essential for all these developments. The picture on the right of Figure 2.18 shows the TBT-mK cryomagnet installed on the ID12 beamline.

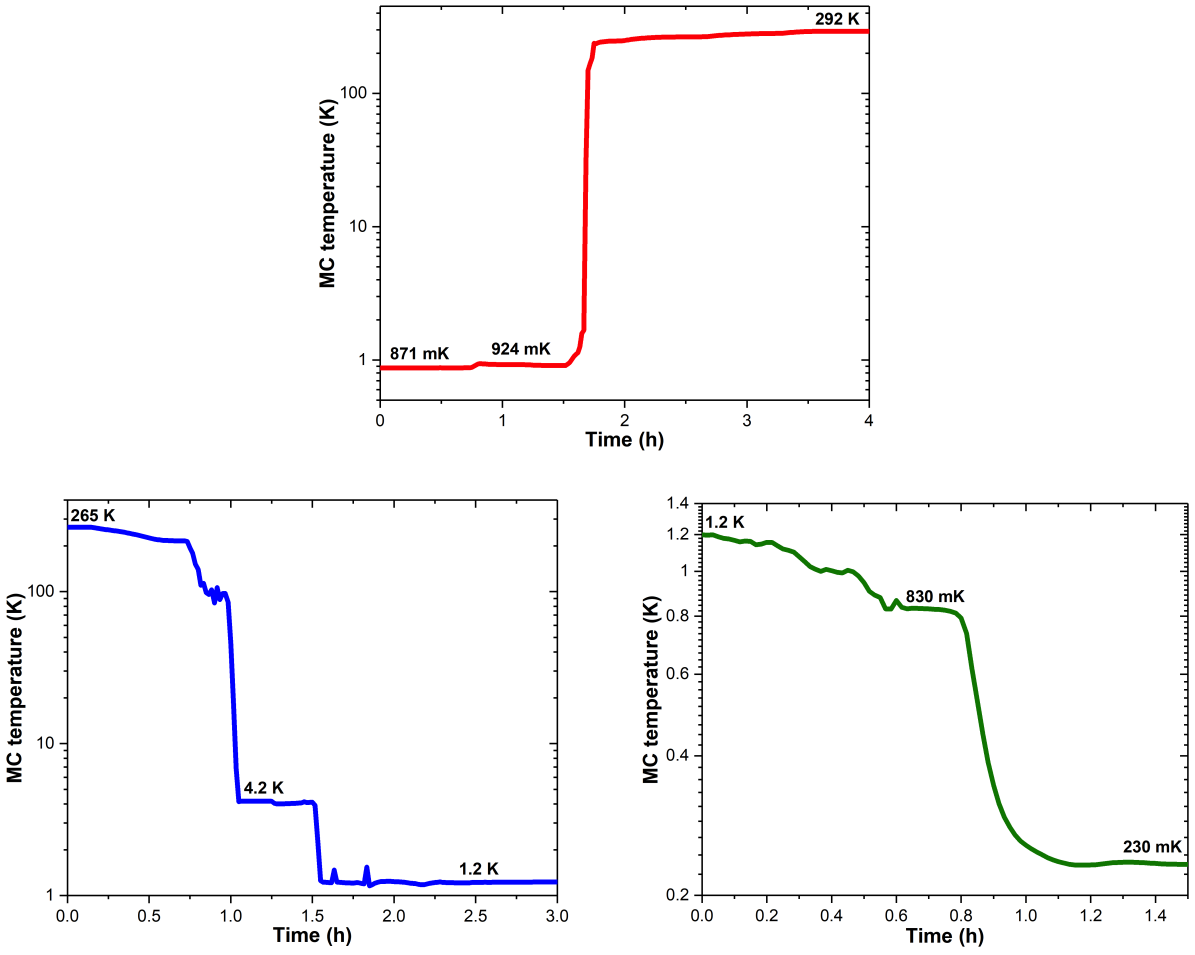

Figure 2.19: (Top) Typical warm-up process of TBT-mK. (Bottom-left) Typical cool-down process of TBT-mK from 265 K to the 1 K range. (Bottom-right) Typical cool-down process of TBT-mK from the 1 K range to the limit minimum.

The main performance improvement of the TBT-mK on ID12 beamline is the control

of the temperature. A heater with a resistance of 66 ohms has been installed for a fine tuning of the mixing chamber temperature. The time necessary to warm-up the sample from the mK range to room temperature has been reduced from more than 10 hours to 4 hours. Therefore, the time necessary for changing the sample, *i.e.* heat the sample from mK range to 300 K, change the sample, cool the sample back to mK has been reduced from more than 24 hours to 12 hours. Figures 2.19 show three typical behaviors of TBT-mK: the warm-up process, the cool-down process to 1 K and the cool-down process to about 230 mK range. The lowest temperature recorded for a sample on TBT-mK@ID12 is 197 mK and it was obtained on October 1st, 2018, at 14:20:24 : the first day of my PhD thesis.

2.6.2 Thermometry measurements of the TBT-mK

Once the TBT-mK was installed on ID12@ESRF, we started a commissioning-like measurement to determine the real temperature on the sample with comparison with the temperature given by the thermometers. In the case of hard X-rays, one expects that the heat load will be larger than what is observed in the soft X-ray range. To check for that, we performed the first XMCD measurement in a Curie-Weiss paramagnetic sample containing "isolated" rhenium ions where the paramagnetic behavior is expected to follow a Curie-Weiss law.

$[ReF_6]^{2-}$ compound sample

The sample was prepared by K. S. Pedersen from Clérac's group at the CRPP, Bordeaux. The sample formula is $(PPh_4)_2[ReF_6]\cdot 2H_2O$ where the rhenium ions are coordinated to 6 fluorine anions. In first approximation, the $[ReF_6]^{2-}$ units are isolated so that it is sensible to expect that the magnetisation of $(PPh_4)_2[ReF_6]\cdot 2H_2O$ would follow a Curie-Weiss law. The magnetic properties of the sample have been previously studied [95].

Rhenium (Re) is a third-row transition metal with an atomic number $Z = 75$. In the $[ReF_6]^{2-}$ unit, rhenium ions is in the form of Re^{4+} ion and its electronic configuration is $[Xe]4f^{14}5d^3$.

Thermometric measurements with Re-$L_{2,3}$ edges on ID12

The heater of 66 ohms can warm up the sample from 4.2 K to 300K and can also finely control the temperature below 4.2 K. For the ultra-low temperature, we achieve to first cool down the sample to the minimal temperature (i.e. around 200 mK on the sample thermometer). We then insert different attenuators of Cu or Al foils with different thicknesses between the sample and the beam in order to remove the X-ray and

check that the ultra-low temperature range is independent of the X-ray flux. The measurements for various series of attenuators was performed to provide a series of thermometric tests.

We recorded the XAS-XMCD spectra at the Re-$L_{2,3}$ edges. Figure 2.20 shows an example recorded with an attenuator of 150 μm of aluminum in an external magnetic field of 6 T. We observe that the XMCD signal of the L_2 edge is much more intense than that at the L_3. For the reader not familiar with XAS and XMCD, Chapter 3 gives a basic introduction to the method. We set the monochromator energy at $E = 11\,970$ eV and vary the external magnetic field between -6 T and 6 T and back to record the Re magnetization curves.

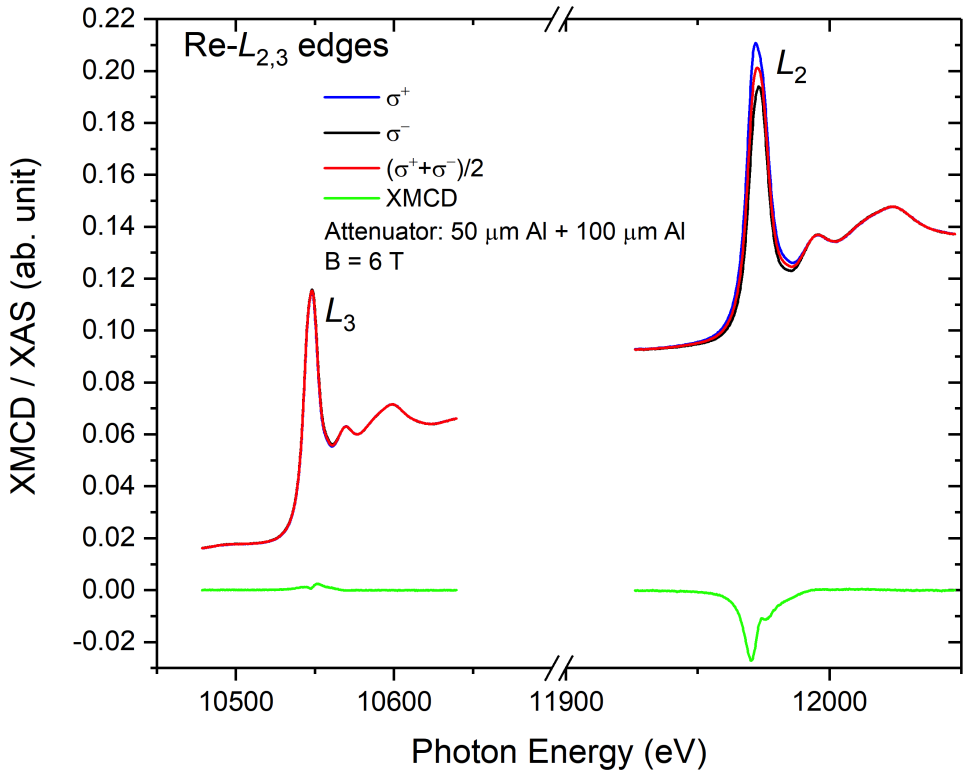

Figure 2.20: Re-$L_{2,3}$ edges at "$T = 230$ mK" displayed on the thermometer. The sample is radiated by synchrotron beam with attenuators under an external magnetic field of 6 T. The actual temperature is about 1.75 K on the sample.

With the attenuators at disposal on ID12 beamline, we performed magnetization measurements for four configurations of the attenuator filters :

- 100 μm Al + 42 μm Cu,
- 100 μm Al + 32 μm Cu,
- 20 μm Cu,
- 50 μm Al + 100 μm Al (=150 μm Al).

We can calculate for $E(L_3) = 10\,500\,\text{eV}$ and $E(L_2) = 12\,000\,\text{eV}$, the transmission rate [96] of the above attenuators in Table 2.2.

	100 μm Al	150 μm Al	20 μm Cu	32 μm Cu	42 μm Cu
$E(L_3) = 10\,500\,\text{eV}$	56%	42%	3%	0.4%	0.1%
$E(L_2) = 12\,000\,\text{eV}$	68%	55%	9%	2%	0.6%

Table 2.2: Transmission rate on Re-L_2 and Re-L_3 edges with different attenuators.

The magnetization curves for the four configuration of attenuators are reported in Figure 2.21. A calculation with equation

$$M = g\,\mu_B\,S\,B_S(x) \tag{2.27}$$

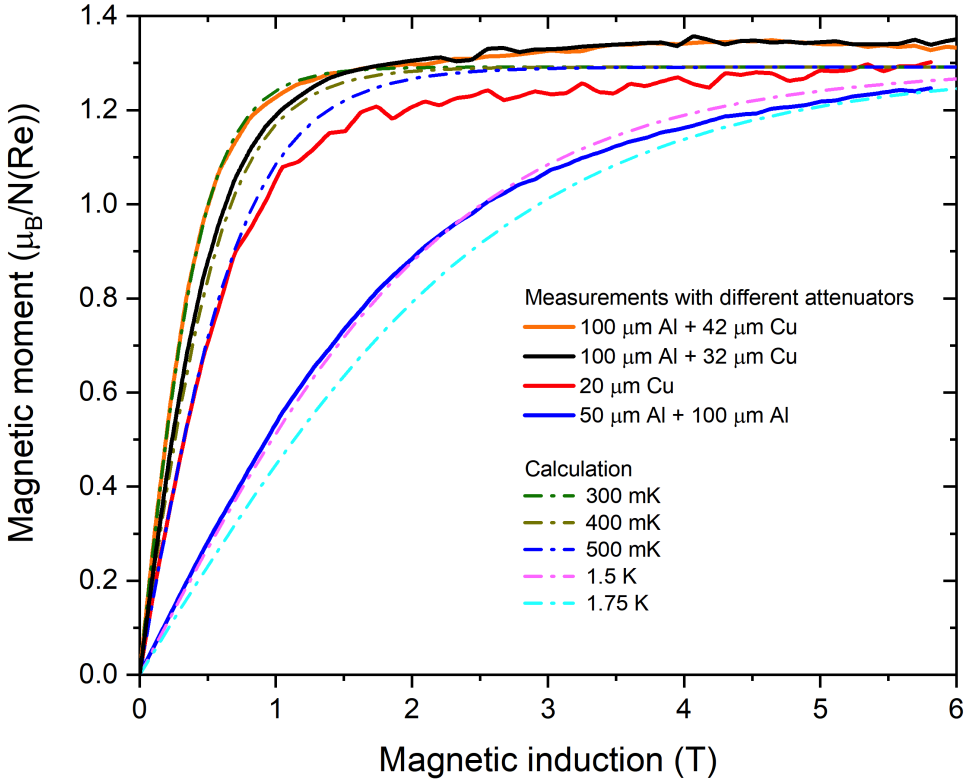

Figure 2.21: magnetization curves the four configuration of attenuators.

accompanying the measurements. $B_S(x)$ is the Brillouin function expressed as:

$$B_S(x) = \frac{2S+1}{2S}\coth\left(\frac{2S+1}{2S}x\right) - \frac{1}{2S}\coth\left(\frac{x}{2S}\right), \tag{2.28}$$

$$x = \frac{g_S \, \mu_B \, S \, B}{k_B \, T}. \tag{2.29}$$

g_S is calculated by LFM calculations by Pedersen *et al.* [95] for $g_{m_S=\pm 3/2} = 1.74$ and $g_{m_S=\pm 1/2} = 1.69$. From my experiments, g_S and S can be obtained experimentally from the sum rules (see Section 3.5) and I found $g_S = 1.53$ and S = 0.842.

	Transmission rate on L_3 edge	Transmission rate on L_2 edge	Temperature
100 μm Al + 42 μm Cu	5.6×10^{-4}	4.08×10^{-3}	300 mK
100 μm Al + 32 μm Cu	2.24×10^{-3}	1.36×10^{-2}	400 mK
20 μm Cu	3%	9%	500 mK
50 μm Al + 100 μm Al	42%	55%	1.5 K-1.75 K

Table 2.3: Performance of four attenuator configurations on Re-L_2 and Re-L_3 transmission rate and their regulation on temperature.

With these values for g and S, it is possible to fit the experimental data presented in Figure 2.21 and then determine the real temperature of the sample for the four sets of attenuators. The data are gathered in Table 2.3. **The main conclusion of the present ID12 measurements is that in order to obtain the lowest possible temperature for an XMCD measurement in the hard X-ray range, one needs to reduce drastically the X-ray flux**.

2.7 Conclusion

CroMag-DICHRO50 on DEIMOS@SOLEIL for soft X-ray XMCD and TBT-mK on ID12@ESRF for hard X-ray XMCD are two unique instruments in the world for synchroton XAS measurements below 1 K. Although the cooling principle is quite common to the typical cryostat, the adaptation on a synchrotron does make a great challenge since the dimension and the geometry as well as the thermal isolation from the outside are completely different from those of a typical cryostat. During my PhD work, these two machines have been well installed on two synchrotron beamlines and they work well.

These two outstanding instruments will make the following projects possible : investigation of the Kondo effect in diluted systems (CuFe [33], YbAu, $La_{1-x}Ce_xB_6$, *etc.*), Kondo lattices (CeB_6), monolayers of single molecule magnets (SMM) [97], prussian blue analogue nanocrystals assembled as a single monolayer [98], light-induced spin-state spin-crossover properties [99], ultra-thin film spin-crossover molecules on metal surfaces [100], photomagnetic prussian blue analogue [101].

Publication.

Journal of Synchrotron Radiation

ISSN 0909-0495

Ultra−low temperature device dedicated to soft x-ray Magnetic Circular Dichroism experiments

J.-P. Kappler,[1] E. Otero,[1]* W. Li,[1] L. Joly,[1,2] G. Schmerber,[2] B. Muller,[2] F. Scheurer,[1,2] F. Leduc,[1] B. Gobaut,[1] L. Poggini,[3] G. Serrano,[3] F. Choueikani,[1] E. Lhotel,[4] A. Cornia,[5] R. Sessoli,[3] M. Mannini,[3] M.-A. Arrio,[6] Ph. Sainctavit[1,6] and P. Ohresser[1]

[1]Synchrotron SOLEIL, L'Orme des Merisiers, BP48, 91192 Gif-sur-Yvette, France, [2]Université de Strasbourg, CNRS, Institut de Physique et Chimie des Matériaux de Strasbourg, UMR 7504, 23 rue du Lœss, 67034 Strasbourg, France, [3]Department of Chemistry "U. Schiff" and INSTM RU, University of Firenze, Via della Lastruccia n. 3, 50019 Sesto Fiorentino (FI), Italy, [4]Institut Néel, 25 rue des Martyrs, 38042 Grenoble, France, [5]Department of Chemical and Geological Sciences and INSTM RU, University of Modena and Reggio Emilia, via G. Campi 103, I-41125 Modena, Italy, and [6]Institut de Minéralogie, de Physique des Matériaux et de Cosmochimie, CNRS, Sorbonne Université, IRD, MNHN, UMR 7590, 4 place Jussieu, 75252 Paris cedex 05, France. Correspondence e-mail: otero@synchrotron-soleil.fr

A new ultra−low temperature set-up dedicated to soft X-ray Absorption Spectroscopy and X-ray Magnetic Circular Dichroism (XMCD) experiments is described. Two experiments, performed on the DEIMOS beamline (SOLEIL synchrotron), demonstrate the outstanding performances of this new platform, in terms of the lowest achievable temperature under x-ray irradiation (T=220 mK), the precision in controlling the temperature during measurements as well as the speed of the cooling down and warming up procedures. Moreover, thanks to the new design of the set-up, eddy current power is strongly reduced allowing fast scanning of the magnetic field in XMCD experiments; these performances lead to a powerful device for x-ray spectroscopies on Synchrotron Radiation beamlines facilities.

© 0000 International Union of Crystallography
Printed in Singapore – all rights reserved

1. Introduction

The synchrotron-based x-ray absorption spectroscopies, x-ray magnetic circular (XMCD) and linear (XLD) dichroism, are particularly useful techniques in physics, chemistry and materials science because of their chemical selectivity and high sensitivity. For instance, they allow investigating diluted elements in the first nanometers of bulk samples down to a concentration of few hundred ppm, and collections of single molecules or atoms on surfaces (Van der Laan & Figueroa, 2014; Stöhr *et al.*, 1998). Moreover, they provide information on both static and dynamic magnetic properties, including magnetic polarization and anisotropy, spin and orbital contributions to magnetic moments (Thole *et al.*, 1992; Carra *et al.*, 1993), magnetic coupling between spins localized on different elements (Joly *et al.*, 2017; Ohresser *et al.*, 2005) and magnetic bistability (Gambardella *et al.*, 2002). A dichroic spectrum is obtained by the difference between two x-ray absorption spectra (XAS) recorded with different light polarizations (circular left and right for XMCD, linear vertical and horizontal for XLD). When measuring XMCD an external magnetic field is generally used to control the magnetic state of the sample. In the case of ferromagnetic samples, with large enough remnant magnetization and small enough coercive fields, XMCD experiments can be also performed in low external magnetic fields or in the remnant state. In order to reach the high sensitivity of this technique, it is crucial that all parameters remain stable over the entire duration of the measurements. This implies a highly reliable photon source ensuring constant polarization rate and photon flux, a very steady optical pathway ensuring high energy stability and a constant sample environment in terms of temperature and magnetic field. The DEIMOS beamline, located on a medium straight section (I07-m) of the storage ring of the French Synchrotron-SOLEIL[1] has been conceived specifically to best fulfil these requirements (Ohresser *et al.*, 2014).

The accessible energy range on the DEIMOS beamline, with the mentioned four polarizations, ranges from 350 eV to 2500 eV. This covers the L absorption edges of 3d and 4d transition elements, the M edges of rare earth elements and the K edge of nitrogen, oxygen and sulfur atoms. All these elements are of particular interest in the field of molecular magnetism, and more generally, in magnetism of nano objects.

Ultra−Low Temperature (ULT, $T < 1$ K) is of primary importance when dealing with new states of matter and the studies of magnetic phenomena as spin transitions, magnetic ordering, relaxation of metastable states, superconductivity, Kondo effect, etc. When the thermal energy is smaller than the energy difference between the ground state and the first excited levels, the ground state properties can be revealed.

Among cryogenic fluids, liquid ^{4}He and ^{3}He allow to reach limit temperatures T_{lim} of about 1 K and 0.3 K, respectively, at sub-atmospheric pressure. To reach even lower temperatures, one takes advantage of the peculiar phase diagram of the

[1] Source Optimisée de Lumière à Energie Intermédiaire du LURE, https://www.synchrotron-soleil.fr/

^{3}He−^{4}He mixture, and in particular of the phase separation appearing below $T < 0.8$ K. This phase separation consists in the coexistence of a concentrated and a diluted phase, the latter having a ^{3}He molar fraction of $x = 0.063$ when extrapolated to $T = 0$. The enthalpy difference of the two phases leads to a net cooling by transferring ^{3}He from the concentrated phase to the diluted, mostly ^{4}He containing phase. For a standard ^{3}He−^{4}He dilution refrigerator T_{lim} is about 10 mK (Pobell, 1992). The basic principles of ^{3}He−^{4}He dilution and the use as refrigerator for XAS measurements are reported in detail in Refs. (Sainctavit & Kappler, 2001) and (Letard *et al.*, 2007).

Three different research teams (LURE[2], IPCMS, IMPMC) joined to develop a first version of a ^{3}He−^{4}He refrigerator dedicated to XMCD measurements and successfully used during the last 15 years on different European synchrotron radiation centers (Sainctavit & Kappler, 2001; Letard *et al.*, 2007), in particular in the field of molecular magnetism (Mannini *et al.*, 2009).

Recently, the setting up of the DiLux Consortium of 10 European laboratories allowed us to propose a new project of ULT equipment on the DEIMOS beamline at SOLEIL.

The present paper deals with the development of a new ^{3}He−^{4}He dilution refrigerator, working under Ultra-High Vacuum conditions (UHV) with significant gain in performance as compared to the previous version, namely, a lower temperature limit ($T_{lim} = 220$ mK), an optimized thermal shielding, the reduction of the eddy current power, easier cooldown and warmup procedures and user-friendly management of the experiments. Furthermore, the installation of this system in the DEIMOS beamline allows *in situ* sample transfer possibility to/from additional UHV chambers and glove box which provide possibilities of specific *in situ* sample preparation (ion sputtering, temperature annealing up to 1000°C, metal and organic layer deposition), and characterization (scanning tunneling microscopy, electron diffraction, Auger spectroscopy). For these *in situ* prepared samples, special holders have been developed which allow to reach sample temperatures very close to T_{lim}.

To illustrate the performances of the new device we describe here two XMCD experiments as a function of temperature (0.3−4.2 K) and magnetic field (±3 T cycle). As a first example, we illustrate the XMCD at the Er-$M_{4,5}$ edges in the paramagnetic $Er_{0.025}Pd_{0.975}$ alloy; second, by recording the Fe-$L_{2,3}$ edges we probe the metastable behavior of a Fe_4 single molecule magnet (SMM)-chemisorbed as a monolayer on Au(111).

2. Description of the specificities of the ULT set-up

This section describes the different prerequisites for performing ULT-XAS experiments with soft x-rays. Dilution refrigerators are of quite widespread use when measuring magnetization, transport properties or neutron diffraction. However, XMCD measurements impose several constraints, such as an UHV environment, a specific pre-cooling of the insert, an electrical sample insulation for the Total Electron Yield (TEY) detection mode, and a shielding of the parasitic infrared (IR) radiations inherent to the optical access.

[2] Laboratoire pour l'Utilisation du Rayonnement Electromgnétique

2.1. Cryomagnet

The new insert has been implemented in the existing cryomagnet of the DEIMOS beamline (Ohresser *et al.*, 2014), that comprised two superconductive magnets delivering magnetic fields up to 7 T and 2 T, along and perpendicular to the x-ray beam, respectively. The maximum sweeping rate is 0.05 T/s. The typical base pressure is in the low 10^{-10} mbar range without any mechanical pump (a possible source of vibrations and noise) thanks to the efficient cryogenic pumping. The dilution refrigerator is mounted in the vertical bore of the cryo-magnet. The sample is centered in a six-flange cross on a vertical (z-axis) translator, having an additional angular degree of freedom θ around the z-axis. A motorized linear motion perpendicular to the z-axis and the x-ray beam is obtained by translating the whole chamber with respect to the x-ray beam (Ohresser *et al.*, 2014). A Computer-Aided Design (CAD) of the cryostat with the dilution refrigerator insert is given Fig. 1.

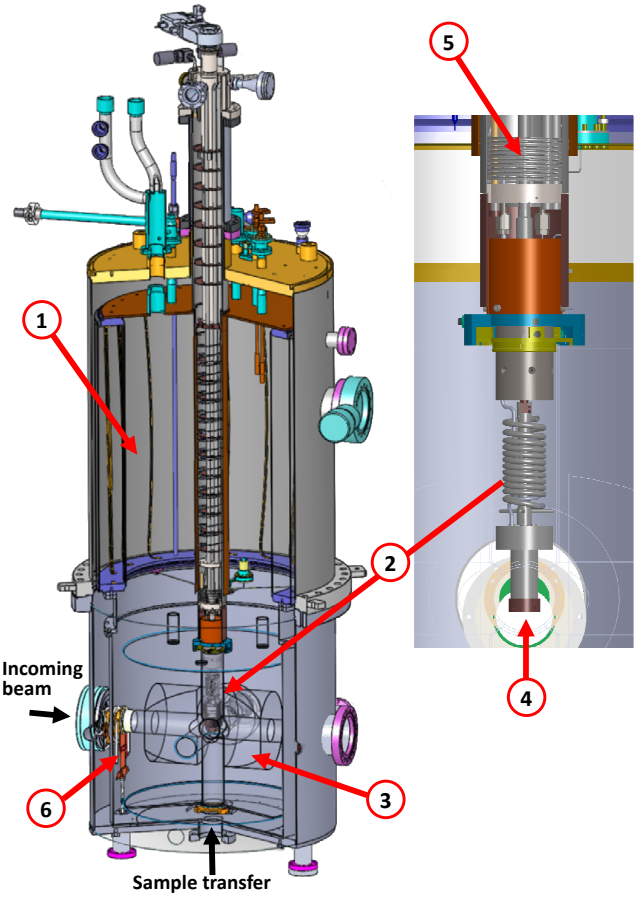

Figure 1
CAD of the cryostat: (1) Main He_{liq} tank. (2) ^{3}He−^{4}He dilution refrigerator. (3) Cryo-magnet. (4) Sample. (5) 4 K tank used for pre-cooling. (6) 4 K thermal retractable shield. Black arrows: the sample transfer and incoming beam axes. The total height is around 200 cm and the diameter 60 cm. The diameter of the bottom part of the refrigerator is ≃50 mm.

2.2. Dilution refrigerator–UHV environment

The ^{3}He–^{4}He dilution refrigerator has been manufactured by the CryoConcept company[3]. The refrigerator benefits from a Joule-Thomson expansion stage which avoids the need of a 1 K tank, and is exclusively built out of UHV compatible materials to avoid pollution of the vacuum and reach ultimate pressures. Stainless steel (grade 316L), Cu (Cu-OF) and Cu:Be alloys have been privileged and the standard wire tin-soldering has been replaced by UHV conductive epoxy gluing. This allows to keep a pressure in the low 10^{-10} mbar range or below, after gentle bake-out.

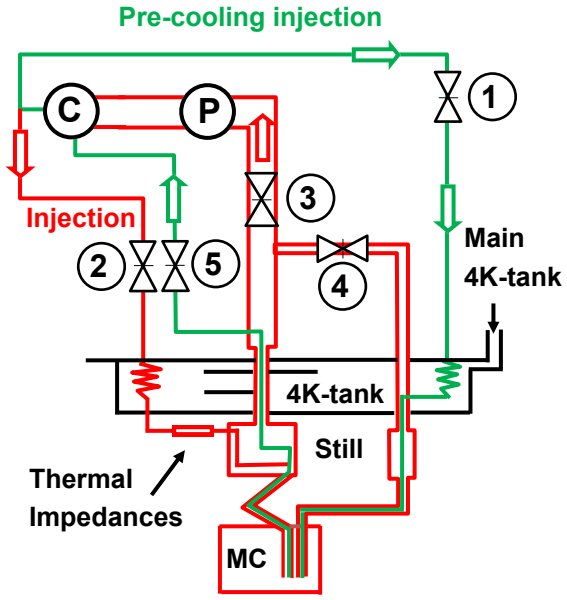

Figure 2
Scheme of the refrigerator circuits (Courtesy of CryoConcept). Green: pre-cooling mode. Red: dilution mode. C=compressor, P= pump. MC= Mixing Chamber. Black: 4 K-tank of the refrigerator, fed by the ^{4}He main reservoir. During the pre-cooling mode the valve positions are: (1), (5) = open; (2), (3), (4) = closed, P=off and C=on. For the dilution mode the valve positions are: (1), (5)=closed; (2), (3)=open; P=on, C=on; (4)=open only for the pre-cooling circuit purging.

2.3. Pre-cooling of the refrigerator

For a standard dilution refrigerator the pre-cooling procedure, which utilizes an exchange gas, takes few minutes. As the current insert cannot be cooled down by this method, a secondary He mixture circuit, which by-passes the thermal impedances, is used. A small fraction (≈10% of the total He mixture) is injected in this by-pass circuit, cooled down by the 4.2 K tank of the variable temperature insert that is fed by the main He reservoir through a capillary and injected directly in the Mixing Chamber (MC) (Fig. 2). The by-pass circuit is purged when the MC temperature reaches about 4 K, and then the condensation process starts. This pre-cooling procedure speeds up the cooldown by a factor 5 compared to our previous version. The MC cooldown from 300 K to 4.2 K lasts less than 45 min (see Fig. 3).

[3] 4, avenue des Andes 91952 Courtaboeuf, France, http://cryoconcept.com/

2.4. Mixing Chamber–TEY detection

The MC, located at the bottom part of the refrigerator, is the crucial part of a dilution fridge in terms of performance. The sample holder is attached (screwed in/out) to the MC to ensure excellent thermal contact, which is mandatory to reach an optimal thermal conduction. Furthermore, low-noise TEY detection requires an electrical insulation of the sample holder larger than hundred gigaohms.

2.4.1. Electrical insulation of the MC – Using the experience of our previous version, we built the MC as an assembly of a top and a lower metal part separated by a sapphire ring which ensures a quasi–perfect electrical insulation ($R > 200$ GΩ) of the lower part of the MC, and correlatively, a high sensitivity of the sample current measurement (a fraction of fA). This technique provides a perfect sealing whatever the temperature, with a He leak rate lower than 3.10^{-10} mbar.L/s. The sapphire ring ensures also an excellent thermal conduction, since the hole through the sapphire permits a direct contact of the cooling He mixture with the bottom of the MC, where the sample-holder is screwed. For more details about the mixing chamber see (Letard *et al.*, 2007).

2.4.2. Sample current measurement – In the soft x-ray range, XAS is most conveniently detected in the TEY mode by measuring the sample drain current (Ebel, 2004). The electrometer is electrically connected to the MC with a pair of twisted Kapton®-isolated manganin wires, one for the grounding and the second for the sample current measurement. A typical measurement with low flux (10^9 photons/s, at E=1000 eV, to avoid beam damage on the sample) yields a sample current of about 10 pA, with a signal to noise ratio in the 10^4 range. Note that Fluorescence Yield (FY) or transmission measurements are also practicable, but present some inconveniences with respect to ULT: FY requires a detector very close to the sample and therefore well thermalized. Transmission requires working with ultrathin samples, which might be difficult to thermalize. In the presence of external magnetic field, Partial Electron Yield (channeltron, electron analyzers, etc) cannot be used efficiently, so that TEY is in most cases preferred for XMCD.

2.5. Radiative heating–Limit temperature

The limit temperature T_{lim} depends on many factors, such as the parasitic IR radiations, the nominal cooling power of the dilution refrigerator and the incoming x-ray beam power.

2.5.1. Thermal shielding–Infrared radiations – Different thermal shields have been placed in the open bores of the cryomagnet:

- at the beam entry there is a 4 K thermalized high-purity Al foil (thickness=0.7 μm). This foil reduces by a factor 2 the flux of the incoming beam at the Fe-$L_{2,3}$ edge energies.
- Along the transfer and back bores there are two retractable IR radiation-proof Cu shields thermalized on the

cryo-magnet (measured temperature $\simeq$15 K).

- The two other bores, perpendicular to the beam axis in the horizontal plane, are dedicated to the lighting and the observation of the sample during sample transfer. They are both shielded by a first sapphire disk placed on the 77 K shield, then a low-pass IR Schott filter followed by a second sapphire disk, both fixed on the 4.2 K canister.
- All bores, except for the upper vertical bore of the cryo-magnet, are also equipped with black painted Cu tubes which are very efficient to reduce IR radiation reflections.

2.5.2. Cooling power of the ^{3}He$-^4$He refrigerator $-$ The preliminary tests of the dilution refrigerator insert in a closed cryostat, without any IR radiations on the MC, led to $T_{lim} =$ 60 mK, with a measured cooling power of 50 μW at 100 mK and 170 μW at 200 mK. Placed in the cryo-magnet the refrigerator yields a limit temperature $T_{lim} =$ 220 mK. In other words, the parasitic radiation heating is about 200 μW, mostly coming from the IR radiations through the different bores, and especially from the one above the cryo-magnet which could be the main limiting cause. Note that T_{lim} of our previous version was 500 mK, as determined through the relaxation time of a SMM (Mannini *et al.*, 2009; Klar *et al.*, 2014). In this device the temperature is measured with a full range thermometer (CryoConcept homemade, radiation protected sensor) inserted in the MC, with a high sensitivity between 10 mK and 350 K, whatever the temperature domain. It has been calibrated at ULT by a reference RuO_2 sensor mounted at the sample position, which implies by construction that $T_{MC} = T_{sample}$. This calibration indeed includes the thermal impedances between the helium mixture and the sample. The precision of the sensor is below 1 mK and the incertainty on the absolute sample temperature will depend on the sample itself and how it is fixed. For the measured samples we estimate it to about $\pm$25 mK.

2.5.3. Power of the incoming x-ray beam $-$ A flux of 10^{11} photons/s (at $E =$ 1000 eV) corresponds to $P =$ 16 μW, that is much lower than the refrigerator power of 50 μW at 100 mK. For these experiments much lower flux has bee used in order to avoid beam damage. Upon x-ray irradiation of about 10^9 photons/s the measured temperature at T_{lim} increases by only 5 mK with an incoming x-ray beam around 1000 eV.

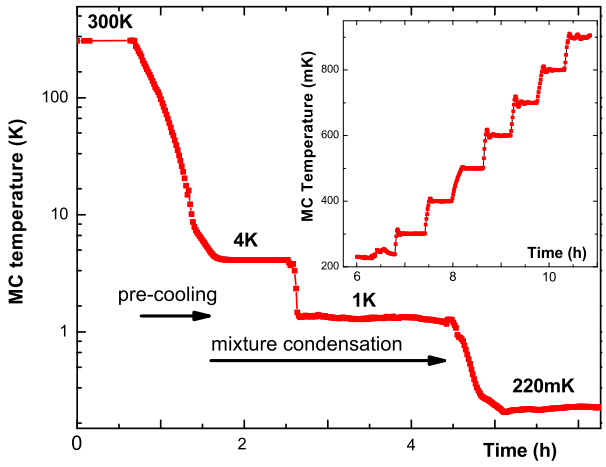

Figure 3
Evolution of the MC temperature in a log scale as a function of time, during the pre-cooling and the mixture condensation procedures. Starting from 300 K, about 4 hours are needed to reach T_{lim}. The inset illustrates the temperature stabilisation at various set points, from 200 to 900 mK, every 100 mK.

2.6. Sample transfer$-$Experimental procedures

For sample transfer the topmost part of the refrigerator is maintained at low temperature in order to avoid an excessive boil-off of the main He liquid tank. The bottom part of the MC is equipped with a heater resistor which permits the MC warmup to $T =$ 300 K for sample transfer; the sample holder, which is at room temperature, is then screwed on the MC. This solution is more convenient compared to a cold sample transfer (Beeck *et al.*, 2016), since it does not require an additional cold finger to pre-cool the sample. Another novelty of this new set-up, is that thermal stabilization, within a few percent, is achieved over a wide range of temperatures (220 mK - 350 K). The refrigerator can maintain a set-point over a period of 1 day or more. Furthermore, the temperature remains stable during the He refill of the reservoir of the superconducting coil, even if the sample is at ULT. All the temperature control is automatic and one needs only to define the temperature set-point into the piloting software. However, the range between 1.2 and 4.0 K is not straightforward to reach since it is just in between the dilution mode and the so-called 1 K-pot mode.

Passing from 4.2 K to 300 K (sample transfer) and back to 4.2 K requires about 90 min. Three additional hours are required to reach the ULT domain. Fig. 3 shows the variation of the MC temperature as a function of time, during the pre-cooling and the mixture injection procedures. These two steps are faster by a factor 5, at least, with respect to our previous version, and even more with respect to other set-ups (Beeck *et al.*, 2016). The insert of Fig. 3 illustrates the stability of temperature regulation at various set-points in the 0.2$-$1 K range.

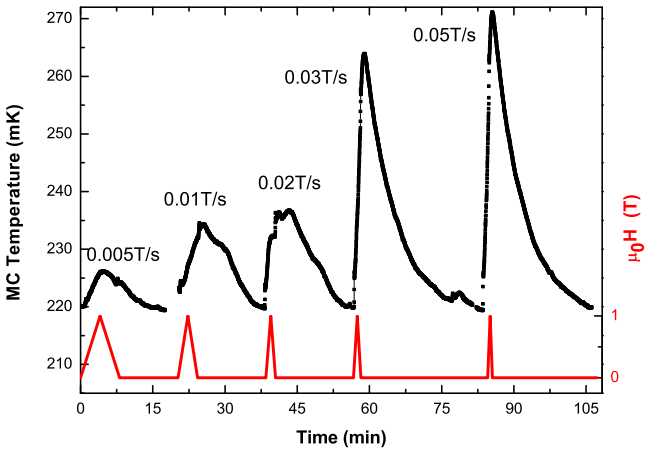

Figure 4
Evolution of the MC temperature for different sweeping rates of the magnetic field. For each rate the field varies continuously from 0 to 1 T and back to 0 (red lines)

2.7. Eddy current effects

The magnetic field sweep induces eddy currents in the MC, the sample holder, and the sample itself. The corresponding heating power is proportional to the square of the magnetic field sweeping rate $(dH/dt)^2$, the electrical conductance and some geometrical factors. To minimize this effect, the sample holder and the MC are built out of a Cu:Be alloy (2% of Be atom), that reduces the conductance in the ULT regime and, correlatively, the heating power of eddy currents, at least by a factor of 10 with respect to pure copper.

In order to find an optimal field sweeping rate, the evolution of the MC temperature was studied for different sweeping rates. For each rate the field varies continuously from 0 to 1 T and back to 0 (Fig. 4). For a 0.02 T/s sweeping rate the temperature increase is below 20 mK, with a return to the initial temperature in 15 min. For the continuous magnetic field variations when measuring XMCD detected magnetization curves, the sweeping rate is fixed to 0.01 T/s leading to a temperature increase of about 50 mK, in the case of a magnetic loop amplitude of ± 3 T.

3. First experimental results obtained with the new set-up

In order to check the ULT device performances we analyzed two different magnetic phenomena showing a strong temperature dependence. First, a paramagnetic $Er_{0.025}Pd_{0.975}$ alloy, and second, a monolayer deposit of a SMM belonging to the widely investigated class of Fe_4 molecules, which present a temperature dependent magnetic hysteresis below 1 K. XMCD experiments on ErPd alloy and SMM layer were performed at the Er-$M_{4,5}$ and Fe-$L_{2,3}$ edges, respectively.

3.1. Er_xPd_{1-x} alloy

The solubility of Er in f.c.c. Pd is about 10 % Er atom (Loebich & Raub, 1973) and the paramagnetic state of Er atoms in such alloys persists down to 400 mK. Therefore they can be used as *in situ* thermometers. When $x \leq 0.1$, the Er_xPd_{1-x} alloy develops a magnetically-ordered state at temperatures lower than a critical value T_o, which is x-dependent. For $x = 0.1$, $T_o \simeq 0.4$ K (Delobbe, 1999; Paulsen, 1999), and we choose $x = 0.025$ as a compromise between lowering T_o as much as possible and ensuring a sufficiently large absorption cross section. Supposing a linear variation of T_o with x, we expect $T_o \approx 100$ mK for $x = 0.025$. Indeed, for $x = 0.025$ and in a low magnetic field ($\mu_0 H = 9$ mT), we did not observe any magnetic coupling for temperatures above 200 mK.

3.1.1. Sample preparation, x-ray diffraction characterisation and magnetic properties – The alloy was prepared by triarc melting of the appropriate amounts of metals in a purified argon atmosphere, using a homemade water-cooled Cu plate and non-consumable thoriated W electrodes. The purities of the starting materials were 99.99 % (Pd) and 99.9% (Er). The ingot was remelted ten times and inverted after each melting to promote mixing. The as-cast $Er_{0.025}Pd_{0.975}$ alloy was homogenized at 900 °C for 24 h in a sealed silica tube, then water quenched.

The crystalline phase of the sample was determined using a Bruker D8 Advance diffractometer equipped with a Lynx-Eye detector at the monochromatic wavelength of Cu $K\alpha_1$, $\lambda = 1.54056$ Å. The expected f.c.c. phase was confirmed (*Fm-3m* space group), with a lattice parameter $a_{ErPd} = (3.9052 \pm 0.0024)$ Å at 300 K, as compared to the pure Pd metal, $a_{Pd} = (3.8921 \pm 0.0017)$ Å; this increase of the lattice parameter means that Er forms actually a solid solution with Pd.

SQUID measurements for the $Er_{0.025}Pd_{0.975}$ alloy, performed in the 0.1−4.2 K and 0−3 T ranges, serve as a reference of the bulk Er magnetization. In order to sort out the Er magnetic contribution, the total magnetization was corrected by subtracting the Pd matrix magnetization (Pd metal and extra impurities) measured in the same T and $\mu_0 H$ ranges.

3.2. Er-$M_{4,5}$ XAS-XMCD of the ErPd alloy

For the XAS-XMCD measurements the sample has been fixed with Cu plates screwed on the sample holder in order to ensure the best thermal conduction with the MC. In an UHV chamber, connected to the main chamber of the cryo-magnet, the surface of the sample has been scrapped with a rotative diamond file for cleaning, in a vacuum of $P \simeq 2.10^{-9}$ mbar, then immediately transferred in the measurement chamber, and screwed on the refrigerator MC.

Two series of experiments were performed: XMCD isotherms as a function of magnetic field and XMCD measurements at different temperatures in a constant magnetic field. Note that the experiments are limited to 300 mK, since the Schott filters were implemented afterwards.

Figure 5 gives an example of XAS and XMCD at the Er-$M_{4,5}$ edges for the $Er_{0.025}Pd_{0.975}$ alloy at $T = 300$ mK and for $\mu_0 H = 0.1$ T. The spectra were recorded by using the fast continuous energy scan mode (Joly *et al.*, 2016), which lasts about 2−3 min, for a spectrum width of about 100 eV, with a remarkable signal to noise ratio larger than 10^4, with a photon flux of

$1.5.10^9$ photons/s at 1400 eV and a beam size of 0.8×0.8 mm^2.

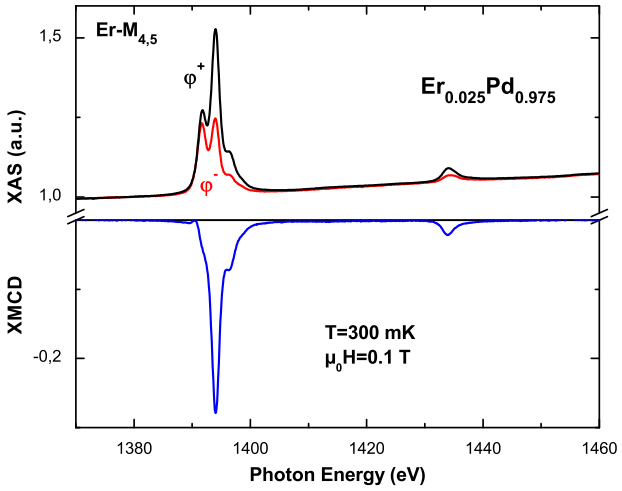

Figure 5
XAS and XMCD at the Er-$M_{4,5}$ edges in the $Er_{0.025}Pd_{0.975}$ alloy, at T = 300 mK and $\mu_0 H = 0.1$ T. The result is extracted from 8 XAS spectra, following the $\varphi^+, \varphi^-, \varphi^-, \varphi^+$ light polarization sequence for two opposite magnetic fields.

As expected for a pure J state, the different structures observed in the XAS spectra correspond to those calculated with a ligand-field multiplet model for an Er^{3+} ion with $J = 15/2, L = 6$ and $S = 3/2$ (Goedkoop *et al.*, 1988). The spectral signatures *i.e.*, the multiplet structure of both XAS and XMCD, are independent of temperature, external magnetic field and electrical crystal field (Schillé *et al.*, 1993). Only their intensity can change.

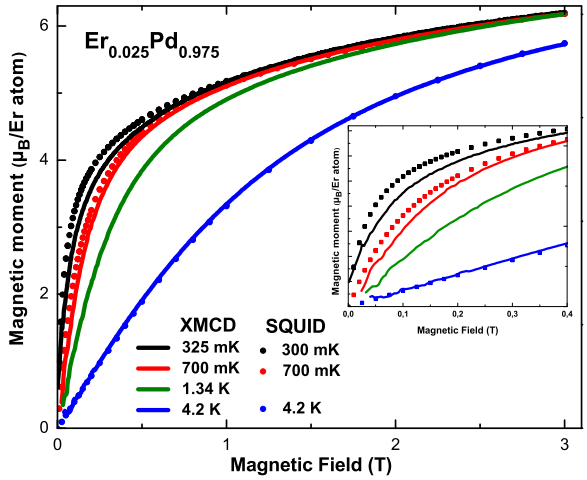

Figure 6
Magnetic characterization of the $Er_{0.025}Pd_{0.975}$ alloy: XMCD isotherms (continuous lines), scaled to the 4.2 K magnetization, *versus* magnetic field ($\mu_0 H$=0−3 T) in the 0.3−4.2 K range. Magnetic isotherms (●-●) from SQUID measurements, in the same temperature range. The inset presents a zoom of the low-field region up to 0.4 T.

3.2.1. XMCD *versus* magnetic field − Figure 6 reports the XMCD and SQUID detected magnetization curves measured between 0.3 and 4.2 K for $\mu_0 H \leq 3$ T. The XMCD magnetization curves are obtained in a fixed energy mode: The TEY signal is recorded as a function of the magnetic field (±3 T) with a constant sweeping rate (0.01 T/s), first at the energy of the maximum XMCD intensity (1394 eV, Er-M_5 edge) and then at the pre-edge (1384 eV), for the two circular light polarizations (∼90 min). The presented XMCD isotherms result of the averaging of 4 curves, the negative field branch has been symmetrized and averaged with the positive field branch.

Since the SQUID and XMCD magnetization curves should yield the same behavior as a function of field, we scale SQUID and XMCD results for $\mu_0 H = 3$ T and 4.2 K and apply the same scaling factor to all other XMCD curves. Doing so, the XMCD detected magnetization curves for all temperatures and all the magnetic fields are automatically expressed in Bohr magnetons. We notice some small shifts between XMCD and SQUID data for low magnetic fields; they are due to temperature increase during the ±3 T cycles, because of eddy current heating. For example, for an initial T=300 mK, the sample temperature oscillates upon field sweep around (325±25) mK. For $T > 400$ mK the cooling power of the device is sufficient to compensate the eddy current heating and this temperature drift no longer appears.

Knowing that the TEY detection mode probes about the first 5 to 10 nm of the sample surface, we checked the validity of the cleaning procedure by comparing the integrated XMCD intensity as a function of magnetic field in the 2−4 K range with that of Er_2O_3. Erbium(III) oxide is an antiferromagnet with $T_N = 3.3$ K (Narang *et al.*, 2014) and is the most probable oxidation product that might form at the surface of the ErPd alloy. The magnetization of Er_2O_3 as a function of external field is almost independent of temperature in the 2−4 K range, contrary to our XMCD detected isotherms, that are characteristic of a paramagnetic system (Fig. 6). We can estimate, within the error of the XMCD signal, that the sample oxidation, if any, concerns less than 5 % of the total amount of Er atoms.

3.2.2. XMCD integrated intensity and bulk magnetization *versus* temperature − Figure 7 presents the magnetization measured by SQUID and XMCD for temperatures varying between 0.3 and 4.2 K in an external magnetic field of $\mu_0 H = 0.1$ T. Each point of the XMCD intensity is extracted from 8 XAS spectra, as explained in the caption of Fig. 5. The XMCD integrated intensity is normalized to the magnetic moment at 4.2 K. The good superposition of the two series of measurements, with a maximum deviation of $\simeq$ 50 mK (Fig. 7), indicates that the temperature of the XMCD measurement is very close to that recorded by the SQUID This excellent agreement, much better than the one in Fig. 6, is due to the fact that after each field inversion the temperature has been left to stabilize before starting the next measurements, which is indeed impossible for a continuous magnetization curve recording.

It is worth noticing that the large variation of magnetization of the Er atoms between 4.2 K and 300 mK (a factor $\simeq$7) is par-

ticularly well suited for using the ErPd alloy as a thermometer. The good agreement between the XMCD and the bulk magnetization at fixed magnetic field down to T_{lim} demonstrates that these XAS measurements reveal the bulk properties of the alloy, and that the sample is very well thermalized on the sample holder. The sample temperature is given with confidence by the calibrated thermometer located in the MC.

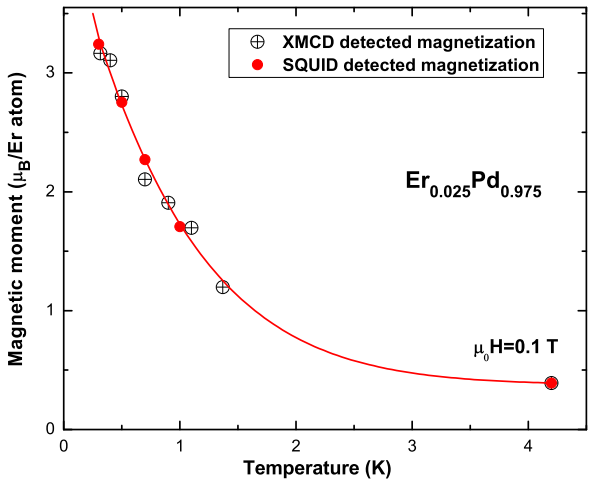

Figure 7
Magnetic moment of Er atoms in the $Er_{0.025}Pd_{0.975}$ alloy at $\mu_0 H = 0.1$ T for temperatures varying between 0.3 and 4.2 K. The red line is a guide for the eye. Since in a standard dilution refrigerator the temperature regulation in the 1.2-4 K range is not straightforward (see text), experimental data are missing in this temperature range.

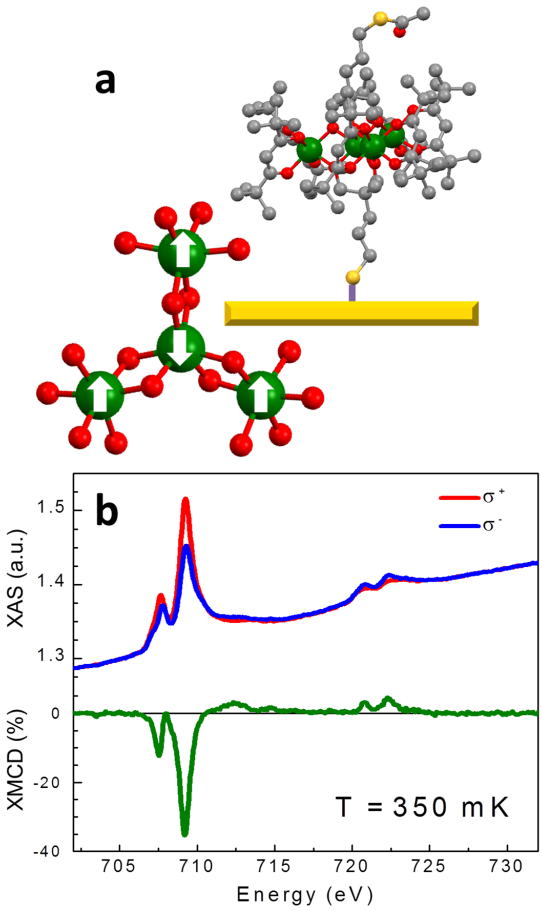

Figure 8
a) Simplified structure of the Fe_4 complex, highlighting the ferrimagnetic structure in the ground state and representation of chemisorption on gold (color code: iron atoms in green, oxygen in red, carbon in black and sulphur in light yellow, hydrogen atoms omitted); b XAS and XMCD spectra of the monolayer of Fe_4 at 0.3 K under an applied magnetic field of $\mu_0 H = 3$ T.

3.3. Investigation of a monolayer of Fe_4 molecules

To further validate the low temperature performance of this set-up we investigated a molecular sample. Here we used a monolayer of a tetrairon (Fe_4) complex, the archetypal SMM for the realization of hybrid nanostructures (Gatteschi *et al.*, 2006). The four Fe^{3+} ions (S= 5/2, high spin) adopt a metal centered triangular topology in the structure, as shown in (Fig. 8a). An antiferromagnetic interaction between the central spin and the peripheral ones is present giving a ground state with total spin S=5, schematized by the arrows in Fig. 8a. They can be chemisorbed on surfaces maintaining almost intact their unique low temperature behavior (Mannini *et al.*, 2009; Cini *et al.*, 2018; Mannini *et al.*, 2010). Below 1 K it is possible to observe a magnetic bistability (*i.e.*, the opening of a hysteresis in the magnetization cycle) due to the slowing down of the thermally activated process to overcome the anisotropy barrier. The low temperature behavior is further enriched by the Quantum Tunneling of the Magnetization (QTM) which occurs whenever the quantized spin levels of the molecules are brought in resonance by an external magnetic field (Gatteschi *et al.*, 2006).

This class of samples represents a valuable benchmark for an ultra−low temperature device requiring at the same time a sub-kelvin temperature range and an extreme sensitivity under a very low dose of photons. In fact, these samples (Totaro *et al.*, 2014) are characterized by a very low concentration of adsorbing atoms (about 2-3 Fe atoms per nm^2). On the other hand, a strongly attenuated and defocused beam must be used to avoid radiation damage. For these experiments the photon flux was about $1.5.10^9$ photons/s at 700 eV and a beam size of 0.8×0.8 mm^2. Such a low photon flux thus imposes a strong optimization of drain current detection in the pA range.

For these tests, a novel Fe_4 derivative has been used, namely $Fe_4(C_3SAc)_2(dpm)_6$, where H_3C_3SAc, is 5-(acetylthio)-2,2-bis(hydroxymethyl)pentan-1-ol and Hdpm is dipivaloylmethane. The synthesis and bulk characterization of this compound will be published elsewhere; here we just briefly report on the magnetic characterization of a chemisorbed monolayer prepared following the protocol we adopted in the past for other Fe_4 derivatives (Mannini *et al.*, 2009; Mannini *et al.*, 2010; To-

taro *et al.*, 2014). The purified crystalline material was dissolved in dichloromethane to give a 2 mM solution, then a 150 nm flame-annealed polycrystalline Au substrate grown on mica was incubated in the solution. A monolayer deposit was achieved removing the excess of physisorbed material by several washing cycles with pure dichloromethane (Mannini *et al.*, 2010). The preparation of the sample was carried out in a glove box unit filled with argon gas and directly connected to the DEIMOS beamline.

XAS/XMCD spectra obtained on this sample at 350 mK and $\mu_0 H = 3$ T (Fig. 8b) evidence the expected spectral features (Mannini *et al.*, 2009). This confirms the capability of the ULT set-up to operate in the required low photon flux regime to investigate fragile molecular systems. The intensity of the XAS signal near the L_3 edge with respect to the background (edge jump, about 10%) is consistent with the presence of a monolayer deposit (Totaro *et al.*, 2014).

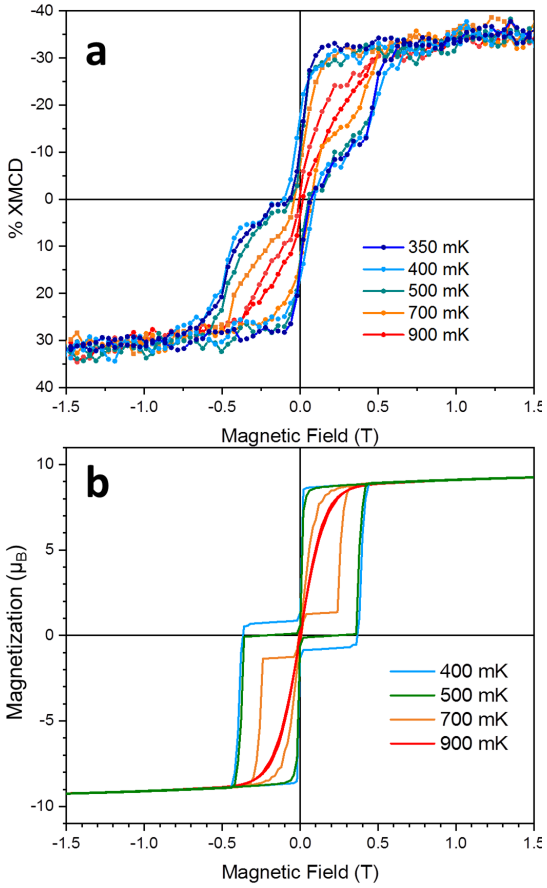

Figure 9
Magnetic characterisation of a monolayer of Fe_4 molecules: a) XMCD detected magnetization curves ($\pm$1.5 T, 0.01 T/s) in the 350−900 mK range; b) simulated hysteresis loops assuming that the easy axis of the molecules forms an angle of 30° with the external magnetic field.

More important, Fig. 9a shows the temperature dependence of the maximum of the dichroism at the Fe-L_3 edges, as a function of the magnetic field. These data portray the typical magnetic behavior of Fe_4 systems, whose hysteresis loops are open below 1 K and become wider with decreasing temperature (Mannini *et al.*, 2010). The hysteresis curves are almost temperature independent below 0.5 K, indicating the onset of a pure quantum tunneling regime. Resonant QTM is also responsible for the magnetization steps at 0 and $\pm$0.5 T. Such steps are here clearly visible because of the preferential orientation of molecules with their easy axis close to the surface normal.

To confirm that a good temperature control is also achieved at intermediate temperatures we have simulated the hysteresis cycles (Fig. 9b) using a quantum master matrix approach we have previously developed (Mannini *et al.*, 2010). The steps in the computed hysteresis curves are more pronounced than observed because only one orientation of the molecules and a unique set of magnetic anisotropy parameters were considered in the calculations. Recent synchrotron-Mössbauer experiments (Cini *et al.*, 2018) have shown that the process of chemisorption leads to a distribution of molecular geometries that has been neglected here.

The results clearly evidence the capability of performing an ULT-XMCD experiment under continuously scanning magnetic field with a 50 mK temperature resolution. Such an achievement is far from being trivial and opens relevant perspectives for the low temperature investigation of hybrid magnetic nanostructures and quantum magnetic systems.

4. Conclusion

In this paper we have described a new ULT-XMCD set-up, installed on the DEIMOS beamline and dedicated to soft x-ray XMCD experiments. Its improved performances, as compared to our previous set-up, have been illustrated by measuring two different physical phenomena with a marked temperature dependence. First, we have measured the magnetization of paramagnetic Er impurities in a palladium ingot. Second, we have measured the opening of magnetic hysteresis loops in an SMM monolayer. Both experiments demonstrate unambiguously that sub-kelvin XMCD data can be recorded on two very different systems, thus indicating the versatility and the enormous potentiality of this spectroscopic tool for magnetic studies well beyond diluted paramagnetic systems or surface science. Despite many worldwide attempts on various synchrotron facilities, this device is certainly unique in providing such performances.

5. Acknowledgments

This project has been financially supported by the DiLux Consortium, composed of the following laboratories:

- Synchrotron SOLEIL, France;
- Institut de Minéralogie, de Physique des Matériaux et de Cosmochimie, France;
- Institut de Chimie Moléculaire et des Matériaux d'Orsay, France;
- Institut de Physique et Chimie des Matériaux de Strasbourg, France;
- Laboratorio di Magnetismo Molecolare, Università degli Studi Firenze, Italy;
- Dipartimento di Scienze Chimiche e Geologiche, Università degli Studi di Modena e Reggio Emilia, Italy.
- Karlsruher Institut für Nanotechnologie, Germany;

- Fakultät für Physik, Universität Duisburg-Essen, Germany;
- Max Planck Institut für Chemische Physik Fester Stoffe, Germany;
- Physikalisches Institut, Universität zu Köln, Germany;

Part of the work describe here was done in the glove box provided by the Institut de Minéralogie et de Physique des Milieux Condensés, and has been funded by the Agence National de la Recherche; grant ANR-07-BLANC-0275 grant.

We acknowledge financial support of the ASTRE (2015-ATDE-058) from the Conseil Général of Essonne and the valorization program of the LabEx PALM (DICHRO50mK). We also acknowledge financial and administrative support from the SATT Paris−Saclay maturation program (dichro50). We thank R. Baehr, A. Boulard and M. Valentin from the IPCMS mechanical workshop.

References

Beeck, T., Baev, I., Gieschen, S., Meyer, H., Meyer, S., Palutke, S., Feulner, P., Uhlig, K., Martins, M. & Wurth, W. (2016). *Review of Scientific Instruments*, **87**(4), 045116.
URL: *https://doi.org/10.1063/1.4947516*

Carra, P., Thole, B. T., Altarelli, M. & Wang, X. (1993). *Physical Review Letters*, **70**(5), 694–697.
URL: *http://link.aps.org/doi/10.1103/PhysRevLett.70.694*

Cini, A., Mannini, M., Totti, F., Fittipaldi, M., Spina, G., Chumakov, A., Rüffer, R., Cornia, A. & Sessoli, R. (2018). *Nature Communications*, **9**, 480.
URL: *https://doi.org/10.1038/s41467-018-02840-w*

Delobbe, A. (1999). Ph.D. thesis, Université Paris XI.

Ebel, H. (2004). *Powder Diffraction*, **1**, 90–96.
URL: *https://doi.org/10.1154/1.1649329*

Gambardella, P., Dallmeyer, A., Maiti, K., Malagoli, M., Eberhardt, W., Kern, K. & Carbone, C. (2002). *Nature*, **416**, 301–304.
URL: *https://doi.org/10.1038//nature/416301a*

Gatteschi, D., Sessoli, R. & Villain, J. (2006). *Molecular Nanomagnets*. Oxford University Press.
URL: *https://doi.org/10.1093/acprof:oso/9780198567530.001.0001*

Goedkoop, J. B., Thole, B. T., van der Laan, G., Sawatzky, G. A., de Groot, F. M. F. & Fuggle, J. C. (1988). *Phys. Rev. B*, **37**, 2086–2093.
URL: *https://link.aps.org/doi/10.1103/PhysRevB.37.2086*

Joly, L., Kappler, J.-P., Ohresser, P., Sainctavit, P., Henry, Y., Gautier, F., Schmerber, G., Kim, D. J., Goyhenex, C., Bulou, H., Bengone, O., Kavich, J., Gambardella, P. & Scheurer, F. (2017). *Phys. Rev. B*, **95**, 041108.
URL: *https://link.aps.org/doi/10.1103/PhysRevB.95.041108*

Joly, L., Muller, B., Sternitzky, E., Faullumel, J.-G., Boulard, A., Otero, E., Choueikani, F., Kappler, J.-P., Studniarek, M., Bowen, M. & Ohresser, P. (2016). *Journal of Synchrotron Radiation*, **23**(3), 652–657.
URL: *https://doi.org/10.1107/S1600577516002551*

Klar, D., Candini, A., Joly, L., Klyatskaya, S., Krumme, B., Ohresser, P., Kappler, J.-P., Ruben, M. & Wende, H. (2014). *Dalton Transactions*, **43**, 10686–10689.
URL: *https://doi.org/10.1039/c4dt01005a*

Van der Laan, G. & Figueroa, A. I. (2014). *Coordination Chemistry Review*, **277-278**, 95–129.
URL: *https://doi.org/10.1016/j.ccr.2014.03.018*

Letard, I., Sainctavit, P., Cartier dit Moulin, C., Kappler, J.-P., Ghigna, P., Gatteschi, D. & Doddi, B. (2007). *Journal of Applied Physics*, **101**, 113920.
URL: *https://doi.org/10.1063/1.2745318*

Loebich, O. & Raub, E. (1973). *Journal of the Less Common Metals*, **30**(1), 47–62.
URL: *http://www.sciencedirect.com/science/article/pii/002250887390006*

Mannini, M., Pineider, F., Danieli, C., Totti, F., Sorace, L., Sainctavit, P., Arrio, M.-A., Otero, E., Joly, L., Cezar, J. C. & et al. (2010). *Nature*, **468**(7322), 417–421.
URL: *https://doi.org/10.1038/nature09478*

Mannini, M., Pineider, F., Sainctavit, P., Danieli, C., Otero, E., Sciancalepore, C., Talarico, A., Arrio, M.-A., Cornia, A., Gatteschi, D. & Sessoli, R. (2009). *Nature materials*, **8**, 194–197.
URL: *https://doi.org/10.1038/nmat2374*

Margheriti, L., Chiappe, D., Mannini, M., Car, Pierre-E, ., Sainctavit, P., Arrio, M. A., De Mongeot, F. B., Cezar, J. C., Piras, F. M., Magnani, A., Otero, E., Caneschi, A. & Sessoli, R. (2010). *Advanced Materials*, **22**(48), 5488–5493.
URL: *https://doi.org/10.1016/j.jmmm.2014.05.026*

Narang, V., Korakakis, D. & Seehra, M. (2014). *Journal of Magnetism and Magnetic Materials*, **368**, 353–359.
URL: *http://www.sciencedirect.com/science/article/pii/S030488531400470*

Ohresser, P., Bulou, H., Dhesi, S., Boeglin, C., Lazarovits, B., Gaudry, E., Chado, I., Faerber, J. & Scheurer, F. (2005). *Physical Review Letters*, **95**, 195901.
URL: *https://doi.org/10.1103/PhysRevLett.95.195901*

Ohresser, P., Otero, E., Choueikani, F., Chen, K., Stanescu, S., Deschamps, F., Moreno, T., Polack, F., Lagarde, B., Daguerre, J.-P. *et al.* (2014). *Review of Scientific Instruments*, **85**(1), 013106.
URL: *https://doi.org/10.1063/1.4861191*

Paulsen, C. (1999). Private communication.

Pobell, F. (1992). *The $^3He-^4He$ Dilution Refrigerator*, pp. 105–137. Berlin, Heidelberg: Springer Berlin Heidelberg.
URL: *https://doi.org/10.1007/978-3-662-08578-3*

Sainctavit, P. & Kappler, J.-P. (2001). *X-ray Magnetic Circular Dichroism at Low Temperature*, pp. 235–253. Berlin, Heidelberg: Springer Berlin Heidelberg.
URL: *https://doi.org/10.1007/3-540-44954-X 10*

Schillé, J. P., Kappler, J. P., Sainctavit, P., Cartier dit Moulin, C., Brouder, C. & Krill, G. (1993). *Phys. Rev. B*, **48**, 9491–9496.
URL: *https://link.aps.org/doi/10.1103/PhysRevB.48.9491*

Stöhr, J., Padmore, H., Anders, S., Stammler, T. & Scheinfein, M. R. (1998). *Surface Review and Letters*, **5**, 1297–1308.
URL: *https://doi.org/10.1142/S0218625X98001638*

Thole, B. T., Carra, P., Sette, F. & van der Laan, G. (1992). *Phys. Rev. Lett.* **68**.
URL: *https://doi.org/10.1103/PhysRevLett.68.1943*

Totaro, P., Poggini, L., Favre, A., Mannini, M., Sainctavit, P., Cornia, A., Magnani, A. & Sessoli, R. (2014). *Langmuir*, **30**(29), 8645–8649.
URL: *https://doi.org/10.1021/la500846a*

Chapter 3

Experimental Principles and Techniques

This chapter is mostly a bibliography study that presents the context of XMCD measurements for rare earths. I nevertheless want to stress that **Section 3.3 "Surface cleaning chamber on DEIMOS beamline" is an original instrumental development** that I have performed in order to make my XMCD measurements possible. The bibliography study covers the production of synchrotron radiation, describes the specificities of DEIMOS beamline at SOLEIL and sumarizes the principle of X-ray absorption spectroscopy (XAS) combined with X-ray magnetic circular dichroism (XMCD) and X-ray Magnetic Linear Dichroism (XMLD). At last, the ultra-high vacuum device developed on DEIMOS beamline dedicated to this thesis is presented.

3.1 The synchrotron radiation at SOLEIL

A large part of the experimental work of this PhD thesis has been performed on Synchrotron SOLEIL. The Synchrotron SOLEIL is a third generation synchrotron. It produces synchrotron radiations with very high brilliance. Figure 3.1 shows that the energy range of the X-rays produced at SOLEIL with different types of undulators or wigglers. The brilliance of the beamline depends on its energy. It varies essentially between 10^{14} and 10^{20} photons/s/(mrad)^2/(mm)^2/(0.1%BW).[1] For comparison, the brilliance of the sunlight is in the range of 10^{10} photons/s/(mrad)^2/(mm)^2/(0.1%BW) and 10^6 photons/s/(mrad)^2/(mm)^2/(0.1%BW) for a 60 W light bulb [102]. The emitted radiation can have a well defined polarization: linear polarization (horizontal or vertical) as well as circular polarization (left or right). All these properties provide photon sources with exceptional quality for the fundamental and applied research such as

[1] BW for bandwidth.

physics, chemistry, geoscience, and space science, and also for the environment, archaeology and cultural heritage.

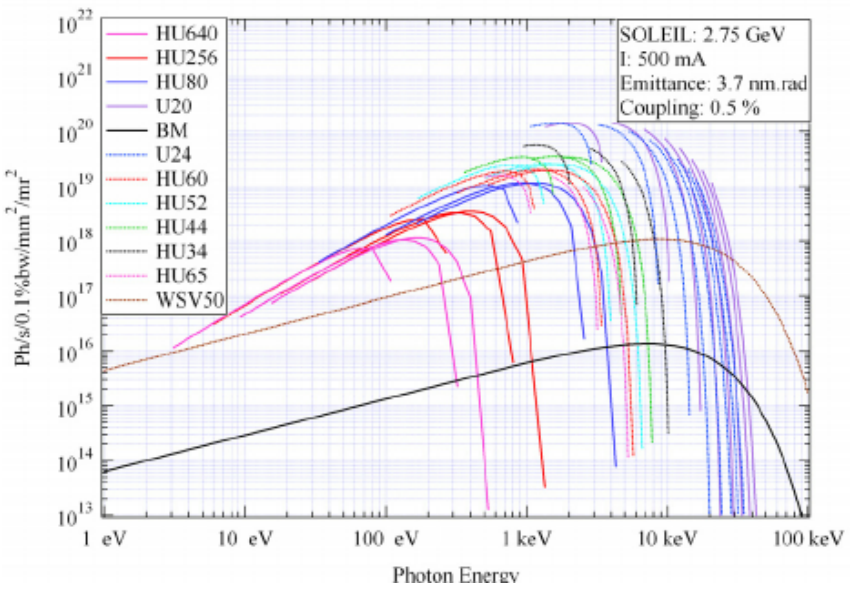

Figure 3.1: SOLEIL synchrotron radiation spectral range for the various insertion devices. BM for bending magnets, HU and U for undulators and WSV for wigglers. (Figure from [103].)

Figure 3.2 shows the basic principles of a synchrotron facility, here SOLEIL. An electron gun emits a beam of electrons that is accelerated by a linear accelerator (LINAC) ① of 16 m. Then the electrons are injected and stocked in a booster ②. When the booster is filled, the electrons are accelerated for a second time to reach the energy of 2.75 GeV which is the energy designed for synchrotron SOLEIL. They are then injected into the principal storage ring ③ whose diameter is 113 m and in which UHV conditions are maintained ($\approx 10^{-10}$ mbar). As the rest mass of an electron is 511 keV [104], the speed of a 2.75 GeV electron is 0.99999998 c, in other words, the electrons are highly relativistic. The ultra-high vacuum in the storage ring minimizes the collisions between the electrons and the residual gas, allowing the electrons to circulate for hours.

All charged particles submitted to an acceleration emit an electromagnetic radiation. In a third generation synchrotron like Synchrotron SOLEIL, different structures are used to produce synchrotron radiation: bending magnets ④, undulators ⑥, and wigglers ⑥ (Figure 3.3).

- **Bending magnets** create uniform and relatively strong magnetic fields that deflect the relativistic electrons. The spectral range of the radiations produced by bending magnets is broad.

- **Undulators** are inserted on straight sections and consist of a series of electromagnets or permanent magnets, which create relatively weak magnetic fields along the

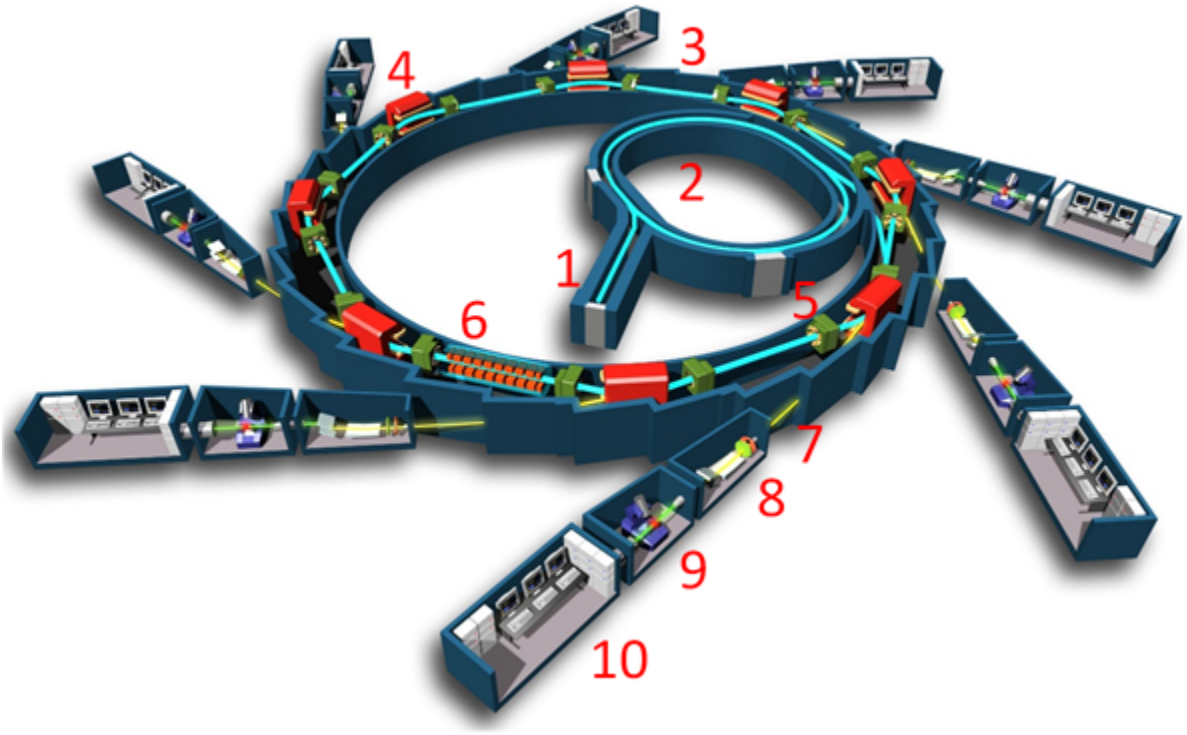

Figure 3.2: **Synchrotron radiation.** (Figure from [105].) (1) Linear accelerator (LINAC). (2) Booster. (3) Storage ring. (4) Bending magnet. (5) radiofrequency cavity. (6) Undulators et wigglers. (7) One of the Beamlines. (8) Optical hutch. (9) Experimental room. (10) Working station.

electrons trajectory. The bunch of electrons submitted to such "weak" periodic magnetic fields undulates with rather weak amplitudes. The "sources" of the undulator are the portions of the trajectory where the acceleration is maximum and due to the smallness of the oscillations, the sources tend to interfere yielding a discontinuous emission spectrum with sharp peaks. By controlling the magnetic field shape and intensity along the electrons bunch trajectory, it is possible to change the energy of the emitted peaks and to control the polarization state of the X-rays.

- **Wigglers** are similar to undulators but have larger magnetic fields so that interferences are killed and the total emitted spectrum is roughly the sum of the emission of each individual source. The radiation spectrum is then comparable to that of a bending magnet but with a larger photon flux since several sources add up.

Figure 3.1 plots the brilliance of the X-ray beams delivered by bending magnets, undulators, or wigglers at SOLEIL.

The emission of photons induces an energy loss for the electrons. To restore this energy several radiofrequency cavities are installed on the storages ring ⑤ so that the energy of the electrons remains fixed to 2.75 GeV. Collisions with the residual gas and

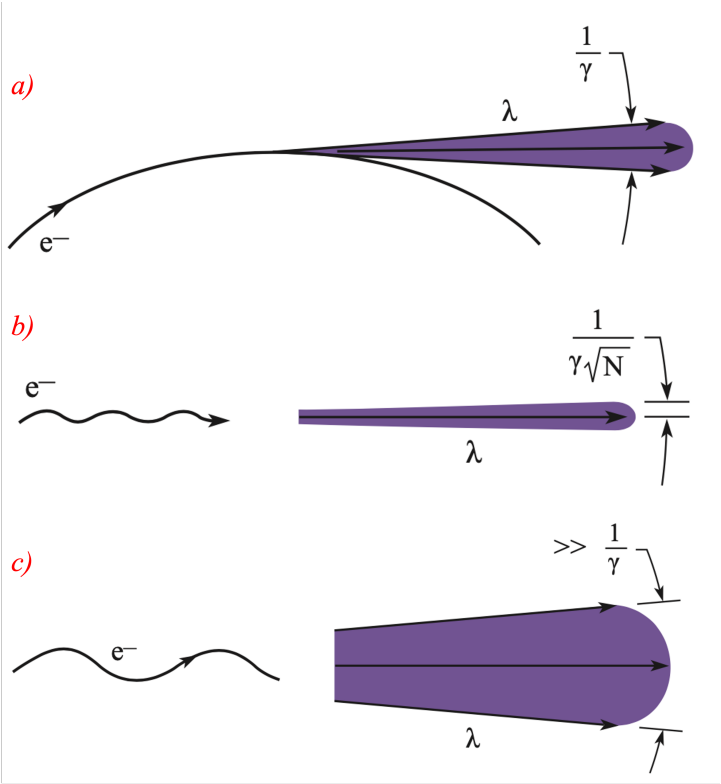

Figure 3.3: Synchrotron radiation emitted by bending magnets (a), undulators (b) and wigglers (c). A relativistic electron goes through one of these devices, emits synchrotron radiation with a wavelength λ. For a bending magnet, the emission angle is typically $1/\gamma$, the natural radiation cone, where γ is the Lorentz factor. For undulators, the emission angle is smaller than the natural radiation cone. For wigglers, the emission angle is larger than the natural radiation cone. (Figures from [106])

inside the electron bunch tend to kill part of the circulating electrons. Since the synchrotron SOLEIL works usually in a "Top-Up" mode, every two or three minutes a few milliamperes are injected from the booster to compensate the electrons loss.

The emitted radiation enters the frontend beamline ⑦, is guided by different optical systems ⑧, and reaches the experimental platform ⑨. In the optical hutchs ⑧, the beam can be focussed, collimated, or monochromatized in order to produce the expected spectral and spatial shapes ⑨. Nowadays, with great developments in computer sciences dedicated to synchrotron facilities, most of the instrumental control is operated from a beamline workstation ⑩. Due to the COVID-19 pandemic, the remote control mode has been made available to users, but it is still rather complicated to have the whole beamline operated from a distant lab in France or abroad.

3.2 DEIMOS beamline at Synchrotron SOLEIL

The DEIMOS beamline, which is short for Dichroic Experiment Installation for Magneto-Optical Spectroscopy, is one of the 29 beamlines at Synchrotron SOLEIL. It is a beamline dedicated to X-ray dichroic measurements in the soft X-ray energy range between 350 eV and 2500 eV, covering the absorption energy range of the $L_{2,3}$ edges of $3d$ transition elements and the $M_{4,5}$ edges of lanthanides. It is also possible to record the K edges of light elements such as carbon, nitrogen, oxygen, up to heavier elements like sulfur. Dichroic measurements are obtained by making the difference between two X-ray absorption spectra recorded with different X-ray polarizations. There are several types of dichroism among which the most common are XMCD (X-ray Magnetic Circular Dichroism), XMLD (X-ray Magnetic Linear Dichroism), XNCD (X-ray Natural Circular Dichroism), and XNLD (X-ray Natural Linear Dichroism).

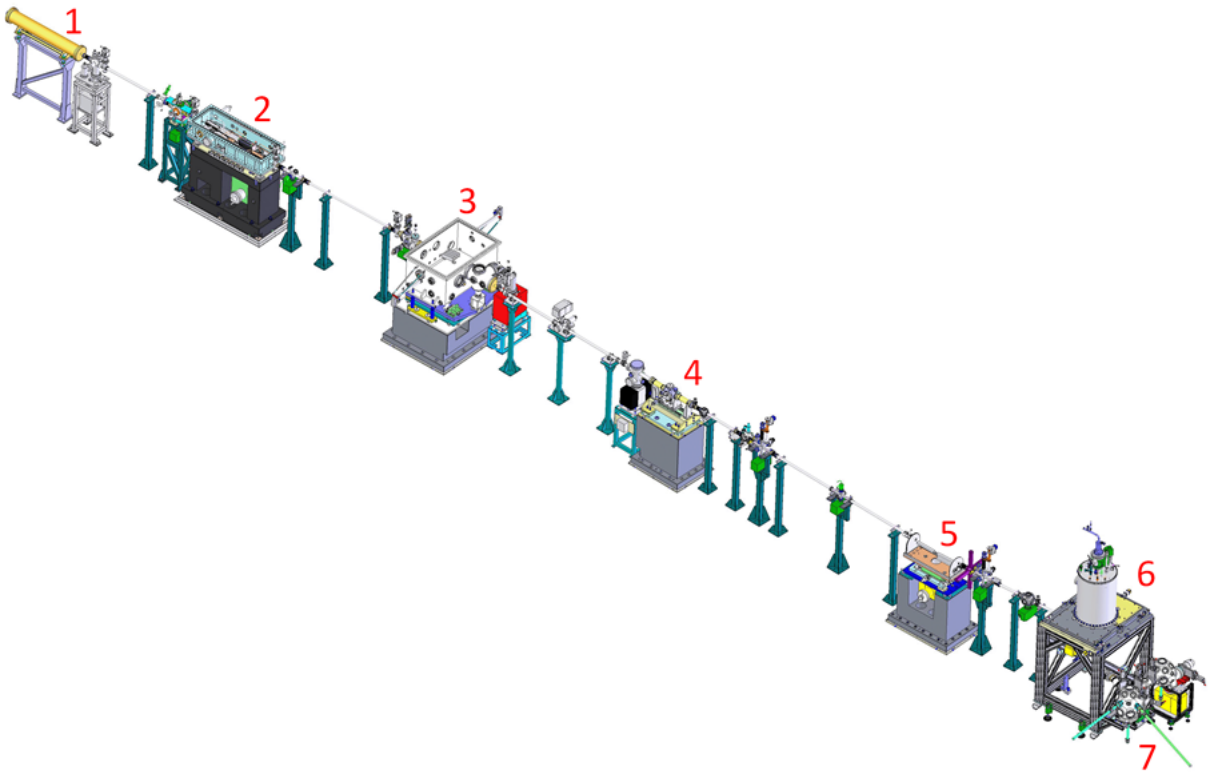

Figure 3.4: **Scheme of DEIMOS beamline.** (1) Buffer chamber. (2) First optical chamber. (3) Monochromator. (4) Exit slits. (5) Refocussing chamber. (6) Endstation - Cryomagnet. (7) Sample preparation chambers. (Courtesy of DEIMOS - Synchrotron SOLEIL)

Two undulators are inserted in the straight section of DEIMOS beamline. One helical undulator Apple-II HU-52 with a period of 52.4 mm which provides circular polar-

ized light (left and right) as well as horizontal and vertical polarized light (and also arbitrarily oriented linear polarization). A second electromagnetic undulator EMPHU-65 (ElectroMagnetic and Permanent-magnet Hybrid Undulator) with a period of 65.0 mm is optimized for fast switching (5 Hz) between left and right circular polarizations [71].

Figure 3.4 shows the schematic structure of DEIMOS beamline. The light emitted by one of the two undulators passes through the buffer chamber ① and arrives in M1, the first optical chamber ② that focalizes the beam and rejects higher harmonics emitted by the undulator. The X-ray photon flux in this chamber is in the range of 2×10^{15} photons/s/0.1%BW at 750 eV. Then the beam enters the monochromator ③ where a series of gratings, mirrors and slits ④ produce a monochromatic beam. Then the beam can be either focused or defocused by various optics ⑤ depending on the type of experiments. The beam can be focussed down to 80 μm $\times$ 80 μm or defocussed to 800 μm $\times$ 800 μm. Then the X-ray enters the CroMag endstation ⑥.

Various chambers are connected to the CroMag, so that transfers under UHV conditions can be performed from a glove box through an air-lock or a MBE chamber ⑦, providing the possibility for specific *in situ* sample preparation (ion sputtering, temperature annealing up to 1000°C, metal and organic layer deposition) and characterization (scanning tunneling microscopy, electron diffraction, Auger spectroscopy).

3.3 Surface cleaning chamber on DEIMOS beamline

In this section, I shall describe a small chamber that I have helped to develop during my PhD with the help of the staff of DEIMOS, especially Florian Leduc, and that has been essential in order to prepare bulk samples with minimal surface contamination. Most of the experiments I recorded dealt with the $M_{4,5}$ edges of rare-earths present in intermetallic systems. For such polycrystalline samples, the surface is always heavily oxidized. Due to the detection mode in TEY, the measurements are extremely sensitive to the surface so that raw samples that have been exposed to air could not be measured. A way out is to develop a chamber that can scrape the surface of the bulk sample in a UHV environment so that the scraped surface reflects the pristine sample. Figure 3.5 shows the chamber that I have installed on DEIMOS. It is a UHV chamber with 6 flanges: 1 on the top, 1 on the bottom and 4 lateral flanges around the chamber. The bottom flange is connected to an air-lock where the sample is introduced. The top flange is connected to a pumping unit (primary pump and turbomolecular pump) and a vertical translator that allows to adjust the position of the sample. A rotatable manipulator is mounted on one of the lateral flanges, the other flanges receive a cleaver, an ion pump, and a viewport for visual control.

Each time after samples are introduced in the air-lock chamber, we perform a com-

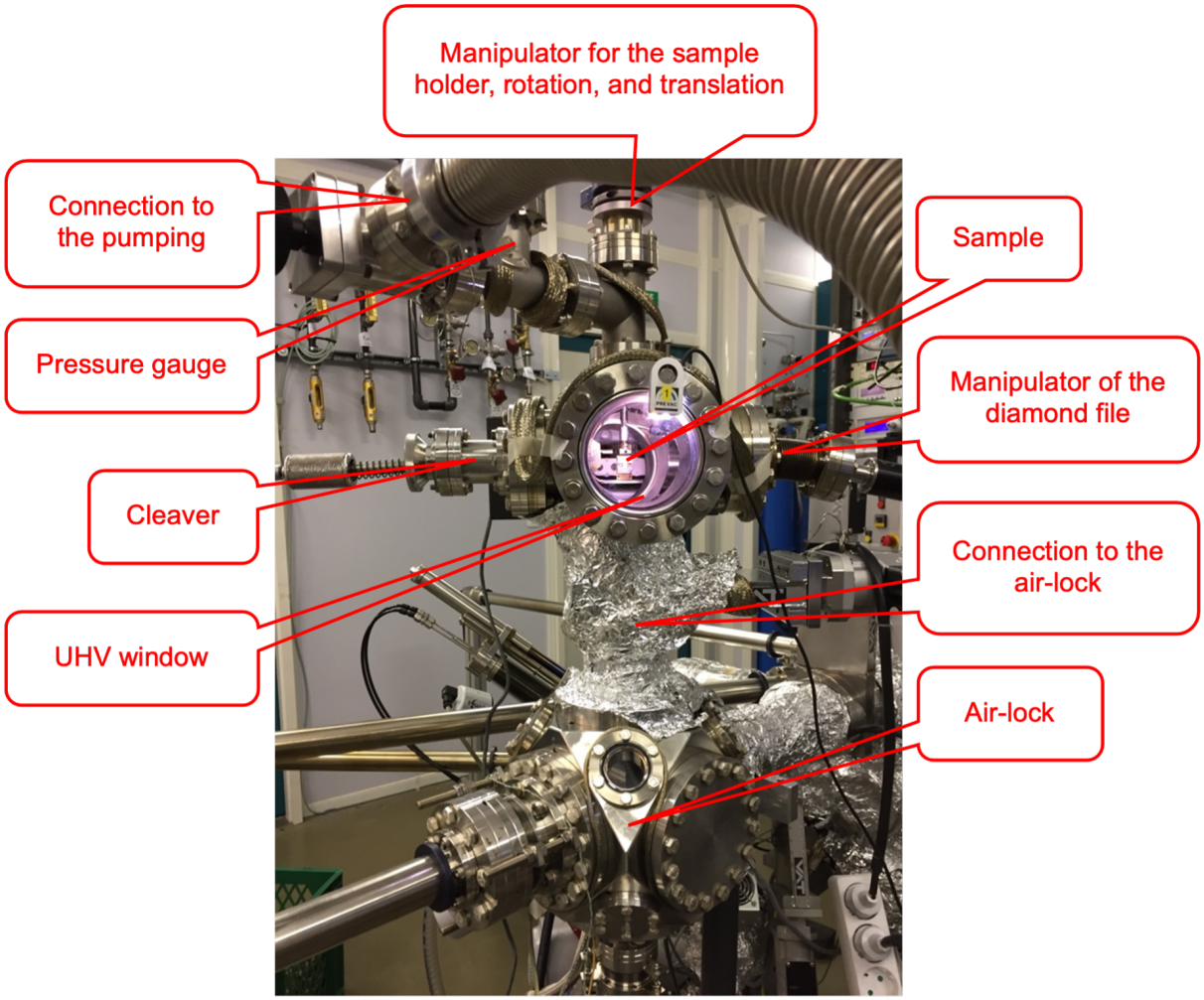

Figure 3.5: UHV surface cleaning chamber installed on DEIMOS beamline with indications of the different parts of the chamber.

plete baking of the air-lock until a pressure of 10^{-8} mbar is reached. After 12 hours with the ion pump on, the pressure in both air-lock and scrapping chambers enters the 10^{-10} mbar range. Figure 3.6 illustrates the timeline of the procedure.

A diamond file is mounted on a rotatable manipulator. Figures 3.7 gives an illustration of the various samples that I have analyzed throughout my PhD years. One sample is fixed to a sample holder, which is mounted on a vertical translator with the diamond file in position to scrap the surface. For polycrystalline, millimeter large, bulk samples such as ErPd or YbAu samples, the file creates a deep groove and x-ray measurements are performed so that the beam is well centered inside the groove. On the other hand, for $La_xCe_{1-x}B_6$ samples that are fragile, needle-shaped, single crystals, I decided to glue one extremity of the crystal so that it could be broken by a gentle push of the file on the other extremity. For these samples, the measurements were performed on the new, fresh section of the crystal. The comparison of the measurements before

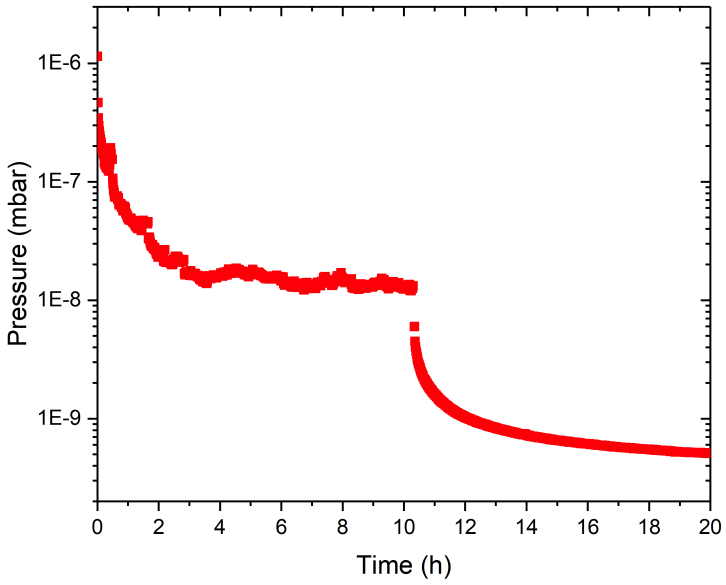

Figure 3.6: Evolution of the pressure in the UHV surface cleaning chamber after baking.

and after the surface cleaning will be presented in Section 5.5 for $Er_{0.025}Pd_{0.975}$ alloy and in Section 6.3.4 for $Yb_{0.005}Au_{0.995}$ alloy.

One should notice that after scraping a first sample, the clean diamond file gets contaminated so that it cannot be used for a second sample if the rare-earth of interest is the same for both samples. In this case, changing the file will be compulsory. On the other hand, if the second sample contains a rare-earth element that is different from the one contained in the first sample, it will be possible to use the same file for the two samples.

3.4 X-ray absorption spectroscopy

In general, spectroscopy means the measurement of the response of the interaction between an exciting source and matter as a function of energy. XAS is short for X-ray absorption spectroscopy which means a spectroscopy where the exciting source is an X-ray photon. Although the term XAS does not reveal the relation of XAS and synchrotron radiation, nowadays, almost all XAS measurements are performed with synchrotron radiation thanks to the properties of the synchrotron radiation explained in Section 3.1.

X-ray absorption by mater (Figure 3.8) follows the Beer-Lambert law and the transmitted intensity $I(E)$ of an incident electromagnetic wave with energy E and intensity

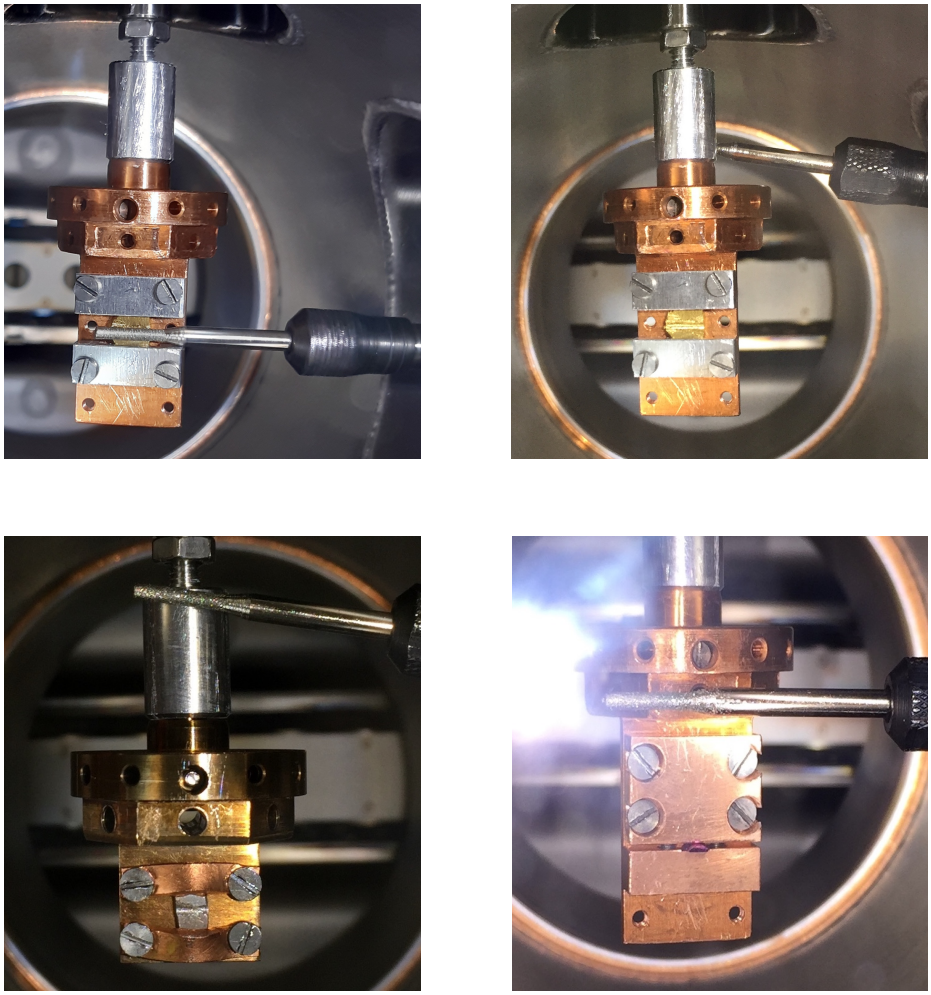

Figure 3.7: Surface cleaning for different samples in the UHV chamber. (Top-Left) $Yb_{0.005}Au_{0.995}$ sample scrapped by the diamond file with a pressure in the 10^{-10} mbar range. (Top-Right) Profile on the $Yb_{0.005}Au_{0.995}$ sample after being scrapped. A groove appears in the middle of the sample. (Bottom-Left) $Er_{0.025}Pd_{0.975}$ sample after being scrapped by the file. (Bottom-Right) $La_{0.96}Ce_{0.04}B_6$ sample before the extremity is broken by a gentle pressure of the diamond file.

$I_0(E)$ through a d thick sample writes

$$I(E) = I_0(E)e^{-\mu(E)d} \tag{3.1}$$

where $\mu(E)$ is an energy dependent linear attenuation coefficient. The absorption cross section σ is defined by :

$$\sigma = \frac{\mu}{N} \tag{3.2}$$

where N is the number of absorbing atoms per unit volume.

The Fermi Golden Rule is a crucial rule that describes the absorption of X-ray by

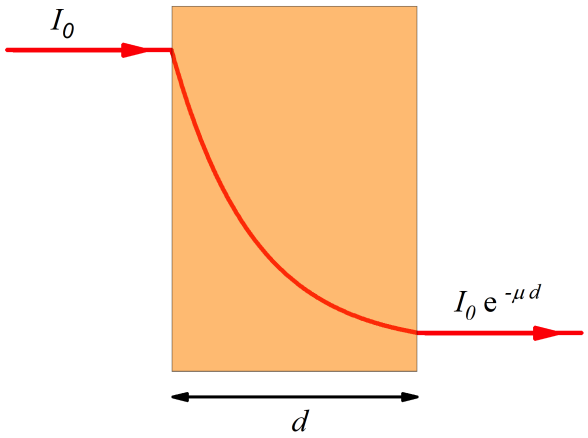

Figure 3.8: An incident beam with intensity I_0 is transmitted by a sample with width d and presenting an attenuation coefficient $\mu(E)$.

matter. When a system transits from an initial state $|i\rangle$ with energy E_i to a final state $|f\rangle$ with energy E_f due to the absorption of a photon with energy E and polarization $\boldsymbol{\epsilon}$, the transition probability $\Gamma_{if}(E)$ is given by

$$\Gamma_{if}(E) = \frac{2\pi}{\hbar}|\langle f|\boldsymbol{\epsilon}\cdot\boldsymbol{r}|i\rangle|^2\delta(E_f - E_i - E). \tag{3.3}$$

The way (Eq.3.3) is written supposes that both the electric dipole approximation and the monoelectronic approximation are satisfied. Then the absorption cross section σ between $|i\rangle$ and $|f\rangle$ is written as [107]:

$$\sigma(E) = 4\pi^2\alpha E\sum_f |\langle f|\boldsymbol{\epsilon}\cdot\boldsymbol{r}|i\rangle|^2\delta(E_f - E_i - E) \tag{3.4}$$

where α is the fine structure constant.

The cross-section from (Eq.3.4) is obtained by summing over all final states. The δ distribution insures energy conservation. Some $\langle f|\boldsymbol{\epsilon}\cdot\boldsymbol{r}|i\rangle$ matrix elements can be zero because of geometrical symmetries most often labeled selection rules. For the electric dipole approximation, the selection rules are [107]:

$$\begin{gathered}\Delta l = l_f - l_i = \pm 1,\ \Delta s = s_f - s_i = 0,\\ \Delta j = j_f - j_i = \pm 1,\ 0,\ \Delta m = m_f - m_i = q = \pm 1,\ 0.\end{gathered} \tag{3.5}$$

where q carries the helicity of the incident photon: $q = +1$ for left helicity, $q = -1$ for right helicity and $q = 0$ for linear polarization parallel to the $\hat{z}$ axis.

For an atom with only one electron, one can classify the edges as a function of

the principal quantum number n, the spin quantum number s, the orbital quantum number l, and the total angular momentum $j = s + l$ of the initial state. Figure 3.9 gives the nomenclature.

XAS is a chemically selective technique that gives information on the electronic and magnetic structures and on the symmetry of the absorbing atom.

Edge	n l j	Configuration	Edge	n l j	Configuration
K	1 0 1/2	$1s$	N_1	4 0 1/2	$4s$
L_1	2 0 1/2	$2s$	N_2	4 1 1/2	$4p_{1/2}$
L_2	2 1 1/2	$2p_{1/2}$	N_3	4 1 3/2	$4p_{3/2}$
L_3	2 1 3/2	$2p_{3/2}$	N_4	4 2 3/2	$4d_{3/2}$
M_1	3 0 1/2	$3s$	N_5	4 2 5/2	$4d_{5/2}$
M_2	3 1 1/2	$3p_{1/2}$	N_6	4 3 5/2	$4f_{5/2}$
M_3	3 1 3/2	$3p_{3/2}$	N_7	4 3 7/2	$4f_{7/2}$
M_4	3 2 3/2	$3d_{3/2}$	O_1	4 0 1/2	$5s$
M_5	3 2 5/2	$3d_{5/2}$	O_2	4 1 1/2	$5p_{1/2}$

Figure 3.9: X-ray absorption edges defined by the quantum numbers n, l, and j of the core-hole. (Table from [108]).

3.5 X-ray magnetic circular dichroism (XMCD)

XMCD is the difference between cross-sections measured first with right polarized X-rays ($q = -1$), then with left polarized X-rays ($q = +1$).

$$\sigma_{\mathrm{XMCD}}(E) = \sigma^{-}(E) - \sigma^{+}(E). \tag{3.6}$$

For the rare earths, in most cases the ground state can be written by one single J, built from one single S and one single L. When the rare earth ion is present in a crystal, its surrounding imposes a crystal field. The ground state is a linear combination of the $2J + 1$ eigenstates. It is generally degenerate. In the presence of an external magnetic field, the degeneracy of the ground state is removed, so that the ground state $|gs\rangle$ is a non-degenerate level with specific values for $\langle gs|J_z|gs\rangle$ and $\langle gs|J_z^2|gs\rangle$. For simplicity, one writes $\langle gs|J_z|gs\rangle = \langle J_z\rangle$ and $\langle gs|J_z^2|gs\rangle = \langle J_z^2\rangle$.

In such a case, Brouder [24] showed that the cross-sections at the $M_{4,5}$ edges for left (σ^+) and right (σ^-) polarized X-rays, with $\boldsymbol{k}$ propagation vector parallel to $\hat{z}$ simplify into the following expressions :

$$\sigma^{+}(E) = \sigma_0(E) - \langle J_z\rangle \sigma_1(E) + \frac{1}{2}\left[\frac{1}{3}J(J+1) - \langle J_z^2\rangle\right]\sigma_2(E) \tag{3.7}$$

and

$$\sigma^{-}(E) = \sigma_0(E) + \langle J_z \rangle \sigma_1(E) + \frac{1}{2}\left[\frac{1}{3}J(J+1) - \langle J_z^2 \rangle\right]\sigma_2(E). \tag{3.8}$$

Note that $\sigma_0(E)$, $\sigma_1(E)$ and $\sigma_2(E)$ are spectral signals that depend on the chemical element for a specific J, S, and L but do not depend on the crystal field parameters, nor on the intensity and direction of the external magnetic field. The average of the left and right absorption cross sections is then :

$$\frac{1}{2}\left[\sigma^{+}(E) + \sigma^{-}(E)\right] = \sigma_0(E) + \frac{1}{2}\left[\frac{1}{3}J(J+1) - \langle J_z^2 \rangle\right]\sigma_2(E) \tag{3.9}$$

and the XMCD signal is :

$$\sigma_{\mathrm{XMCD}} = \sigma^{-}(E) - \sigma^{+}(E) = 2\langle J_z \rangle \sigma_1(E). \tag{3.10}$$

In addition, when the X-rays are lineraly polarized with polarization along $\hat{z}$, the cross section can be written as

$$\sigma_{\parallel}(E) = \sigma_0(E) - \left[\frac{1}{3}J(J+1) - \langle J_z^2 \rangle\right]\sigma_2(E), \tag{3.11}$$

so that $\sigma_0(E) = \frac{1}{3}\left[\sigma^{+} + \sigma^{-} + \sigma_{\parallel}\right]$. $\sigma_0(E)$ is the isotropic cross section in the electric dipole approximation. From (Eq.3.7), (Eq.3.8) and (Eq.3.11), one sees that the spectral shape of XMCD is given by $\sigma_1(E)$ and the spectral shape of XMLD and XNLD is given by $\sigma_2(E)$. The intensity of these dichroic signals are then simple functions of $\langle J_z \rangle$ and $\langle J_z^2 \rangle$ [24].

Magneto-optical sum rules

In order to analyze the XMCD data, B.T. Thole developed the magneto-optical sum rules [22, 21]. There are many magneto-optical sum rules [109, 110, 111, 18, 112, 113] and the most common are the ones connecting the XMCD signal to the orbital magnetic moment and the one connecting the XMCD signal to the spin magnetic moment.

The sum rule for the orbital magnetic moment is:

$$\frac{\int_{j^+ + j^-} \mathrm{d}E(\sigma^{+} - \sigma^{-})}{\int_{j^+ + j^-} \mathrm{d}E(\sigma^{+} + \sigma^{-} + \sigma_{\parallel})} = \frac{l(l+1) + 2 - c(c+1)}{2l(l+1)(4l + 2 - n)}\langle L_z \rangle, \tag{3.12}$$

and the sum rule for the spin magnetic moment is :

$$\frac{\int_{j^+} \mathrm{d}E(\sigma^+ - \sigma^-) - [(c+1)/c] \int_{j^-} \mathrm{d}E(\sigma^+ - \sigma^-)}{\int_{j^+ + j^-} \mathrm{d}E(\sigma^+ + \sigma^- + \sigma_\parallel)} =$$
$$\frac{l(l+1) - 2 - c(c+1)}{3c(4l+2-n)} \langle S_z \rangle + \frac{l(l+1)[l(l+1) + 2c(c+1) + 4] - 3(c-1)^2(c+2)^2}{6lc(l+1)(4l+2-n)} \langle T_z \rangle. \tag{3.13}$$

In the case of the $M_{4,5}$ edges of rare earths, n is the number of electrons on the $4f$ shell, $l = 3$ is the orbital quantum number of the $4f$ shell, $c = 2$ is the orbital quantum number of the $3d$ core shell on which the core hole is created, $j^\pm = c \pm 1/2$ are the core levels split by the spin-orbit interaction, σ^+ and σ^- are the absorption spectra recorded for left and right polarized photons, with propagation vector parallel to the external magnetic field. $\sigma_\parallel$ is the absorption spectrum recorded with the linear polarization parallel to the external magnetic field. T_z is the projection along $\hat{z}$ of $\mathbf{T}$, the magnetic dipole operator. $\mathbf{T}$ is defined as

$$\mathbf{T} = \sum_i \left(\mathbf{s}_i - \frac{3\mathbf{r}_i (\mathbf{r}_i \cdot \mathbf{s}_i)}{r_i^2} \right), \tag{3.14}$$

where the sum over i is over all the electrons of the rare earth, $\mathbf{s}_i$ is the spin angular momemtum of electron i with position $\mathbf{r}_i$, and $r_i^2 = \mathbf{r}_i^2$. For transition elements, $\mathbf{T}$ is a term difficult to determine but in many cases, $\mathbf{T}$ is small enough to be neglected [2]. On the contrary, for most rare earths, T_z is large and can be calculated explicitly.

3.6 X-ray magnetic linear dichroism (XMLD)

By definition, the X-ray magnetic linear dichroism (XMLD) is the difference between the absorption cross section measured for linear polarization parallel to the external magnetic field ($\sigma_\parallel$) and the absorption cross section measured for linear polarization perpendicular to the external magnetic field ($\sigma_\perp$),

$$\sigma_{\mathrm{XMLD}}(E) = \sigma_\perp(E) - \sigma_\parallel(E). \tag{3.15}$$

Difference from XMCD, there is no precise definition for XMLD so that the coefficient $\frac{1}{3}$ that we use here, can be absent in other research papers and in a similar way, the sign of XMLD can be reversed. For comparison with other studies, one needs to check carefully the experimental procedures, the geometry, and the definitions of the various cross-sections.

One of the applications of the XMLD measurements is the investigation of the mag-

netic properties of antiferromagnetic materials which have no net total magnetic moment [114]. If the sample presents some magnetic anisotropy induced by the crystal field, the XMLD signals can be non zero. XMLD gives magnetic properties distinct from that of XMCD. The intensity of the XMCD signal is related to $\langle J_z \rangle$, whereas the XMLD signal is related to $\langle J_z^2 \rangle$. For a powder, where the only anisotropy comes from the external magnetic field applied along $\hat{z}$, one can show that [24]

$$\langle J_x^2 \rangle = \langle J_y^2 \rangle = \frac{1}{2} \left[J\left(J+1\right) - \langle J_z^2 \rangle \right]. \tag{3.16}$$

For sake of clarity, (Eq.3.16) is only valid for a completely disordered powder or for a material with cubic crystal symmetry. In the chapters to come, all the samples we measured belonged to one of this two classes. One can notice, that $\sigma_\perp = \frac{1}{2}\left[\sigma^+ + \sigma^-\right]$, so that

$$\sigma_{\mathrm{XMLD}}(E) = \sigma_\perp(E) - \sigma_\parallel(E) = \frac{3}{2}\left[\sigma^+\left(E\right) + \sigma^-\left(E\right)\right] - 3\sigma_0\left(E\right). \tag{3.17}$$

The above equation (Eq.3.17) states that to measure the XMLD signals, one simply needs to measure σ^+ and σ^- (as for XMCD) and with the additional measurement of σ_0 (*i.e.* the cross section in the absence of an external magnetic field), it is possible to determine the XMLD signal.

From (Eq.3.7) and (Eq.3.8), one finds that

$$\sigma_{\mathrm{XMLD}}(E) = \frac{1}{2}\left[J\left(J+1\right) - 3\left\langle J_z^2 \right\rangle \right] \sigma_2\left(E\right), \tag{3.18}$$

from which it is clear that the XMLD signal is related to the anisotropy of $\langle \boldsymbol{J}^2 \rangle$.

Chapter 4

Calculation Methods

In this chapter, I present the general ideas behind the calculation of the eigenstates, the energy levels, the orbital magnetic moment, the spin magnetic moment and averaged operators such as $\langle J_z \rangle$ and $\langle J_z^2 \rangle$. The validity of the calculations is limited to the case of rare earths when the ground state can be determined by a single J, stemming from a single L and a single S. We particularly address the question of the variation of these quantities with temperature. All that is presented in the following is common, atomic physics that I had to learn for the analysis of the XMCD data at $M_{4,5}$ edges of rare earths. The presentation is mine but the physics is well known.

For an atom present in a crystal and submitted to an external magnetic field, one can solve the Schrödinger equation

$$H\,|\psi\rangle = E\,|\psi\rangle \tag{4.1}$$

to determine the energy eigenvalues E, and the associated eigenstates $|\psi\rangle$. The Hamiltonian H can be expressed as

$$H = H_0 + H_c + H_{Zee} \tag{4.2}$$

where H_c is the crystal field Hamiltonian representing an electrostatic potential imposed by the neighbours of the atom, H_{Zee} is the Zeeman Hamiltonian representing the action of an external magnetic field, and H_0 is the multielectronic, atomic, spherical Hamiltonian defined by

$$H_0 = H_{kin} + H_{pot} + H_{ee} + H_{SO}. \tag{4.3}$$

where H_{kin} is the kinetic energy Hamiltonian, H_{pot} is the Coulomb Hamiltonian between the nucleus and the core electrons, H_{ee} is the multielectronic Hamiltonian representing the electron-electron Coulomb repulsions, and H_{SO} is the spin-orbit coupling

Hamiltonian. The expression for H_0, the spherical, atomic, multielectronic Hamiltonian is standard and I shall not develop it here. I shall focus on the expressions for the crystal field Hamiltonian and for the Zeeman Hamiltonian.

4.1 The crystal field Hamiltonian

For rare earths where the $4f$ shell is an open shell, H_c can be expressed by the sum of a term of fourth degree and a term of sixth degree as [115]

$$H_c = C_4\beta\left(O_4^0 + 5O_4^4\right) + C_6\gamma\left(O_6^0 - 21O_6^4\right) \tag{4.4}$$

where [116]

$$\begin{aligned}
O_4^0 &= 35J_z^4 - [30J(J+1) - 25]J_z^2 - 6J(J+1) + 3J^2(J+1)^2, \\
O_4^4 &= \tfrac{1}{2}(J_+^4 + J_-^4), \\
O_6^0 &= 231J_z^6 - 105[3J(J+1) - 7]J_z^4 + [105J^2(J+1)^2 - 525J(J+1) + 294]J_z^2 \\
&\quad -5J^3(J+1)^3 + 40J^2(J+1)^2 - 60J(J+1), \\
O_6^6 &= \tfrac{1}{4}[11J_z^2 - J(J+1) - 38](J_+^4 + J_-^4) + \tfrac{1}{4}(J_+^4 + J_-^4)[11J_z^2 - J(J+1) - 38].
\end{aligned} \tag{4.5}$$

The above expressions suppose that the spherical ground state is defined by a unique triad $J(L,S)$, where J is an integer or a half-integer. On the contrary, J_z, J_+, and J_- are scalar operators of the total angular momentum. Values for the different operators O_4^0, O_4^4, O_6^0 and O_6^6 can be explicitly calculated or found in reference [117].

Lea *et al.* rewrote the Hamiltonian in the following form [116]

$$H_c = B_4F(4)\frac{O_4}{F(4)} + B_6F(6)\frac{O_6}{F(6)} \tag{4.6}$$

where $O_4 = \left(O_4^0 + 5O_4^4\right)$ and $O_6 = \left(O_6^0 - 21O_6^4\right)$. A scale factor W has been defined to cover all possible values of the ratio between the fourth and sixth degree terms:

$$B_4F(4) = Wx, \tag{4.7}$$

$$B_6F(6) = W(1 - |x|) \tag{4.8}$$

where $-1 < x < 1$. We have then

$$H_c = W\left[x\left(\frac{O_4}{F(4)}\right) + (1 - |x|)\left(\frac{O_6}{F(6)}\right)\right]. \tag{4.9}$$

The ratio between B_4 and B_6 can be expressed by x:

$$\frac{B_4}{B_6} = \frac{x}{1-|x|}\frac{F(6)}{F(4)} \tag{4.10}$$

where $F(4)$ and $F(6)$ are factors which can be found in reference [116] and $x = 0$ for $B_4/B_6 = 0$, $x = \pm 1$ while $B_4/B_6 = \pm\infty$. B_4 and B_6 are related to the crystal field parameters $A_4 \langle r^4 \rangle$ and $A_6 \langle r^6 \rangle$:

$$\begin{aligned} B_4 &= A_4 \langle r^4 \rangle \beta \\ B_6 &= A_6 \langle r^6 \rangle \gamma \end{aligned} \tag{4.11}$$

where β and γ are the Stevens multiplicative factors which can be found in references [117] [116].

4.2 The Zeeman Hamiltonian

Here we present the calculation method of the Zeeman effect and the application will be shown in the following chapters for the concrete example of rare earths. The Zeeman Hamiltonian under external magnetic field $\mathbf{B}$ is

$$H_{\text{Zee}} = -\boldsymbol{\mu} \cdot \mathbf{B} = \frac{\mu_B}{\hbar} \left(\mathbf{L} + g_s \mathbf{S} \right) \mathbf{B}. \tag{4.12}$$

where g_s is the gyromagnetic ratio of the spin of electron and μ_B is the Bohr magneton. We choose here by convention

$$\mu_B = \frac{e\hbar}{2m_e} > 0. \tag{4.13}$$

We use the eigenfunction $|\alpha JM\rangle$ of the operators $\mathbf{J^2}$ and J_z^2 where $\mathbf{J}$ is the total angular momentum $\mathbf{J} = \mathbf{L} + \mathbf{S}$. The total magnetic moment is

$$m = m_{orbit} + m_{spin} = \frac{\mu_B}{\hbar} \langle \alpha JM | \left(\mathbf{L} + g_s \mathbf{S} \right) | \alpha' J' M' \rangle . \tag{4.14}$$

To calculate the matrix elements of (Eq.4.14), we use the Wigner-Eckart theorem which states that the matrix elements of irreducible spherical tensor operators $T_q^{(k)}$ between the angular momentum eigenstates satisfy [118]

$$\langle \alpha JM | T_q^{(k)} | \alpha', J'M' \rangle = (-1)^{J-M} \begin{pmatrix} J & k & J' \\ -M & q & M \end{pmatrix} \langle \alpha J || \mathbf{T}^{(k)} || \alpha' J' \rangle \tag{4.15}$$

where k is the rank of the tensor $T_q^{(k)}$, q is a variable between $-k$ and k in steps of 1, $(-1)^{J-M} \begin{pmatrix} J & k & J' \\ -M & q & M \end{pmatrix}$ is Wigner $3j$ symbol equivalent to a Clebsch-Gordan coeffi-

cient and $\langle \alpha J||\mathbf{T}^{(k)}||\alpha' J'\rangle$ are the reduced matrix elements which do not depend on M, M' or q.

A spherical tensor of rank 1 is a 3-component, vector operator and $\mathbf{J}$ is a spherical tensor of rank 1.

We assume that the magnetic field $\mathbf{B}$ is along the $\hat{z}$ axis, with the application of the Wiger-Eckart theorem, we can calculate the matrix elements of the total magnetic moment of (Eq.4.14). We have

$$\langle \alpha JM|\left(\mathbf{L}+g_s\mathbf{S}\right)|\alpha' J'M'\rangle = (-1)^{J-M}\begin{pmatrix} J & k & J' \\ -M & q & M\end{pmatrix}\langle \alpha J||\left(\mathbf{L}+g_s\mathbf{S}\right)||\alpha' J'\rangle\,. \quad (4.16)$$

The reduced matrix elements $\langle \alpha J||\left(\mathbf{L}+g_s\mathbf{S}\right)||\alpha' J'\rangle$ can be decomposed as

$$\langle \alpha J||\left(\mathbf{L}+g_s\mathbf{S}\right)||\alpha' J'\rangle = \langle LSJ||\left(\mathbf{L}+g_s\mathbf{S}\right)||L'S'J'\rangle = \langle LSJ||\mathbf{L}||L'S'J'\rangle + g_s\langle LSJ||\mathbf{S}||L'S'J'\rangle\,. \quad (4.17)$$

Thus (Eq.4.16) can be rewritten as

$$\begin{aligned}
&\langle \alpha JM|\left(\mathbf{L}+g_s\mathbf{S}\right)|\alpha' J'M'\rangle = (-1)^{J-M}\begin{pmatrix} J & k & J' \\ -M & q & M\end{pmatrix}\langle \alpha J||\left(\mathbf{L}+g_s\mathbf{S}\right)||\alpha' J'\rangle \\
&= (-1)^{J-M}\begin{pmatrix} J & k & J' \\ -M & q & M\end{pmatrix}\langle LSJ||\mathbf{L}||L'S'J'\rangle + g_s\,(-1)^{J-M}\begin{pmatrix} J & k & J' \\ -M & q & M\end{pmatrix}\langle LSJ||\mathbf{S}||L'S'J'\rangle \\
&= (-1)^{J-M}\begin{pmatrix} J & k & J' \\ -M & q & M\end{pmatrix}\langle L||\mathbf{L}||L\rangle\,\delta_{S,S'}\delta_{L,L'}[J,J']^{1/2}\,(-1)^{S+L+J'+k}\begin{Bmatrix} L & S & J \\ J' & k & L'\end{Bmatrix} \\
&+ g_s\,(-1)^{J-M}\begin{pmatrix} J & k & J' \\ -M & q & M\end{pmatrix}\langle S||\mathbf{S}||S\rangle\,\delta_{S,S'}\delta_{L,L'}[J,J']^{1/2}\,(-1)^{S+L+J'+k}\begin{Bmatrix} L & S & J \\ k & J' & S'\end{Bmatrix}.
\end{aligned} \quad (4.18)$$

By definition and also after some calculations [118], $[J,J']^{1/2} = [(2J+1)(2J'+1)]^{1/2}$, $\langle L||\mathbf{L}||L\rangle = [L(L+1)(2L+1)]^{1/2}$ and $\langle S||\mathbf{S}||S\rangle = [S(S+1)(2S+1)]^{1/2}$.

m then can be obtained by applying (Eq.4.14). If we assume that the magnetic field $\mathbf{B}$ is along the $\hat{z}$ axis, the diagonal matrix elements which gives the Zeeman energy can be written as

$$E_{Zee} = \langle \alpha JM|H_{Zee}|\alpha JM\rangle = \frac{\mu_B}{\hbar}M\,\hbar\,B\,g_J \quad (4.19)$$

where g_J is Landé g factor expressed as

$$g_J = g_{\text{orbit}}\frac{J(J+1)-S(S+1)+L(L+1)}{2J(J+1)} + g_{\text{spin}}\frac{J(J+1)+S(S+1)-L(L+1)}{2J(J+1)}. \quad (4.20)$$

We take $g_{\text{orbit}} = 1$ and $g_{\text{spin}} = g_s = 2$ for the numerical applications.

4.3 Matrix representation of the crystal field Hamiltonian and the Zeeman Hamiltonian

The angular momentum vectorial operator **J** is written from its three scalar operators J_x, J_y and J_z verifying

$$\mathbf{J}^2 = J_x^2 + J_y^2 + J_z^2, \tag{4.21}$$

and if the basis is the orthonormal basis $|\alpha, J, M\rangle$ of J_z eigenstates, one has

$$\langle \alpha JM | J_z | \alpha' J' M' \rangle = M\hbar \, \delta_{\alpha,\alpha'} \delta_{J,J'} \delta_{M,M'}. \tag{4.22}$$

We can build two ladder operators:

$$\begin{aligned} J_+ &= J_x + iJ_y \\ J_- &= J_x - iJ_y. \end{aligned} \tag{4.23}$$

The matrix elements of J_+ and J_- can be represented in the basis $\{|\alpha JM\rangle\}$ as

$$\langle \alpha JM | J_+ | \alpha' J' M' \rangle = \hbar \sqrt{J(J+1) - M'(M'+1)} \, \delta_{\alpha,\alpha'} \delta_{J,J'} \delta_{M,M'+1}, \tag{4.24}$$

and

$$\langle \alpha JM | J_- | \alpha' J' M' \rangle = \hbar \sqrt{J(J+1) - M'(M'-1)} \, \delta_{\alpha,\alpha'} \delta_{J,J'} \delta_{M,M'-1}. \tag{4.25}$$

The matrix elements J_x and J_y in the $\{|\alpha JM\rangle\}$ basis can be calculated with the following formulas [119]:

$$\begin{aligned} \langle \alpha JM | J_x | \alpha' J' M' \rangle &= \frac{\hbar}{2} \delta_{\alpha,\alpha'} \delta_{J,J'} \\ &\times \left[\sqrt{J(J+1) - M'(M'+1)} \delta_{M,M'+1} + \sqrt{J(J+1) - M'(M'-1)} \delta_{M,M'-1} \right], \end{aligned} \tag{4.26}$$

$$\begin{aligned} \langle \alpha JM | J_y | \alpha' J' M' \rangle &= \frac{\hbar}{2i} \delta_{\alpha,\alpha'} \delta_{J,J'} \\ &\times \left[\sqrt{J(J+1) - M'(M'+1)} \delta_{M,M'+1} - \sqrt{J(J+1) - M'(M'-1)} \delta_{M,M'-1} \right]. \end{aligned} \tag{4.27}$$

And the matrix elements of $\mathbf{J}^2$ in the $\{|\alpha JM\rangle\}$ basis is

$$\left\langle \alpha JM \middle| \mathbf{J}^2 \middle| \alpha' J' M' \right\rangle = J(J+1) \hbar^2 \delta_{\alpha,\alpha'} \delta_{J,J'} \delta_{M,M'}. \tag{4.28}$$

In the previous equations, the matrix elements are written between $|\alpha JM\rangle$ and

$|\alpha' J' M'\rangle$. In the case of rare earths, it is usually sufficient to focus on the subset built with the $(2J+1)$ basis elements $\{|\alpha JM\rangle\}$ with $-J \leq M \leq J$. So that equations greatly simplify when $\alpha = \alpha'$ and $J = J'$.

For polycrystaline materials or a perfect powder, we denote J_{zp} the projection of the total angular momentum along the $\hat{z}$ direction which can be written as:

$$J_{zp} = aJ_x + bJ_y + cJ_z \tag{4.29}$$

with a, b, c three constants that satisfy $a^2 + b^2 + c^2 = 1$. We suppose that a, b, c are real numbers in order to simplify the calculation. In the case of cubic symmetry, three families of directions are possible : $[110]$ or C_2, $[111]$ or C_3 and $[001]$ or C_4. With a simple calculation, we obtain:

$$\begin{aligned} C_2 : &\quad J_{zp\_C_2} = \tfrac{1}{\sqrt{2}} J_x + \tfrac{1}{\sqrt{2}} J_y, \\ C_3 : &\quad J_{zp\_C_3} = \tfrac{1}{\sqrt{3}} J_x + \tfrac{1}{\sqrt{3}} J_y + \tfrac{1}{\sqrt{3}} J_z, \\ C_4 : &\quad J_{zp\_C_4} = J_z. \end{aligned} \tag{4.30}$$

Now we calculate the square of (Eq.4.29) and (Eq.4.30) and we obtain:

$$J_{zp}^2 = a^2 J_x^2 + b^2 J_y^2 + c^2 J_z^2 + abJ_xJ_y + baJ_yJ_x + acJ_xJ_z + caJ_zJ_x + bcJ_yJ_z + cbJ_zJ_y, \tag{4.31}$$

and

$$\begin{aligned} J_{zp\_C_2}^2 &= \tfrac{1}{2} J_x^2 + \tfrac{1}{2} J_y^2 + \tfrac{1}{2} J_xJ_y + \tfrac{1}{2} J_yJ_x, \\ J_{zp\_C_3}^2 &= \tfrac{1}{3} J_x^2 + \tfrac{1}{3} J_y^2 + \tfrac{1}{3} J_z^2 + \tfrac{1}{3} J_xJ_y + \tfrac{1}{3} J_yJ_x + \tfrac{1}{3} J_xJ_z + \tfrac{1}{3} J_zJ_x + \tfrac{1}{3} J_yJ_z + \tfrac{1}{3} J_zJ_y, \\ J_{zp\_C_4}^2 &= J_z^2. \end{aligned} \tag{4.32}$$

Now let's study the Hamiltonian. For three kinds of symmetries C_2, C_3 and C_4, the Hamiltonian can be written as the the sum of the Hamiltonian of the crystal field and

the Hamiltonian of the Zeeman effect:

$$\begin{aligned} H_{C_2} &= H_c + H_{Zee_{C_2}}, \\ H_{C_3} &= H_c + H_{Zee_{C_3}}, \\ H_{C_4} &= H_c + H_{Zee_{C_4}}. \end{aligned} \tag{4.33}$$

The H_{C_i} ($i = 2, 3, 4$) matrix elements can be written in the $|\Gamma_j^\sigma\rangle$ basis where σ is a sign indicator for the Zeeman level which can take the sign of $+$ or $-$. j is the index that represents the different crystal field splitting levels. *A priori*, H_{C_i} is not diagonal in this basis. The diagonalization of H_{C_i} is necessary.

Supposing for a given symmetry (a fixed i), H_{C_i} is diagonal in the basis $|\zeta_{C_i}^l\rangle$ with $l = 1, 2, ...$ to distinguish the different basis elements. A change-of-basis matrix P_{C_i} can transform the matrix elements between the two representations:

$$\left\langle \zeta_{C_i}^l \middle| H_{C_i} \middle| \zeta_{C_i}^{l'} \right\rangle = P_{C_i}^{-1} \left\langle \Gamma_j^\sigma \middle| H_{C_i} \middle| \Gamma_{j'}^{\sigma'} \right\rangle P_{C_i}. \tag{4.34}$$

And the $J_{zp\_C_i}$ and $J_{zp\_C_i}^2$ can be written in the new basis $|\zeta_{C_i}^l\rangle$ as:

$$\begin{aligned} \left\langle \zeta_{C_i}^l \middle| J_{zp\_C_i} \middle| \zeta_{C_i}^{l'} \right\rangle &= P_{C_i}^{-1} \left\langle \Gamma_j^\sigma \middle| J_{zp\_C_i} \middle| \Gamma_{j'}^{\sigma'} \right\rangle P_{C_i} \\ \left\langle \zeta_{C_i}^l \middle| J_{zp\_C_i}^2 \middle| \zeta_{C_i}^{l'} \right\rangle &= P_{C_i}^{-1} \left\langle \Gamma_j^\sigma \middle| J_{zp\_C_i}^2 \middle| \Gamma_{j'}^{\sigma'} \right\rangle P_{C_i}. \end{aligned} \tag{4.35}$$

In the $|\zeta_{C_i}^l\rangle$ ($i = 2, 3, 4$) basis, the wavefunctions can be expressed as:

$$\left|\psi_{C_i}\right\rangle = \sum_l \alpha_l \left|\zeta_{C_i}^l\right\rangle. \tag{4.36}$$

We assume that α is a real coefficient and we obtain

$$\left\langle \psi_{C_i} \middle| J_{zp\_C_i}^2 \middle| \psi'_{C_i} \right\rangle = \sum_{l,l'} \alpha_{l,l'} \left\langle \zeta_{C_i}^l \middle| J_{zp\_C_i}^2 \middle| \zeta_{C_i}^{l'} \right\rangle. \tag{4.37}$$

where the coefficient $\alpha_{l,l'}$ can be expressed by the Maxwell-Boltzmann distribution as a function of temperature:

$$\alpha_{l,l'} = \frac{\exp\left(-\frac{E_{C_i}^{l,l'}}{k_B T}\right)}{\sum_{l,l'} \exp\left(-\frac{E_{C_i}^{l,l'}}{k_B T}\right)} = \frac{\exp\left(-\frac{\left\langle \zeta_{C_i}^l \middle| H_{C_i} \middle| \zeta_{C_i}^{l'} \right\rangle}{k_B T}\right)}{\sum_{l,l'} \exp\left(-\frac{\left\langle \zeta_{C_i}^l \middle| H_{C_i} \middle| \zeta_{C_i}^{l'} \right\rangle}{k_B T}\right)}. \tag{4.38}$$

By using (Eq.4.37) and (Eq.4.38), we can calculate all matrix elements for three different symmetries: $\left\langle \psi_{C_2} \middle| J^2_{zp\_C_2} \middle| \psi'_{C_2} \right\rangle$, $\left\langle \psi_{C_3} \middle| J^2_{zp\_C_3} \middle| \psi'_{C_3} \right\rangle$ and $\left\langle \psi_{C_4} \middle| J^2_{zp\_C_4} \middle| \psi'_{C_4} \right\rangle$ as a function of temperature. For each symmetry, summation of all the matrix elements gives the $\langle J^2_{zp\_C_i} \rangle$ for a giving temperature.

For the powder, in the case of cubic symmetry, one has [120, 121]

$$\sigma_{\text{powder}} = \frac{176}{385}\sigma\left(B||C_2\right) + \frac{99}{385}\sigma\left(B||C_3\right) + \frac{110}{385}\sigma\left(B||C_4\right) \tag{4.39}$$

where $\sigma\left(B||C_2\right)$, $\sigma\left(B||C_3\right)$ and $\sigma\left(B||C_4\right)$ are the cross sections corresponding to the magnetic field B along the C_2, C_3 and C_4 directions. Finally, similar expressions can be obtained for $\langle J^2_z \rangle$

$$\langle J^2_z \rangle = \frac{176}{385}\left\langle \psi_{C_2} \middle| J^2_{zp\_C_2} \middle| \psi'_{C_2} \right\rangle + \frac{99}{385}\left\langle \psi_{C_3} \middle| J^2_{zp\_C_3} \middle| \psi'_{C_3} \right\rangle + \frac{110}{385}\left\langle \psi_{C_4} \middle| J^2_{zp\_C_4} \middle| \psi'_{C_4} \right\rangle. \tag{4.40}$$

For a given rare earth with a ground state at $T = 0\,\text{K}$ that can be written $\sum_M \lambda_M \left|\alpha JM\right\rangle$, (Eq.4.40) allows to compute $J(J+1)/3 - \langle J^2_z \rangle$ which is closely related to the XMLD signals defined in (Eq.3.17) so that theoretical prediction can be compared to experimental data.

4.4 Ligand field multiplet (LFM) calculations codes

Besides of the analytic calculations discussed in the section above, for the more complicated cases, numerical calculations become indispensable. The numerical tools used in this thesis is the Crispy interface based on the QUANTY package.

QUANTY is a computational package developed by Haverkort *et al.* [122, 123, 124, 125]. It can perform general simulation in quantum physics and chemistry and it is especially used for calculations of the spectroscopies and dynamics of correlated electron systems [126].

Using QUANTY necessitates programming. Based on the QUANTY package Retegan developed a very user friendly graphical interface Crispy that can be installed on Windows® and MacOS® providing the enormous convenience for the users [127] of a Python programmation interaction [126]. It is very useful for the simulation of core-level spectra like XAS/XMCD for transition metals and lanthanides. The user fixes the temperature, the external magnetic field, the energy range, the distribution form (Lorentzian or Gaussian) of the spectrum, the wave and polarization vectors, the spin-orbit coupling strength, the crystal field parameters exchange field parameters, etc.; Crispy gives a simulated spectrum in the configured condition. Crispy is also able to load the experimental data in order to allow to users to compare visually the quality

of the simulation. Figures 4.1 shows the Crispy main window displaying a simulation spectrum of Er^{3+} comparing to a experimental spectrum with the setting configuration parameters.

4.4. Ligand field multiplet (LFM) calculations codes

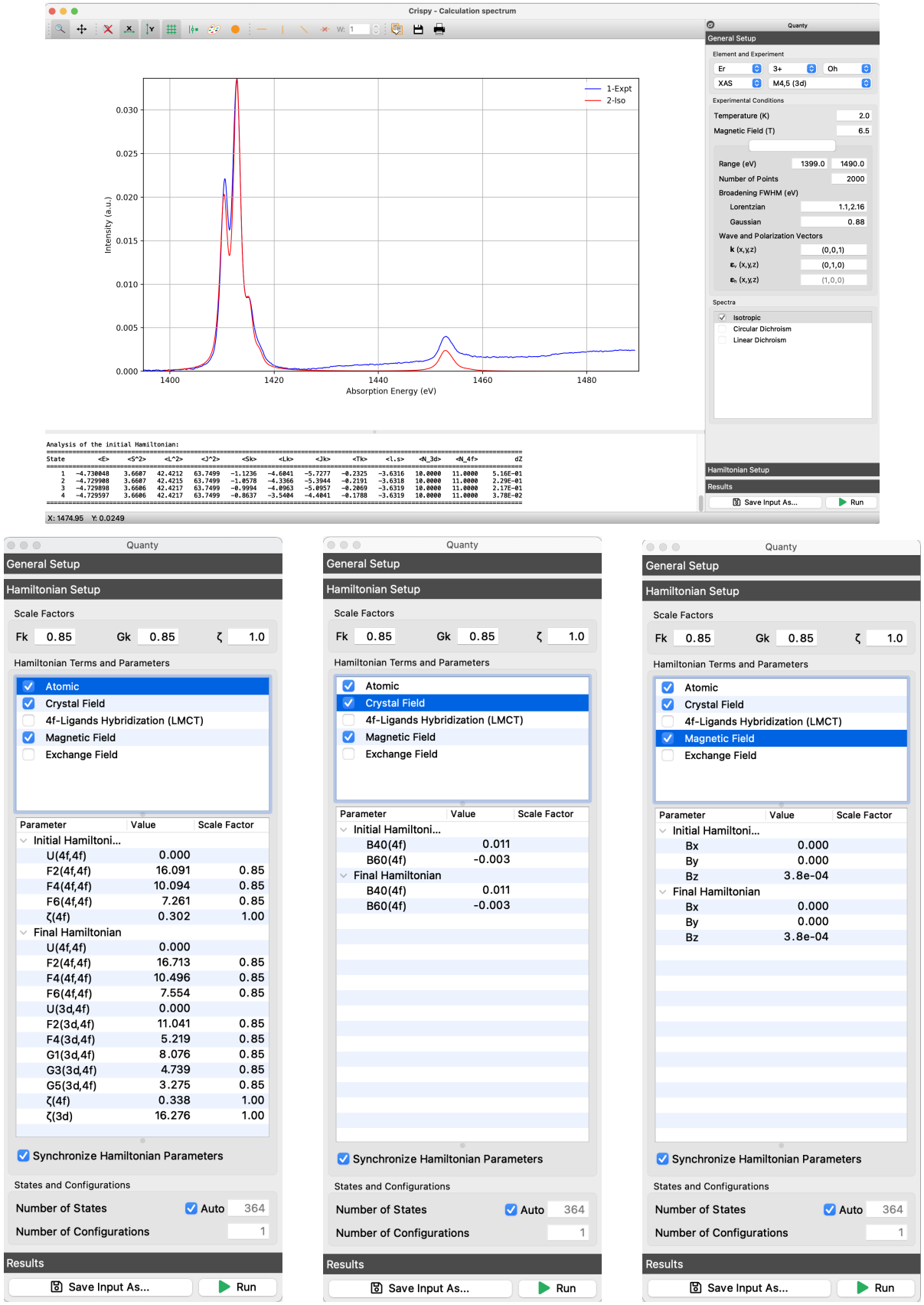

Figure 4.1: In using Crispy for LFM calculations. (Top) Crispy main window showing the experimental data (Spectrum 1-Expt) compared to the simulated XAS spectrum (spectrum 2-Iso) of Er^{3+} with the configurations displayed (Bottom).

Chapter 5

Intermetallic $Er_{0.025}Pd_{0.975}$ Alloy

5.1 Motivations of the study

In this chapter, the experimental analysis of the intermetallic $Er_{0.025}Pd_{0.975}$ sample (very diluted erbium atoms in palladium) will be presented. Erbium is one of the rare earths that is part of the series of lanthanide elements where the $4f$ electronic shell is open (*i.e.* not completely empty, nor completely full).

RE−Pd (RE: rare earth) binary intermetallic systems have been investigated [128, 129] to determine the electronic structures and the stability of the crystalline phases as a function of the rare earth nature and concentration. Despite a rather simple composition, the peculiarity of the magnetic properties of most RE-Pd compounds is far from being fully understood [130]. ErPd is one of these binary intermetallic systems. The magnetic properties have been investigated by Guertin *et al.* [131] and the crystal field parameters of ErPd have also been investigated by neutron spectroscopy [132]. The determined crystal field parameters can be found in two different series: one where both $A_4 \langle r_4 \rangle$ and $A_6 \langle r_6 \rangle$ parameters are negative and one where $A_4 \langle r_4 \rangle$ is positive and $A_6 \langle r_6 \rangle$ is negative. In addition, it was said that the magnitude of $A_6 \langle r_6 \rangle$ was the same for all binary compounds ErM (M: Rh, Pd, Ag, Cu, Zn, Mg). However, the origin of this constant $A_6 \langle r_6 \rangle$ crystal field parameter remains unexplained [132] and could be attributed to the lack of direct measurement of the crystal field parameters.

From previous measurements, it is also believed that there is no Kondo effect down to temperatures as low as 100 mK. Then Er should behave as a paramagnetic impurity in a metallic matrix and could be used for thermometric purposes. Indeed, the magnetization of Er in an external magnetic field of 0.1 T varies by a factor of 7 between 300 mK to 4.2 K (Figure 5.1). This wide variation of the magnetization makes it possible to use Er as a thermometer in order to check that the actual temperature of the sample is indeed closely following the one determined by the RuO_2 probe fixed on the mixing chamber (see Chapter 2).

This is what I have done with the DICHRO50 variable temperature insert inserted in the CroMag cryomagnet on DEIMOS beamline. I recorded the intensity of the XMCD signal at Er-$M_{4,5}$ edges in order to check by a physical measurement the temperature that was given by the RuO_2 thermal probe. The analysis of these thermometric measurements has been an important instrumental achievement of my PhD work.

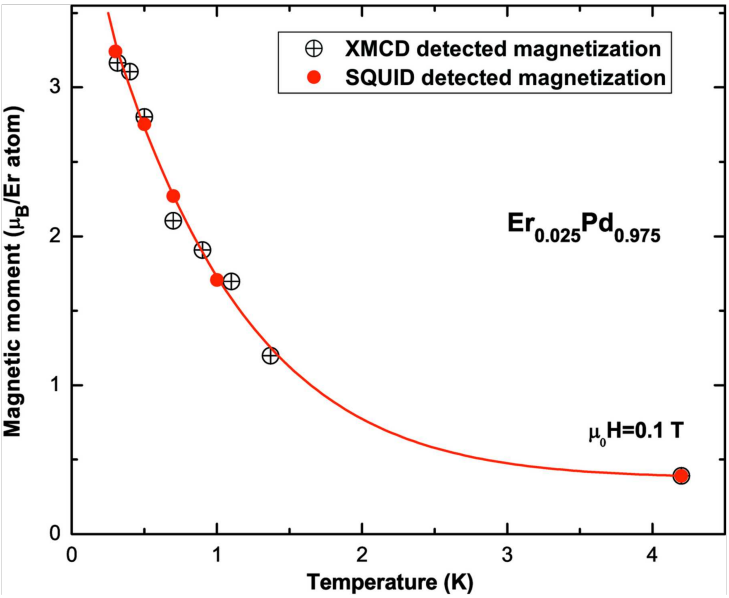

Figure 5.1: Magnetic moment of Er^{3+} in the $Er_{0.025}Pd_{0.975}$ alloy under an external magnetic field of 0.1 T as a function of the temperature between 300 mK and 4.2 K measured by XMCD and SQUID (Figure from [36]).

In addition to the instrumental caracterization of DICHRO50 VTI, I also used this set of data to bring new information to the crystal field acting on Er ions. I recorded the Er-$M_{4,5}$ edges between 300 K and 200 mK with an external magnetic field varying between -6.5 T to $+6.5$ T. Numerical calculations of the XAS, XMCD and XMLD spectra were performed with ligand field multiplet (LFM) theory using the Crispy interface (see Section 4.4) and from comparison between the experiments and LFM calculations, a set of crystal field parameters has been determined.

5.2 Properties of the erbium trivalent ion

The atomic number of erbium is 68 and its molar mass is 167.259 (3) g/mol [133]. In general, erbium is in the form of a trivalent cation ion Er^{3+} in a solid. The electronic configuration of Er^{3+} is [Xe]$4f^{11}$ so that the $4f$ shell is open. Because of the Coulomb repulsion and Pauli exclusion principle, the ground state of Er^{3+} is paramagnetic.

By definition, the quantum numbers l and s for one electron on the f shell are $l = 3$

and $s = 1/2$ [134]. The one-electron orbital angular momentum, l_z can take integer values from -3 to 3 and the one-electron spin angular momentum, s_z can take the integer values $-1/2$ and $+1/2$. To determine the total spin ($S = \sum_{i=1}^{11} s^i$) and orbital angular ($L = \sum_{i=1}^{11} l^i$) momenta of the Er^{3+} ground state, one has to determine the spin (S) and orbital angular (L) momenta of the $4f^{11}$ shell (the other shells are closed so that $S_{\text{other-shells}} = 0$ and $L_{\text{other-shells}} = 0$). Following the "rule of thumb method" to determine S and L, one fills the $2l + 1$ boxes with the 11 electrons, where the two first Hund rules are fulfilled (*i.e.* S and L are maximized). From the $2l + 1$ boxes scheme, one finds that $S_z = 3/2$ and $L_z = -6$, so that a good possible guess with regard to the two first Hund rules is $S = 3/2$ and $L = 6$. The third Hund rule states that J has to be maximized because there are more than 7 electrons on the $4f$ shell. Then $J = L + S = 15/2$ state built from $L = 6$ and $S = 3/2$ configurations is the ground state of erbium. It is a 16-fold degenerate ground state.

m_L	+3	+2	+1	0	-1	-2	-3
m_S	$\uparrow\downarrow$	$\uparrow\downarrow$	$\uparrow\downarrow$	$\uparrow\downarrow$	$\uparrow$	$\uparrow$	$\uparrow$

$$J = S + L = \frac{15}{2}. \tag{5.1}$$

The term symbol $^{2S+1}L_J$ describing Er ground state is then $^4I_{15/2}$. The Hund rules suppose that the ion is in a spherical environment so that the 16-fold degenerate $^4I_{15/2}$ ground state is only valid in a spherical symmetry.

If we simply consider a spherical Er^{3+} ion, we can easily calculate the action of an external field B so that the magnetization at temperature T is given by :

$$M = g_J \, \mu_B \, J \, B_J(x). \tag{5.2}$$

where μ_B is the Bohr magneton expressed by $\mu_B = e\hbar/(2m_e) = 9.274 \times 10^{-24}$ A m^2 in S.I. For Er^{3+} ion, $J = 15/2$, $L = 6$, $S = 3/2$ (Eq.5.1), and the Landé factor g_J is given by

$$g_J = g_{\text{orbit}} \frac{J(J+1) - S(S+1) + L(L+1)}{2J(J+1)} + g_{\text{spin}} \frac{J(J+1) + S(S+1) - L(L+1)}{2J(J+1)}. \tag{5.3}$$

If we take the conventional approximate values $g_{\text{orbit}} = 1$ et $g_{\text{spin}} \approx 2$, the numerical application gives $g_J = 6/5$. $B_J(x)$ is the Brillouin function expressed as:

$$B_J(x) = \frac{2J+1}{2J} \coth\left(\frac{2J+1}{2J}x\right) - \frac{1}{2J} \coth\left(\frac{x}{2J}\right) \tag{5.4}$$

with

$$x = \frac{g_J \, \mu_B \, J \, B}{k_B \, T}. \tag{5.5}$$

Alternative computation of the magnetic moment at T= 0 K

For Er^{3+} ion, there is another way to compute the magnetization in spherical symmetry. The total Zeeman energy is given by $\mu_B/\hbar(g_{\text{orbit}}\boldsymbol{L} + g_{\text{spin}}\boldsymbol{S}).\boldsymbol{B}$, where the total magnetic moment is given by the operator $-\mu_B/\hbar(g_{\text{orbit}}\boldsymbol{L} + g_{\text{spin}}\boldsymbol{S})$ acting on the ground state. The $4f$ shell is more than half filled, so that $J = L + S$ and $J_z = L_z + S_z$ (this is due to the fact that there is only one Clebsch-Gordan coefficient connecting $[J(L,S);-J]$ and $[(L;-L),(S;-S)]$ and it is equal to 1 (*i.e.* $[J(L,S);-J] = [(L;-L),(S;-S)]$). Then the total magnetic moment m_{Total} at $T = 0\,\text{K}$ is simply given by

$$m_{\text{Total}} = m_{\text{orbit}} + m_{\text{spin}} = -\frac{\mu_B}{\hbar}\left(g_{\text{orbit}}.L + g_{\text{spin}}.S\right), \tag{5.6}$$

where L and S are scalars and not operators. The connection between (Eq.5.2) and (Eq.5.6) is an example of the Wigner-Eckart theorem.

Figure 5.2 shows the evolution of the magnetic moment as a function of the external magnetic induction from 0 T to 7 T for different low temperatures. We see that the magnetic moment per Er atom of the spherical Er^{3+} ion saturates at $M = 9\,\mu_B$ $(9 = 6 + 2 \times 3/2)$. (Eq.5.2) states the the magnetization is a function of B/T, so that the lower the temperature T, the smaller the induction B needed to obtain a given magnetization. We see that for a spherical, paramagnetic Er^{3+} ion in a weak external induction $B = 0.1\,\text{T}$, the magnetization between 0.2 K and 4.2 K varies by an order of magnitude. Then measuring the magnetization of Er^{3+} in $B = 0.1\,\text{T}$ external induction could be a precise measure of the real temperature of an erbium ion contained in the sample. We have used this property for the thermometric calibration of DICHRO50.

5.3 $Er_{0.025}Pd_{0.975}$ sample

$Er_{0.025}Pd_{0.975}$ is a solid solution with very few erbium atoms diluted in a palladium matrix. The atomic proportion is 2.5% erbium atoms vs 97.5% of palladium atoms. Erbium is a rather stable rare earth and that only slowly oxidizes [135]. The solubility of erbium in the face-centered cubic (fcc) palladium is up to 10% and consequently, it is not difficult to synthesize $Er_{0.025}Pd_{0.975}$ [136]. Figure 5.3 shows the fcc structure of the ErPd alloy. Every atom is surrounded by 12 neighboring atoms. If the erbium atoms are randomly diluted in palladium, for the concentration Er_xPd_{1-x}, we can calculate the probability p for an erbium atom to be surrounded by 12 palladium atoms with the formula

$$p = (1 - x)^n. \tag{5.7}$$

where n is the number of the nearest neighbors (in the fcc structure $n = 12$). With $x =$ 2.5%, we find the $p = 73.8\%$ so that only 73.8% of the erbium atoms are surrounded

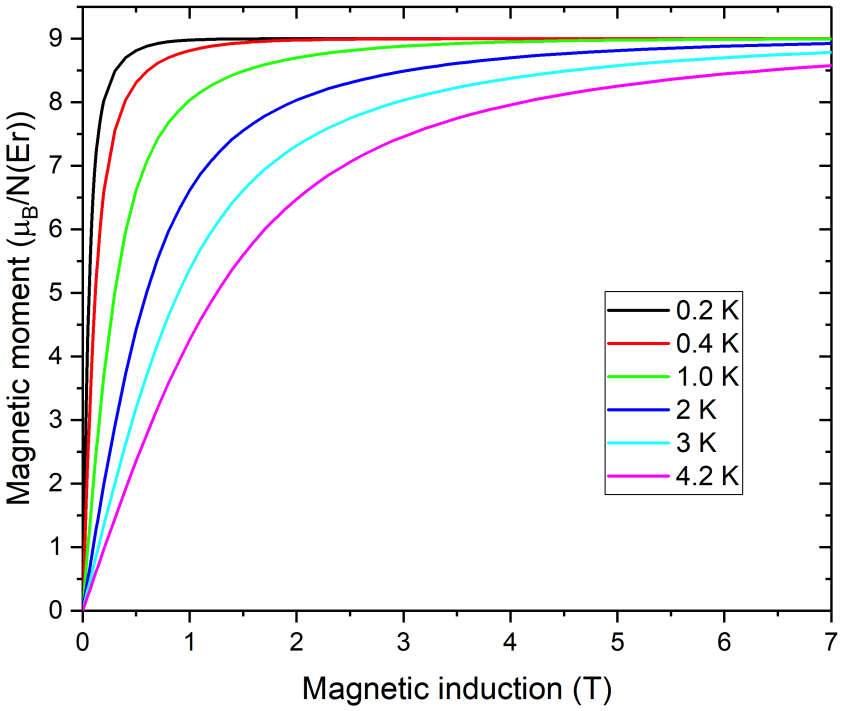

Figure 5.2: Evolution of the magnetic moment of spherical Er^{3+} ion as a function of magnetic induction at different low temperatures.

by 12 palladium atoms. The remaining 26.2% of erbium atoms have at least 1 erbium neighbor.

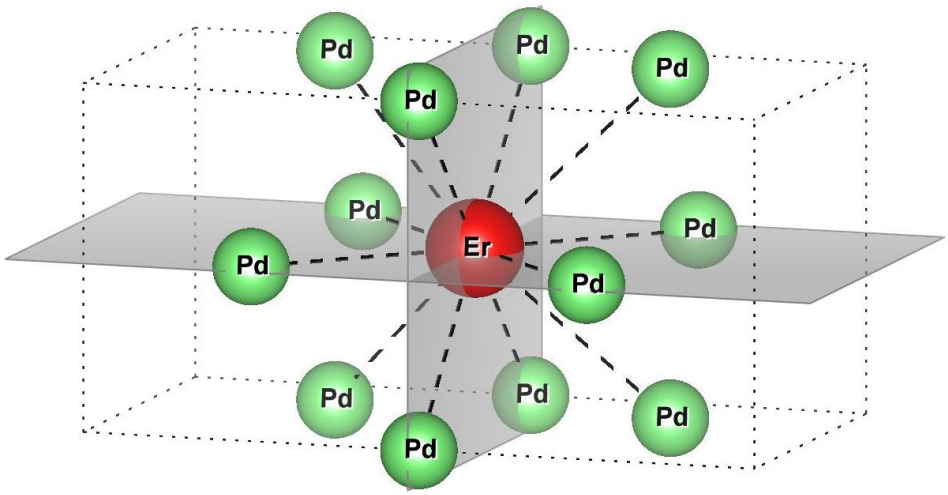

Figure 5.3: *fcc* structure of the ErPd alloy. Every atom is surrounded by 12 neighboring atoms.

Erbium has a Curie-Weiss paramagnetic behavior and for the concentration of er-

bium less than 3%, we can consider that there is no magnetic order (ferromagnetic, ferrimagnetic or antiferromagnetic) once the temperature is higher than few millikelvins [36]. Besides the use of the $Er_{0.025}Pd_{0.975}$ sample for the first series of calibration for the DICHRO50 [36] performed in 2018, another sample, $Er_{0.1}Pd_{0.9}$, has been used for thermometry and calibration of the TBT-mK installed on SU22 beamline at Super-ACO in LURE in 1998. Delobbe *et al.* showed that for x less than 10%, the Er_xPd_{1-x} sample develops a magnetically ordered state at a critical temperature T_0 that depends on the concentration x [31]. As expected, the larger the x, the larger the number of Er-Er pairs. From (Eq.5.7), no more than 28.2% of erbium atoms are surrounded by 12 palladium atoms in $Er_{0.1}Pd_{0.9}$. The other 71.8% Er atoms that have at least one Er neighbor complicates the analysis of the magnetic properties so that $Er_{0.025}Pd_{0.975}$ has mostly been preferred for magnetometry.

5.3.1 Sample preparation

$Er_{0.025}Pd_{0.975}$ sample has been synthesised by Guy Schmerber from the *Institut de Physique et Chimie des Matériaux de Strasbourg* (IPCMS) by triarc melting of the appropriate amounts of metals under a purified argon atmosphere, using a homemade water-cooled Cu plate and non-consumable thoriated tungsten electrodes. The purities of the starting materials were 99.99% for palladium and 99.9% for erbium. The ingot was remelted ten times and inverted after each melting to promote mixing. The as-cast $Er_{0.025}Pd_{0.975}$ alloy was homogenized at 900 °C for 24 hours in a sealed silica tube and then water quenched. With this kind of preparation, we can consider that the sample is a polycrystal, with no privileged orientation. The sample is shown in Figure 5.4 and Figure 3.7.

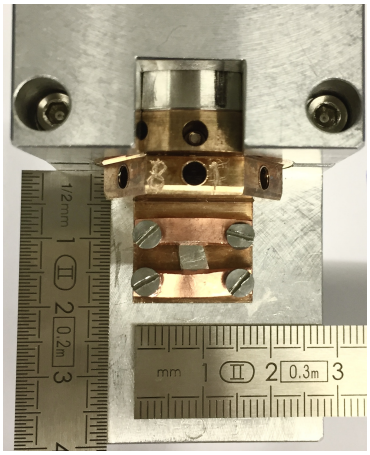

Figure 5.4: $Er_{0.025}Pd_{0.975}$ sample mounted on the sample holder of DEIMOS beamline with the measures of the dimension.

5.3.2 X-ray diffraction characterization

The crystalline phase of the sample was determined using a Bruker D8 Advance diffractometer equipped with a LynxEye detector at the monochromatic wavelength of Cu $K_{\alpha 1}$, $\lambda = 1.54$ Å. The expected fcc phase was confirmed with the determination of $Fm\bar{3}m$ space group, with a lattice parameter $a_{Er_{0.025}Pd_{0.975}} = 3.91 \pm 0.01$Å at room temperature ($a_{Pd} = 3.89 \pm 0.01$Å for pure palladium).

5.4 SQUID measurements

Prior to XMCD, a series of SQUID measurements has been undertaken in the Institut Néel in Grenoble by Elsa Lhotel.

SQUID is short for Superconducting QUantum Interference Device. It measures not only the total magnetic moment of the sample but also the contribution of the sample holder. If the contribution of the sample holder can be considered negligible, SQUID magnetometry provides information on the magnetic moments from both erbium and palladium atoms. The magnetic moment of the palladium atoms can be decomposed into two contributions:

1. The magnetic moment M_{Pd} of the bulk palladium ions that has been determined from the SQUID measurement of a pure palladium sample.

2. The additional magnetic moment of palladium atoms due to the presence of the neighboring erbium atoms. This contribution is difficult to determine from SQUID magnetometry. We propose in the following sections a way to determine this magnetic contribution by combining SQUID and XAS-XMCD measurements.

Let us focus on the first contribution as it is discussed above. By using the method described above for the first contribution, the magnetic moment of erbium measured by SQUID without the magnetic moment of the "far" palladium ion is:

$$M(\mu_B/N(\text{atom})) = \frac{M_{SQ}\mathscr{M}_{ErPd} - 0.975 M_{Pd}\mathscr{M}_{Pd}}{0.025 \times 9.274 \times 10^{-21}\mathscr{N}_A} \tag{5.8}$$

where M_{SQ} is the magnetic moment measured of 1 g of $Er_{0.025}Pd_{0.975}$ measured by SQUID in unity emu/g, M_{Pd} is the magnetic moment measured of 1 g of pure palladium measured by SQUID in unity emu/g, $\mathscr{M}_{Pd}$ is the molar mass of palladium with $\mathscr{M}_{Pd}$=106.42 g/mol [133], $\mathscr{M}_{ErPd}$ is the average molar mass of the $Er_{0.025}Pd_{0.975}$ with $\mathscr{M}_{ErPd}$=107.94 g/mol, and $\mathscr{N}_A$ is the Avogadro constant. With this formula, we obtain M directly in $\mu_B/N(\text{atom})$. For the conversion, we have $1\,\mu_B = 9.274 \times 10^{-21}$ emu.

Figure 5.5 shows the magnetic moment measured by SQUID magnetometry for the temperature between 100 mK and 4.2 K corrected from the *bulk* palladium contribution (the first contribution discussed above). For an external magnetic induction of 8 T, the

magnetic moment of each Er ion is reduced from $7.39\mu_B$ to $6.9\mu_B$ per Er atom after removing the bulk palladium contribution.

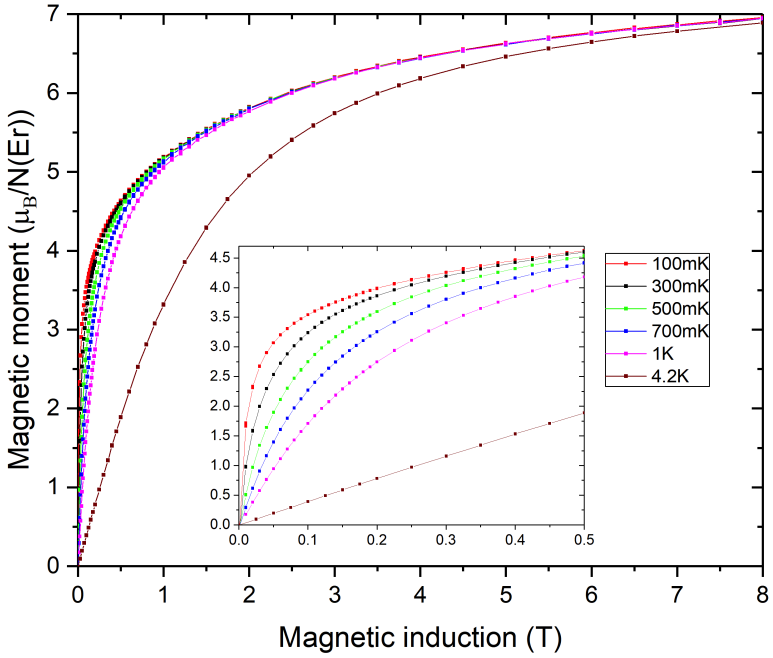

Figure 5.5: Net magnetic moment per erbium atom measured by SQUID as a function of the magnetic induction without palladium's distribution. A zoom shows the zone from 0 T to 0.5 T.

By comparing the numbers from Section 5.2 with Figure 5.2, we observe that the Er magnetic moment in $Er_{0.025}Pd_{0.975}$ is much smaller than the one expected from spherical symmetry and given by Brillouin function where the magnetic moment at saturation would be close to $9\,\mu_B$ per Er atom. This clearly indicates that the crystal field cannot be neglected since it clearly modifies the expected "spherical" Zeeman effect of (Eq.5.2).

5.5 Sample preparation and surface cleaning for XAS measurements

The sample was fixed with copper plates screwed tightly on the sample holder (Figure 5.4) in order to ensure the best thermal contact with the mixing chamber[1]. DEIMOS

[1]Note that from an experimental point of view, the fixation of a sample is usually treated as an easy subject but it is not the case for the measurements at ultra-low temperature and it may even become a crucial point for a successful experiment at ULT. This configuration of fixation has been decided after numerous tests: for example, if we use an epoxy glue instead of screwed copper plates, the thermal impedance becomes so important that the temperature of the sample does not go below 2 K whereas the mixing chamber temperature is 0.2 K.

beamline at Synchrotron SOLEIL is a soft X-ray beamline, and for soft X-rays, the penetration depth is between 50 nm and 100 nm. When measurements are performed in TEY, the probed depth is even smaller and no larger than 5 nm. That is why cleaning the surface of the sample is essential on a soft X-ray synchrotron beamline.

The first experiments were performed in 2018 between 200 mK and 4.2 K. The sample was scraped with a rotative diamond file for cleaning in UHV conditions close to 2×10^{-9} mbar then immediately transferred into the measurement chamber and screwed and connected tightly on the DICHRO50 mixing chamber [36]. Since 2018, I have developed and implemented a special UHV surface cleaning chamber (see Section 3.3) where the UHV conditions have been improved down to 4.5×10^{-10} mbar. More recently, measurements for temperatures ranging from 2 K to 300 K have been performed and then the sample was prepared in the surface cleaning chamber, in UHV pressure below 5×10^{-10} mbar.

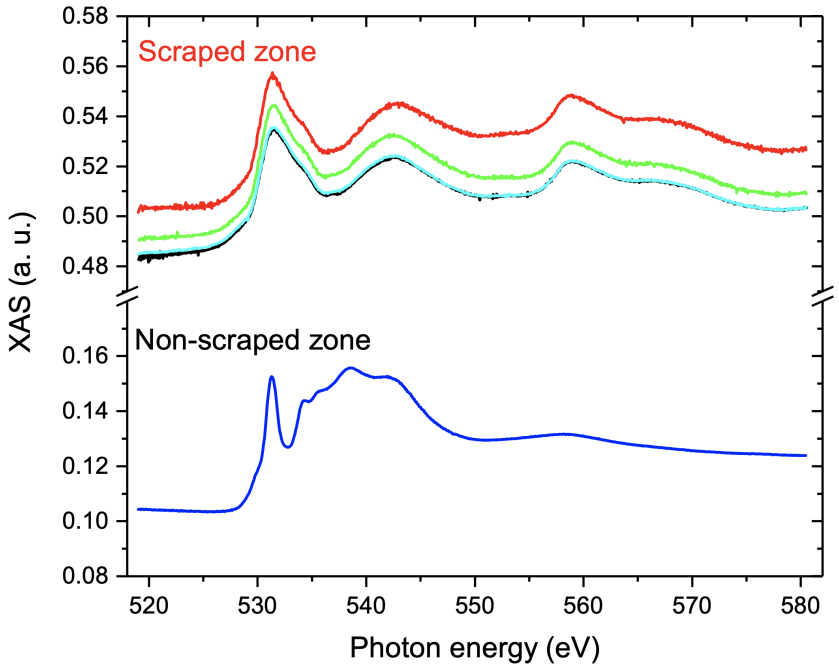

Figure 5.6: XAS measurements at Pd-$M_{2,3}$ edges in different points of the scrapped zone compared to a measure in a non-scrapped zone.

Several XAS measurements of the Pd-$M_{2,3}$ edges have been performed to test the quality of the surface cleaning (see Figure 5.6). We recorded the Pd-$M_{2,3}$ edges for different zones either in the scraped groove (Figure 3.7-Bottom-Right), or outside the scrapped groove. Firstly, we observe that the profile of the XAS spectra is the same for all the different scraped zones. The profile for a non-scraped zone is quite different from the one of the scraped groove. Moreover, the energy of the Pd-$M_{2,3}$ edges coincides with the oxygen K pre-edge at 543.1 eV. We see that after scraping the sample, the

sharp feature at 543.1 eV has been removed, indicating that contamination by oxygen has been almost completely removed.

5.6 XAS-XMCD measurements

The XAS-XMCD measurements of the Er-$M_{4,5}$ edges were performed on DEIMOS beamline at Synchrotron SOLEIL. We change the magnetic field from 6.5 T to -6.5 T then from -6.5 T back to 6.5 T for the XMCD measurements. We have also recorded the spectra without the presence of magnetic field for the σ_0 spectrum. To reduce the eddy current, for the ultra-low temperature ($T < 1$ K), we fix the variation rate for the magnetic field at 0.02 T/s.

One series of XAS-XMCD measurements contains eight usable spectra[2]. They are $\sigma_1(\phi^+)$ (left polarization), $\sigma_2(\phi^-)$ (right polarization), $\sigma_3(\phi^-)$, $\sigma_4(\phi^+)$ with a magnetic field along the propagation direction of the photon and $\sigma_5(\phi^-)$, $\sigma_6(\phi^+)$, $\sigma_7(\phi^+)$, $\sigma_8(\phi^-)$ with inverse magnetic field with respect to the former four spectra. Figure 5.7 shows an example of one series of measurements realized at 4.25 K with a 6.5 T external magnetic field. In this figure, the black spectrum is the average of the four "+" spectra and the green one is the average of the four "−" spectra. By definition, the sign of a spectrum is the sign of the product of the phase with the field so that the "+" spectra are σ_1, σ_4, σ_6, and σ_7 and the "−" spectra are σ_2, σ_3, σ_5, and σ_8.

The orange spectrum is the average of the black and green spectra. The blue spectrum is the XMCD spectrum which is the difference between the "−" green and the "+" black spectra

$$\frac{\sigma^+ + \sigma^-}{2} = [\sigma_1(\phi^+) + \sigma_2(\phi^-) + \sigma_3(\phi^-) + \sigma_4(\phi^+) + \sigma_5(\phi^+) + \sigma_6(\phi^-) + \sigma_7(\phi^-) + \sigma_8(\phi^+)]/8, \quad (5.9)$$

and

$$\sigma_{\mathrm{XMCD}} = [\sigma_2(\phi^-) + \sigma_3(\phi^-) + \sigma_5(\phi^+) + \sigma_8(\phi^+)]/4 - [\sigma_1(\phi^+) + \sigma_4(\phi^+) + \sigma_6(\phi^-) + \sigma_7(\phi^-)]/4. \quad (5.10)$$

Remind that the energy separation of the M_4 and M_5 edges is due to the $3d$ spin-orbit coupling acting on the core-hole. In the monoelectronic picture of a $3d$ core-hole, spin-orbit coupling splits the $l = 2$, $s = 1/2$ 10-fold degenerate levels into $3d_{3/2}$ (the M_4 edge at $E = 1434$ eV) and $3d_{5/2}$ (the M_5 edge at $E = 1394$ eV). We remark the

[2]There are two additional conditioning spectra each time after modifying the magnetic field.

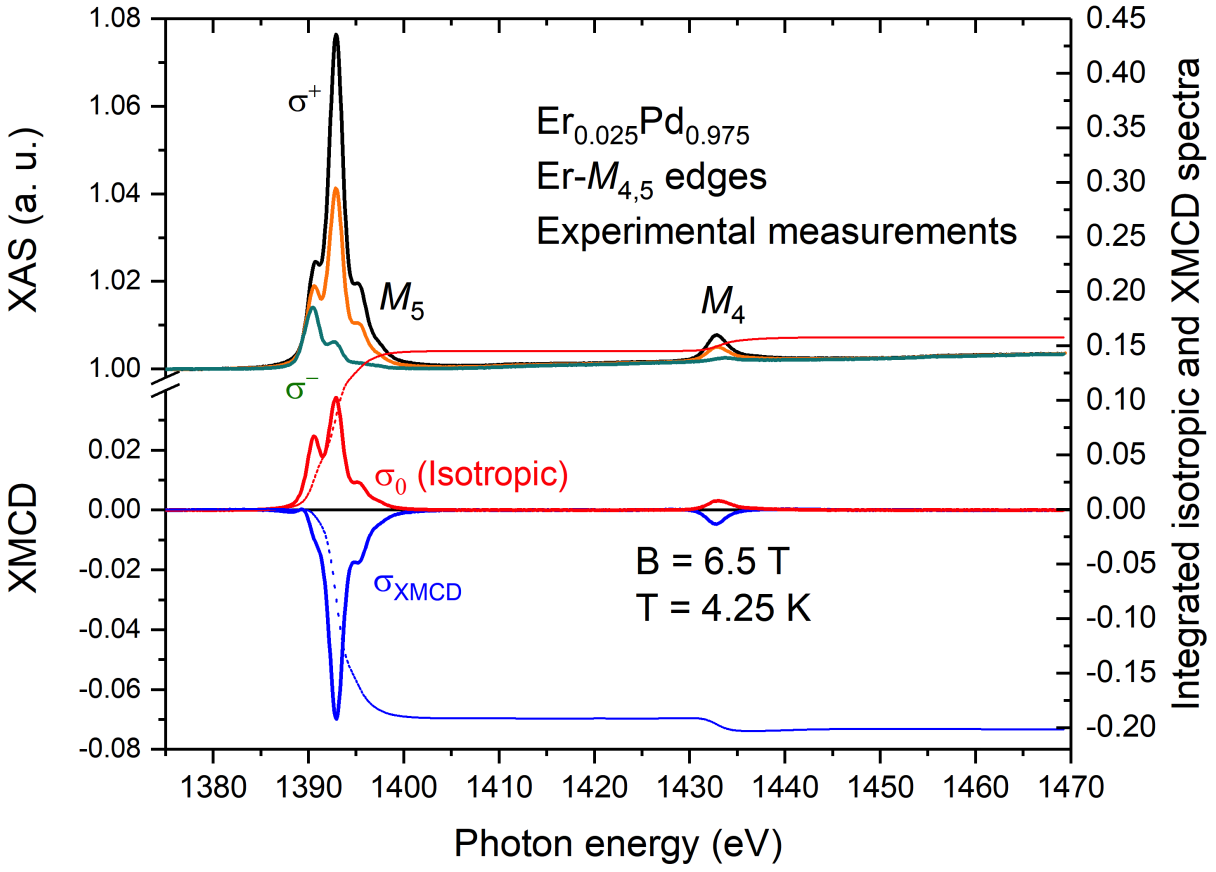

Figure 5.7: XAS-XMCD measurement of the Er-$M_{4,5}$ of the $Er_{0.025}Pd_{0.975}$ sample at 4.25 K with an external magnetic field of 6.5 T. The black spectrum is the average of the spectra σ^+, the green spectrum is the average of the spectra σ^-. The average of the green spectrum and the black one gives the $\frac{\sigma^+ + \sigma^-}{2}$ spectrum in orange. The red isotropic spectrum σ_0 is recorded without magnetic field and the background baseline has been removed. The green spectrum minus the black spectrum gives the XMCD spectrum in blue. The red dotted line is the integral of the red isotropic spectrum and the blue dotted line is the integral of the XMCD spectrum. The two integrals start from zero and stabilize at the end which prove a good deletion of the background.

excellent quality of the spectra with a signal-to-noise ratio larger than 10^4 despite the small concentration of Er.

To analyze the spectra, especially for the integral treatments of the application of the sum rules, it is necessary to remove the backgrounds. We present the red isotropic spectrum σ_0 in Figure 5.7 after removing the background. See publication Kappler *et al.* for additional details [36] on the thermometric measurements.

5.7 XMLD spectra

In the present section, we plan to record XMLD and I shall show that XMLD is highly dependent on the crystal field. By the way, later analysis of XMCD (Section 5.10) will show that XMCD signals also depend on the crystal field.

From the discussion in Section 3.6, we can calculate the XMLD spectra from the XAS measurements of σ^+, σ^- and σ_0. From literature, one estimates that the amplitudes of the XMLD signals are quite small [26], usually smaller than the intensity of XMCD. As a consequence, we only consider the XMLD signals for $B = \pm 6.5\,\mathrm{T}$ that is the largest (in absolute value) external magnetic induction available on DEIMOS. Hence, the XMLD measurements were recorded for temperatures ranging between 2 K to 300 K, in an external magnetic induction of 6.5 T.

From (Eq.3.17), we can calculate the XMLD signal with

$$\frac{\sigma_{\mathrm{XMLD}}(E)}{3} = \left(\frac{\sigma^+(E) + \sigma^-(E)}{2}\right) - \sigma_0(E), \tag{5.11}$$

where σ^+ and σ^- are recorded with magnetic inductions of $\pm 6.5\,\mathrm{T}$ and σ_0 is the isotropic cross section and we consider that σ_0 is obtained by measuring the Er-M_5 edge with no external magnetic field. This definition for σ_0 does not introduce additional approximations since :

- XMLD can be safely computed in the electric dipole approximation,
- the space group for all the ErPd samples is a cubic space group,
- all the samples are polycrystalline compounds with no texture observed by XRD.

Technically, all the calculations of the present chapter have been performed on $\sigma_{\mathrm{XMLD}}/3$. For illustration, the signal $\sigma_{\mathrm{XMLD}}/3$ at 1.7 K and 6.5 T is reported in Figure 5.8.

5.8 Crystal field parameters determination

In this section, we present the connection between the crystal field parameters of Er ions in $Er_{0.025}Pd_{0.975}$ and the XAS, XMCD, and XMLD measurements.

5.8.1 Previous studies

Morin *et al.* have performed the measures of neutron spectroscopy in *Institut Laue-Langevin* (ILL) in 1976 for a ErPd sample between 20 K to 55 K [132]. The cubic cell parameter is $a = 3.445$Å and erbium ions are said to be diluted in palladium but with no precise determination of the Er concentration. To our knowledge, there are no other research dealing with the crystal field parameters for ErPd samples. Morin *et al.* found

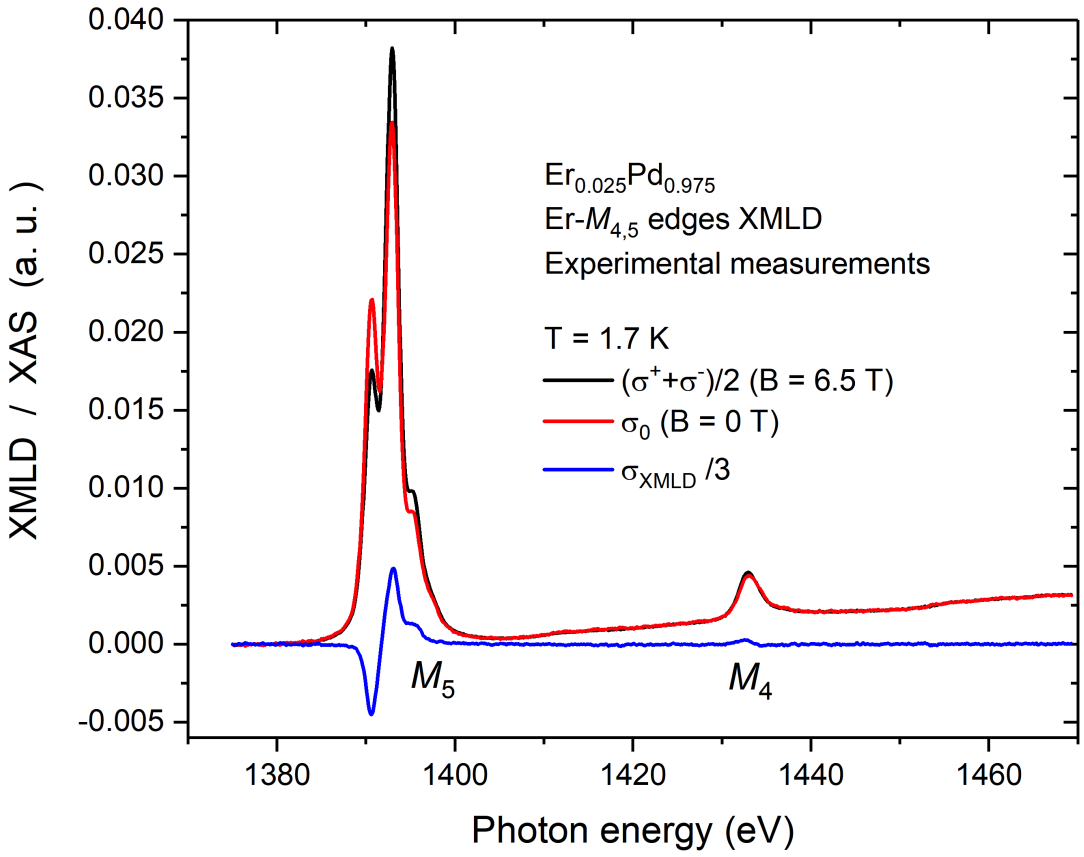

Figure 5.8: Er^{3+}-$M_{4,5}$ XAS and XMLD spectra at 1.7 K. The black spectrum is the average of the two phase σ^+ and σ^- and the isotropic (red) spectrum is recorded without magnetic field. The blue spectra is the difference between the black and the red spectrum applying (Eq. 5.11) which is, by definition, one third of the XMLD signal.

two series of possible crystal field parameters that fit their experimental data which are reported in Table 5.1.

	$W(K)$	x	$A_4\langle r^4\rangle$ (K)	$A_6\langle r^6\rangle$ (K)
1^{st} series	-0.575	-0.22	47.5	-15.7
2^{nd} series	-0.65	0.48	-117.1	-11.8

Table 5.1: Previous results of crystal field parameters of ErPd found by neutron spectroscopy [132]. All symbols are defined in Section 4.1.

In the following section, we check whether these two series of crystal field parameters are compatible with our measurements and when necessary, we propose a new series of parameters for $Er_{0.025}Pd_{0.975}$.

5.8.2 Normalization methods

In order to make the connection between XAS, XMCD and XMLD, we have used the Crispy interface of the ligand field multiplet QUANTY code to compute the cross sections (Section 4.4). Wybourne crystal field notations are used in Crispy and the transformations between Stevens parameters and Wybourne parameter are [137]

$$B_4 = \beta A_4 \langle r^4 \rangle = \beta B_{40}/8, \qquad B_6 = \gamma A_6 \langle r^6 \rangle = \gamma B_{60}/16, \tag{5.12}$$

so that from Table 5.1

$$\begin{aligned} A_4 \langle r^4 \rangle = 47.5\,\mathrm{K} \rightarrow B_{40} = 32.75\,\mathrm{meV}, \\ A_6 \langle r^6 \rangle = -15.7\,\mathrm{K} \rightarrow B_{60} = -21.65\,\mathrm{meV}. \end{aligned} \tag{5.13}$$

The first step is to normalize properly the calculated and the experimental spectra with respect to each other so that they can be compared. We process with the following steps applied to the isotopic simulated and experimental spectra :

- Set the crystal field parameters as presented in (Eq.5.13) and the other experimental parameters (temperature, magnetic field, energy range).

- Define the photon propagation vector $\mathbf{k} = (0, 0, 1)$ and the polarization vectors. The definition of $\mathbf{k}$ is required by Crispy but has no impact since all the calculations are restricted to the electric dipole approximation.

- Set the energy range so that both experimental and theoretical ranges coincide.

- Multiply the experimental spectrum so that both experimental and theoretical spectra are similar.

- Adjust the simulated spectra by playing with the Coulomb repulsion and convolution parameters :

  $\omega_{\mathrm{Lorentzian}} = 1.1\,\mathrm{eV}$ at the M_5 edge and = 2.16 eV at the M_4 edge,
  $\omega_{\mathrm{Gaussian}} = 0.88\,\mathrm{eV}$ at both $M_{4,5}$ edges,
  $\kappa_F = 85\%$ and $\kappa_G = 85\%$.

- Fix the energy separation between the Er-M_4 and Er-M_5 edges by setting the spin-orbit parameter $\zeta(3\mathrm{d}) = 16.276\,\mathrm{eV}$.

With the above normalization, experimental and simulated spectra can be compared.

We notice that the simulated isotropic spectra σ_0 is almost independent from the temperature from 2 K to 300 K as well as for slight modifications, *i.e.* $\pm 100\,\mathrm{meV}$, for B_{40} and B_{60}. Note that if the simulated isotropic spectrum changes with crystal field parameters, the above normalization steps must performed.

When both theoretical and experimental spectra are properly normalized, we can apply (Eq.5.11) to yield experimental and simulated XMLD signals.

5.8.3 A verification of crystal field parameters by XAS measurements

We carry out the verification of the two published series of crystal field parameters. Figure 5.9 reports the $T = 2\,\mathrm{K}$ and $B = 6.5\,\mathrm{T}$ XMLD spectrum.

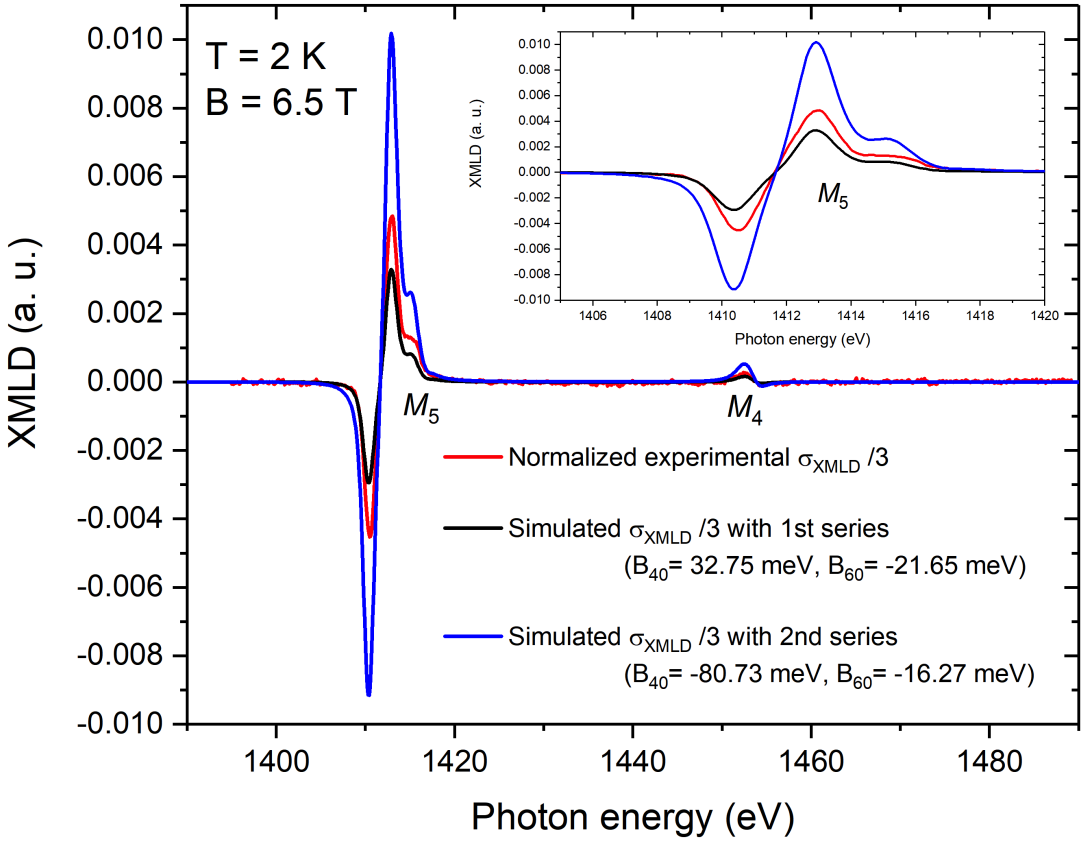

Figure 5.9: Normalized experimental and simulated Er^{3+}-$M_{4,5}$ XMLD spectra at $T = 2\,\mathrm{K}$ and $B = 6.5\,\mathrm{T}$ with a zoom for the M_5 edge.

The amplitudes of the isotropic spectra are identical but we clearly see that it is not the case for the XMLD signals for both series of crystal field parameters. It might be due to Er concentration much different than 2.5% or to the difficulty of extraction crystal field parameters, either from Neutron spectroscopy or X-ray spectroscopy. The results provided by the series with $B_{40} = -80.73\,\mathrm{meV}$ and $B_{60} = -16.27\,\mathrm{meV}$ is so far away from the experimental XMLD that it can be excluded for the further discussion. For the series with $B_{40} = 32.75\,\mathrm{meV}$ and $B_{60} = -21.65\,\mathrm{meV}$, the simulated signal is close to the signal with non negligible differences. This result obtained at 2 K needs to be extended to spectra at higher temperatures.

5.8.4 Fitting methods of crystal field parameters

The intensity of the XMLD signal is decreasing with increasing temperature and the largest XMLD signal has been measured at 2 K. To well visualize the comparison between the calculations and the experiments, we propose here to fit all simulated spectra at temperatures above 2 K with respect to the spectra obtained at 2 K. From Brouder rule for rare earth $M_{4,5}$ edges, one knows that all XMLD signals should have the same shape but for a multiplication coefficient, so that

$$\sigma_{\mathrm{XMLD(simu)}}(T) = a_{\mathrm{simu}}(T)\,\sigma_{\mathrm{XMLD(simu)}}(T = 2\,\mathrm{K}), \tag{5.14}$$

$$\sigma_{\mathrm{XMLD(exp)}}(T) = a_{\mathrm{exp}(T)}\,\sigma_{\mathrm{XMLD(exp)}}(T = 2\,\mathrm{K}), \tag{5.15}$$

where the indices simu and exp mean either simulated or experimental XMLD signals. To make a good comparison, we define then

$$a_{\mathrm{simu}} = a\,\frac{\sigma_{\mathrm{XMLD(simu)}}(T = 2\,\mathrm{K})}{\sigma_{\mathrm{XMLD(exp)}}(T = 2\,\mathrm{K})}. \tag{5.16}$$

and we plot the fitting factor a_{simu} as a function of temperature.

For the experimental spectra, we may apply the above Formula 5.15. But the experimental XMLD signal is not perfect and may contain spurious additional signals such as a derivative signal (always present when a difference is performed between two spectra), and also a slight vertical shift of the signals, so that (Eq.5.15) can be rewritten as

$$\sigma_{\mathrm{XMLD(exp)}}(T) = a_{\mathrm{exp}(T)}\,\sigma_{\mathrm{XMLD(exp)}}(T = 2\,\mathrm{K}) + b(T)\,\sigma'_{\mathrm{XMLD(exp)}}(T = 2\,\mathrm{K}) + c(T), \tag{5.17}$$

where $\sigma'_{\mathrm{XMLD(exp)}}(T = 2\,\mathrm{K})$ is defined

$$\mathrm{d}\sigma_{\mathrm{XMLD(exp)}}(T = 2\,\mathrm{K}) = \sigma'_{\mathrm{XMLD(exp)}}(T = 2\,\mathrm{K})\mathrm{d}E, \tag{5.18}$$

$b(T)$ is a multiplicative factor associated to $\sigma'_{\mathrm{XMLD(exp)}}(T)$ and $c(T)$ is a rigid vertical shift.

One finds that c is less than 10^{-5} (with XMLD maximum equal to 10^{-2}) which proves that $c(T)$ can be neglected. We can plot $a_{\mathrm{simu}}(T)$ and $a_{\mathrm{exp}}(T)$ (Figure 5.10) and see that the agreement is fair at high temperature but not for temperatures below 100 K. None of the set of parameters determined by Morin *et al.* allows to mimic the experimental XMLD trends.

Now we look for a series of crystal field parameters. We change B_{40} and B_{60} to obtain a new series of XMLD spectra from 2 K to 300 K. We fit the spectra at the other

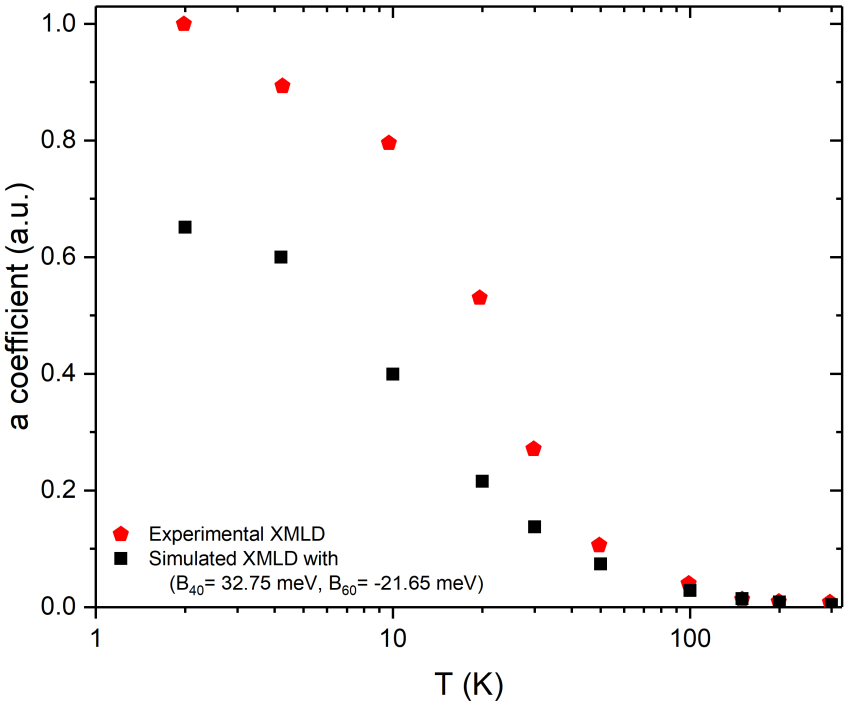

Figure 5.10: The fitting factor a_{simu} and a_{exp} as a function of temperature (T is represented in logarithmic scale.).

temperatures to the spectra simulated at 2 K as we have done before and we plot the coefficient a_{simu} and a_{exp} as a function of temperature. Since we start to search the spectrum from 2 K so that we can make the $\sigma_{\text{XMLD(simu)}}(T = 2\,\text{K})$ as close as possible to $\sigma_{\text{XMLD(exp)}}(T = 2\,\text{K})$, the two "$a$" coefficients for $T = 2\,\text{K}$ are equal or almost equal (see Figure 5.13).

A couple of series was found that fit the experimental data in Figure 5.10 (red points) when we use only the XMLD spectra. To determine the unique series of crystal field parameters, we combine the XMLD spectra with the XMCD spectra.

Once we obtained all possible series for the crystal field parameters by the methods described above, we calculate also their XMCD spectra, apply these simulated XMCD spectra by the first sum rule and we plot the variation of the magnetic moment as we have done for Figure 5.12 in order to define the possible unique crystal field parameters. Figure 5.11 reports the experimental (left panel) and LFM simulated (right panel) Isotropic, XMLD and XMCD signals, at $T = 2\,\text{K}$ and $B = 6.5\,\text{T}$. The agreement between experiments and calculations is quite good.

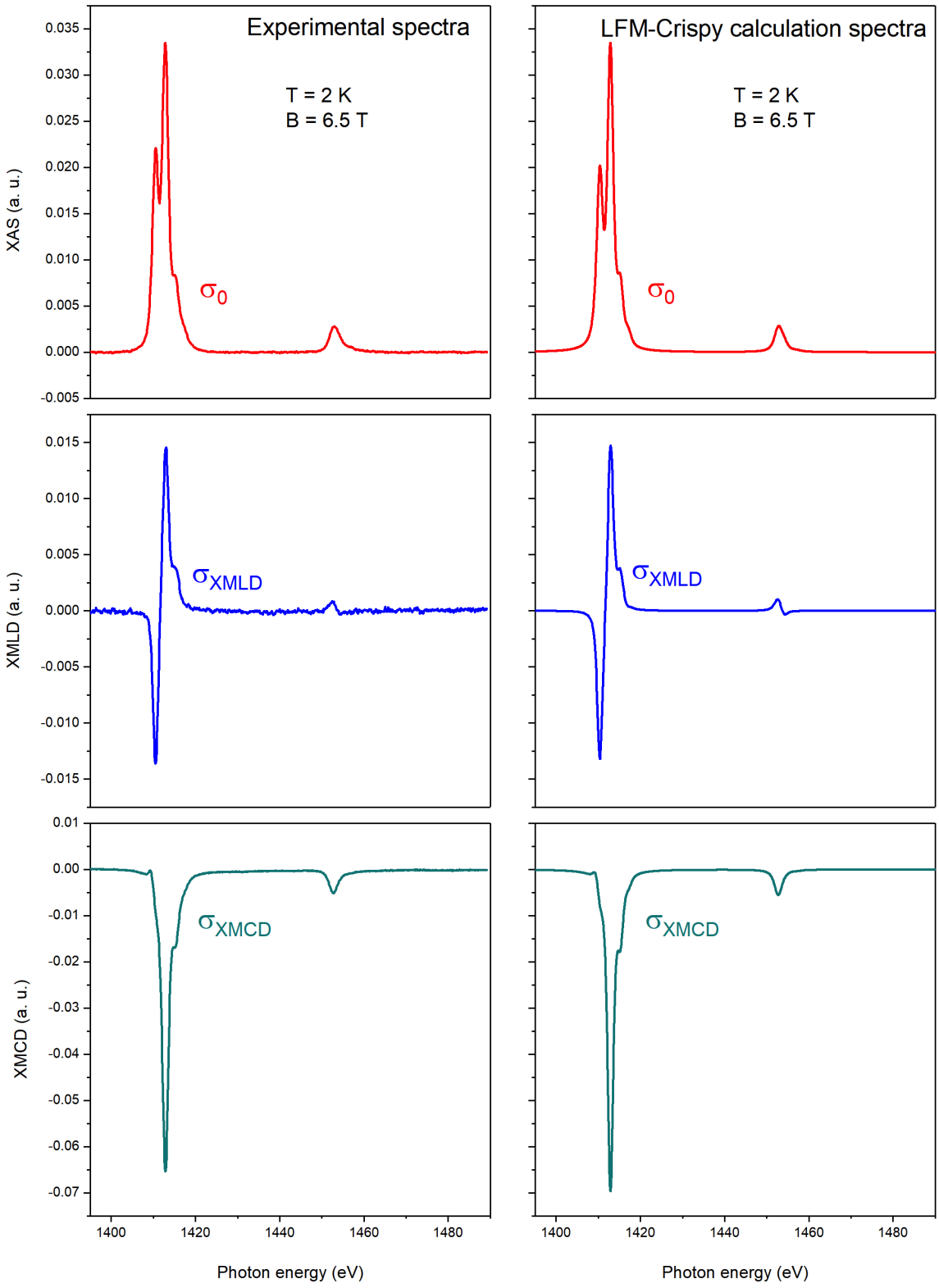

Figure 5.11: Experimental isotropic, XMLD and XMCD spectra recorded at $T = 2\,\mathrm{K}$ and $B = 6.5\,\mathrm{T}$ compared to the LFM-Crispy calculations with crystal parameters $B_{40} = 11.3\,\mathrm{meV}$ and $B_{60} = -3\,\mathrm{meV}$ at the same temperature and magnetic field.

5.9 Application of the sum rules

In this section, we show the details of the application of the XMCD sum rules. From the discussion in the Section 5.2, for Er^{3+} ion, the spherical ground state is defined by $J = 15/2$, $L = 6$, $S = 3/2$. For the magneto-optical sum rules, we are dealing with Er $M_{4,5}$, *i.e.* transitions between the $3d$ shell and the $4f$ shell so that in (Eq.3.12) and (Eq.3.13), $l = 3$ and $c = 2$. There are $n = 11$ electrons on the $4f$ shell so that the number of holes is $(4l + 2) - 11 = 3$. Then (Eq.3.12) and (Eq.3.13) write

$$\frac{\int_{j^+ + j^-} \mathrm{d}E(\sigma^+ - \sigma^-)}{\int_{j^+ + j^-} \mathrm{d}E(\sigma^+ + \sigma^- + \sigma_\parallel)} = \frac{1}{9}\langle L_z \rangle \tag{5.19}$$

and

$$\frac{\int_{j^+} \mathrm{d}E(\sigma^+ - \sigma^-) - (3/2)\int_{j^-} \mathrm{d}E(\sigma^+ - \sigma^-)}{\int_{j^+ + j^-} \mathrm{d}E(\sigma^+ + \sigma^- + \sigma_\parallel)} = \frac{2}{9}\langle S_z \rangle + \frac{2}{3}\langle T_z \rangle. \tag{5.20}$$

In the case of rare earths where the ground state is defined by the $(2J + 1)$-fold degenerate $J(L,S)$ multiplet, with additional splitting due to crystal field inside the $(2J + 1)$-fold subspace, all the rank-1 tensors are proportional as a simple consequence of the Wigner-Eckart theorem. Then if $\langle L_z \rangle$ is known then the other quantities such as $\langle S_z \rangle$, $\langle T_z \rangle$, and $\langle J_z \rangle$ can be easily computed. The first sum rule (Eq.5.19) is very robust and provides $\langle L_z \rangle$ so that the other quantities $\langle S_z \rangle$, $\langle T_z \rangle$, and $\langle J_z \rangle$ follow.

Practically, I first remove the background for the XAS spectra and integrate from 1380 eV to 1460 eV. One example for the various integrals is reported in Figure 5.7. In the following, I present here the detail of an application of the first sum rule for $T = 4.25\,\mathrm{K}$ and $B = 6.5\,\mathrm{T}$ (Eq.5.19). We get the ratio:

$$\frac{\int_{j^+ + j^-} \mathrm{d}E(\sigma^+ - \sigma^-)}{\int_{j^+ + j^-} \mathrm{d}E(\sigma^+ + \sigma^- + \sigma_\parallel)} = \frac{1}{9}\langle L_z \rangle = -0.48\ \hbar. \tag{5.21}$$

Then

$$\langle L_z \rangle = -4.28\ \hbar, \tag{5.22}$$

so that we have

$$M_\mathrm{L} = -\frac{\mu_\mathrm{B}}{\hbar}\langle L_z \rangle = 4.28\ \mu_\mathrm{B}. \tag{5.23}$$

Applying the Wigner-Eckart theorem, we obtain:

$$\frac{\langle L_z \rangle}{\langle S_z \rangle} = \frac{2 - g_J}{g_J - 1} = 4, \tag{5.24}$$

so that

$$\langle S_z \rangle = -1.07\ \hbar, \tag{5.25}$$

and

$$M_S = -2\frac{\mu_B}{\hbar}\langle S_z \rangle = 2.14\ \mu_B. \tag{5.26}$$

Finally, the total magnetic moment of the Er^{3+} ion as determined from XMCD is

$$M_{XMCD} = M_S + M_L = 6.42\ \mu_B. \tag{5.27}$$

The SQUID measurements (Figure 5.5) yield $M_{SQUID} = 6.72\ \mu_B$ for the same condition of magnetic field and temperature. The difference between the SQUID and XAS-XMCD is 0.30 μ_B per erbium atom.

In the same way, we apply the first sum rule for a magnetic field of 3 T and 0.1 T and the results are provided in Table 5.2.

	XAS-XMCD					SQUID	
	$\langle L_z \rangle$ ($\hbar$)	$\langle S_z \rangle$ ($\hbar$)	M_L (μ_B/N)	M_S (μ_B/N)	M_{Er} (μ_B/N)	M_{total} (μ_B/N)	Δ (μ_B/N)
$B = 6.5$ T	-4.28	-1.07	4.28	2.14	6.42	6.72	0.30
$B = 3$ T	-3.66	-0.92	3.66	1.83	5.49	5,74	0.25
$B = 0.1$ T	-0.25	-0.06	0.25	0.13	0.38	0.39	0.016

Table 5.2: Results of the application of the first sum rule for $T = 4.25$ K with different magnetic inductions. $\Delta = M_{total}(\text{SQUID}) - M_{Er}$.

5.10 Magnetic moment as a function of temperature

We apply the first sum rule in the same way for all the XAS-XMCD spectra recorded at other temperatures and under different magnetic fields. We obtain the evolution of the magnetic moment per Er^{3+} ion as a function of temperature.

Figure 5.12 shows the SQUID measurements and the XAS-XMCD measurements.

- For the SQUID measurement, the points are extracted from the series of magnetization curves (Figure 5.4) from which the bulk palladium contribution has been removed.

- For the XAS-XMCD measurements, we collected 8 scans at each temperature (Section 5.6) and applied the first sum rule in connection with the Wigner-Eckart theorem to yield the erbium spin and orbit magnetic moments.

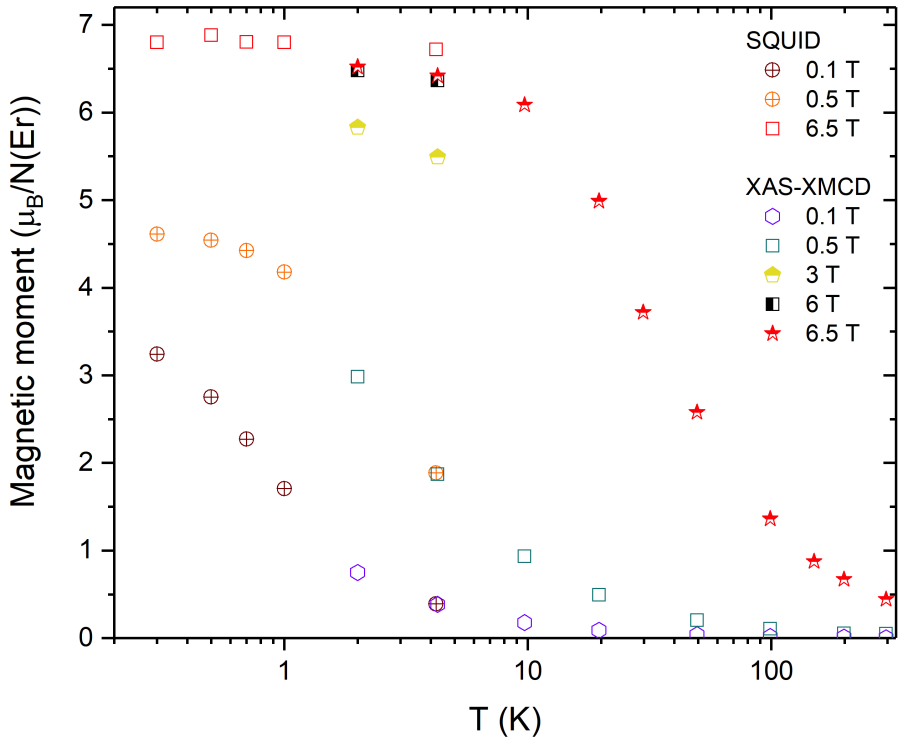

Figure 5.12: Evolution of the magnetic moment as a function of temperature for Er^{3+} ion measured by SQUID and XAS-XMCD. T is presented in a logarithmic axis.

Both SQUID and XAS-XMCD measurements have been performed at 4.2 K (special point for the liquid ^{4}He) that is usually a quite stable temperature in most VTI. Except for 4.2 K, the temperatures of measurements for the two series do not perfectly match. The difference between the SQUID and XAS-XMCD measurements is larger for large magnetic inductions 6.5 T than for weak magnetic inductions (0.5 T and 0.1 T). From Figure 5.12, the magnetic saturation is reached at $T \leq 4.2$ K for an external magnetic induction of 6.5 T. When the external magnetic induction is as low as $B = 0.5$ T, saturation is reached for $T \leq 0.4$ K. At even lower external magnetic induction, saturation is not reached above 200 mK. One can notice, that the value of largest magnetization (*i.e.* the one that would be observed at $T = 0$ K) depends on the external magnetic field. This is a clear sign of the impact of the crystal field since in spherical symmetry the magnetic moment at saturation does not depend on B.

5.10.1 Fitting results

The best crystal field parameters determined by XAS-XMCD measurements combining the LFM calculations is found for the $Er_{0.025}Pd_{0.975}$ sample with

$$B_{40} = 11.3\,\text{meV}, \qquad B_{60} = -3\,\text{meV}. \tag{5.28}$$

The variation of the simulated and experimental fitting factors a_{simu} and a_{exp} has good agreement (Figure 5.13). With these crystal field parameters, the agreement can be observed for the variation of the magnetic moment (Figure 5.14). Two exceptional measurements are plotted for a magnetic induction of $B = 3\,\text{T}$ at 2 K and 4.2 K which also prove a good agreement.

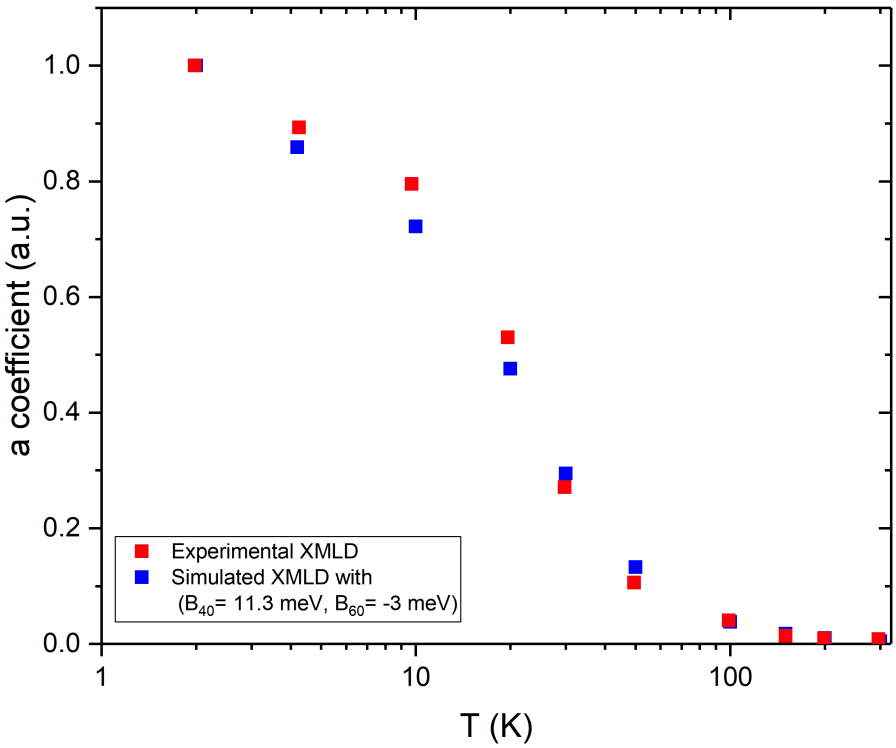

Figure 5.13: The fitting factor a_{simu} and a_{exp} determined by XMLD spectra with $B = 6.5\,\text{T}$ as a function of temperature (T is represented in logarithmic scale.).

One may note that the general thermal behaviours of XMLD and XMCD intensities are well reproduced in our model with some slight deviations for temperatures close to 10 K.

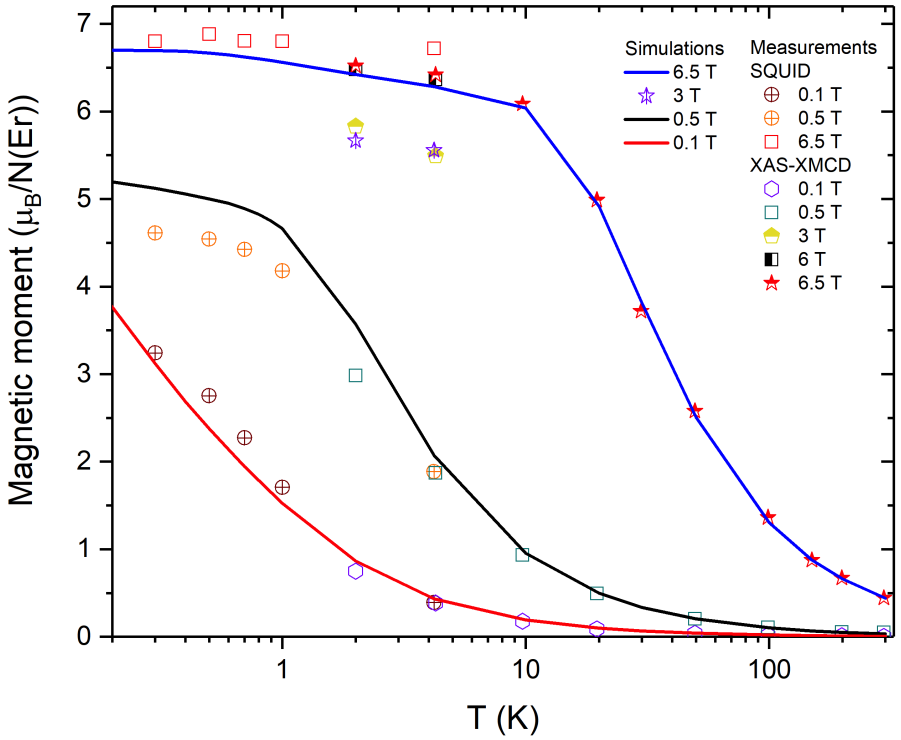

Figure 5.14: Variation of the magnetic moment of Er^{3+} ion as a function of temperature (T is represented in logarithmic scale.). The simulation with $B_{40} = 11.3\,\text{meV}$ and $B_{60} = -3\,\text{meV}$ is compared to the measurements.

5.11 Magnetic polarization of palladium due to erbium

We remark that there is a small difference between the magnetic moment of the SQUID and the XAS-XMCD measurements. This difference can be only due to the polarization of palladium atoms under the influence of erbium. We know that thanks to the chemical selectivity of the XAS measurement, XAS-XMCD data give only the magnetic moment of erbium. But for the SQUID, we measure the total magnetic moment which is the sum of the erbium plus the magnetic polarization of the palladium due to the presence of erbium (we remind the reader that the bulk paramagnetic contribution from palladium has already been removed, see Section 5.4) which can be expressed as

$$M_{\text{SQUID}} = M_{\text{XAS-XMCD}} + M_{\text{induced}}(\text{Pd}). \tag{5.29}$$

Figure 5.15 shows in 2D the polarization (in black) of the palladium.

We obtain that $M_{\text{induced}}(\text{Pd}) = 0.30\,\mu_B$ ($T = 4.25\,\text{K}$, $B = 6.5\,\text{T}$). In the fcc structure of the $Er_{0.025}Pd_{0.975}$ (Figure 5.3) if we consider that the Pd polarization due to Er is limited to the Er coordination sphere, *i.e.* $\approx$ 12 palladium atoms, then the additional polarization is $0.025\,\mu_B$ per Pd atom. The data have been gathered for 0.1 T, 3 T,

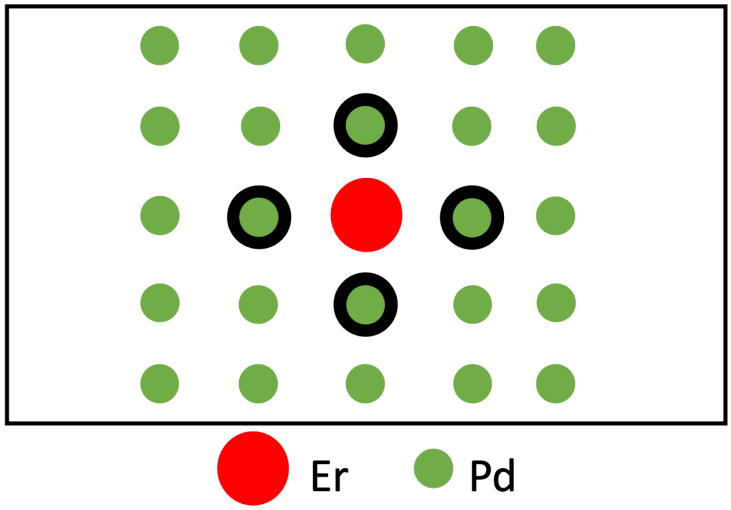

Figure 5.15: The polarization (in black) of the palladium atoms under the influence of an isolated erbium atom.

and 6.5 T, see Table 5.2. If we suppose that Δ (Table 5.2) is related to the Er magnetic moment, we can state that

$$M_{\text{induced}}(\text{Pd}) = \Delta = k \cdot M_{\text{Er}}. \tag{5.30}$$

and we get

$$\begin{aligned} k &= 4.73 \times 10^{-2} \text{ for } T = 4.25\,\text{K},\ B = 6.5\,\text{T}, \\ k &= 4.56 \times 10^{-2} \text{ for } T = 4.25\,\text{K},\ B = 3\,\text{T}, \\ k &= 4.27 \times 10^{-2} \text{ for } T = 4.25\,\text{K},\ B = 0.1\,\text{T}. \end{aligned} \tag{5.31}$$

so that one observes a linear relation between the erbium spin and orbit magnetic moments and the Pd polarization induced by the Er atoms : $M_{\text{induced}}(\text{Pd}) \approx 4.5 \times 10^{-2} \cdot M_{\text{Er}}$.

5.12 Conclusion

We have performed a detailed experimental study of the variations of the XMCD and XMLD signals in a ErPd polycrystalline sample. From the application of the orbital magneto-optical sum rule coupled to the Wigner-Eckart theorem, we have determined the variation of the spin and orbit magnetic moments of Er ions as a function of an external magnetic induction B and temperature T (Figure 5.14). In our measurements B and T have spanned quite large ranges, since the largest magnetic inductions are $\pm$6.5 T and the temperature varies between 200 mK and 300 K.

Making use of the Brouder formula, we have been able to measure the variation of the XMLD signal for $B = \pm 6.5\,\mathrm{T}$ and temperatures between 2 K and 300 K. Thanks to LFM simulations performed with the Crispy interface of QUANTY, we have been able to determine the set of crystal field parameters that best fits the experimental data. Firstly, we found that the parameters published in the literature are in disagreement with our experimental data. Secondly, after applying a fitting procedure it has been possible to determine a best set of parameters in line with our experimental results : $B_{40} = 11.3\,\mathrm{meV}$ and $B_{60} = -3\,\mathrm{meV}$. Whether this set of parameters is unique remains an open question.

Thanks to the new set of parameters ($B_{40} = 11.3\,\mathrm{meV}$, $B_{60} = -3\,\mathrm{meV}$), it has been possible to compute the theoretical XMCD signals and compare them with the experiments. This has been done successfully for $B = \pm 6.5\,\mathrm{T}$, $B = \pm 0.5\,\mathrm{T}$, and $B = \pm 0.1\,\mathrm{T}$ in the temperature range between 2 K and 300 K. It has been found that the calculated XMCD spectra nicely follow the experimental ones.

Finally, one should notice that all these calculations have been performed with no consideration for any Kondo screening in line with what is found in the literature. The pretty nice agreement between experiments and calculations tends to confirm the absence of Kondo screening at temperatures above 200 mK.

Chapter 6

Kondo Intermetallic Compounds : $Yb_{0.005}Au_{0.995}$

6.1 Motivations of the study

In this chapter, the calculations and the experimental analysis of the intermetallic sample $Yb_{0.005}Au_{0.995}$ (very diluted ytterbium atoms in gold) will be presented. Ytterbium is one of the lanthanide rare earth elements.

Like the ErPd alloy, YbAu is a binary intermetallic alloy system which has been studied by different investigation techniques because of a strong Kondo anomaly [44], first observed below 6 K by Mössbauer measurements [138]. In addition, resistivity measurements of Yb_xAu_{1-x} alloys with $x = 0.38\%$, $x = 0.22\%$ and $x = 0.18\%$ show a minimum of resistivity around $T = 5$ K with the expected Kondo logarithmic variation for lower temperatures [139] and a Kondo temperature that has been estimated to $T_K = 10$ mK as deduced from nuclear orientation experiments [140]. $T_K = 10$ mK means that between 10 mK and 5 K (resistivity minimum), the numerical Renormalization Group method of Wilson [55] is well adapted to understand the Kondo electronic structure.

Yb_xAu_{1-x} alloys has a fcc structure where the Yb atoms are said to be present in form of Yb^{3+}. The electronic atomic structure of Yb^{3+} is characterized by 13 electrons on the $4f$ shell so that the 8-fold degenerate ground state is best described by $L = 3$, $S = 1/2$, and $J = 7/2$. In the multiplet $^2F_{7/2}$, the action of the cubic crystal field on the eigenfunctions can be found in Lea *et al.* [116] and also in Baker *et al.* [141] and Williams *et al.* [115]. From these expressions cited in (Eq.A.1) of Appendix A, the variation of the projection of the total angular momentum $\langle J_z \rangle$ and of $\langle J_z^2 \rangle$ as a function of temperature and an external magnetic induction can be obtained analytically. These calculations, where the crystal field and the Zeeman interaction are considered, are purely atomic so that the Kondo effect is completely out of the scheme.

The XAS measurements have been performed on DEIMOS beamline at Synchrotron

SOLEIL between 200 mK and 300 K in the presence of an external magnetic field between -6.5 T and $+6.5$ T. As presented in the previous section, the variation of the values of the operators $\langle J_z \rangle$ and $\langle J_z^2 \rangle$ as a function of T and B can be obtained by the measurements of both XMCD and XMLD.

My strategy is the following. I will determine the crystal field parameters by fitting the observed variations of $\langle J_z \rangle$ and $\langle J_z^2 \rangle$ for $B = \pm 6.5$ T and 200 mK$\leq T \leq$300 K. Then I shall compute the variation of the Yb magnetic moment for the two series $B = \pm 0.5$ T with 200 mK$\leq T \leq$300 K and $B = \pm 0.1$ T with 200 mK$\leq T \leq$300 K. The differences between the calculated and experimental magnetic moments for $B = \pm 0.5$ T and $B = \pm 0.1$ T can be interpreted as a sign of presence of the Kondo interaction. I recognize that this sensible strategy is minimal.

6.2 Properties of the ytterbium trivalent ion in gold

The atomic number of ytterbium is 70 and its molar mass is 173.045 (10) g/mol [133]. Experiment shows that ytterbium is best described as a form of trivalent cation ion Yb^{3+} in gold [142]. The electronic configuration of Yb^{3+} is [Xe]$4f^{13}$ which means that the only open shell is the $4f$ shell. The ground state of Yb^{3+} is paramagnetic.

With the same method of determination of L and S as the one presented for Er^{3+} in Section 5.2, we have

m_L	+3	+2	+1	0	-1	-2	-3
m_S	$\uparrow\downarrow$	$\uparrow\downarrow$	$\uparrow\downarrow$	$\uparrow\downarrow$	$\uparrow\downarrow$	$\uparrow\downarrow$	$\uparrow$

from which we deduce $L = 3$ and $S = 1/2$. There are more than 7 electrons on the $4f$ shell so that J is given by

$$J = S + L = \frac{7}{2}. \tag{6.1}$$

The solubility of ytterbium is up to 7% in gold [142, 140, 143]. Because of the fcc structure of YbAu, if the random distribution of the Yb atoms in Au is satisfied, applying (Eq.5.7), one notices that 94.16% of ytterbium atoms are surrounded by 12 Au atoms for $x = 0.005$ (0.5% atom) so that Yb can be treated as an isolated ion and the Yb-Yb pairs can be safely neglected.

The term symbol for Yb ground state is ${}^2F_{7/2}$. By applying the formula

$$M = g_J \, \mu_B \, J \, B_J(x). \tag{6.2}$$

with $L = 3$, $S = 1/2$, $J = 7/2$ and $g_J = 8/7$ calculated by (Eq.5.3) and $B_J(x)$ calculated by (Eq.5.4) and (Eq.5.5), we obtain the calculation for magnetization M as the function of magnetic induction B for a spherical Yb^{3+} ion. Figure 6.1 shows this magnetization

evolution. We see that the saturation for the spherical ion is at $4\,\mu_B$ per Yb atom, as can be expected from $\langle L_z \rangle = -3\hbar$ and $\langle S_z \rangle = -\hbar/2$ for the 1-fold, non-degenerate ground state, when $B \neq 0$.

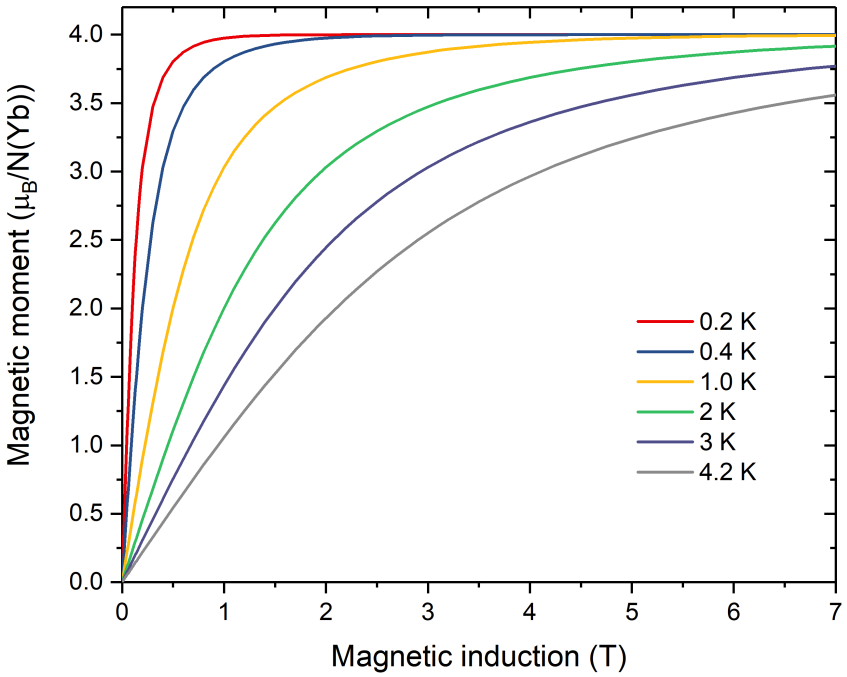

Figure 6.1: Evolution of the magnetic moment of a spherical Yb^{3+} ion as a function of an external magnetic induction and for temperatures between 0.2 K and 4.2 K.

Under cubic crystal field, the ground state $^2F_{7/2}$ splits into a doublet Γ_7, a quartet Γ_8 and a doublet Γ_6 where Γ_i are irreducible representations of the double group of the cubic group O_h [116]. In Bethe's notation [144], for integral value of J, i can take the values between 1, 2, 3, 4, 5 and for half-integral value of J, i takes the values between 6, 7, 8. From literature, Γ_7 has the lowest energy. Since the difference in energy between the ground state multiplet $^2F_{7/2}$ and the first excited multiplet $^2F_{5/2}$ is about $10\,300\,cm^{-1}$ (14 820 K) [145], at 4.2 K, a simple Boltzmann populations calculation gives the probability for a Yb^{3+} ion at $^2F_{7/2}$ ground state is in the order of $1/(1+10^{-1531})$ and for 300 K, the probability becomes in the order of $1/(1+10^{-22})$. In other words, for our study, the higher level $^2F_{5/2}$ can be completely neglected and the Yb^{3+} ion can be treated as 100% in the $^2F_{7/2}$ ground state multiplet.

The difference in energy between the Γ_7 level and the next level Γ_8 is about 80 K and Γ_6 is close to Γ_8 [146]. The same Boltzmann population calculation gives for 4.2 K, a probability for a Yb^{3+} ion in Γ_7 in the order of $1/(1+2.10^{-8}) \approx 100\%$, but for 300 K, the probability is reduced to 30.3%.

6.2.1 Zeeman effect and calculation of $\langle J_z \rangle$

2-fold Γ_7 ground state

We assume that at low temperature (*e.g.* $T = 4.2\,\mathrm{K}$), that all Yb^{3+} ions are in the Γ_7 state and we apply (Eq.4.18) (see the discussions presented in Section 4.2). In the present case, $k = 1$, $q = 0$, $L = L' = 3$, $S = S' = 1/2$, $J = J' = 7/2$ so that $\langle L||\mathbf{L}||L\rangle = 2\sqrt{21}\hbar$, $\langle S||\mathbf{S}||S\rangle = \sqrt{\frac{3}{2}}\hbar$. Thus we have $[J, J']^{1/2} = [7/2, 7/2]^{1/2} = 8$.

The eigenfunction of Γ_7 level are given by [116]

$$\Gamma_7 : \begin{array}{l} \left|\Gamma_7^+\right\rangle = \dfrac{\sqrt{3}}{2}\left|+\dfrac{5}{2}\right\rangle - \dfrac{1}{2}\left|-\dfrac{3}{2}\right\rangle, \\ \left|\Gamma_7^-\right\rangle = \dfrac{\sqrt{3}}{2}\left|-\dfrac{5}{2}\right\rangle - \dfrac{1}{2}\left|+\dfrac{3}{2}\right\rangle. \end{array} \tag{6.3}$$

J_z can be expressed as

$$\left\langle \Gamma_7^{\sigma}\middle|J_z\middle|\Gamma_7^{\sigma'}\right\rangle = \begin{array}{c} \\ \langle\Gamma_7^+| \\ \langle\Gamma_7^-| \end{array} \begin{array}{c} \begin{array}{cc} |\Gamma_7^+\rangle & |\Gamma_7^-\rangle \end{array} \\ \begin{pmatrix} \frac{3}{2} & 0 \\ 0 & -\frac{3}{2} \end{pmatrix} \end{array} \tag{6.4}$$

in units of $\hbar$, so that

$$E_{\mathrm{Zee}}\left(\Gamma_7^+\right) = +\frac{3}{2}g_J\mu_B B \text{ and } E_{\mathrm{Zee}}\left(\Gamma_7^-\right) = -\frac{3}{2}g_J\mu_B B. \tag{6.5}$$

For information, a straightforward calculation from (Eq.4.18) where spin and orbit magnetic contributions to the energy are separated gives

$$E_{\mathrm{Zee}}\left(\Gamma_7^+\right) = +\frac{3}{2}g_J\mu_B B = \left(\frac{9}{7} + g_s\frac{3}{14}\right)\mu_B B, \tag{6.6}$$

and

$$E_{\mathrm{Zee}}\left(\Gamma_7^-\right) = -\frac{3}{2}g_J\mu_B B = -\left(\frac{9}{7} + g_s\frac{3}{14}\right)\mu_B B. \tag{6.7}$$

The difference of the two Zeeman energy levels is

$$\Delta E = E_{\mathrm{Zee}}\left(\Gamma_7^+\right) - E_{\mathrm{Zee}}\left(\Gamma_7^-\right) = \frac{24}{7}\mu_B B. \tag{6.8}$$

Then we can deduce the magnetic moment distribution as a function of temperature. Let us make E_0 for the initial energy level before the Zeeman splitting and E' for the Zeeman splitting level Γ_7^- and $E' + \Delta E$ for the Zeeman splitting level Γ_7^+ as shown in

Figure 6.2. The following relations can be easily verified:

$$E' = E_0 - |E_{Zee}|, \tag{6.9}$$

$$E' + \Delta E = E_0 + |E_{Zee}|. \tag{6.10}$$

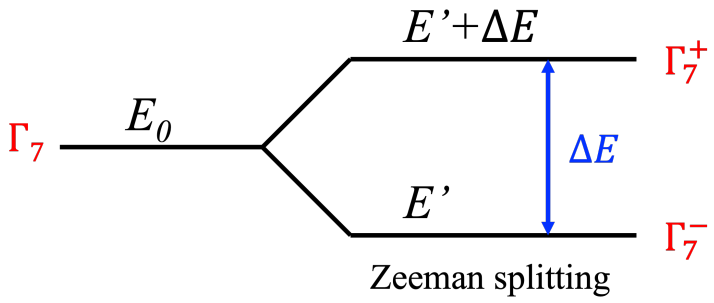

Figure 6.2: The energy levels of the Γ_7, 2-fold degenerate state for an Yb^{3+} ion in a cubic crystal field.

The distribution of probability for Γ_7^- and Γ_7^+ levels is given by

$$p\left(\Gamma_7^-\right) = \frac{\exp\left(-\frac{E'}{k_B T}\right)}{\exp\left(-\frac{E'}{k_B T}\right) + \exp\left(-\frac{E'+\Delta E}{k_B T}\right)}, \tag{6.11}$$

$$p\left(\Gamma_7^+\right) = \frac{\exp\left(-\frac{E'+\Delta E}{k_B T}\right)}{\exp\left(-\frac{E'}{k_B T}\right) + \exp\left(-\frac{E'+\Delta E}{k_B T}\right)}. \tag{6.12}$$

so that

$$p\left(\Gamma_7^-\right) = \frac{1}{1 + \exp\left(-\frac{\Delta E}{k_B T}\right)}, \tag{6.13}$$

$$p\left(\Gamma_7^+\right) = \frac{1}{1 + \exp\left(\frac{\Delta E}{k_B T}\right)}. \tag{6.14}$$

The energy distribution as a function of temperature can be calculated as

$$\begin{aligned}\langle E\rangle &= p\left(\Gamma_7^-\right) E\left(\Gamma_7^-\right) + p\left(\Gamma_7^+\right) E\left(\Gamma_7^+\right) \\ &= -\frac{12}{7}\mu_B B\left[\frac{1}{1+\exp\left(-\frac{\Delta E}{k_B T}\right)} - \frac{1}{1+\exp\left(\frac{\Delta E}{k_B T}\right)}\right] \\ &= -\frac{12}{7}\mu_B B \tanh\left(\frac{\Delta E}{2k_B T}\right) \\ &= -\frac{12}{7}\mu_B B \tanh\left[\frac{3}{2k_B T}\left(\frac{6}{7}+g_s\frac{1}{7}\right)\mu_B B\right].\end{aligned} \tag{6.15}$$

Then the magnetic moment distribution as a function of temperature can be deduced by derivating the energy with respect to the magnetic field

$$\langle m\rangle = -\frac{\partial\langle E\rangle}{\partial B}. \tag{6.16}$$

We have

$$\langle m\rangle = \frac{12}{7}\mu_B \tanh\left[\frac{3}{2k_B T}\left(\frac{6}{7}+g_e\frac{1}{7}\right)\mu_B B\right] = \frac{12}{7}\mu_B \tanh\left(\frac{12\mu_B B}{7k_B T}\right). \tag{6.17}$$

We plot the isothermal variation of the magnetization in Figure 6.3. Comparing to Figure 6.1 obtained only by consideration of spherical ion, the consideration of cubic crystal field and Zeeman effect reduces the magnetic moment at saturation by more than a factor of 2, *i.e.* $1.714\,\mu_B$ per Yb atom with cubic crystal field versus $4\,\mu_B$ per Yb atom with no crystal field. Note that this simple calculation is only valid at low temperatures, *i.e.* T well below 80 K. When Γ_8 and Γ_6 levels become populated, the above expression is no more valid.

8-fold $^2F_{7/2}$ ground state

For arbitrary temperatures well below 14 820 K, the consideration of all Γ_7, Γ_8 and Γ_6 is necessary. The energy gap between Γ_7 and Γ_8 (denoted Δ_1) is very close to that between Γ_7 and Γ_6 (denoted Δ_2) [146]. The different magnetic susceptibility measurements show that $\Delta_1 = 80$ K, $\Delta_2 = 83$ K [147] or $\Delta_1 = 94$ K, $\Delta_2 = 91$ K [148, 149]. If we take the series $\Delta_1 = 80$ K, $\Delta_2 = 83$ K, a scheme (Figure 6.4) shows the 8-fold energy levels of $^2F_{7/2}$ ground state under cubic crystal field and Zeeman effect with external magnetic field.

The details of the calculations are presented in Appendix A.1 and Appendix A.2. There are no simple analytic expressions for the energies because the 8x8 Hamiltonian is fully non-degenerate. The variation of magnetization calculated with consideration

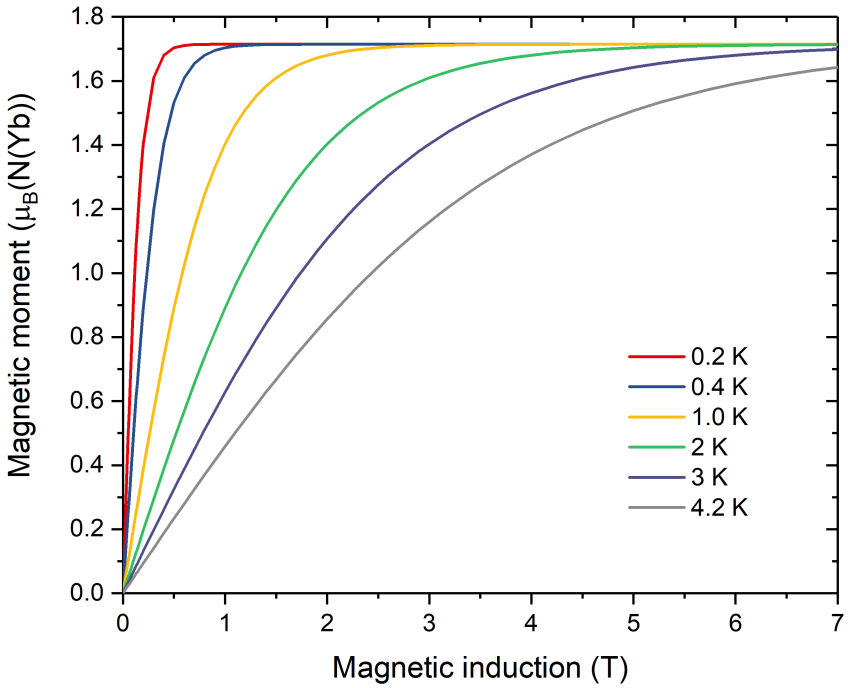

Figure 6.3: Evolution of the magnetic moment of Yb^{3+} ion as a function of an external magnetic induction, at different low temperatures with assuming that the ground state is a pure Γ_7 level.

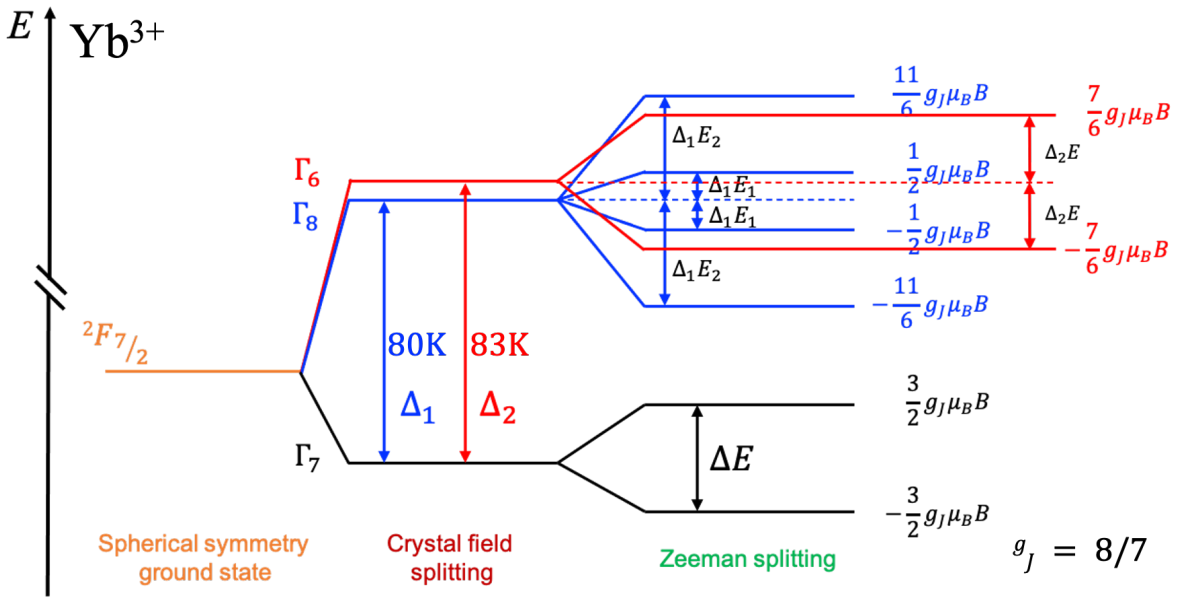

Figure 6.4: 8-fold energy levels of $^2F_{7/2}$ ground state under cubic crystal field and Zeeman effect with external magnetic field. Note that this is a qualitative scheme.

of 8-fold levels of $^2F_{7/2}$ and the cubic symmetry of the powder is plotted in Figure 6.5. Comparing to Figure 6.3, for low temperature (*e.g.* $T = 0.2\,\mathrm{K}$), from $B = 1\,\mathrm{T}$ to $B = 7\,\mathrm{T}$, a linear increasing zone of magnetization replaces the saturation zone of Figure 6.3. At $T = 0.2\,\mathrm{K}$ and $B = 7\,\mathrm{T}$, $M = 1.817\,\mu_B$ per Yb atom compared to $M = 1.714\,\mu_B$ per Yb atom in Figure 6.3.

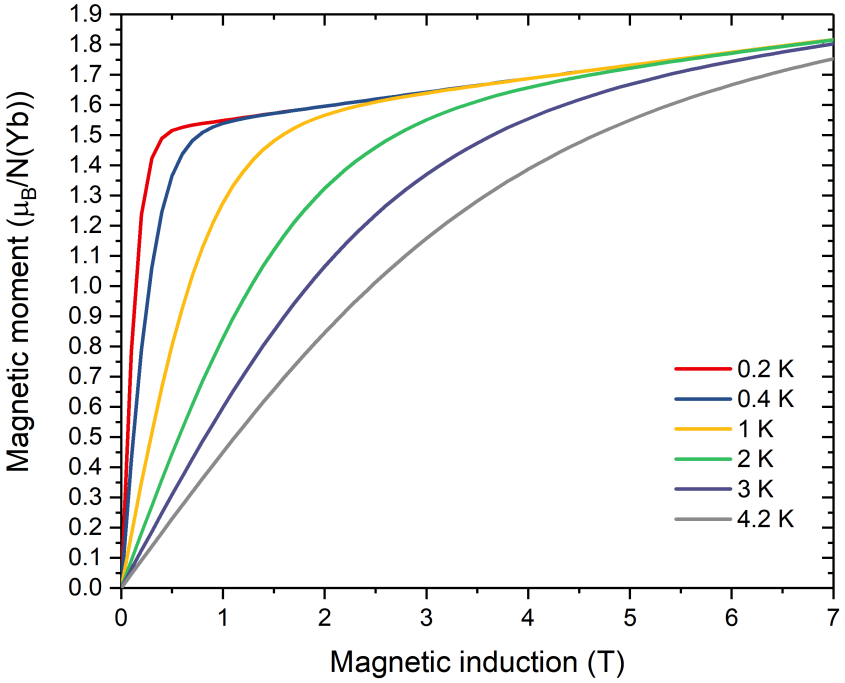

Figure 6.5: Evolution of the magnetic moment of Yb^{3+} ion as a function of magnetic induction with consideration of 8-fold energy levels of $^2F_{7/2}$ ground state under cubic crystal field and Zeeman effect.

6.2.2 Calculations of $\langle J_z^2 \rangle$

By definition in (Eq.3.18), the XMLD signal is related to $\langle J_z^2 \rangle$. For a given J, one has only to calculate $\langle J_z^2 \rangle$ by the same method as what we have done for $\langle J_z \rangle$. The details of calculation are presented in Appendix A.3. Once $\langle J_z^2 \rangle$ is known, we can deduce the amplitude of the XMLD signal as a function of temperature by applying (Eq.3.18). Figure 6.6 reports the evolution of the amplitude of the XMLD signal, apart from the multiplicative factor $\sigma_2(E)$ (Eq.3.18), as a function of temperature.

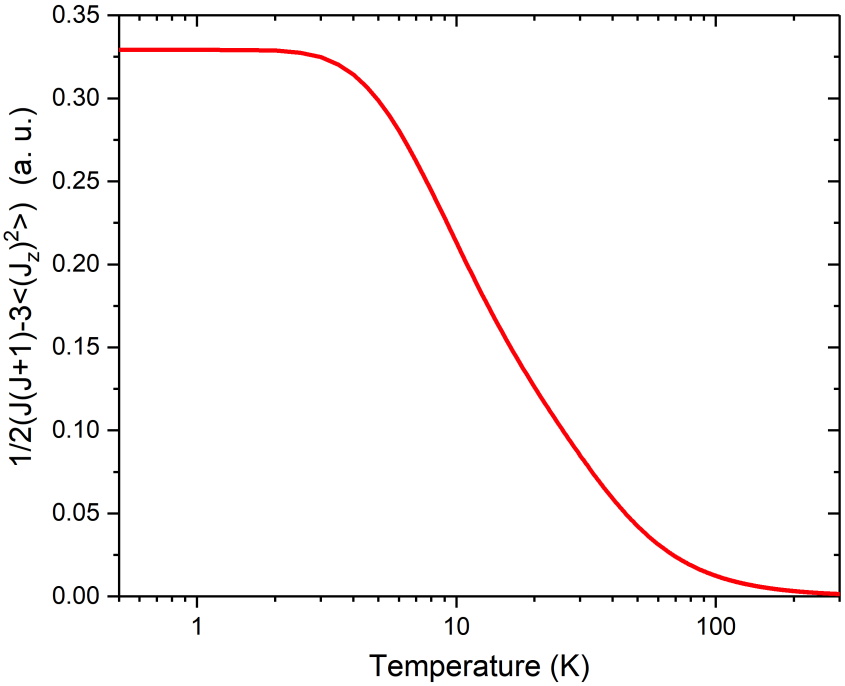

Figure 6.6: $\frac{1}{2}\left[J\left(J+1\right)-3\left\langle J_z^2\right\rangle\right]$ as a function of temperature (in a logarithmic scale). This quantity is related directly to the XMLD signal by multiplying a factor $\sigma_2\left(E\right)$.

6.3 Sample preparation and characterization

6.3.1 Sample preparation

$Yb_{0.005}Au_{0.995}$ sample has been synthesised by Guy Schmerber from the *Institut de Physique et Chimie des Matériaux de Strasbourg* (IPCMS) by triarc melting of the appropriate amounts of metals under a purified argon atmosphere, using a homemade water-cooled Cu plate and non-consumable thoriated tungsten electrodes. The purities of the starting materials were 99.99% for Au and 99.9% for Yb. The ingot was remelted ten times and inverted after each melting to promote mixing. The as-cast $Yb_{0.005}Au_{0.995}$ alloy was homogenized at 900 °C for 24 hours in a sealed silica tube and then water quenched. With this kind of preparation, we can consider that the sample is a polycrystal, with no privileged orientation. The sample mounted on the CroMag sample holder is shown in Figure 6.7 (see also Figure 3.7).

An other sample ($Yb_{0.005}Ag_{0.995}$) where ytterbium is introduced in a silver matrix has also been synthesized following the above method presented for $Yb_{0.005}Au_{0.995}$. This sample has almost not been studied and it is not much commented.

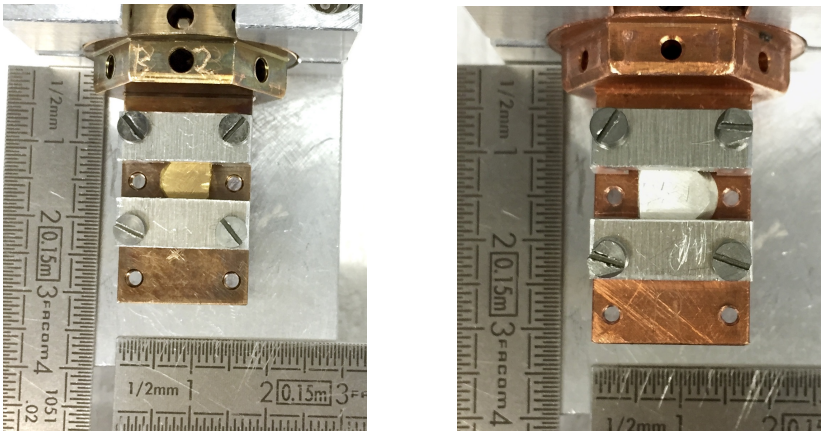

Figure 6.7: $Yb_{0.005}Au_{0.995}$ (left) and $Yb_{0.005}Ag_{0.995}$ (right) samples mounted on the sample holder of DEIMOS beamline.

6.3.2 X-ray diffraction

The crystalline phase of the sample was determined using a Bruker D8 Advance diffractometer equipped with a LynxEye detector at the monochromatic wavelength of Cu $K_{\alpha 1}$, $\lambda = 1.54\,\text{Å}$. The expected fcc phase was confirmed: $Fm\bar{3}m$ space group, with the lattice parameters $a_{Yb_{0.005}Au_{0.995}} = 4.08 \pm 0.01\text{Å}$ and $a_{Yb_{0.005}Ag_{0.995}} = 4.09 \pm 0.01\text{Å}$ at room temperature ($a_{Au} = 4.07 \pm 0.01\text{Å}$ for pure gold and $a_{Ag} = 4.09 \pm 0.01\text{Å}$ for pure silver).

6.3.3 SQUID measurements

Isothermal magnetization curves at $T = 2\,\text{K}$ have been undertaken in *Institut de Physique et Chimie des Matériaux de Strasbourg* (IPCMS) by Guy Schmerber with a SQUID magnetometer. The magnetic field varied between $-7\,\text{T}$ to $7\,\text{T}$ and the results are reported in the quadrant for positive induction and positive magnetic moment. Figure 6.8 reports the SQUID measurements of $Yb_{0.005}Au_{0.995}$ and the calculated magnetic moments from Section 6.2.1.

We remark that for the strong magnetic induction, the simulation with the consideration of only the 2 lowest levels under Zeeman effect is different from the measurements. The saturation is not evident until $7\,\text{T}$ at $2\,\text{K}$. However the calculation with 8 states of $^2F_{7/2}$ with cubic symmetry consideration gives a better prediction. The behavior for strong magnetic field is similar to the measurements. The difference of magnetic moments ($1.96\,\mu_B$ per Yb atom for SQUID at $B = 7\,\text{T}$ vs. $1.82\,\mu_B$ per Yb atom for the 8-fold calculations in the same condition) is very likely due to the magnetization of the pure paramagnetic gold atoms and the induced magnetization of gold atoms neighboring the Yb atoms. Suzuki *et al.* [150] showed that bulk gold (Au) exhibits temperature-

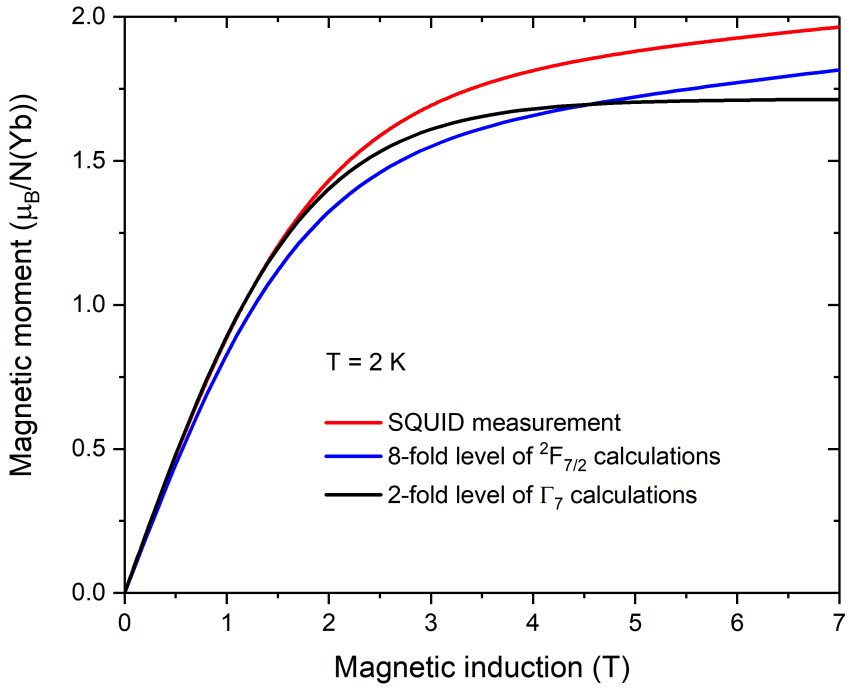

Figure 6.8: SQUID measurements of isothermal magnetization curves of $Yb_{0.005}Au_{0.995}$ sample at 2 K compared to the two calculation approaches (2-fold vs 8-fold ground state) discussed in Section 6.2.1.

independent paramagnetism in an external magnetic field by XMCD measurements at the Au $L_{2,3}$ edges. By applying magneto-optical sum rules, Suzuki *et al.* obtained a magnetic moment of $1.3 \times 10^{-4}\,\mu_B$/atom in an external magnetic field of 10 T. We remove the magnetic moment contribution of Au from the magnetic moment of Yb^{3+} for $Yb_{0.005}Au_{0.995}$. With a simple calculation, we obtain that for 6.5 T, the SQUID magnetic moment for one ytterbium atom will be reduced by $1.68 \times 10^{-2}\,\mu_B$.

6.3.4 Surface cleaning and sample preparation for XAS

In the present section, we mainly focus on sample $Yb_{0.005}Au_{0.995}$. The sample was fixed with copper plates screwed tightly on the sample holder (Figure 6.8) in order to ensure the best thermal contact with the mixing chamber. Like for the ErPd sample, the surface cleaning is necessary for the measurement of $Yb_{0.005}Ag_{0.995}$ on DEIMOS beamline. All the surface scraping manipulations are done in the UHV surface cleaning chamber (Section 3.3). The sample is scraped at $P = 4 \times 10^{-10}$ mbar during about 15 minutes. The sample is then transported to the CroMag without breaking the UHV.

To check the efficiency of the surface cleaning, we realized a test on the silver sample, $Yb_{0.005}Ag_{0.995}$ sample. We know that Yb is divalent in YbAg alloys and trivalent in YbAu alloys [142, 151, 143]. Trivalent ytterbium is paramagnetic with a $4f^{13}$ configu-

ration while divalent ytterbium is diamagnetic with $4f^{14}$ configuration [152]. Since the $4f$ shell of divalent ytterbium is full, the $M_{4,5}$ edges correspond to transitions from a $3d$ core-hole to $5d$ levels and f levels of the continuum. The large white line observed at the M_5 edge for trivalent ytterbium is then supposed to disappear for Yb^{2+} and the edges are expected to be broad arctangent-shaped transitions. The measurement of the $M_{4,5}$ edges of $Yb_{0.005}Ag_{0.995}$ prior to surface scraping show that $Yb_{0.005}Ag_{0.995}$ is mostly covered with ytterbium sesquioxide, Yb_2O_3, with trivalent Yb^{3+}. One expects that after scraping most of the sesquioxide has disappeared (but for grain boundary), hence the difference between the $M_{4,5}$ edges for non-scraped and scraped samples should be a large reduction of the intensity of the M_5 edge.

XAS signals at $T = 4.2\,\mathrm{K}$ and $B = 6.5\,\mathrm{T}$ of Yb-M_5 edge have been recorded by TEY and TFY detection mode. TEY is surface sensitive ($\approx 5\,\mathrm{nm}$) and TFY is more bulk sensitive ($\approx 250\,\mathrm{nm}$) [153, 154]. Figure 6.9 shows the measurements before and after the surface scraping manipulations. We see that at the surface as detected by TEY (*i.e.* the first 5 nm), the presence of oxidation has been reduced by a factor of 3 after scraping the sample surface. The oxidation decrease is larger for the TFY measurements (reduction by a factor 13). The depth of the scrapping groove shown in Figure 3.7 is at least 1 mm so that the residual of the oxidation seen by TEY and TFY can be attributed to residual oxidation at the grain boundary of the polycrystals. For polycrystaline intermetallic systems, there is no way that this grain boundary oxidation ($\approx 7\%$) can be removed.

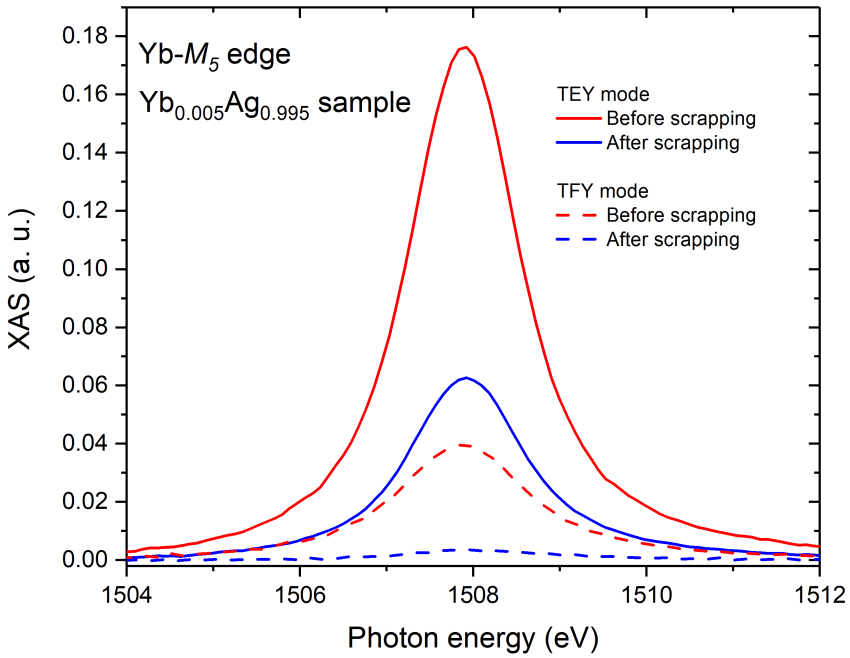

Figure 6.9: XAS measurements of Yb M_5 edge detected in TEY or in TFY, before and after scraping the surface of $Yb_{0.005}Ag_{0.995}$.

6.4 Yb XAS at $M_{4,5}$ edges

The ground state multiplet of Yb^{3+} is $2F_{7/2}$. When dealing with Yb $M_{4,5}$ edges, the configuration of the multielectronic final state is $3d^9 4f^{14}$ for which the excited states with core-hole are the spin-orbit split multiplets $2D_{5/2}$ and $2D_{3/2}$. The multiplet $2D_{5/2}$ is associated to the M_5 edge and the multiplet $2D_{3/2}$ is associated to the M_4 edge. The selection in the electric dipole approximations states $\Delta J = \pm 1, 0$, so that the M_5 edge corresponds to $\Delta J = -1$ where as the M_4 edge corresponds $\Delta J = -2$. Hence the M_4 edge would be zero in the electric dipole approximation. Crystal field and Zeeman effect very partially lift this interdiction but the large spin-orbit ζ_{3d} constant compared to crystal field and Zeeman contributions actually kills the M_4 edge.

The XAS measurements of the Yb-M_5 edges were performed on DEIMOS beamline at Synchrotron SOLEIL. We change the magnetic field from 6.5 T to -6.5 T then from -6.5 T back to 6.5 T for the XMCD measurements. We have also recorded the spectra without the presence of magnetic field in order to record σ_0 that is the isotropic cross-section. To reduce the eddy current, for the ultra-low temperature ($T < 1$ K), we fix the variation rate for the magnetic field at 0.02 T/s.

One series of XAS-XMCD measurements contains eight usable spectra[1] : $\sigma_1(\phi^+)$ (left polarization), $\sigma_2(\phi^-)$ (right polarization), $\sigma_3(\phi^-)$, $\sigma_4(\phi^+)$ with a magnetic field along the propagation direction of the photons and $\sigma_5(\phi^-)$, $\sigma_6(\phi^+)$, $\sigma_7(\phi^+)$, $\sigma_8(\phi^-)$ with inverse magnetic field with respect to the former four spectra.

Since the M_4 edge has zero intensity and the shape of the M_5 edge has mainly a Lorentzian shape with no multiplet features, the normalization of the experimental spectra is difficult to perform. To solve this question, we inserted a $\approx 1\mu$m-thick aluminium foil in between the I_0 detector and the sample. The energy of the Al-K edge is 40 eV above the Yb-M_5 edge and its shape obviously does not depend on the sample temperature, nor the external magnetic induction applied to the sample. We then used the Al-K edge jump as a normalization constant for the Yb-M_5 edge.

Figure 6.10 shows an example of one series of Yb-M_5 edge measurements performed at 217 mK with a 6.5 T external magnetic field. The energy of the Yb-M_5 edge is 1507.5 eV. The structure from 1550 eV to 1580 eV is the absorption of the Al-K edge measured in transmission. By using the amplitude normalization, we can easily normalize the different Yb-M_5 spectra.

Figure 6.11 shows a zoom of the Yb-M_5 edge. The black spectrum is the average of the four "+" spectra and the green one is the average of the four "−" spectra. By definition, the sign of a spectrum is the sign of the product of the phase with the field so that the "+" spectra are σ_1, σ_4, σ_6, and σ_7 and the "−" spectra are σ_2, σ_3, σ_5, and σ_8. The orange spectrum is the average of the black and green spectra (calculations

[1] Two additional conditioning spectra each time after modifying the magnetic field.

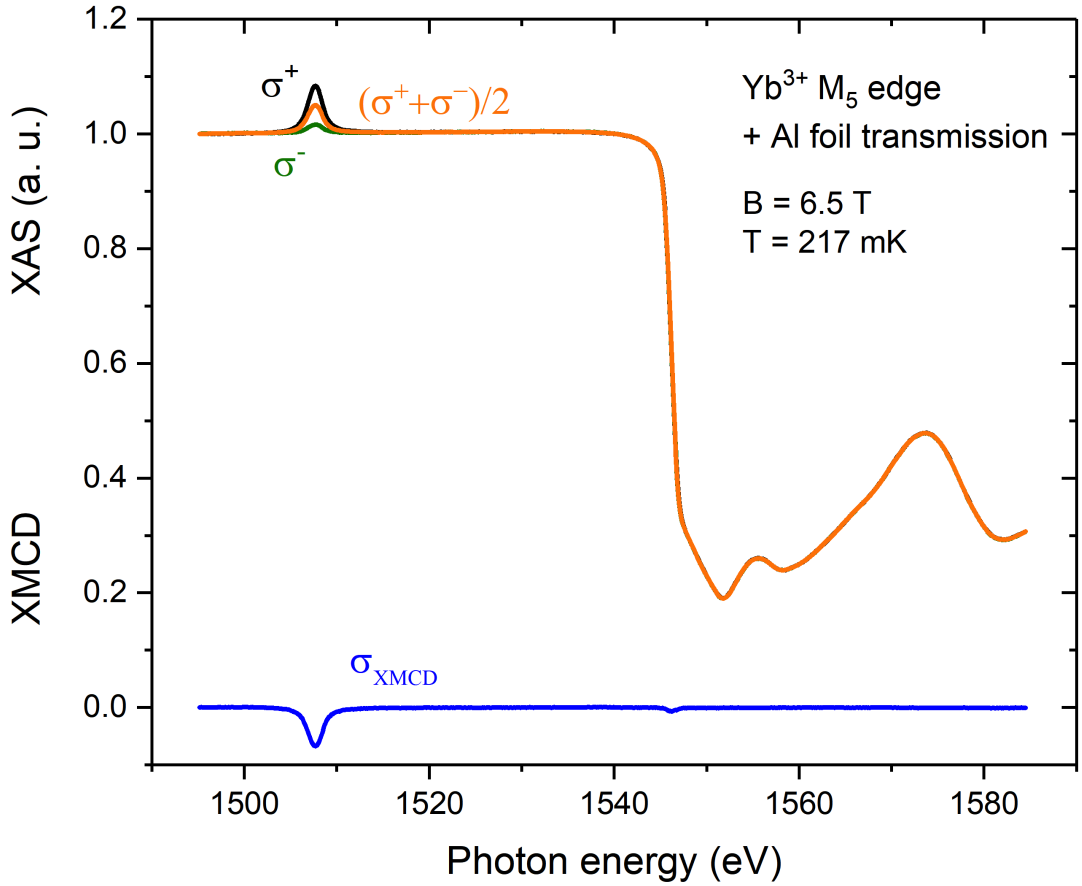

Figure 6.10: XAS-XMCD measurements of Yb-M_5 edge (1507.5 eV) at $T = 217$ mK and $B = 6.5$ T. The structure from 1550 eV to 1580 eV is the Al-K edge measured in transmission of the inserted aluminum foil between the beam the the sample served as a normalization reference between different series of measurement.

similar to what has been developed for ErPd by using (Eq.5.9)). The blue spectrum is the XMCD spectrum which is the difference between the "−" green and the "+" black spectra (calculations similar to (Eq.5.10) for ErPd). The red isotropic spectrum σ_0 is recorded without magnetic field.

6.4.1 Applications of the sum rules

From the discussion in Section 6.2, for the Yb^{3+} ion, the spherical ground state is defined by $J = 7/2$, $L = 3$, $S = 1/2$. For the magneto-optical sum rules, we are dealing with Yb-M_5, i.e. transitions between the $3d$ shell and the $4f$ shell so that in (Eq.3.12) and (Eq.3.13), $l = 3$ and $c = 2$. There are $n = 13$ electrons on the $4f$ shell so

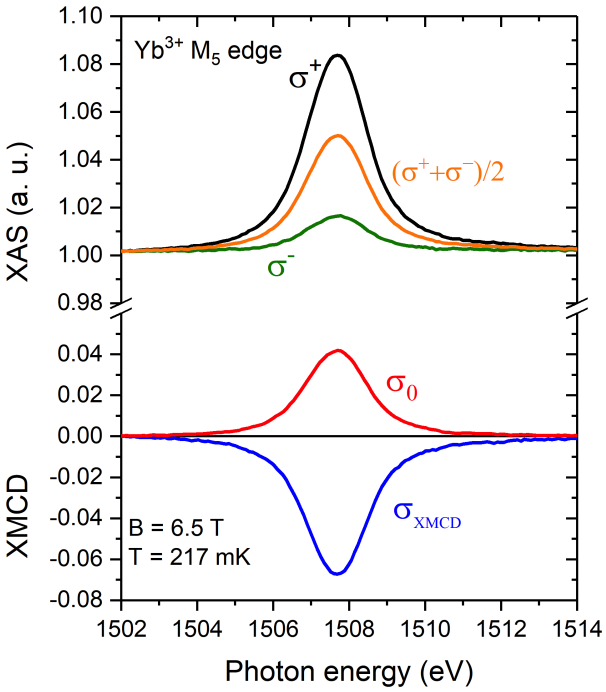

Figure 6.11: Zoom of the Yb-M_5 edge. The black spectrum is the average of the spectra σ^+, the green spectrum is the average of the spectra σ^-. The average of the green spectrum and the black one gives the $\frac{\sigma^+ + \sigma^-}{2}$ spectrum in orange. The red isotropic spectrum σ_0 is recorded without magnetic field. The green spectrum minus the black spectrum gives the XMCD spectrum in blue.

that the number of holes is $(4l+2) - 13 = 1$. Then (Eq.3.12) writes

$$\frac{\int_{j^+ + j^-} \mathrm{d}E(\sigma^+ - \sigma^-)}{\int_{j^+ + j^-} \mathrm{d}E(\sigma^+ + \sigma^- + \sigma_{\|})} = \frac{1}{3}\langle L_z \rangle. \tag{6.18}$$

By calculating the integrals of σ^+, σ^- and $\sigma_{\|}$ spectra, we obtain $\langle L_z \rangle$. $\langle S_z \rangle$ is deduced by applying the Wigner-Eckart theorem with $g_J = 8/7$ for Yb^{3+} :

$$\frac{\langle L_z \rangle}{\langle S_z \rangle} = \frac{2 - g_J}{g_J - 1} = 6, \tag{6.19}$$

so that

$$\langle S_z \rangle = \frac{1}{6}\langle L_z \rangle. \tag{6.20}$$

The total magnetic moment can be easily obtained by applying

$$M_{\text{total}} = M_{\text{L}} + M_{\text{S}} = -\frac{\mu_{\text{B}}}{\hbar}\langle L_z \rangle - 2\frac{\mu_{\text{B}}}{\hbar}\langle S_z \rangle. \tag{6.21}$$

Since in most cases, we have set $\hbar = 1$, the above expression resumes to

$$M_{\text{total}} = M_{\text{L}} + M_{\text{S}} = -\mu_{\text{B}}\langle L_z\rangle - 2\mu_{\text{B}}\langle S_z\rangle = -\frac{4}{3}\mu_{\text{B}}\langle L_z\rangle. \tag{6.22}$$

6.5 Magnetic moment distribution as a function of temperature

By applying the sum rules from Section 6.4.1, we have obtained the magnetic moment from 200 mK to 300 K with external magnetic fields of 6.5 T, 0.5 T and 0.1 T. The experimental results are plotted in Figure 6.12 and are compared to the calculations from Section 6.2.1.

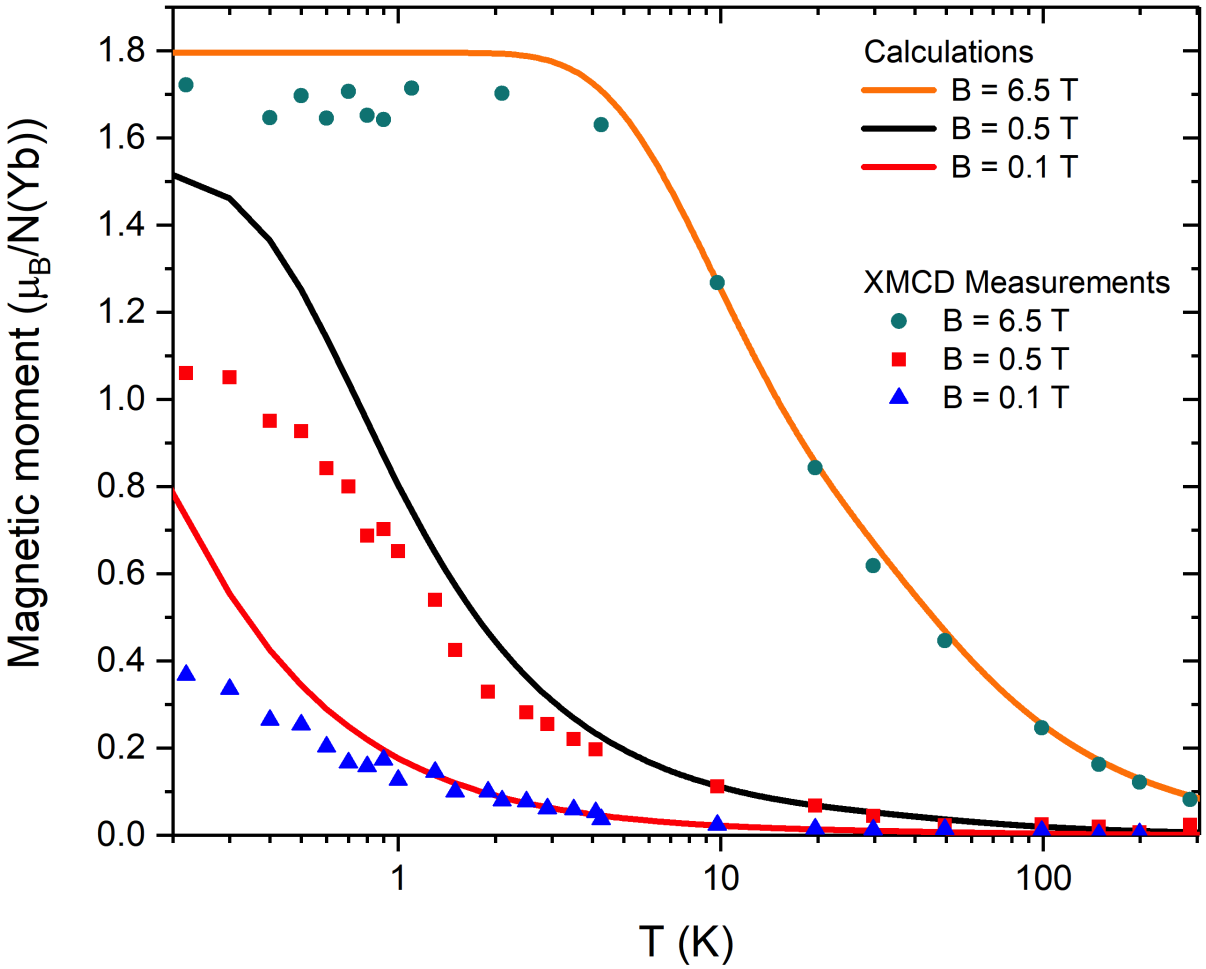

Figure 6.12: Variation of the magnetic moment of Yb^{3+} ion as a function of temperature (T is represented in logarithmic scale.) with magnetic field of 6.5 T, 0.5 T and 0.1 T. The calculated curves (solid lines) are obtained from the method discussed in Section 6.2.1.

For the three magnetic fields (strong or weak inductions), a good agreement is found for the high temperature side which present a typical paramagnetic behavior.

For $B = 6.5\,\mathrm{T}$, at low temperature, *i.e.* $T \leq 10\,\mathrm{K}$, the Yb magnetic moment tends to a saturation of $1.7\,\mu_B$ per Yb atom (experiment) vs. $1.8\,\mu_B$ per Yb atom (calculations) so that there is a fair agreement between the experiments and the calculation, with a difference less than 5.6%.

For $B = 0.5\,\mathrm{T}$, one observes that the calculations overestimate the Yb experimentally determined magnetization and the difference is as large as $\approx 26\%$ for $T = 0.2\,\mathrm{K}$.

For $B = 0.1\,\mathrm{T}$, the differences between experimental and calculated magnetizations are even larger (it is 50% for $T = 0.2\,\mathrm{K}$).

At the difference of SQUID magnetic measurements that probe all magnetic moments, *i.e.* Yb and Au conduction electrons, XAS-XMCD are sensitive to the Yb local magnetic, thus probing one of the element building the Kondo singlet. The weaker the magnetic field, the larger the difference between measurements and calculations. We interpret this difference as a signature of the Kondo effect in $Yb_{0.005}Au_{0.995}$. For weak magnetic fields and at low temperature, the magnetic moment of the Yb^{3+} ion and the conduction electrons couple antiferromagnetically and form a Kondo singlet, so that the magnetic moment of Yb^{3+} tends to be locally screened by the building of the Kondo singlet. In a strong external magnetic field (*e.g.* $B = 6.5\,\mathrm{T}$), the Kondo singlet is broken so that the "standard" paramagnetic behavior reappears.

6.5.1 Interpretation of Kondo effect

Schotte and Schotte have proposed a "resonance level model" to calculate the magnetization and the magnetic susceptibility in Kondo systems [70]. This model has successfully explained the data recorded for AgFe intermetallic systems where Fe is an impurity diluted in a silver matrix [155, 156]. This model describes the interaction of the impurities with the conduction electrons by a virtual bound state, located at the Fermi level, with a Lorentzian shape and width Δ. Δ is the Kondo energy that is related to the Kondo temperature by $\Delta \simeq k_B T_K$. From Ref.[70], the free energy can be written as

$$F = -k_B T \int_{-\infty}^{\infty} \rho(\epsilon) \ln\left[1 + \exp\left(-\frac{\epsilon}{k_B T}\right)\right] \mathrm{d}\epsilon \tag{6.23}$$

where

$$\rho(\epsilon) = \frac{\Delta/\pi}{\epsilon^2 + \Delta^2}. \tag{6.24}$$

In the original work by Schotte and Schotte [70], where the orbital magnetic momentum of Fe is zero (*i.e.* $L = 0$), the free energy is generalized for a finite spin S, in an external magnetic induction B and at finite temperature. Here we propose to generalize the free energy to the case of an Yb atom with total angular momentum $J = 7/2$. We have

$$F_{2J+1} = -k_B T \int_{-\infty}^{\infty} \frac{(\Delta/\pi)\,\mathrm{d}\epsilon}{(\epsilon - g_J \mu_B B)^2 + \Delta^2} \ln\left[\sum_{-J}^{J} \exp\left(\frac{\epsilon J}{k_B T}\right)\right]. \tag{6.25}$$

From the calculation by Schotte and Schotte [70], we get an expression of the magnetization as a function of an external induction B and temperature T as

$$M = g_J \mu_B \mathrm{Im}\left\{\frac{2J+1}{\pi}\psi\left[1 + \frac{\Delta + i g_J \mu_B B}{2\pi k_B T}(2J+1)\right] - \frac{1}{\pi}\psi\left[1 + \frac{\Delta + i g_J \mu_B B}{2\pi k_B T}\right]\right\} \tag{6.26}$$

where ψ is the digamma function defined as the logarithmic derivative of the gamma function, *i.e.* for a complex number z with $\mathrm{Re}\{z\} > 0$ [157]

$$\psi(z) = \frac{\mathrm{d}}{\mathrm{d}z}\ln(\Gamma(z)) = \frac{\Gamma'(z)}{\Gamma(z)}, \tag{6.27}$$

where the Γ function is defined by [158]

$$\Gamma(z) = \int_0^{\infty} t^{z-1} e^{-t} \mathrm{d}t. \tag{6.28}$$

In the above formula (Eq.6.26), the sum is performed over equally spaced eigenenergies. The Zeeman split levels are only equally spaced in spherical symmetry, when no crystal field is considered. Then (Eq.6.26) gives the magnetization of a Yb ion, building a Kondo singlet in spherical symmetry. In the present model, the crystal field splitting of the 8-fold $J = 7/2$ levels is completely absent.

By applying the above formula with $g_J = 8/7$, $J = 7/2$ and for various B and T, we can fit the experimental magnetization curves so that it provides the Kondo temperature T_K. Figure 6.13 shows the simulation with (Eq.6.26) compared to the measurements with a Kondo temperature fitted at $T_K = 0.7\,\mathrm{K}$.

The simulation curve (Figure 6.13) at $B = 6.5\,\mathrm{T}$ differs a lot to the measurements which saturates at $3.64\,\mu_B$ per Yb atom for $T = 0.2\,\mathrm{K}$. Costi found that for an impurity with $S = 1/2$, the Kondo singlet exists if the Zeeman energy roughly satisfies $g_J \mu_B |B| \leq 0.5\, k_B T_K$ or $|B| \leq k_B T_K/(2 g_J \mu_B)$ [60]. When $|B| > k_B T_K/(2 g_J \mu_B)$, the Kondo singlet is destroyed and the Kondo effect disappears [60]. With our T_K estimated at 0.7 K, $0.5\, k_B T_K = 0.030\,\mathrm{meV}$, and $g_J \mu_B |B|(B = 0.1\,\mathrm{T}) = 0.0066\,\mathrm{meV}$, $g_J \mu_B |B|(B = 0.5\,\mathrm{T}) = 0.033\,\mathrm{meV}$ and $g_J \mu_B |B|(B = 6.5\,\mathrm{T}) = 0.430\,\mathrm{meV}$. For $B = 0.5\,\mathrm{T}$,

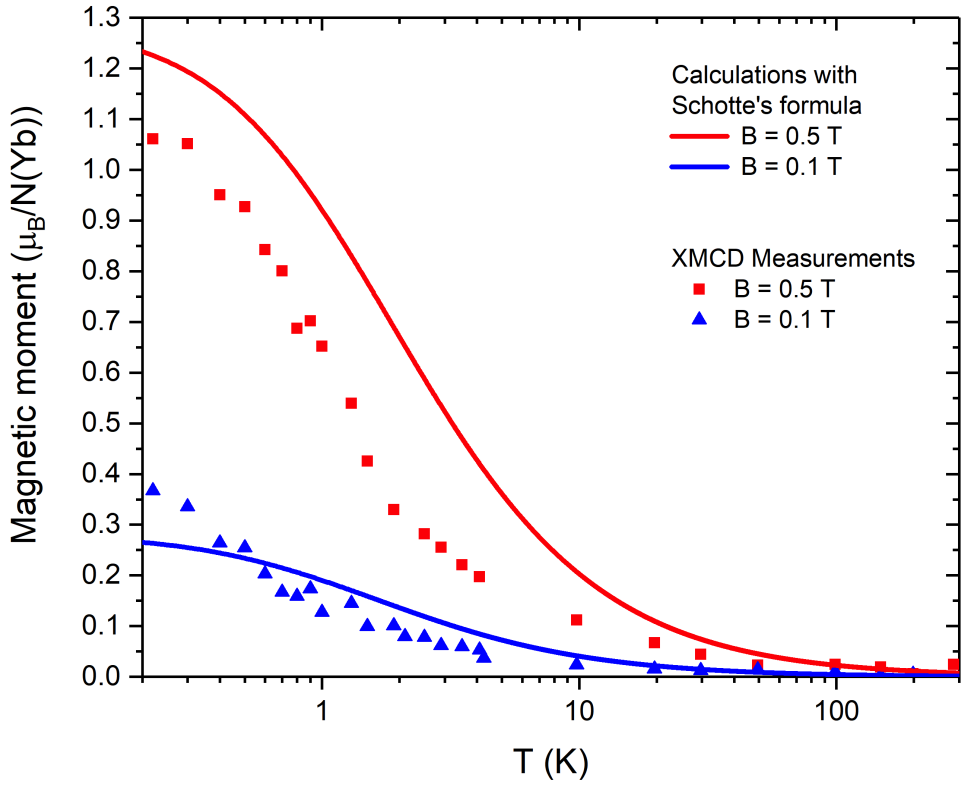

Figure 6.13: Yb magnetic moment (solid lines) calculated with (Eq.6.26) describing the Kondo interaction in spherical symmetry and experimental magnetic moments (dots) as a function of temperature for $B = 0.5\,\mathrm{T}$ and $B = 0.1\,\mathrm{T}$.

we arrive at the limit of the appearance of the Kondo interaction and for $B = 6.5\,\mathrm{T}$, the Kondo singlet is destroyed so that Schotte and Schotte's model (Eq.6.26) is no more valid.

It is interesting to compare this simulation where the Kondo effect has been considered to the calculations shown in Figure 6.12 where there is no Kondo effect but the cubic crystal field is present. The Kondo effect is well presented for the weak magnetic field. However, a more accurate calculation model should include all effects: crystal filed, Zeeman effect and Kondo effect. In the absence of such a model where Kondo interaction and crystal field are both present, the Kondo temperature of $T_K = 0.7\,\mathrm{K}$ is only a fitting parameter.

6.5.2 XMLD spectra

In the present section, we propose to deduce the XMLD spectra. From the discussion in Section 3.6, we can calculate the XMLD spectra from the XAS measurements of σ^+, σ^- and σ^0. From literature, one estimates that the amplitude of the XMLD signals are quite small, usually smaller than the intensity of XMCD. As a consequence, we

only consider the XMLD signals for $B = \pm 6.5\,\mathrm{T}$ that is the largest (in absolute value), external magnetic inductions available on DEIMOS. Hence, the XMLD measurements were recorded for temperatures ranging between 0.5 K and 200 K, in an external magnetic induction of 6.5 T. Figure 6.14 shows an example of how to calculate the XMLD spectra at $T = 0.5\,\mathrm{K}$ and the XMLD spectra at other temperatures are shown in Figure 6.15.

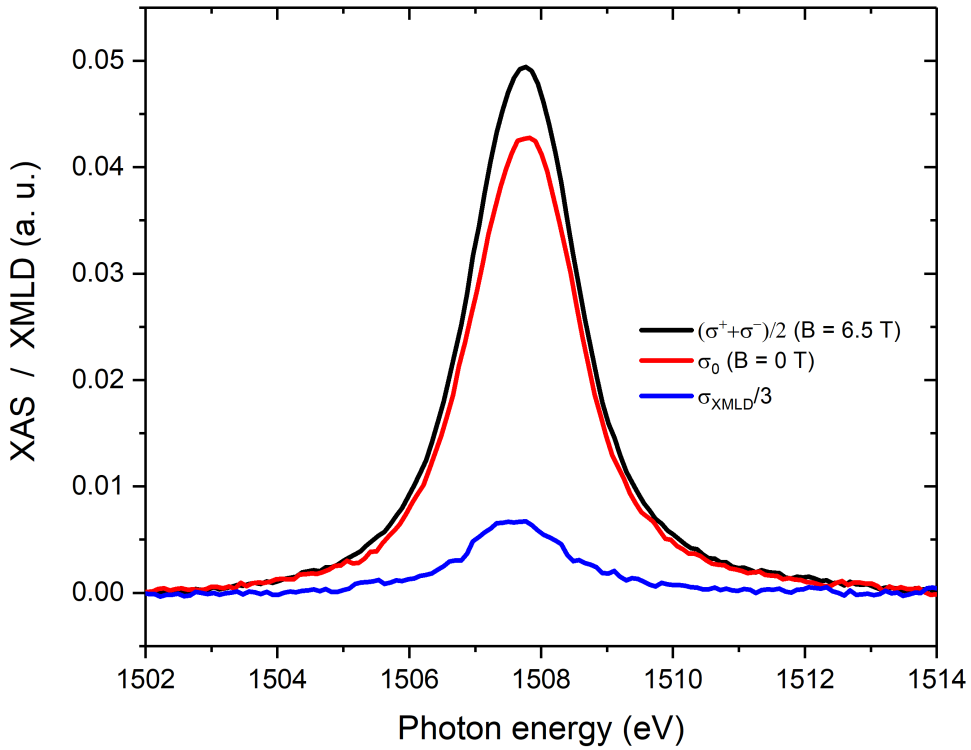

Figure 6.14: Experimental Yb^{3+}-M_5 XAS and XMLD spectra at 0.5 K. The black spectrum is the average of the two phases σ^+ and σ^- and the isotropic (red) spectrum is recorded without magnetic field. The blue spectrum is the difference between the black and the red spectra applying (Eq.5.11). It is one third of the XMLD signal.

We see from Figure 6.15 that when $T > 20\,\mathrm{K}$, the amplitude is experimentally zero, *i.e.* smaller than the experimental noise. Qualitatively, we see that the amplitude does not change for the spectra recorded at $T < 2.5\,\mathrm{K}$ which agrees with the calculations presented in Figure 6.6.

We calculate the variation of the amplitude of the experimental XMLD signal and compare with calculations. I first wrote

$$\sigma_{\mathrm{XMLD}}(T) = \frac{a(T)}{a(0.5\,\mathrm{K})}\,\sigma_{\mathrm{XMLD}}(0.5\,\mathrm{K}), \tag{6.29}$$

and obtained a distribution of $a(T)$ as a function of temperature. By definition, we set

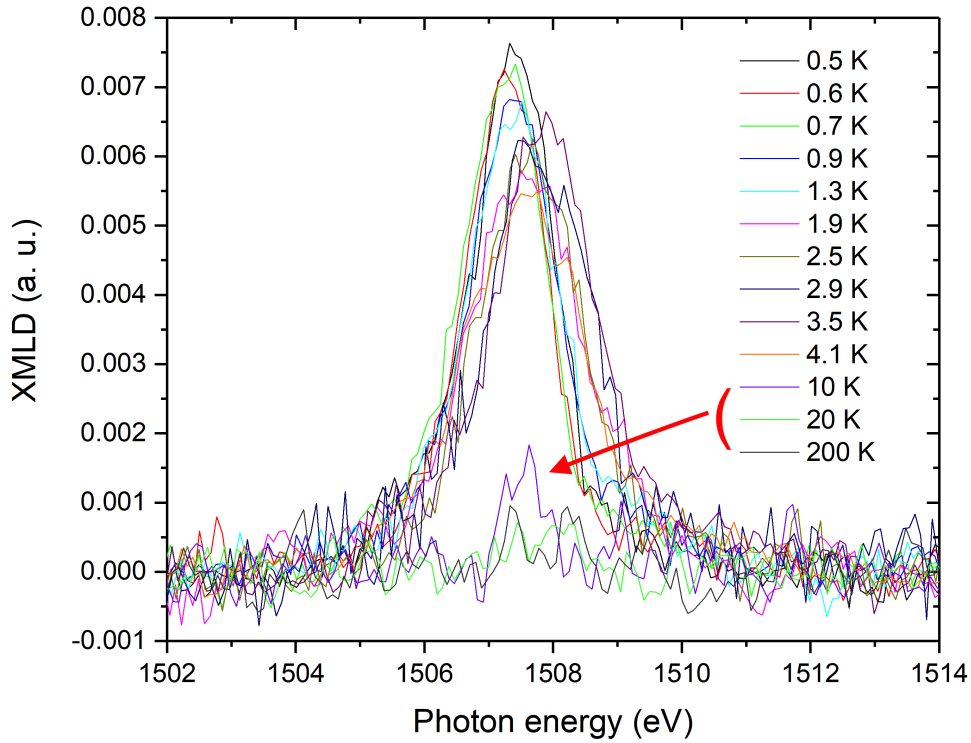

Figure 6.15: Experimental Yb^{3+}-M_5 XMLD spectra from 0.5 K to 200 K.

$a(0.5\,\mathrm{K}) \approx 0.33$, so that it corresponds to the value determined from Figure 6.6. There are two regimes: at low temperatures, the intensity of the XMLD signals is almost constant and at high temperature is also constant close to zero. The black, solid, square dots in Figure 6.16 report the variation of the XMLD signals between 0.5 K and 200 K. The red curve in Figure 6.16 is the general trend for $\frac{1}{2}\left(J(J+1) - 3\left\langle J_z^2 \right\rangle\right)$ that had been calculated in Figure 6.6.

6.6 Conclusion

We have performed a detailed experimental study of the variations of the XMCD and XMLD signals in a $Yb_{0.005}Au_{0.995}$ polycrystalline sample. From the application of the orbital magneto-optical sum rule coupled to the Wigner-Eckart theorem, we have determined the variation of the spin and orbit magnetic moments of Yb^{3+} ions as a function of an external magnetic field B and temperature T.

Compared to the analysis of the variation fo the magnetic moment done for the $Er_{0.025}Pd_{0.975}$ sample, differences between the calculations with crystal field only parameters and the measurements have been observed for $T \leq 1\,\mathrm{K}$ and for weak magnetic fields (*i.e.* $B = 0.1\,\mathrm{T}$ and $B = 0.5\,\mathrm{T}$. Note that the calculations (see Section 6.2.1) are done with the only consideration of the cubic crystal field and Zeeman interac-

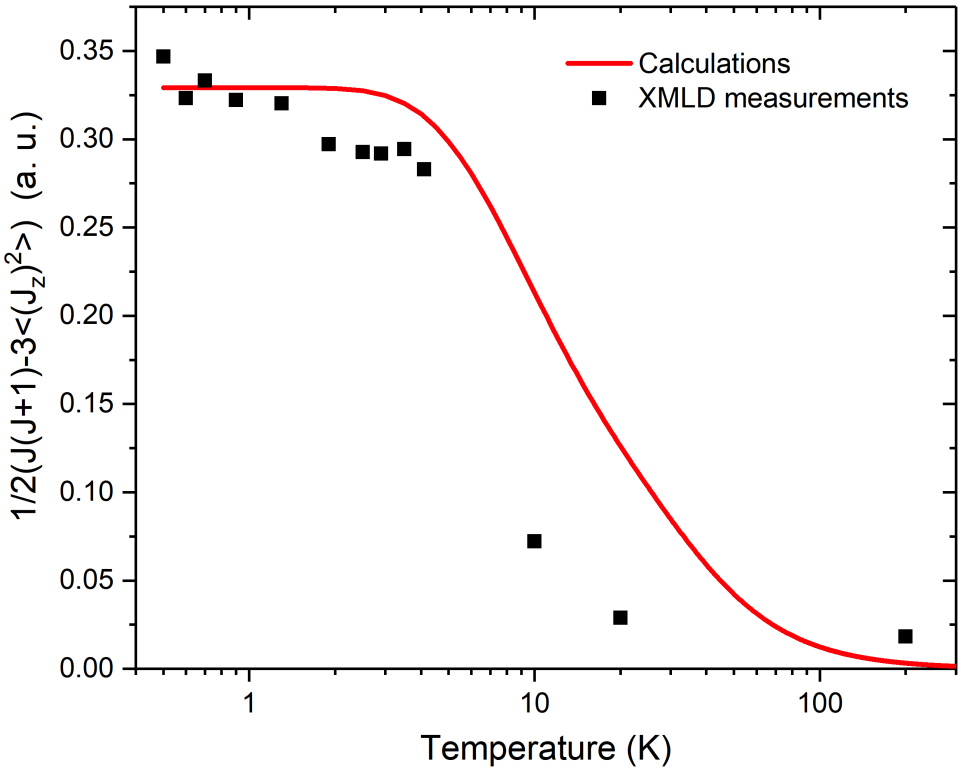

Figure 6.16: Amplitudes of the experimental XMLD signals (black, square dots) and variation of $\frac{1}{2}\left(J(J+1)-3\left\langle J_z^2\right\rangle\right)$ (solid, red line) as a function of temperature.

tion, so that the Kondo interaction is not considered. We ascribe the difference to the Kondo screening. We have also applied the model developed by Schotte and Schotte and found that for small magnetic fields, the model describes well the Kondo singlet.

The analysis of the experimental XMLD shows that XMLD signals follow roughly the calculated $\left\langle J_z^2\right\rangle$ values when the external induction is as large as 6.5 T.

Chapter 7

Conclusions and Perspectives

In this thesis, we investigated two diluted intermetallic systems: one is a non-Kondo system, $Er_{0.025}Pd_{0.975}$, and another is a Kondo system, $Yb_{0.005}Pd_{0.995}$. In a general way, we see the power of XAS-XMCD: We probed the local magnetic moment of the absorbing atom in a macroscopic way (The size of the beam is either $80\,\mu m \times 80\,\mu m$ or $800\,\mu m \times 800\,\mu m$). The application of the sum rules gives without ambiguity the spin magnetic moment and the orbital magnetic moment. With this analysis, the Kondo signature is well presented by XMCD measurements.

$Er_{0.025}Pd_{0.975}$ alloy

For the $Er_{0.025}Pd_{0.975}$ alloy, we proposed a possible way for the research of the crystal field parameters, by combing the magnetization and XMLD variation as a function of temperature and the ligand field multiplet calculation with consideration of crystal field splitting and Zeeman splitting. By varying only the crystal field parameters in the ligand field calculation, the best fit of the curves gives the most probable crystal field parameters. We found that the crystal field parameters are $B_{40} = 11.3\,\text{meV}$, $B_{60} = -3\,\text{meV}$ which is different from the values presented in a previous investigation based on neutron spectroscopy [132]. The calculations were performed with the Crispy interface of the QUANTY LFM code. In fact, an almost analytic calculations is possible, though difficult, since the 16-fold eigenfunctions of Er^{3+} have been tabulated [116] but parametrized by the unknowns relative separations between Γ_6, Γ_7 and Γ_8. As a conclusion, the calculations nicely reproduce the experimental magnetization curves (Figure 7.1-Left). It should be noticed that in this case, no Kondo interaction is expected.

Interestingly, a further work could be the measurements of the Pd-$L_{2,3}$ edges in ErPd that would give directly the magnetic polarization of palladium that could be compared to what has been found from XAS, XMCD and SQUID measurements. The application of this idea to samples with different erbium concentrations (for instance

$Er_{0.015}Pd_{0.985}$ or $Er_{0.005}Pd_{0.995}$) would be highly informative since it could correlate the Er magnetic moment and the induced Pd magnetic moments to the building of Er-Er pairs.

$Yb_{0.005}Au_{0.995}$ alloy

For the $Yb_{0.005}Au_{0.995}$ alloy, the 8-fold eigenfunctions [116] of Yb^{3+} are much easier to handle than the 16 eigenfunctions for Er^{3+}. A special care has to be brought to changing the orientation of the magnetic induction with respect to the cubic crystallographic axes (See Section A.2). For a powder with cubic symmetry, the spin and orbit magnetic moments as well as the averaged value of $\langle J_z^2 \rangle$ are given by the weighted sum of contributions when $\boldsymbol{B}$ is along the C_2, C_3 and C_4 symmetry axes (*i.e.* the [110], [111], and [100] directions) of the multiple cubic cell (See Ayant formula in (Eq.4.39)).

We observe a different behavior (Figure 7.1-Right) from that of ErPd alloy for the magnetization curves: the atomic model with no Kondo interactions fails to reproduce the experimental data for $B = 0.5\,\mathrm{T}$ and $B = 0.1\,\mathrm{T}$ when $T < 0.5\,\mathrm{T}$ and this suggests that a Kondo singlet has formed so that the ytterbium magnetic moment is partially screened. Note that for high temperature (*i.e.* $T \geq 10\,\mathrm{K}$) or for a large external magnetic induction, such as $B = 6.5\,\mathrm{T}$, the calculations nicely follow the measurements. In these cases, the Kondo singlet is destroyed by thermal fluctuations or by the magnetic field.

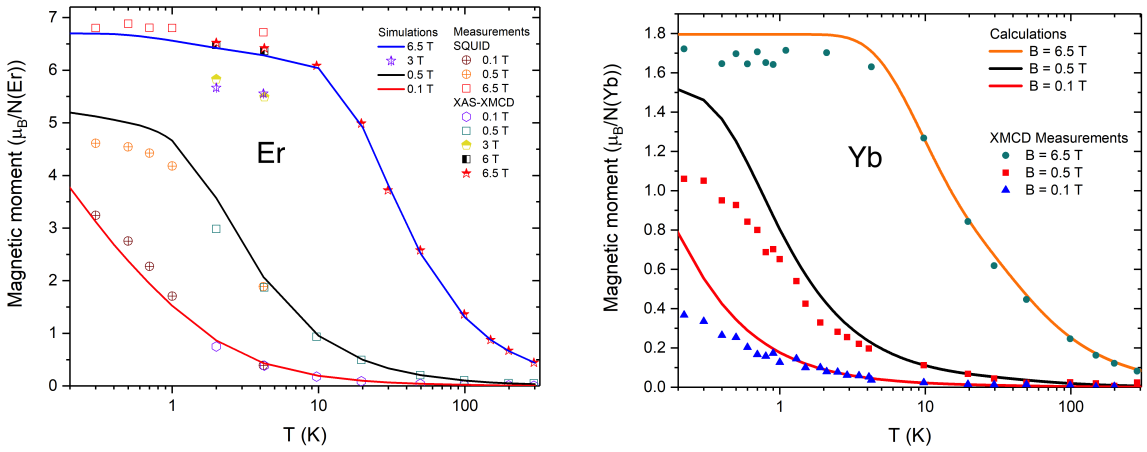

Figure 7.1: The comparison of a non-Kondo $Er_{0.025}Pd_{0.975}$ alloy and a Kondo system, the $Yb_{0.005}Au_{0.995}$ alloy. (Left) Reproduction of Figure 5.14. Experimental and calculated variations of the magnetic moment of Er^{3+} ion as a function of temperature. (Right) Reproduction of Figure 6.12. Experimental and calculated variations of the magnetic moment of Yb^{3+} ion as a function of temperature.

By applying the Schotte & Schotte formula in (Eq.6.26), the Kondo temperature $T_K = 0.7\,\mathrm{K}$ has been determined (Figure 6.13). Following Costi's paper, the critical

magnetic field $|B| \sim k_B T_K/(2g_J\mu_B)$ [60] that kills the Kondo resonance is in between $B = 0.5\,\mathrm{T}$ and $B = 6.5\,\mathrm{T}$.

Although the XMLD signals of Yb^{3+} are quite weak, we succeeded in recording the variation of $\langle J_z^2 \rangle$ in Figure 6.16 and in fitting these data in a LFM model.

The first interesting further work for the YbAu alloy is an extension of the calculations I made for this thesis: Figure 7.1-Right takes into account the crystal field and the Zeeman effect in the absence of Kondo interaction while Figure 6.13 takes into account the Kondo interaction and the Zeeman effect but in spherical symmetry (*i.e.* with no crystal field). A more accurate calculation model should take into account the three kinds of interactions (crystal field, Zeeman and Kondo interactions) and this is no doubt a rather easy and necessary development.

The second further work might be the measure of samples with various concentrations (*e.g.* $Yb_{0.0025}Au_{0.9975}$). By applying Schotte & Schotte formula (Eq.6.26) or a better descriptive model as described above, we might get an estimation of the variation of the Kondo temperature with the ytterbium concentration.

Cryogenics instrumentation

Progress on DEIMOS beamline never stops. Although DICHRO50 was one of the most advanced devices on synchrotron, we decided to break the record and a new projet called DryDichro50 is planned where a cryo-free 7 T magnet with UHV sample environment is housing a variable temperature insert consisting of a top removable dilution fridge with vertical translation and rotation degrees of freedom along the vertical axis. The most expensive part of the running costs is the price for liquid helium. Although helium is recovered, there are inevitable losses when filling the CroMag tank from a Dewar. The new project would be a cryo-free solution where the cooling is provided by cryocoolers with no need for external cryogenic liquids. In this new set up, the temperature on the sample mounted on the VTI would go down to 50 mK.

Appendix A

Calculations of Yb^{3+} Ion

The fundamental state of Yb^{3+} is ${}^2F_{7/2}$. The eigenfunctions are given by [116]:

$$
\begin{aligned}
\Gamma_7 = & \quad |\Gamma_7^+\rangle = \tfrac{\sqrt{3}}{2}\,|+\tfrac{5}{2}\rangle - \tfrac{1}{2}\,|-\tfrac{3}{2}\rangle\,, \\
& \quad |\Gamma_7^-\rangle = \tfrac{\sqrt{3}}{2}\,|-\tfrac{5}{2}\rangle - \tfrac{1}{2}\,|+\tfrac{3}{2}\rangle\,; \\
\\
\Gamma_8 = & \quad |\Gamma_{8,1}^+\rangle = \sqrt{\tfrac{7}{12}}\,|+\tfrac{7}{2}\rangle - \sqrt{\tfrac{5}{12}}\,|-\tfrac{1}{2}\rangle\,, \\
& \quad |\Gamma_{8,1}^-\rangle = \sqrt{\tfrac{7}{12}}\,|-\tfrac{7}{2}\rangle - \sqrt{\tfrac{5}{12}}\,|+\tfrac{1}{2}\rangle\,; \\
& \quad |\Gamma_{8,2}^+\rangle = \tfrac{1}{2}\,|-\tfrac{5}{2}\rangle + \tfrac{\sqrt{3}}{2}\,|+\tfrac{3}{2}\rangle\,; \\
& \quad |\Gamma_{8,2}^-\rangle = \tfrac{1}{2}\,|+\tfrac{5}{2}\rangle + \tfrac{\sqrt{3}}{2}\,|-\tfrac{3}{2}\rangle\,; \\
\\
\Gamma_6 = & \quad |\Gamma_6^+\rangle = \sqrt{\tfrac{5}{12}}\,|+\tfrac{7}{2}\rangle + \sqrt{\tfrac{7}{12}}\,|-\tfrac{1}{2}\rangle\,, \\
& \quad |\Gamma_6^-\rangle = \sqrt{\tfrac{5}{12}}\,|-\tfrac{7}{2}\rangle + \sqrt{\tfrac{7}{12}}\,|+\tfrac{1}{2}\rangle\,.
\end{aligned}
\tag{A.1}
$$

A.1 Crystal field calculations

The operator J_z acting on the states A.1 above gives

$$
\begin{aligned}
J_z\left|\Gamma_7^+\right\rangle &= \tfrac{5\sqrt{3}}{4}\hbar\left|+\tfrac{5}{2}\right\rangle + \tfrac{3}{4}\hbar\left|-\tfrac{3}{2}\right\rangle, \\
J_z\left|\Gamma_7^-\right\rangle &= -\tfrac{5\sqrt{3}}{4}\hbar\left|-\tfrac{5}{2}\right\rangle - \tfrac{3}{4}\hbar\left|+\tfrac{3}{2}\right\rangle;
\end{aligned}
$$

$$
\begin{aligned}
J_z\left|\Gamma_{8,1}^+\right\rangle &= \tfrac{7}{2}\sqrt{\tfrac{7}{12}}\hbar\left|+\tfrac{7}{2}\right\rangle + \tfrac{1}{2}\sqrt{\tfrac{5}{12}}\hbar\left|-\tfrac{1}{2}\right\rangle, \\
J_z\left|\Gamma_{8,1}^-\right\rangle &= -\tfrac{7}{2}\sqrt{\tfrac{7}{12}}\hbar\left|-\tfrac{7}{2}\right\rangle - \tfrac{1}{2}\sqrt{\tfrac{5}{12}}\hbar\left|+\tfrac{1}{2}\right\rangle; \\
J_z\left|\Gamma_{8,2}^+\right\rangle &= -\tfrac{5}{4}\hbar\left|-\tfrac{5}{2}\right\rangle + \tfrac{3\sqrt{3}}{4}\hbar\left|+\tfrac{3}{2}\right\rangle; \\
J_z\left|\Gamma_{8,2}^-\right\rangle &= \tfrac{5}{4}\hbar\left|+\tfrac{5}{2}\right\rangle - \tfrac{3\sqrt{3}}{4}\hbar\left|-\tfrac{3}{2}\right\rangle;
\end{aligned}
$$

$$
\begin{aligned}
J_z\left|\Gamma_6^+\right\rangle &= \tfrac{7}{2}\sqrt{\tfrac{5}{12}}\hbar\left|+\tfrac{7}{2}\right\rangle - \tfrac{1}{2}\sqrt{\tfrac{7}{12}}\hbar\left|-\tfrac{1}{2}\right\rangle, \\
J_z\left|\Gamma_6^-\right\rangle &= -\tfrac{7}{2}\sqrt{\tfrac{5}{12}}\hbar\left|-\tfrac{7}{2}\right\rangle + \tfrac{1}{2}\sqrt{\tfrac{7}{12}}\hbar\left|+\tfrac{1}{2}\right\rangle.
\end{aligned}
\tag{A.2}
$$

With (Eq.A.1) and (Eq.A.2), we calculate the average value of $\left\langle \Gamma_i^\sigma \middle| J_z \middle| \Gamma_{i'}^{\sigma'} \right\rangle$ where i and i' are index of 6, 7, 8.1 or 8.2. σ and σ' are sign indicators. The results can be written in the matrix form:

$$
\left\langle \Gamma_i^\sigma \middle| J_z \middle| \Gamma_{i'}^{\sigma'} \right\rangle =
$$

$$
\begin{array}{c}
 \\
\langle\Gamma_7^+| \\
\langle\Gamma_7^-| \\
\langle\Gamma_{8,1}^+| \\
\langle\Gamma_{8,1}^-| \\
\langle\Gamma_{8,2}^+| \\
\langle\Gamma_{8,2}^-| \\
\langle\Gamma_6^+| \\
\langle\Gamma_6^-|
\end{array}
\begin{array}{c}
\begin{array}{cccccccc}
|\Gamma_7^+\rangle & |\Gamma_7^-\rangle & |\Gamma_{8,1}^+\rangle & |\Gamma_{8,1}^-\rangle & |\Gamma_{8,2}^+\rangle & |\Gamma_{8,2}^-\rangle & |\Gamma_6^+\rangle & |\Gamma_6^-\rangle
\end{array} \\
\begin{pmatrix}
\frac{3}{2}\hbar & 0 & 0 & 0 & 0 & \sqrt{3}\hbar & 0 & 0 \\
0 & -\frac{3}{2}\hbar & 0 & 0 & -\sqrt{3}\hbar & 0 & 0 & 0 \\
0 & 0 & \frac{11}{6}\hbar & 0 & 0 & 0 & \frac{\sqrt{35}}{3}\hbar & 0 \\
0 & 0 & 0 & -\frac{11}{6}\hbar & 0 & 0 & 0 & -\frac{\sqrt{35}}{3}\hbar \\
0 & -\sqrt{3}\hbar & 0 & 0 & \frac{1}{2}\hbar & 0 & 0 & 0 \\
\sqrt{3}\hbar & 0 & 0 & 0 & 0 & -\frac{1}{2}\hbar & 0 & 0 \\
0 & 0 & \frac{\sqrt{35}}{3}\hbar & 0 & 0 & 0 & \frac{7}{6}\hbar & 0 \\
0 & 0 & 0 & -\frac{\sqrt{35}}{3}\hbar & 0 & 0 & 0 & -\frac{7}{6}\hbar
\end{pmatrix}
\end{array}
\tag{A.3}
$$

Note that the basis $|\Gamma_7^+\rangle$, ... , $|\Gamma_6^-\rangle$ are not the orthonormal basis but are the combination of the orthonomal basis $|-\frac{7}{2}\rangle$, ..., $|\frac{7}{2}\rangle$. We can apply (Eq.4.26) and (Eq.4.27) to the orthonomal basis$|-\frac{7}{2}\rangle$, ..., $|\frac{7}{2}\rangle$ and rewrite them in combination for the $|\Gamma_7^+\rangle$, ... , $|\Gamma_6^-\rangle$

basis. We obtain the matrix $\left\langle \Gamma_i^{\sigma} \middle| J_x \middle| \Gamma_{i'}^{\sigma'} \right\rangle$ and $\left\langle \Gamma_i^{\sigma} \middle| J_y \middle| \Gamma_{i'}^{\sigma'} \right\rangle$:

$$\left\langle \Gamma_i^{\sigma} \middle| J_x \middle| \Gamma_{i'}^{\sigma'} \right\rangle =$$

$$\begin{array}{c} \\ \langle\Gamma_7^+| \\ \langle\Gamma_7^-| \\ \langle\Gamma_{8,1}^+| \\ \langle\Gamma_{8,1}^-| \\ \langle\Gamma_{8,2}^+| \\ \langle\Gamma_{8,2}^-| \\ \langle\Gamma_6^+| \\ \langle\Gamma_6^-| \end{array} \begin{array}{c} \begin{array}{cccccccc} |\Gamma_7^+\rangle & |\Gamma_7^-\rangle & |\Gamma_{8,1}^+\rangle & |\Gamma_{8,1}^-\rangle & |\Gamma_{8,2}^+\rangle & |\Gamma_{8,2}^-\rangle & |\Gamma_6^+\rangle & |\Gamma_6^-\rangle \end{array} \\ \begin{pmatrix} 0 & -\frac{3}{2}\hbar & \frac{3}{2}\hbar & 0 & \frac{\sqrt{3}}{2}\hbar & 0 & 0 & 0 \\ -\frac{3}{2}\hbar & 0 & 0 & \frac{3}{2}\hbar & 0 & \frac{\sqrt{3}}{2}\hbar & 0 & 0 \\ \frac{3}{2}\hbar & 0 & 0 & \frac{5}{6}\hbar & 0 & -\frac{\sqrt{3}}{3}\hbar & 0 & -\frac{\sqrt{35}}{6}\hbar \\ 0 & \frac{3}{2}\hbar & \frac{5}{6}\hbar & 0 & -\frac{\sqrt{3}}{3}\hbar & 0 & -\frac{\sqrt{35}}{6}\hbar & 0 \\ \frac{\sqrt{3}}{2}\hbar & 0 & 0 & -\frac{\sqrt{3}}{3}\hbar & 0 & \frac{3}{2}\hbar & 0 & \frac{\sqrt{105}}{6}\hbar \\ 0 & \frac{\sqrt{3}}{2}\hbar & -\frac{\sqrt{3}}{3}\hbar & 0 & \frac{3}{2}\hbar & 0 & \frac{\sqrt{105}}{6}\hbar & 0 \\ 0 & 0 & 0 & -\frac{\sqrt{35}}{6}\hbar & 0 & \frac{\sqrt{105}}{6}\hbar & 0 & \frac{7}{6}\hbar \\ 0 & 0 & -\frac{\sqrt{35}}{6}\hbar & 0 & \frac{\sqrt{105}}{6}\hbar & 0 & \frac{7}{6}\hbar & 0 \end{pmatrix} \end{array} \tag{A.4}$$

and

$$\left\langle \Gamma_i^{\sigma} \middle| J_y \middle| \Gamma_{i'}^{\sigma'} \right\rangle =$$

$$\begin{array}{c} \\ \langle\Gamma_7^+| \\ \langle\Gamma_7^-| \\ \langle\Gamma_{8,1}^+| \\ \langle\Gamma_{8,1}^-| \\ \langle\Gamma_{8,2}^+| \\ \langle\Gamma_{8,2}^-| \\ \langle\Gamma_6^+| \\ \langle\Gamma_6^-| \end{array} \begin{array}{c} \begin{array}{cccccccc} |\Gamma_7^+\rangle & |\Gamma_7^-\rangle & |\Gamma_{8,1}^+\rangle & |\Gamma_{8,1}^-\rangle & |\Gamma_{8,2}^+\rangle & |\Gamma_{8,2}^-\rangle & |\Gamma_6^+\rangle & |\Gamma_6^-\rangle \end{array} \\ \begin{pmatrix} 0 & \frac{3}{2}i\hbar & \frac{3}{2}i\hbar & 0 & -\frac{\sqrt{3}}{2}i\hbar & 0 & 0 & 0 \\ -\frac{3}{2}i\hbar & 0 & 0 & -\frac{3}{2}i\hbar & 0 & \frac{\sqrt{3}}{2}i\hbar & 0 & 0 \\ -\frac{3}{2}i\hbar & 0 & 0 & \frac{5}{6}i\hbar & 0 & \frac{\sqrt{3}}{3}i\hbar & 0 & -\frac{\sqrt{35}}{6}i\hbar \\ 0 & \frac{3}{2}i\hbar & -\frac{5}{6}i\hbar & 0 & -\frac{\sqrt{3}}{3}i\hbar & 0 & \frac{\sqrt{35}}{6}i\hbar & 0 \\ \frac{\sqrt{3}}{2}i\hbar & 0 & 0 & \frac{\sqrt{3}}{3}i\hbar & 0 & \frac{3}{2}i\hbar & 0 & -\frac{\sqrt{105}}{6}i\hbar \\ 0 & -\frac{\sqrt{3}}{2}i\hbar & -\frac{\sqrt{3}}{3}i\hbar & 0 & -\frac{3}{2}i\hbar & 0 & \frac{\sqrt{105}}{6}i\hbar & 0 \\ 0 & 0 & 0 & -\frac{\sqrt{35}}{6}i\hbar & 0 & -\frac{\sqrt{105}}{6}i\hbar & 0 & \frac{7}{6}i\hbar \\ 0 & 0 & \frac{\sqrt{35}}{6}i\hbar & 0 & \frac{\sqrt{105}}{6}i\hbar & 0 & -\frac{7}{6}i\hbar & 0 \end{pmatrix} \end{array} \tag{A.5}$$

With the definition of J_{zp}, $J_{zp\_C_2}$, $J_{zp\_C_3}$ and $J_{zp\_C_4}$ by (Eq.4.29) and (Eq.4.30), we can

write the matrix elements

$$\left\langle \Gamma_i^{\sigma} \middle| J_{zp\_C_2} \middle| \Gamma_{i'}^{\sigma'} \right\rangle =$$

$$\begin{array}{c} \\ \langle\Gamma_7^+| \\ \langle\Gamma_7^-| \\ \langle\Gamma_{8,1}^+| \\ \langle\Gamma_{8,1}^-| \\ \langle\Gamma_{8,2}^+| \\ \langle\Gamma_{8,2}^-| \\ \langle\Gamma_6^+| \\ \langle\Gamma_6^-| \end{array} \begin{array}{c} \begin{array}{cccccccc} |\Gamma_7^+\rangle & |\Gamma_7^-\rangle & |\Gamma_{8,1}^+\rangle & |\Gamma_{8,1}^-\rangle & |\Gamma_{8,2}^+\rangle & |\Gamma_{8,2}^-\rangle & |\Gamma_6^+\rangle & |\Gamma_6^-\rangle \end{array} \\ \begin{pmatrix} 0 & -\frac{\left(\frac{3}{2}-\frac{3i}{2}\right)\hbar}{\sqrt{2}} & \frac{\left(\frac{3}{2}+\frac{3i}{2}\right)\hbar}{\sqrt{2}} & 0 & \left(\frac{1}{2}-\frac{i}{2}\right)\sqrt{\frac{3}{2}}\hbar & 0 & 0 & 0 \\ -\frac{\left(\frac{3}{2}+\frac{3i}{2}\right)\hbar}{\sqrt{2}} & 0 & 0 & \frac{\left(\frac{3}{2}-\frac{3i}{2}\right)\hbar}{\sqrt{2}} & 0 & \left(\frac{1}{2}+\frac{i}{2}\right)\sqrt{\frac{3}{2}}\hbar & 0 & 0 \\ \frac{\left(\frac{3}{2}-\frac{3i}{2}\right)\hbar}{\sqrt{2}} & 0 & 0 & \frac{\left(\frac{5}{6}+\frac{5i}{6}\right)\hbar}{\sqrt{2}} & 0 & -\frac{(1-i)\hbar}{\sqrt{6}} & 0 & \left(-\frac{1}{6}-\frac{i}{6}\right)\sqrt{\frac{35}{2}}\hbar \\ 0 & \frac{\left(\frac{3}{2}+\frac{3i}{2}\right)\hbar}{\sqrt{2}} & \frac{\left(\frac{5}{6}-\frac{5i}{6}\right)\hbar}{\sqrt{2}} & 0 & -\frac{(1+i)\hbar}{\sqrt{6}} & 0 & \left(-\frac{1}{6}+\frac{i}{6}\right)\sqrt{\frac{35}{2}}\hbar & 0 \\ \left(\frac{1}{2}+\frac{i}{2}\right)\sqrt{\frac{3}{2}}\hbar & 0 & 0 & -\frac{(1-i)\hbar}{\sqrt{6}} & 0 & \frac{\left(\frac{3}{2}+\frac{3i}{2}\right)\hbar}{\sqrt{2}} & 0 & \left(\frac{1}{2}-\frac{i}{2}\right)\sqrt{\frac{35}{6}}\hbar \\ 0 & \left(\frac{1}{2}-\frac{i}{2}\right)\sqrt{\frac{3}{2}}\hbar & -\frac{(1+i)\hbar}{\sqrt{6}} & 0 & \frac{\left(\frac{3}{2}-\frac{3i}{2}\right)\hbar}{\sqrt{2}} & 0 & \left(\frac{1}{2}+\frac{i}{2}\right)\sqrt{\frac{35}{6}}\hbar & 0 \\ 0 & 0 & 0 & \left(-\frac{1}{6}-\frac{i}{6}\right)\sqrt{\frac{35}{2}}\hbar & 0 & \left(\frac{1}{2}-\frac{i}{2}\right)\sqrt{\frac{35}{6}}\hbar & 0 & \frac{\left(\frac{7}{6}+\frac{7i}{6}\right)\hbar}{\sqrt{2}} \\ 0 & 0 & \left(-\frac{1}{6}+\frac{i}{6}\right)\sqrt{\frac{35}{2}}\hbar & 0 & \left(\frac{1}{2}+\frac{i}{2}\right)\sqrt{\frac{35}{6}}\hbar & 0 & \frac{\left(\frac{7}{6}-\frac{7i}{6}\right)\hbar}{\sqrt{2}} & 0 \end{pmatrix} \end{array} \tag{A.6}$$

$$\left\langle \Gamma_i^{\sigma} \middle| J_{zp\_C_3} \middle| \Gamma_{i'}^{\sigma'} \right\rangle =$$

$$\begin{array}{c} \\ \langle\Gamma_7^+| \\ \langle\Gamma_7^-| \\ \langle\Gamma_{8,1}^+| \\ \langle\Gamma_{8,1}^-| \\ \langle\Gamma_{8,2}^+| \\ \langle\Gamma_{8,2}^-| \\ \langle\Gamma_6^+| \\ \langle\Gamma_6^-| \end{array} \begin{array}{c} \begin{array}{cccccccc} |\Gamma_7^+\rangle & |\Gamma_7^-\rangle & |\Gamma_{8,1}^+\rangle & |\Gamma_{8,1}^-\rangle & |\Gamma_{8,2}^+\rangle & |\Gamma_{8,2}^-\rangle & |\Gamma_6^+\rangle & |\Gamma_6^-\rangle \end{array} \\ \begin{pmatrix} \frac{\sqrt{3}\hbar}{2} & \left(-\frac{1}{2}+\frac{i}{2}\right)\sqrt{3}\hbar & \left(\frac{1}{2}+\frac{i}{2}\right)\sqrt{3}\hbar & 0 & \left(\frac{1}{2}-\frac{i}{2}\right)\hbar & \hbar & 0 & 0 \\ \left(-\frac{1}{2}-\frac{i}{2}\right)\sqrt{3}\hbar & -\frac{\sqrt{3}\hbar}{2} & 0 & \left(\frac{1}{2}-\frac{i}{2}\right)\sqrt{3}\hbar & -\hbar & \left(\frac{1}{2}+\frac{i}{2}\right)\hbar & 0 & 0 \\ \left(\frac{1}{2}-\frac{i}{2}\right)\sqrt{3}\hbar & 0 & \frac{11\hbar}{6\sqrt{3}} & \frac{\left(\frac{5}{6}+\frac{5i}{6}\right)\hbar}{\sqrt{3}} & 0 & \left(-\frac{1}{3}+\frac{i}{3}\right)\hbar & \frac{1}{3}\sqrt{\frac{35}{3}}\hbar & \left(-\frac{1}{6}-\frac{i}{6}\right)\sqrt{\frac{35}{3}}\hbar \\ 0 & \left(\frac{1}{2}+\frac{i}{2}\right)\sqrt{3}\hbar & \frac{\left(\frac{5}{6}-\frac{5i}{6}\right)\hbar}{\sqrt{3}} & -\frac{11\hbar}{6\sqrt{3}} & \left(-\frac{1}{3}-\frac{i}{3}\right)\hbar & 0 & \left(-\frac{1}{6}+\frac{i}{6}\right)\sqrt{\frac{35}{3}}\hbar & -\frac{1}{3}\sqrt{\frac{35}{3}}\hbar \\ \left(\frac{1}{2}+\frac{i}{2}\right)\hbar & -\hbar & 0 & \left(-\frac{1}{3}+\frac{i}{3}\right)\hbar & \frac{\hbar}{2\sqrt{3}} & \left(\frac{1}{2}+\frac{i}{2}\right)\sqrt{3}\hbar & 0 & \left(\frac{1}{6}-\frac{i}{6}\right)\sqrt{35}\hbar \\ \hbar & \left(\frac{1}{2}-\frac{i}{2}\right)\hbar & \left(-\frac{1}{3}-\frac{i}{3}\right)\hbar & 0 & \left(\frac{1}{2}-\frac{i}{2}\right)\sqrt{3}\hbar & -\frac{\hbar}{2\sqrt{3}} & \left(\frac{1}{6}+\frac{i}{6}\right)\sqrt{35}\hbar & 0 \\ 0 & 0 & \frac{1}{3}\sqrt{\frac{35}{3}}\hbar & \left(-\frac{1}{6}-\frac{i}{6}\right)\sqrt{\frac{35}{3}}\hbar & 0 & \left(\frac{1}{6}-\frac{i}{6}\right)\sqrt{35}\hbar & \frac{7\hbar}{6\sqrt{3}} & \frac{\left(\frac{7}{6}+\frac{7i}{6}\right)\hbar}{\sqrt{3}} \\ 0 & 0 & \left(-\frac{1}{6}+\frac{i}{6}\right)\sqrt{\frac{35}{3}}\hbar & -\frac{1}{3}\sqrt{\frac{35}{3}}\hbar & \left(\frac{1}{6}+\frac{i}{6}\right)\sqrt{35}\hbar & 0 & \frac{\left(\frac{7}{6}-\frac{7i}{6}\right)\hbar}{\sqrt{3}} & -\frac{7\hbar}{6\sqrt{3}} \end{pmatrix} \end{array} \tag{A.7}$$

and

$$\left\langle \Gamma_i^{\sigma} \middle| J_{zp\_C_4} \middle| \Gamma_{i'}^{\sigma'} \right\rangle =$$

$$\begin{array}{c} \\ \langle\Gamma_7^+| \\ \langle\Gamma_7^-| \\ \langle\Gamma_{8,1}^+| \\ \langle\Gamma_{8,1}^-| \\ \langle\Gamma_{8,2}^+| \\ \langle\Gamma_{8,2}^-| \\ \langle\Gamma_6^+| \\ \langle\Gamma_6^-| \end{array} \begin{array}{c} \begin{array}{cccccccc} |\Gamma_7^+\rangle & |\Gamma_7^-\rangle & |\Gamma_{8,1}^+\rangle & |\Gamma_{8,1}^-\rangle & |\Gamma_{8,2}^+\rangle & |\Gamma_{8,2}^-\rangle & |\Gamma_6^+\rangle & |\Gamma_6^-\rangle \end{array} \\ \begin{pmatrix} \frac{3}{2}\hbar & 0 & 0 & 0 & 0 & \sqrt{3}\hbar & 0 & 0 \\ 0 & -\frac{3}{2}\hbar & 0 & 0 & -\sqrt{3}\hbar & 0 & 0 & 0 \\ 0 & 0 & \frac{11}{6}\hbar & 0 & 0 & 0 & \frac{\sqrt{35}}{3}\hbar & 0 \\ 0 & 0 & 0 & -\frac{11}{6}\hbar & 0 & 0 & 0 & -\frac{\sqrt{35}}{3}\hbar \\ 0 & -\sqrt{3}\hbar & 0 & 0 & \frac{1}{2}\hbar & 0 & 0 & 0 \\ \sqrt{3}\hbar & 0 & 0 & 0 & 0 & -\frac{1}{2}\hbar & 0 & 0 \\ 0 & 0 & \frac{\sqrt{35}}{3}\hbar & 0 & 0 & 0 & \frac{7}{6}\hbar & 0 \\ 0 & 0 & 0 & -\frac{\sqrt{35}}{3}\hbar & 0 & 0 & 0 & -\frac{7}{6}\hbar \end{pmatrix} \end{array} . \tag{A.8}$$

Now, let us try to write the Hamiltonian (Eq.4.4) or (Eq.4.6). To simplify the notation, we make $\hbar = 1$. For $J = 7/2$, by applying (Eq.4.5), we obtain

$$\begin{aligned}
J_z = \pm\tfrac{1}{2}, &\quad \left\langle \tfrac{1}{2}\middle|O_4^0\middle|\tfrac{1}{2}\right\rangle = \left\langle -\tfrac{1}{2}\middle|O_4^0\middle|-\tfrac{1}{2}\right\rangle = 540,\\
J_z = \pm\tfrac{3}{2}, &\quad \langle \tfrac{3}{2}|O_4^0|\tfrac{3}{2}\rangle = \langle -\tfrac{3}{2}|O_4^0|-\tfrac{3}{2}\rangle = -180,\\
J_z = \pm\tfrac{5}{2}, &\quad \langle \tfrac{5}{2}|O_4^0|\tfrac{5}{2}\rangle = \langle -\tfrac{5}{2}|O_4^0|-\tfrac{5}{2}\rangle = -780,\\
J_z = \pm\tfrac{7}{2}, &\quad \langle \tfrac{7}{2}|O_4^0|\tfrac{7}{2}\rangle = \langle -\tfrac{7}{2}|O_4^0|-\tfrac{7}{2}\rangle = 420;
\end{aligned} \tag{A.9}$$

$$\begin{aligned}
J_z = \pm\tfrac{1}{2}, &\quad \left\langle \tfrac{1}{2}\middle|O_6^0\middle|\tfrac{1}{2}\right\rangle = \left\langle -\tfrac{1}{2}\middle|O_6^0\middle|-\tfrac{1}{2}\right\rangle = -6300,\\
J_z = \pm\tfrac{3}{2}, &\quad \langle \tfrac{3}{2}|O_6^0|\tfrac{3}{2}\rangle = \langle -\tfrac{3}{2}|O_6^0|-\tfrac{3}{2}\rangle = 11340,\\
J_z = \pm\tfrac{5}{2}, &\quad \langle \tfrac{5}{2}|O_6^0|\tfrac{5}{2}\rangle = \langle -\tfrac{5}{2}|O_6^0|-\tfrac{5}{2}\rangle = -6300,\\
J_z = \pm\tfrac{7}{2}, &\quad \langle \tfrac{7}{2}|O_6^0|\tfrac{7}{2}\rangle = \langle -\tfrac{7}{2}|O_6^0|-\tfrac{7}{2}\rangle = 1260.
\end{aligned}$$

And also for $J = \frac{7}{2}$, we have the no vanishing matrix elements O_4^4 and O_6^4 [141]

$$\begin{aligned}
&\langle \tfrac{5}{2}|O_4^4|-\tfrac{3}{2}\rangle = \langle -\tfrac{5}{2}|O_4^4|\tfrac{3}{2}\rangle = \langle \tfrac{3}{2}|O_4^4|-\tfrac{5}{2}\rangle = \langle -\tfrac{3}{2}|O_4^4|\tfrac{5}{2}\rangle = 60\sqrt{3},\\
&\left\langle \tfrac{7}{2}\middle|O_4^4\middle|-\tfrac{1}{2}\right\rangle = \left\langle -\tfrac{7}{2}\middle|O_4^4\middle|\tfrac{1}{2}\right\rangle = \left\langle \tfrac{1}{2}\middle|O_4^4\middle|-\tfrac{7}{2}\right\rangle = \left\langle -\tfrac{1}{2}\middle|O_4^4\middle|\tfrac{7}{2}\right\rangle = 12\sqrt{35},\\
&\langle \tfrac{5}{2}|O_6^4|-\tfrac{3}{2}\rangle = \langle -\tfrac{5}{2}|O_6^4|\tfrac{3}{2}\rangle = \langle \tfrac{3}{2}|O_4^4|-\tfrac{5}{2}\rangle = \langle -\tfrac{3}{2}|O_4^4|\tfrac{5}{2}\rangle = -420\sqrt{3},\\
&\left\langle \tfrac{7}{2}\middle|O_6^4\middle|-\tfrac{1}{2}\right\rangle = \left\langle -\tfrac{7}{2}\middle|O_6^4\middle|\tfrac{1}{2}\right\rangle = \left\langle \tfrac{1}{2}\middle|O_4^4\middle|-\tfrac{7}{2}\right\rangle = \left\langle -\tfrac{1}{2}\middle|O_4^4\middle|\tfrac{7}{2}\right\rangle = 180\sqrt{35}.
\end{aligned} \tag{A.10}$$

We can easily check that the correspondence of the factor between (Eq.4.4) and (Eq.4.6) satisfies

$$B_4 = C_4\beta, \quad B_6 = C_6\gamma. \tag{A.11}$$

C_4, C_6 are given by [159]

$$C_4 = -30\,\mathrm{K}, \quad C_6 = 6\,\mathrm{K}, \tag{A.12}$$

And in the reference [115], these parameters are given by

$$C_4 = -27\,\mathrm{K} \pm 3\,\mathrm{K}, \quad C_6 = 4.5\,\mathrm{K} \pm 0.3\,\mathrm{K}. \tag{A.13}$$

β and γ are no dimensional parameters which are [116]

$$\beta = -1.7316 \times 10^{-3}, \quad \gamma = 1,48 \times 10^{-4}. \tag{A.14}$$

With (Eq.4.4), (Eq.4.5), (Eq.A.9) and (Eq.A.10), we can calculate each element of the

matrix $\left\langle \Gamma_i^{\sigma} \middle| H_c \middle| \Gamma_{i'}^{\sigma'} \right\rangle$. The calculations show that

$$\left\langle \Gamma_i^{\sigma} \middle| H_c \middle| \Gamma_{i'}^{\sigma'} \right\rangle =$$

$$\begin{array}{c} \\ \langle\Gamma_7^+| \\ \langle\Gamma_7^-| \\ \langle\Gamma_{8,1}^+| \\ \langle\Gamma_{8,1}^-| \\ \langle\Gamma_{8,2}^+| \\ \langle\Gamma_{8,2}^-| \\ \langle\Gamma_6^+| \\ \langle\Gamma_6^-| \end{array} \begin{array}{c} \begin{array}{cccccccc} |\Gamma_7^+\rangle & |\Gamma_7^-\rangle & |\Gamma_{8,1}^+\rangle & |\Gamma_{8,1}^-\rangle & |\Gamma_{8,2}^+\rangle & |\Gamma_{8,2}^-\rangle & |\Gamma_6^+\rangle & |\Gamma_6^-\rangle \end{array} \\ \begin{pmatrix} -1080C_4\beta - 15120C_6\gamma & 0 & 0 & 0 & 0 & 0 & 0 & 0 \\ 0 & -1080C_4\beta - 15120C_6\gamma & 0 & 0 & 0 & 0 & 0 & 0 \\ 0 & 0 & 120C_4\beta + 20160C_6\gamma & 0 & 0 & 0 & 0 & 0 \\ 0 & 0 & 0 & 120C_4\beta + 20160C_6\gamma & 0 & 0 & 0 & 0 \\ 0 & 0 & 0 & 0 & 120C_4\beta + 20160C_6\gamma & 0 & 0 & 0 \\ 0 & 0 & 0 & 0 & 0 & 120C_4\beta + 20160C_6\gamma & 0 & 0 \\ 0 & 0 & 0 & 0 & 0 & 0 & 840C_4\beta - 25200C_6\gamma & 0 \\ 0 & 0 & 0 & 0 & 0 & 0 & 0 & 840C_4\beta - 25200C_6\gamma \end{pmatrix} \end{array} \tag{A.15}$$

We take $C_4 = -30\,\mathrm{K}$ and $C_6 = 6\,\mathrm{K}$. By doing the numerical application with (Eq.A.14), the matrix (A.15) can be expressed in kelvin:

$$\left\langle \Gamma_i^{\sigma} \middle| H_c \middle| \Gamma_{i'}^{\sigma'} \right\rangle (\text{in K}) =$$

$$\begin{array}{c} \\ \langle\Gamma_7^+| \\ \langle\Gamma_7^-| \\ \langle\Gamma_{8,1}^+| \\ \langle\Gamma_{8,1}^-| \\ \langle\Gamma_{8,2}^+| \\ \langle\Gamma_{8,2}^-| \\ \langle\Gamma_6^+| \\ \langle\Gamma_6^-| \end{array} \begin{array}{c} \begin{array}{cccccccc} |\Gamma_7^+\rangle & |\Gamma_7^-\rangle & |\Gamma_{8,1}^+\rangle & |\Gamma_{8,1}^-\rangle & |\Gamma_{8,2}^+\rangle & |\Gamma_{8,2}^-\rangle & |\Gamma_6^+\rangle & |\Gamma_6^-\rangle \end{array} \\ \begin{pmatrix} -69.53 & 0 & 0 & 0 & 0 & 0 & 0 & 0 \\ 0 & -69.53 & 0 & 0 & 0 & 0 & 0 & 0 \\ 0 & 0 & 24.14 & 0 & 0 & 0 & 0 & 0 \\ 0 & 0 & 0 & 24.14 & 0 & 0 & 0 & 0 \\ 0 & 0 & 0 & 0 & 24.14 & 0 & 0 & 0 \\ 0 & 0 & 0 & 0 & 0 & 24.14 & 0 & 0 \\ 0 & 0 & 0 & 0 & 0 & 0 & 21.26 & 0 \\ 0 & 0 & 0 & 0 & 0 & 0 & 0 & 21.26 \end{pmatrix} \end{array}. \tag{A.16}$$

The diagonal matrix elements in (A.16) show that the energy of Γ_6 and Γ_8 is very close. The energy gap Δ_1 between Γ_7 and Γ_8 is 93.67 K and the energy gap Δ_2 between Γ_7 and Γ_6 is 90.79 K. The results are similar to the other measurements ($\Delta_1 = 80\,\mathrm{K}$, $\Delta_2 = 83\,\mathrm{K}$ [147] or $\Delta_1 = 94\,\mathrm{K}$, $\Delta_2 = 91\,\mathrm{K}$ [148] [149]).

A.2 $\langle J_z \rangle$ calculations

Now, let us focus on the Zeeman Hamiltonian. Supposing the the magnetic field is along the $\hat{z}$ direction. With the discussion in the part of Zeeman splitting, the elements of the matrix of the hamiltonian of Zeeman in the basis of $\left|\Gamma_i^{\sigma}\right\rangle$ can be calculated

explicitly by

$$\left\langle \Gamma_i^\sigma \middle| H_{Zee_{C_2}} \middle| \Gamma_{i'}^{\sigma'} \right\rangle = \left\langle \Gamma_i^\sigma \middle| \frac{\mu_B}{\hbar} J_{zp\_C_2} B \middle| \Gamma_{i'}^{\sigma'} \right\rangle = \frac{\mu_B}{\hbar} g_J B \left\langle \Gamma_i^\sigma \middle| J_{zp\_C_2} \middle| \Gamma_{i'}^{\sigma'} \right\rangle, \tag{A.17}$$

$$\left\langle \Gamma_i^\sigma \middle| H_{Zee_{C_3}} \middle| \Gamma_{i'}^{\sigma'} \right\rangle = \left\langle \Gamma_i^\sigma \middle| \frac{\mu_B}{\hbar} J_{zp\_C_3} B \middle| \Gamma_{i'}^{\sigma'} \right\rangle = \frac{\mu_B}{\hbar} g_J B \left\langle \Gamma_i^\sigma \middle| J_{zp\_C_3} \middle| \Gamma_{i'}^{\sigma'} \right\rangle, \tag{A.18}$$

$$\left\langle \Gamma_i^\sigma \middle| H_{Zee_{C_4}} \middle| \Gamma_{i'}^{\sigma'} \right\rangle = \left\langle \Gamma_i^\sigma \middle| \frac{\mu_B}{\hbar} J_{zp\_C_4} B \middle| \Gamma_{i'}^{\sigma'} \right\rangle = \frac{\mu_B}{\hbar} g_J B \left\langle \Gamma_i^\sigma \middle| J_{zp\_C_4} \middle| \Gamma_{i'}^{\sigma'} \right\rangle, \tag{A.19}$$

where the matrix elements is expressed explicitly in A.6, A.7 and A.8. $g_J = 8/7$ for $J = 7/2$.

By applying (Eq.4.33), we can obtain explicitly

$$\left\langle \Gamma_i^\sigma \middle| H_{C_2} \middle| \Gamma_{i'}^{\sigma'} \right\rangle = \left\langle \Gamma_i^\sigma \middle| H_c \middle| \Gamma_{i'}^{\sigma'} \right\rangle + \left\langle \Gamma_i^\sigma \middle| H_{Zee_{C_2}} \middle| \Gamma_{i'}^{\sigma'} \right\rangle, \tag{A.20}$$

$$\left\langle \Gamma_i^\sigma \middle| H_{C_3} \middle| \Gamma_{i'}^{\sigma'} \right\rangle = \left\langle \Gamma_i^\sigma \middle| H_c \middle| \Gamma_{i'}^{\sigma'} \right\rangle + \left\langle \Gamma_i^\sigma \middle| H_{Zee_{C_3}} \middle| \Gamma_{i'}^{\sigma'} \right\rangle, \tag{A.21}$$

$$\left\langle \Gamma_i^\sigma \middle| H_{C_4} \middle| \Gamma_{i'}^{\sigma'} \right\rangle = \left\langle \Gamma_i^\sigma \middle| H_c \middle| \Gamma_{i'}^{\sigma'} \right\rangle + \left\langle \Gamma_i^\sigma \middle| H_{Zee_{C_4}} \middle| \Gamma_{i'}^{\sigma'} \right\rangle. \tag{A.22}$$

$\left\langle \Gamma_i^\sigma \middle| H_{C_2} \middle| \Gamma_{i'}^{\sigma'} \right\rangle$, $\left\langle \Gamma_i^\sigma \middle| H_{C_3} \middle| \Gamma_{i'}^{\sigma'} \right\rangle$ and $\left\langle \Gamma_i^\sigma \middle| H_{C_4} \middle| \Gamma_{i'}^{\sigma'} \right\rangle$ are not diagonal. We look for a change-of-basis P_{C_i} to rewrite H_{C_2}, H_{C_3} and H_{C_4} in new basis: $\left\langle \zeta_{C_2}^l \middle| H_{C_2} \middle| \zeta_{C_2}^{l'} \right\rangle$, $\left\langle \zeta_{C_3}^l \middle| H_{C_3} \middle| \zeta_{C_3}^{l'} \right\rangle$ and $\left\langle \zeta_{C_4}^l \middle| H_{C_4} \middle| \zeta_{C_4}^{l'} \right\rangle$ by using (Eq.4.34), where l and l' take the value from 1 to 8 to distinguish different states.

As an example, we make $g_J = \frac{8}{7}$, $B = 6.5\,\mathrm{T}$. With numerical application, we have

$\left\langle \Gamma_i^\sigma \middle| H_{C_2} \middle| \Gamma_{i'}^{\sigma'} \right\rangle$ (in meV) =

	$\lvert\Gamma_7^+\rangle$	$\lvert\Gamma_7^-\rangle$	$\lvert\Gamma_{8,1}^+\rangle$	$\lvert\Gamma_{8,1}^-\rangle$	$\lvert\Gamma_{8,2}^+\rangle$	$\lvert\Gamma_{8,2}^-\rangle$	$\lvert\Gamma_6^+\rangle$	$\lvert\Gamma_6^-\rangle$
$\langle\Gamma_7^+\rvert$	-6.00	$-0.46+0.46i$	$0.46+0.46i$	$0.$	$0.26-0.26i$	0	0	0
$\langle\Gamma_7^-\rvert$	$-0.46-0.46i$	-6.00	0	$0.46-0.46i$	0	$0.26+0.26i$	0	0
$\langle\Gamma_{8,1}^+\rvert$	$0.46-0.46i$	0	2.08	$0.25+0.25i$	$0.$	$-0.18+0.18i$	$0.$	$-0.30-0.30i$
$\langle\Gamma_{8,1}^-\rvert$	0	$0.46+0.46i$	$0.25-0.25i$	2.08	$-0.18-0.18i$	$0.$	$-0.30+0.30i$	$0.$
$\langle\Gamma_{8,2}^+\rvert$	$0.26+0.26i$	0	0	$-0.18+0.18i$	2.08	$0.46+0.46i$	0	$0.52-0.52i$
$\langle\Gamma_{8,2}^-\rvert$	0	$0.26-0.26i$	$-0.18-0.18i$	0	$0.46-0.46i$	2.08	$0.52+0.52i$	0
$\langle\Gamma_6^+\rvert$	0	0	0	$-0.30-0.30i$	0	$0.52-0.52i$	1.83	$0.35+0.35i$
$\langle\Gamma_6^-\rvert$	0	0	$-0.30+0.30i$	0	$0.52+0.5i$	0	$0.35-0.35i$	1.83

(A.23)

A.2. $\langle J_z \rangle$ calculations

$\left\langle \Gamma_i^\sigma \middle| H_{C_3} \middle| \Gamma_{i'}^{\sigma'} \right\rangle$ (in meV) =

$$\begin{array}{c} \\ \langle\Gamma_7^+| \\ \langle\Gamma_7^-| \\ \langle\Gamma_{8,1}^+| \\ \langle\Gamma_{8,1}^-| \\ \langle\Gamma_{8,2}^+| \\ \langle\Gamma_{8,2}^-| \\ \langle\Gamma_6^+| \\ \langle\Gamma_6^-| \end{array} \begin{array}{c} \begin{array}{cccccccc} |\Gamma_7^+\rangle & |\Gamma_7^-\rangle & |\Gamma_{8,1}^+\rangle & |\Gamma_{8,1}^-\rangle & |\Gamma_{8,2}^+\rangle & |\Gamma_{8,2}^-\rangle & |\Gamma_6^+\rangle & |\Gamma_6^-\rangle \end{array} \\ \begin{pmatrix} -5.62 & -0.37+0.37i & 0.37+0.37i & 0 & 0.21-0.21i & 0.43 & 0 & 0 \\ -0.37-0.37i & -6.36 & 0. & 0.37-0.37i & -0.43 & 0.21+0.21i & 0 & 0 \\ 0.37-0.37i & 0 & 2.54 & 0.21+0.21i & 0 & -0.14+0.14i & 0.49 & -0.24-0.24i \\ 0 & 0.37+0.37i & 0.21-0.21i & 1.62 & -0.14-0.14i & 0 & -0.24+0.24i & -0.49 \\ 0.21+0.21i & -0.43 & 0 & -0.14+0.14i & 2.20 & 0.37+0.37i & 0 & 0.42-0.42i \\ 0.43 & 0.21-0.21i & -0.14-0.14i & 0 & 0.37-0.37i & 1.96 & 0.42+0.42i & 0 \\ 0 & 0 & 0.49 & -0.24-0.24i & 0 & 0.42-0.42i & 2.12 & 0.29+0.29i \\ 0 & 0 & -0.24+0.24i & -0.49 & 0.42+0.42i & 0. & 0.29-0.29i & 1.54 \end{pmatrix} \end{array}$$

(A.24)

$\left\langle \Gamma_i^\sigma \middle| H_{C_4} \middle| \Gamma_{i'}^{\sigma'} \right\rangle$ (in meV) =

$$\begin{array}{c} \\ \langle\Gamma_7^+| \\ \langle\Gamma_7^-| \\ \langle\Gamma_{8,1}^+| \\ \langle\Gamma_{8,1}^-| \\ \langle\Gamma_{8,2}^+| \\ \langle\Gamma_{8,2}^-| \\ \langle\Gamma_6^+| \\ \langle\Gamma_6^-| \end{array} \begin{array}{c} \begin{array}{cccccccc} |\Gamma_7^+\rangle & |\Gamma_7^-\rangle & |\Gamma_{8,1}^+\rangle & |\Gamma_{8,1}^-\rangle & |\Gamma_{8,2}^+\rangle & |\Gamma_{8,2}^-\rangle & |\Gamma_6^+\rangle & |\Gamma_6^-\rangle \end{array} \\ \begin{pmatrix} -5.35 & 0 & 0 & 0 & 0 & 0.74 & 0 & 0 \\ 0 & -6.64 & 0 & 0 & -0.74 & 0 & 0 & 0 \\ 0 & 0 & 2.87 & 0 & 0 & 0 & 0.85 & 0 \\ 0 & 0 & 0 & 1.29 & 0 & 0 & 0 & -0.85 \\ 0 & -0.74 & 0 & 0 & 2.29 & 0 & 0 & 0 \\ 0.74 & 0 & 0 & 0 & 0 & 1.86 & 0 & 0 \\ 0 & 0 & 0.85 & 0 & 0 & 0 & 2.33 & 0 \\ 0 & 0 & 0 & -0.85 & 0 & 0 & 0 & 1.33 \end{pmatrix} \end{array}$$

(A.25)

We found the change of basis matrix P_{C_i}:

$$P_{C_2} = \begin{pmatrix} -0.704i & -0.704i & 0.0451i & 0.0235i & 0.0383i & 0.0431i & 0.0339i & 0.0393i \\ 0.498-0.498i & -0.498+0.498i & 0.0319-0.0319i & -0.0166+0.0166i & 0.0271-0.0271i & -0.0305+0.0305i & 0.0239-0.0239i & -0.0278+0.0278i \\ 0.0389+0.0389i & 0.0403+0.0403i & 0.305+0.305i & -0.0167-0.0167i & 0.394+0.394i & 0.449+0.449i & -0.015-0.015i & 0.216+0.216i \\ -0.0551 & 0.057 & 0.432 & 0.0235 & 0.557 & -0.635 & -0.0211 & -0.306 \\ -0.021+0.021i & -0.0261+0.0261i & -0.198+0.198i & -0.461+0.461i & 0.14-0.14i & 0.071-0.071i & -0.436+0.436i & -0.179+0.179i \\ 0.0297i & -0.0369i & -0.28i & 0.652i & 0.198i & -0.100i & -0.617i & 0.253i \\ -0.00398-0.00398i & 0.00467+0.00467i & -0.341-0.341i & 0.192+0.192i & 0.274+0.274i & 0.206+0.206i & 0.243+0.243i & -0.413-0.413i \\ 0.00562 & 0.00661 & -0.482 & -0.272 & 0.387 & -0.292 & 0.343 & 0.584 \end{pmatrix}$$

(A.26)

$$P_{C_3} = \begin{pmatrix} -0.458i & -0.884i & 0.0704i & -0.02i & 0 & 0 & -0.0367i & 0.046i \\ 0.625-0.625i & -0.324+0.324i & 0.0258-0.0258i & 0.0273-0.0273i & 0 & 0 & 0.0501-0.0501i & 0.0168-0.0168i \\ 0.0208+0.0208i & 0.0417+0.0417i & 0.398+0.398i & -0.128-0.128i & 0.423+0.558i & 0.0715+0.0657i & -0.19-0.19i & 0.193+0.193i \\ -0.0568 & 0.0305 & 0.291 & 0.349 & 0.0962+0.0132i & -0.7+0.0295i & 0.519 & 0.142 \\ 0.0208-0.0208i & -0.0417+0.0417i & -0.398+0.398i & -0.128+0.128i & 0.385-0.292i & -0.349+0.38i & -0.19+0.19i & -0.193+0.193i \\ 0.0568i & 0.0305i & 0.291i & -0.349i & 0.0703-0.511i & -0.0203-0.483i & -0.519i & 0.142i \\ -0.00533-0.00533i & -0.00384-0.00384i & 0.142+0.142i & -0.521-0.521i & 0 & 0 & 0.35+0.35i & -0.292-0.292i \\ -0.0039 & 0.0105 & -0.389 & -0.382 & 0 & 0 & 0.256 & 0.798 \end{pmatrix}$$

(A.27)

$$P_{C_4} = \begin{pmatrix} 0 & -0.995 & 0 & 0 & 0 & 0.102 & 0 & 0 \\ 0.997 & 0 & 0 & 0.0825 & 0 & 0 & 0 & 0 \\ 0 & 0 & 0.806 & 0 & 0 & 0 & -0.591 & 0 \\ 0 & 0 & 0 & 0 & -0.699 & 0 & 0 & 0.715 \\ 0.0825 & 0 & 0 & -0.997 & 0 & 0 & 0 & 0 \\ 0 & 0.102 & 0 & 0 & 0 & 0.995 & 0 & 0 \\ 0 & 0 & 0.591 & 0 & 0 & 0 & 0.806 & 0 \\ 0 & 0 & 0 & 0 & 0.715 & 0 & 0 & 0.699 \end{pmatrix}. \quad \text{(A.28)}$$

Finally, we have the numerical application for the matrix in new basis:

$\left\langle \zeta^l_{C_2} \middle| H_{C_2} \middle| \zeta^{l'}_{C_2} \right\rangle$ (in meV) =

$$\begin{array}{c} \\ \langle\zeta^1_{C_2}| \\ \langle\zeta^2_{C_2}| \\ \langle\zeta^3_{C_2}| \\ \langle\zeta^4_{C_2}| \\ \langle\zeta^5_{C_2}| \\ \langle\zeta^6_{C_2}| \\ \langle\zeta^7_{C_2}| \\ \langle\zeta^8_{C_2}| \end{array} \begin{array}{c} \begin{array}{cccccccc} |\zeta^1_{C_2}\rangle & |\zeta^2_{C_2}\rangle & |\zeta^3_{C_2}\rangle & |\zeta^4_{C_2}\rangle & |\zeta^5_{C_2}\rangle & |\zeta^6_{C_2}\rangle & |\zeta^7_{C_2}\rangle & |\zeta^8_{C_2}\rangle \end{array} \\ \begin{pmatrix} -6.703 & 0 & 0 & 0 & 0 & 0 & 0 & 0 \\ 0 & -5.418 & 0 & 0 & 0 & 0 & 0 & 0 \\ 0 & 0 & 3.140 & 0 & 0 & 0 & 0 & 0 \\ 0 & 0 & 0 & 3.054 & 0 & 0 & 0 & 0 \\ 0 & 0 & 0 & 0 & 2.100 & 0 & 0 & 0 \\ 0 & 0 & 0 & 0 & 0 & 2.000 & 0 & 0 \\ 0 & 0 & 0 & 0 & 0 & 0 & 1.039 & 0 \\ 0 & 0 & 0 & 0 & 0 & 0 & 0 & 0.790 \end{pmatrix} \end{array} \quad \text{(A.29)}$$

$\left\langle \zeta^l_{C_3} \middle| H_{C_3} \middle| \zeta^{l'}_{C_3} \right\rangle$ (in meV) =

$$\begin{array}{c} \\ \langle\zeta^1_{C_3}| \\ \langle\zeta^2_{C_3}| \\ \langle\zeta^3_{C_3}| \\ \langle\zeta^4_{C_3}| \\ \langle\zeta^5_{C_3}| \\ \langle\zeta^6_{C_3}| \\ \langle\zeta^7_{C_3}| \\ \langle\zeta^8_{C_3}| \end{array} \begin{array}{c} \begin{array}{cccccccc} |\zeta^1_{C_3}\rangle & |\zeta^2_{C_3}\rangle & |\zeta^3_{C_3}\rangle & |\zeta^4_{C_3}\rangle & |\zeta^5_{C_3}\rangle & |\zeta^6_{C_3}\rangle & |\zeta^7_{C_3}\rangle & |\zeta^8_{C_3}\rangle \end{array} \\ \begin{pmatrix} -6.704 & 0 & 0 & 0 & 0 & 0 & 0 & 0 \\ 0 & -5.417 & 0 & 0 & 0 & 0 & 0 & 0 \\ 0 & 0 & 3.063 & 0 & 0 & 0 & 0 & 0 \\ 0 & 0 & 0 & 2.902 & 0 & 0 & 0 & 0 \\ 0 & 0 & 0 & 0 & 2.725 & 0 & 0 & 0 \\ 0 & 0 & 0 & 0 & 0 & 1.435 & 0 & 0 \\ 0 & 0 & 0 & 0 & 0 & 0 & 1.078 & 0 \\ 0 & 0 & 0 & 0 & 0 & 0 & 0 & 0.920 \end{pmatrix} \end{array} \quad \text{(A.30)}$$

$$\left\langle \zeta_{C_4}^{l} \middle| H_{C_4} \middle| \zeta_{C_4}^{l'} \right\rangle \text{(in meV)} =$$

$$\begin{array}{c} \\ \langle\zeta_{C_4}^1| \\ \langle\zeta_{C_4}^2| \\ \langle\zeta_{C_4}^3| \\ \langle\zeta_{C_4}^4| \\ \langle\zeta_{C_4}^5| \\ \langle\zeta_{C_4}^6| \\ \langle\zeta_{C_4}^7| \\ \langle\zeta_{C_4}^8| \end{array} \begin{array}{c} \begin{array}{cccccccc} |\zeta_{C_4}^1\rangle & |\zeta_{C_4}^2\rangle & |\zeta_{C_4}^3\rangle & |\zeta_{C_4}^4\rangle & |\zeta_{C_4}^5\rangle & |\zeta_{C_4}^6\rangle & |\zeta_{C_4}^7\rangle & |\zeta_{C_4}^8\rangle \end{array} \\ \begin{pmatrix} -6.698 & 0 & 0 & 0 & 0 & 0 & 0 & 0 \\ 0 & -5.423 & 0 & 0 & 0 & 0 & 0 & 0 \\ 0 & 0 & 3.490 & 0 & 0 & 0 & 0 & 0 \\ 0 & 0 & 0 & 2.159 & 0 & 0 & 0 & 0 \\ 0 & 0 & 0 & 0 & 2.357 & 0 & 0 & 0 \\ 0 & 0 & 0 & 0 & 0 & 1.941 & 0 & 0 \\ 0 & 0 & 0 & 0 & 0 & 0 & 1.712 & 0 \\ 0 & 0 & 0 & 0 & 0 & 0 & 0 & 0.463 \end{pmatrix} \end{array} \tag{A.31}$$

According to (Eq.4.35) we can represent $J_{zp\_C_2}$, $J_{zp\_C_3}$ and $J_{zp\_C_4}$ in this new basis. We apply

$$\left\langle \psi_{C_i} \middle| J_{zp\_C_i} \middle| \psi'_{C_i} \right\rangle = \sum_{l,l'} \alpha_{l,l'} \left\langle \zeta_{C_i}^{l} \middle| J_{zp\_C_i} \middle| \zeta_{C_i}^{l'} \right\rangle \tag{A.32}$$

where $\alpha_{l,l'}$ can be calculated by (Eq.4.38). Once $\left\langle \psi_{C_2} \middle| J_{zp\_C_2} \middle| \psi'_{C_2} \right\rangle$, $\left\langle \psi_{C_3} \middle| J_{zp\_C_3} \middle| \psi'_{C_3} \right\rangle$ and $\left\langle \psi_{C_4} \middle| J_{zp\_C_4} \middle| \psi'_{C_4} \right\rangle$ are obtained, we can apply (Eq.4.39) for a powder in the case of cubic symmetry. We get

$$\langle J_z \rangle = \frac{176}{385} \left\langle \psi_{C_2} \middle| J_{zp\_C_2} \middle| \psi'_{C_2} \right\rangle + \frac{99}{385} \left\langle \psi_{C_3} \middle| J_{zp\_C_3} \middle| \psi'_{C_3} \right\rangle + \frac{110}{385} \left\langle \psi_{C_4} \middle| J_{zp\_C_4} \middle| \psi'_{C_4} \right\rangle. \tag{A.33}$$

A.3 $\langle J_z^2 \rangle$ calculations

The method to calculate $\langle J_z^2 \rangle$ is the same as the calculation of $\langle J_z \rangle$. We aim to rewrite $\left\langle \Gamma_i^{\sigma} \middle| J_{zp\_C_k}^2 \middle| \Gamma_{i'}^{\sigma'} \right\rangle$ $(k = 2, 3, 4)$ in the new basis $\left\langle \zeta_{C_k}^{l} \middle| J_{zp\_C_k}^2 \middle| \zeta_{C_k}^{l'} \right\rangle$ $(k = 2, 3, 4)$ where $\left\langle \zeta_{C_k}^{l} \middle| H_{C_k} \middle| \zeta_{C_k}^{l'} \right\rangle$ $(k = 2, 3, 4)$ are diagonal matrices.

By using (Eq.4.32), we can write explicitly ($\hbar = 1$)

$$\left\langle \Gamma_i^{\sigma} \middle| J^2_{zp\_C_2} \middle| \Gamma_{i'}^{\sigma'} \right\rangle =$$

$$\begin{array}{c} \\ \langle\Gamma_7^+| \\ \langle\Gamma_7^-| \\ \langle\Gamma_{8,1}^+| \\ \langle\Gamma_{8,1}^-| \\ \langle\Gamma_{8,2}^+| \\ \langle\Gamma_{8,2}^-| \\ \langle\Gamma_6^+| \\ \langle\Gamma_6^-| \end{array} \begin{array}{c} \begin{array}{cccccccc} |\Gamma_7^+\rangle & |\Gamma_7^-\rangle & |\Gamma_{8,1}^+\rangle & |\Gamma_{8,1}^-\rangle & |\Gamma_{8,2}^+\rangle & |\Gamma_{8,2}^-\rangle & |\Gamma_6^+\rangle & |\Gamma_6^-\rangle \end{array} \\ \begin{pmatrix} \frac{21}{4} & 0 & 0 & 4i & 0 & -\frac{1}{2}\sqrt{3} & 0 & -\frac{1}{2}i\sqrt{35} \\ 0 & \frac{21}{4} & -4i & 0 & -\frac{1}{2}\sqrt{3} & 0 & \frac{1}{2}i\sqrt{35} & 0 \\ 0 & 4i & \frac{17}{4} & 0 & -\frac{3}{2}i\sqrt{3} & 0 & -\frac{1}{2}\sqrt{35} & 0 \\ -4i & 0 & 0 & \frac{17}{4} & 0 & \frac{3}{2}i\sqrt{3} & 0 & -\frac{1}{2}\sqrt{35} \\ 0 & -\frac{1}{2}\sqrt{3} & \frac{3}{2}i\sqrt{3} & 0 & \frac{25}{4} & 0 & 0 & 0 \\ -\frac{1}{2}\sqrt{3} & 0 & 0 & -\frac{3}{2}i\sqrt{3} & 0 & \frac{25}{4} & 0 & 0 \\ 0 & -\frac{1}{2}i\sqrt{35} & -\frac{1}{2}\sqrt{35} & 0 & 0 & 0 & \frac{21}{4} & 0 \\ \frac{1}{2}i\sqrt{35} & 0 & 0 & -\frac{1}{2}\sqrt{35} & 0 & 0 & 0 & \frac{21}{4} \end{pmatrix} \end{array} \tag{A.34}$$

$$\left\langle \Gamma_i^{\sigma} \middle| J^2_{zp\_C_3} \middle| \Gamma_{i'}^{\sigma'} \right\rangle =$$

$$\begin{array}{c} \\ \langle\Gamma_7^+| \\ \langle\Gamma_7^-| \\ \langle\Gamma_{8,1}^+| \\ \langle\Gamma_{8,1}^-| \\ \langle\Gamma_{8,2}^+| \\ \langle\Gamma_{8,2}^-| \\ \langle\Gamma_6^+| \\ \langle\Gamma_6^-| \end{array} \begin{array}{c} \begin{array}{cccccccc} |\Gamma_7^+\rangle & |\Gamma_7^-\rangle & |\Gamma_{8,1}^+\rangle & |\Gamma_{8,1}^-\rangle & |\Gamma_{8,2}^+\rangle & |\Gamma_{8,2}^-\rangle & |\Gamma_6^+\rangle & |\Gamma_6^-\rangle \end{array} \\ \begin{pmatrix} \frac{21}{4} & 0 & \frac{4}{3}+\frac{4i}{3} & \frac{8i}{3} & \frac{4-4i}{\sqrt{3}} & 0 & \left(\frac{1}{3}+\frac{i}{3}\right)\sqrt{35} & -\frac{1}{3}i\sqrt{35} \\ 0 & \frac{21}{4} & -\frac{8i}{3} & -\frac{4}{3}+\frac{4i}{3} & 0 & -\frac{4+4i)}{\sqrt{3}} & \frac{1}{3}i\sqrt{35} & \left(-\frac{1}{3}+\frac{i}{3}\right)\sqrt{35} \\ \frac{4}{3}-\frac{4i}{3} & \frac{8i}{3} & \frac{21}{4} & 0 & -i\sqrt{3} & (1-i)\sqrt{3} & 0 & 0 \\ -\frac{8i}{3} & -\frac{4}{3}-\frac{4i}{3} & 0 & \frac{21}{4} & (-1-i)\sqrt{3} & i\sqrt{3} & 0 & 0 \\ \frac{4+4i}{\sqrt{3}} & 0 & i\sqrt{3} & (-1+i)\sqrt{3} & \frac{21}{4} & 0 & 0 & 0 \\ 0 & -\frac{4-4i}{\sqrt{3}} & (1+i)\sqrt{3} & -i\sqrt{3} & 0 & \frac{21}{4} & 0 & 0 \\ \left(\frac{1}{3}-\frac{i}{3}\right)\sqrt{35} & -\frac{1}{3}i\sqrt{35} & 0 & 0 & 0 & 0 & \frac{21}{4} & 0 \\ \frac{1}{3}i\sqrt{35} & \left(-\frac{1}{3}-\frac{i}{3}\right)\sqrt{35} & 0 & 0 & 0 & 0 & 0 & \frac{21}{4} \end{pmatrix} \end{array} \tag{A.35}$$

and

$$\left\langle \Gamma_i^{\sigma} \middle| J^2_{zp\_C_4} \middle| \Gamma_{i'}^{\sigma'} \right\rangle =$$

$$\begin{array}{c} \\ \langle\Gamma_7^+| \\ \langle\Gamma_7^-| \\ \langle\Gamma_{8,1}^+| \\ \langle\Gamma_{8,1}^-| \\ \langle\Gamma_{8,2}^+| \\ \langle\Gamma_{8,2}^-| \\ \langle\Gamma_6^+| \\ \langle\Gamma_6^-| \end{array} \begin{array}{c} \begin{array}{cccccccc} |\Gamma_7^+\rangle & |\Gamma_7^-\rangle & |\Gamma_{8,1}^+\rangle & |\Gamma_{8,1}^-\rangle & |\Gamma_{8,2}^+\rangle & |\Gamma_{8,2}^-\rangle & |\Gamma_6^+\rangle & |\Gamma_6^-\rangle \end{array} \\ \begin{pmatrix} \frac{21}{4} & 0 & 0 & 0 & 0 & \sqrt{3} & 0 & 0 \\ 0 & \frac{21}{4} & 0 & 0 & \sqrt{3} & 0 & 0 & 0 \\ 0 & 0 & \frac{29}{4} & 0 & 0 & 0 & \sqrt{35} & 0 \\ 0 & 0 & 0 & \frac{29}{4} & 0 & 0 & 0 & \sqrt{35} \\ 0 & \sqrt{3} & 0 & 0 & \frac{13}{4} & 0 & 0 & 0 \\ \sqrt{3} & 0 & 0 & 0 & 0 & \frac{13}{4} & 0 & 0 \\ 0 & 0 & \sqrt{35} & 0 & 0 & 0 & \frac{21}{4} & 0 \\ 0 & 0 & 0 & \sqrt{35} & 0 & 0 & 0 & \frac{21}{4} \end{pmatrix} \end{array} \tag{A.36}$$

The matrix for a basis change P_{C_i} that satisfies (Eq.4.34) can be calculated. For $g_J = 8/7$, $B = 6.5\,\mathrm{T}$, the matrix is given in (Eq.A.26), (Eq.A.27) and (Eq.A.28) and in this case, we have

$$\left\langle \zeta^l_{C_2} \middle| J^2_{zp\_C_2} \middle| \zeta^{l'}_{C_2} \right\rangle =$$

$$\begin{array}{c} \\ \langle\zeta^1_{C_2}| \\ \langle\zeta^2_{C_2}| \\ \langle\zeta^3_{C_2}| \\ \langle\zeta^4_{C_2}| \\ \langle\zeta^5_{C_2}| \\ \langle\zeta^6_{C_2}| \\ \langle\zeta^7_{C_2}| \\ \langle\zeta^8_{C_2}| \end{array} \begin{array}{c} \begin{array}{cccccccc} |\zeta^1_{C_2}\rangle & |\zeta^2_{C_2}\rangle & |\zeta^3_{C_2}\rangle & |\zeta^4_{C_2}\rangle & |\zeta^5_{C_2}\rangle & |\zeta^6_{C_2}\rangle & |\zeta^7_{C_2}\rangle & |\zeta^8_{C_2}\rangle \end{array} \\ \begin{pmatrix} 6.006 & 0 & 0 & -0.3482 & 0 & 2.134 & 0 & 4.746 \\ 0 & 4.587 & -4.478 & 0 & -1.445 & 0 & 0.923 & 0 \\ 0 & -4.478 & 9.372 & 0 & 0.717 & 0 & 0.961 & 0 \\ -0.348 & 0 & 0 & 6.046 & 0 & 1.035 & 0 & 0.654 \\ 0 & -1.445 & 0.717 & 0 & 1.156 & 0 & 0.523 & 0 \\ 2.134 & 0 & 0 & 1.035 & 0 & 1.336 & 0 & 1.502 \\ 0 & 0.923 & 0.961 & 0 & 0.523 & 0 & 5.884 & 0 \\ 4.746 & 0 & 0 & 0.654 & 0 & 1.502 & 0 & 7.611 \end{pmatrix} \end{array} \tag{A.37}$$

$$\left\langle \zeta^l_{C_3} \middle| J^2_{zp\_C_3} \middle| \zeta^{l'}_{C_3} \right\rangle =$$

$$\begin{array}{c} \\ \langle\zeta^1_{C_3}| \\ \langle\zeta^2_{C_2}| \\ \langle\zeta^3_{C_3}| \\ \langle\zeta^4_{C_3}| \\ \langle\zeta^5_{C_3}| \\ \langle\zeta^6_{C_3}| \\ \langle\zeta^7_{C_3}| \\ \langle\zeta^8_{C_3}| \end{array} \begin{array}{c} \begin{array}{cccccccc} |\zeta^1_{C_3}\rangle & |\zeta^2_{C_3}\rangle & |\zeta^3_{C_3}\rangle & |\zeta^4_{C_3}\rangle & |\zeta^5_{C_3}\rangle & |\zeta^6_{C_3}\rangle & |\zeta^7_{C_3}\rangle & |\zeta^8_{C_3}\rangle \end{array} \\ \begin{pmatrix} 6.164 & 0 & 0 & 0.134 & 0 & 0 & -5.886 & 0 \\ 0 & 4.493 & -5.324 & 0 & 0 & 0 & 0 & 1.197 \\ 0 & -5.324 & 8.548 & 0 & 0 & 0 & 0 & 1.377 \\ 0.134 & 0 & 0 & 6.201 & 0 & 0 & 1.151 & 0 \\ 0 & 0 & 0 & 0 & 2.25 & 0 & 0 & 0 \\ 0 & 0 & 0 & 0 & 0 & 2.25 & 0 & 0 \\ -5.886 & 0 & 0 & 1.151 & 0 & 0 & 6.385 & 0 \\ 0 & 1.197 & 1.377 & 0 & 0 & 0 & 0 & 5.709 \end{pmatrix} \end{array} \tag{A.38}$$

$$\left\langle \zeta^{l}_{C_4} \middle| J^2_{zp\_C_4} \middle| \zeta^{l'}_{C_4} \right\rangle =$$

$$\begin{array}{c} \\ \langle\zeta^1_{C_4}| \\ \langle\zeta^2_{C_4}| \\ \langle\zeta^3_{C_4}| \\ \langle\zeta^4_{C_4}| \\ \langle\zeta^5_{C_4}| \\ \langle\zeta^6_{C_4}| \\ \langle\zeta^7_{C_4}| \\ \langle\zeta^8_{C_4}| \end{array} \begin{array}{c} \begin{array}{cccccccc} |\zeta^1_{C_4}\rangle & |\zeta^2_{C_4}\rangle & |\zeta^3_{C_4}\rangle & |\zeta^4_{C_4}\rangle & |\zeta^5_{C_4}\rangle & |\zeta^6_{C_4}\rangle & |\zeta^7_{C_4}\rangle & |\zeta^8_{C_4}\rangle \end{array} \\ \begin{pmatrix} 5.521 & 0 & 0 & -1.544 & 0 & 0 & 0 & 0 \\ 0 & 4.879 & 0 & 0 & 0 & -1.899 & 0 & 0 \\ 0 & 0 & 12.193 & 0 & 0 & 0 & 0.825 & 0 \\ -1.544 & 0 & 0 & 2.979 & 0 & 0 & 0 & 0 \\ 0 & 0 & 0 & 0 & 0.3126 & 0 & 0 & -0.865 \\ 0 & -1.899 & 0 & 0 & 0 & 3.621 & 0 & 0 \\ 0 & 0 & 0.825 & 0 & 0 & 0 & 0.307 & 0 \\ 0 & 0 & 0 & 0 & -0.865 & 0 & 0 & 12.187 \end{pmatrix} \end{array} \tag{A.39}$$

We can apply (Eq.4.37) where $\alpha_{l,l'}$ can be calculated by (Eq.4.38). $\left\langle \psi_{C_2} \middle| J^2_{zp\_C_2} \middle| \psi'_{C_2} \right\rangle$, $\left\langle \psi_{C_3} \middle| J^2_{zp\_C_3} \middle| \psi'_{C_3} \right\rangle$ and $\left\langle \psi_{C_4} \middle| J^2_{zp\_C_4} \middle| \psi'_{C_4} \right\rangle$ as a function of temperature. With the discussion in Section 4.3 we can obtain $\langle J^2_z \rangle$ by applying (Eq.4.40).

Résumé en français

XAS, XMCD et XMLD

Depuis la mise en évidence expérimentale du signal XMCD ("X-ray Magnetic Circular Dichroism" en anglais) dans les années 1980 par Schütz *et al.* [17, 20], la technique XMCD est devenue une technique synchrotron très puissante et très efficace pour étudier les propriétés magnétiques des atomes. Le XMCD est basé sur le XAS ("X-ray Absorption Spectroscopy" en anglais) et possède donc des caractéristiques de la spectroscopie d'absorption des rayons X qui permet une sélectivité chimique et orbitalaire. La grande force du XMCD réside dans l'application des règles de sommes magnéto-optiques, proposées par Thole et Carra entre 1992 et 1993, qui permettent d'extraire le moment magnétique de spin [22] et le moment magnétique d'orbite [21] de l'atome sondé. Dans à-peu-près la même période, le XMLD ("X-ray Magneitc Linear Dichroism" en anglais) a été prédit par Thole *et al.* (1985) [18] et a été observé expérimentalement par van der Laan *et al.* en 1986 [19]. Le XMCD donne accès au paramètre $\langle J_z \rangle$ et le XMLD est relié au paramètre $\langle J_z^2 \rangle$. L'analyse du signal XMCD et XMLD révèle des propriétés magnétiques bien différentes. Grâce à ces techniques très poussées, de nos jours, plus de 50 lignes de lumière dédiées ont été construites et mises en service [25].

L'équipement à très basse température

Pour étudier des propriétés magnétiques, une grande variation de l'aimantation est nécessaire pour l'analyse. Selon la loi de Curie $\mathbf{M} = C\,\mathbf{B}/T$ où $\mathbf{M}$ est l'aimantation, $\mathbf{B}$ est le champ magnétique, T est la température et C est la constante de Curie du matériaux, deux paramètres peuvent être utilisés pour faire varier $\mathbf{M}$: le champ magnétique et la température. A ce jour, on a des moyens très limités pour créer un champ magnétique fort alors que la température est une variable plutôt facile à faire varier dans une large gamme. En plus, un système se rapproche de son état fondamental quand la température diminue. L'énergie de séparation entre l'état fondamental et le premier niveau excité est inférieur à 1 meV pour beaucoup de systèmes. Et pour sonder des propriétés exotiques comme une transition du spin, une transition métal-isolant,

un ordre magnétique, la relaxation d'un état métastable, la supraconductivité et l'effet Kondo, la température critique est inférieure à 1 K pour beaucoup de cas. Pour cela, une série d'instruments dédiés aux mesures de XAS à très basse température ($T < 1\,\mathrm{K}$) est devenue indispensable.

En 2018, une nouvelle canne DICHRO50 qui fonctionne sur le principle d'une dilution d'^{3}He – ^{4}He a été installée dans la station expérimentale de la ligne DEIMOS au Synchrotron SOLEIL. Cette canne permet l'accès à une gamme complète de la température de $T_{\mathrm{min}} = 180\,\mathrm{mK}$ à $T_{\mathrm{max}} = 300\,\mathrm{K}$ sous ultra-vide ($P \simeq 2 \times 10^{-10}\,\mathrm{mbar}$ pendant les mesures). On souligne surtout les températures entre 180 mK et 4.2 K qui rendent cet instrument unique au monde pour des mesures de XAS avec des rayons X mous. En fin de cette même année 2018, un autre cryo-aimant qui s'appelle TBT-mK qui a les fonctionnalités proches de celles de DICHRO50 a été installé sur la linge ID12 de l'ESRF, ligne dédiée aux mesures de XAS avec des rayons X durs.

Motivations de cette thèse

Grâce aux techniques de synchrotron et en particulier du XAS, ainsi qu'à l'installation de ces deux cryo-aimants sur des lignes de lumière donnant accès aux mesures de XAS dans la gamme des millikelvins, on veut étudier dans cette thèse les propriétés magnétiques, le champ cristallin et l'effet Kondo dans deux systèmes intermétalliques :

- Le polycristal d'$Er_{0.025}Pd_{0.975}$ avec 2.5% d'atomes d'erbium dilués dans le palladium. L'Er se présente comme l'ion Er^{3+} dans cet alliage, et est traité comme l'impureté dans le Pd. C'est un système qui ne présente pas de phénomène Kondo.

- Le polycristal d'$Yb_{0.005}Au_{0.995}$ avec 0.5% des atomes d'ytterbium dilués dans l'or. L'Yb se présente comme l'ion Yb^{3+} dans cet alliage et est traité comme l'impureté dans l'Au. C'est un système connu pour présenter un phénomène Kondo [138, 139, 140].

L'effet Kondo

Pour un métal normal pur (non supraconducteur), sa résistivité électrique diminue de façon monotone avec la température et tend vers une résistivité résiduelle. Cependant en 1934, de Haas *et al.* ont observé que si très peu d'impuretés sont ajoutées dans l'or pur, un minimum de résistivité se présente pour une température; en dessous de cette température, la résistivité remonte si la température continue à diminuer [40]. Ce phénomène est resté non expliqué jusqu'en 1964, lorsque J. Kondo a proposé un modèle soi-disant "s-d modèle" pour expliquer ce phénomène. Avec ce modèle, la résistance électrique totale du composé qui dépend de la température peut s'exprimer

par [44, 45, 46, 47]

$$R = aT^5 + cR_A + cR_{\mathrm{m}}\left[1 + 4\mathscr{J}\rho_0 \ln\left(\frac{k_B T}{D}\right)\right], \tag{40}$$

avec a une constante, c la concentration des impuretés, R_{m} une constante liée à la résistance résiduelle, $\mathscr{J}$ le paramètre de couplage d'échange ($\mathscr{J} > 0$ pour l'interaction ferromagnétique et $\mathscr{J} < 0$ pour l'interaction antiferromagnétique), ρ_0 la densité d'état de la bande de conduction au niveau de Fermi, D la largeur de la bande de conduction, k_B la constante de Boltzmann et T la température. On suppose qu'ici, la condition $k_B T \ll D$ est vérifiée. C'est le troisième terme de cette formule qui décrit l'effet Kondo. Avec cette formule, pour l'interaction ferromagnétique, la résistance diminue de façon monotone avec la température et pour l'interaction antiferromagnétique, quand la température est élevée, c'est le terme aT^5 qui domine et c'est le terme logarithmique qui domine à basse température. Historiquement, le problème de divergence venant du terme logarithmique est résolu par Anderson [50, 51, 53] et Wilson [54, 55, 56, 57, 58].

Pour une image de physique (Figure 1), une certaine impureté est diluée dans certain métal pur, à basse température (proche du régime de Kondo), le moment magnétique de l'impureté est couplé avec un spin de l'électron de conduction et il se forme un état lié : un singulet. Par conséquence, le moment magnétique de l'impureté est écranté et il se présente comme une impureté non-magnétique. Il augmente la probabilité de diffusion et donc la résistivité augmente avec une température qui diminue. Le singulet peut être détruit par l'agitation thermique quand la température est bien supérieure à celle de la température critique ou par un champ magnétique extérieur fort par l'effet Zeeman. Costi a montré que pour un système $S = 1/2$, l'induction doit approximativement respecter $|B| \leq k_B T_K/(2g_J\mu_B)$ [60]. Sous l'effet de l'écrantage du moment magnétique de l'impureté, on s'attend à ce que le moment magnétique mesuré soit inférieur à celui d'un modèle paramagnétique usuel.

Plan de la recherche

D'un côté, on mesure des spectres de XAS avec un faisceau de rayons X polarisé circulairement à gauche et à droite sous un champ magnétique de $\pm 6.5\,\mathrm{T}$ (champ fort), $\pm 0.5\,\mathrm{T}$ (champ faible) et $\pm 0.1\,\mathrm{T}$ (champ faible) avec des températures différentes à partir de 200 mK à 300 K. On déduit et on analyse des spectres XMCD et XMLD pour essayer d'extraire des propriétés magnétiques et des propriétés du champ cristallin.

D'un autre côté, on réalise des calculs et des simulations numériques se basant sur la théorie LFM ("Ligand Field Multiplet" en anglais). On précise que ces calculs prennent en compte l'effet du champ cristallin et l'effet Zeeman mais ne considèrent pas l'effet Kondo. À priori, les comportements magnétiques prévus par ces calculs doivent

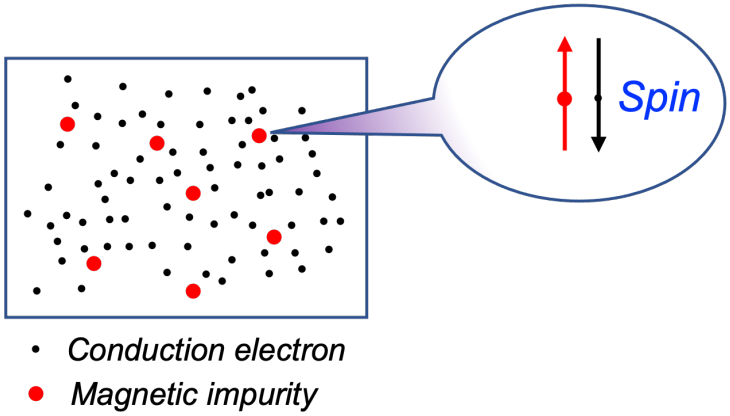

Figure 1: Illustration d'impuretés magnétiques diluées dans un métal pur. Une impureté est couplée avec un spin d'un électron de conduction et ils forment un état singulet qui se comporte comme une impureté non-magnétique.

être en accord avec un système non-Kondo par exemple $Er_{0.025}Pd_{0.975}$ intermétallique. En revanche, les déviations entre ces modèles de calcul et les mesures doivent être constatées pour un système Kondo par exemple $Yb_{0.005}Au_{0.995}$ lorsque les phénomènes Kondo apparaissent.

Avec les comparaisons entre les zones où l'effet Kondo apparaît (aux alentours de la température critique de l'effet Kondo T_K et à champ magnétique faible) et disparaît (à une température élevée ou avec un champ magnétique fort) pour l'intermétallique d'$Yb_{0.005}Au_{0.995}$ et avec la comparaison entre un système non-Kondo d'$Er_{0.025}Pd_{0.975}$ et un système Kondo d'$Yb_{0.005}Au_{0.995}$, on estime pouvoir extraire la signature de l'effet Kondo d'$Yb_{0.005}Au_{0.995}$ avec nos mesures de XAS-XMCD.

Résumés des chapitres

Le **Chapitre 1** est l'introduction générale de cette thèse. Une description historique du développement de XAS, XMCD et XMLD, des instruments à très basse température pour des mesures de XAS sur synchrotron ainsi que l'introduction de l'effet Kondo sont présentés. On détaille par la suite l'objectif de cette thèse.

Le **Chapitre 2** est la présentation détaillée des principes cryogéniques et ses applications. On détaille dans un premier temps les motivations pour des mesures de XAS à très basse température $T < 1\,\mathrm{K}$. Dans un deuxième temps, on présente le fonctionnement d'un réfrigérateur à dilution $^3He-^4He$.

Le principe d'un réfrigérateur à dilution repose sur l'existence des deux phases, la phase diluée et la phase concentrée, et sur le transfert d'atomes d'^3He de la phase concentrée vers la phase diluée.

L'enthalpie de la phase diluée en ^{3}He est plus grande que celle de la phase concentrée en ^{3}He. Quand un atome d'^{3}He passe de la phase concentrée à la phase diluée, l'augmentation d'enthalpie est compensée parce qu'une quantité de chaleur est arrachée au système. On observe alors un refroidissement du système. Le fonctionnement d'un réfrigérateur à dilution repose ainsi sur :

- l'existence de deux phases dans une boîte qui s'appelle la boîte à mélange se trouvant au bout de la canne à dilution,

- le fait que le transfert d'atomes d'^{3}He de la phase riche à la phase pauvre en ^{3}He est endothermique.

Un système à dilution ^{3}He – ^{4}He est basé sur ces principes et la figure 2 montre le fonctionnement de ce système. A cause de l'existence très rare et du coût élevé de l'^{3}He, le système fonctionne en circuit fermé et il n'y a aucune perte d'^{3}He. Dans le bouilleur, la température est environ de 0.7 K et il y a équilibre entre la phase liquide et la phase gazeuse du mélange d'^{3}He – ^{4}He. A 0.7 K, la pression de vapeur saturante de l'^{3}He étant bien plus grande que celle de l'^{4}He, $\sim$ 99% de la phase vapeur est constituée d'^{3}He. En pompant sur le bouilleur, on récupère principalement de l'^{3}He, ce qui conduit à diminuer la concentration d'^{3}He dans la phase liquide du bouilleur. La phase liquide du bouilleur étant à l'équilibre thermodynamique avec la phase liquide diluée de la boîte à mélange, la concentration d'^{3}He dans la phase liquide diluée dans la boîte à mélange diminue aussi. Des atomes d'^{3}He de la phase concentrée peuvent alors passer dans la phase diluée et la variation d'enthalpie refroidit la boîte à mélange.

La vapeur collectée à la sortie du bouilleur est pompée, réchauffée à 300 K puis compressée pour être réinjectée en direction de la boîte à mélange. Divers échangeurs thermiques refroidissent le gaz et le liquéfient avant de l'injecter dans la boîte à mélange. La circulation de l'^{3}He est continue et refroidit la boîte à mélange jusqu'à 180 mK.

L'installation de la canne à 2K sur DEIMOS et l'installation du TBT-mK sur la ligne ID12 à l'ESRF seront également présentées.

Le **Chapitre 3** présente dans un premier temps les caractéristiques des rayonnements synchrotron et la configuration de la ligne DEIMOS du synchrotron SOLEIL. Ensuite, on présente une chambre de limage et de grattage exclusivement dédiée à cette thèse pour le nettoyage de la surface des échantillons sous ultra-vide (de l'ordre de 10^{-10} mbar) afin d'enlever la partie oxydée sur la surface de l'échantillon.

Finalement, le principe du XAS, les règles de sélection des transitions, les principes de l'XMCD et de l'XMLD sont présentés. Le spectre de XMCD est obtenu par

$$\sigma_{\mathrm{XMCD}}(E) = \sigma^{-}(E) - \sigma^{+}(E), \tag{41}$$

où $\sigma^{-}(E)$ est le spectre XAS enregistré avec le faisceau polarisé circulairement à droite

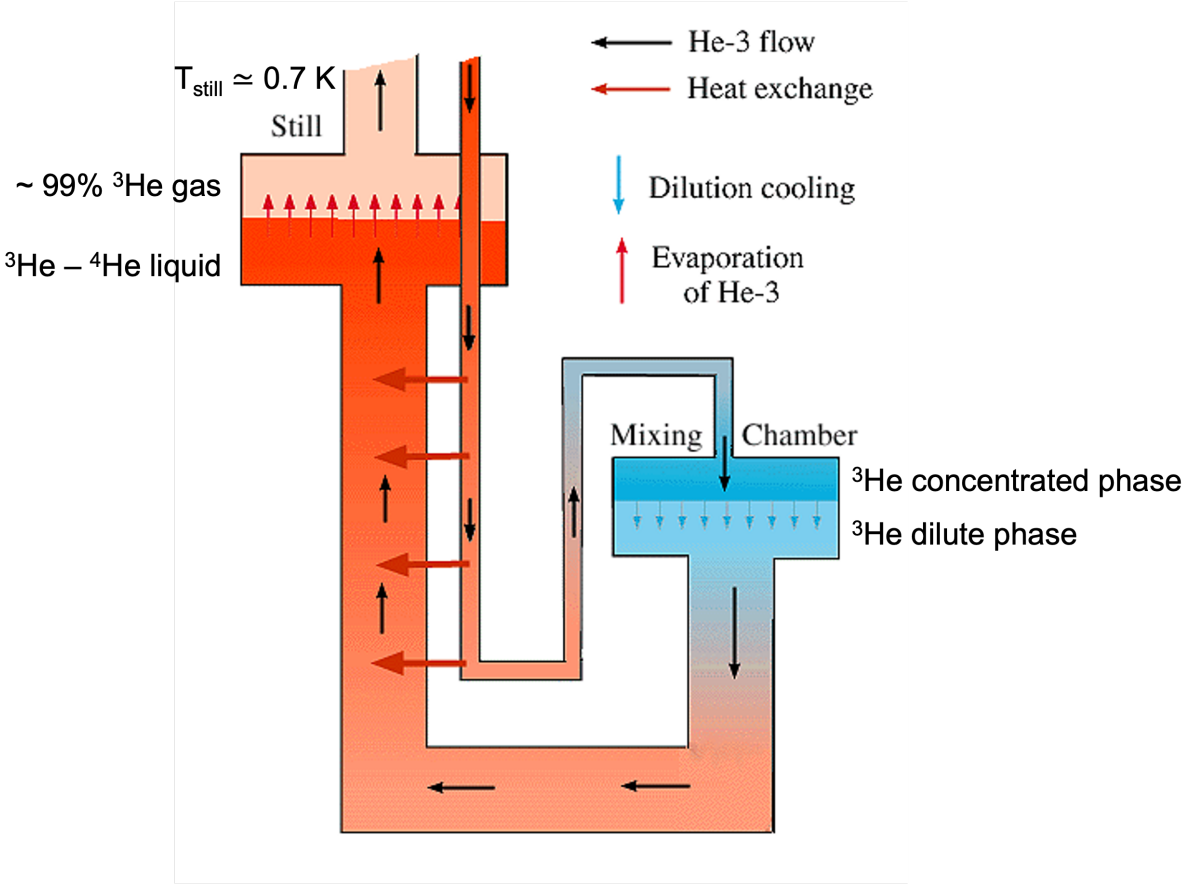

Figure 2: Schéma du concept d'un réfrigérateur à dilution. La couleur bleue indique les zones les plus froides et la couleur rouge les zones les plus chaudes. Dans le bouilleur, on a un mélange des phases liquide et gazeuse, partout ailleurs on a une phase liquide. Les dispositifs cryogéniques qui refoidissent le mélange injecté (pot à 4K) ne sont pas représentés [93].

et $\sigma^+(E)$ est le spectre XAS enregistré avec le faisceau polarisé circulairement à gauche. Schillé *et al.* ont donné une méthode pour déduire le spectre XMLD sur une poudre à partir des mesures avec un faisceau circulairement polarisé [24]. On définit le spectre de XMLD comme suit

$$\sigma_{\mathrm{XMLD}}(E) = \sigma_{\perp}(E) - \sigma_{\parallel}(E) = \frac{3}{2}\left[\sigma^{+}(E) + \sigma^{-}(E)\right] - 3\sigma_0(E)\,, \tag{42}$$

où σ_0 est le spectre isotrope avec l'approximation dipolaire électrique. Avec une symétrie de poudre, on obtient aisément une relation entre le signal XMLD et $\langle J_z^2 \rangle$:

$$\sigma_{\mathrm{XMLD}}(E) = \frac{1}{2}\left[J(J+1) - 3\langle J_z^2 \rangle\right]\sigma_2(E)\,. \tag{43}$$

où $\sigma_2(E)$ est une signature spectrale qui dépend de l'élément chimique avec un J, S

et L spécifique mais ne dépend pas des paramètres du champ cristallin ni du champ magnétique extérieur. On pourra le considérer comme un facteur multiplicatif. Ceci dit l'analyse des signaux XMLD donne accès à $\langle J_z^2 \rangle$.

Les calculs avec les règles de somme magnéto-optiques de l'XMCD sont détaillés dans ce chapitre. L'application des règles de somme donne accès au moment magnétique du spin et d'orbite des atomes absorbeurs.

Le **Chapitre 4** détaille des méthodes de calcul basées sur la théorie de LFM. Pour un atome dans un cristal soumis à un champ magnétique, on peut résoudre l'équation de Schrödinger

$$H \left| \psi \right\rangle = E \left| \psi \right\rangle . \tag{44}$$

L'hamiltonien se décompose par

$$H = H_0 + H_C + H_{Zee} \tag{45}$$

où H_C est l'hamiltonien du champ cristallin, H_{Zee} est l'hamiltonien Zeeman. H_0 est la somme de l'hamiltonien de l'énergie cinétique H_{kin}, l'hamiltonien de l'énergie potentielle H_{pot}, l'hamiltonien multi-électronique H_{ee} et l'hamiltonien du couplage spin-orbite H_{SO}.

Pour des terres rares dont la couche électronique $4f$ n'est pas complètement remplie, l'hamiltonien du champ cristallin peut s'exprimer par la somme d'un terme d'ordre 4 et un terme d'ordre 6 comme suit

$$H_c = C_4 \beta \left(O_4^0 + 5O_4^4 \right) + C_6 \gamma \left(O_6^0 - 21 O_6^4 \right) \tag{46}$$

où β et γ sont deux constantes qui diffèrent d'un élément à un l'autre. Les calculs des paramètres d'ordre 4 (O_4^0, O_4^4) et des paramètres d'ordre 6 (O_6^0, O_6^4) sont détaillés dans la Section 4.1.

L'hamiltonien Zeeman s'exprime par

$$H_{\text{Zee}} = -\boldsymbol{\mu} \cdot \mathbf{B} = \frac{\mu_B}{\hbar} \left(\mathbf{L} + g_s \mathbf{S} \right) \mathbf{B}, \tag{47}$$

où g_s est le rapport gyromagnétique du spin et on adopte la convention pour le magnéton de Bohr $\mu_B > 0$. L'énergie Zeeman pourra être calculée.

Les fonctions propres des niveaux d'énergie séparés sous l'effet du champ cristallin sont données dans la littérature [116]. On pourra donc écrire la somme de H_c et H_{Zee} dans les bases de ces fonctions propres. En tenant compte de la symétrie C_2, C_3 et C_4 pour une poudre, on propose une méthode pour calculer la variation de $\langle J_z \rangle$ et de $\langle J_z^2 \rangle$ en fonction de la température.

On présente également un code QUANTY développé par Haverkort *et al.* pour calculer des spectres XAS/XMCD [122, 123, 124, 125]. Une interface facile à utiliser qui s'appelle Crispy a été développée par Retegan [127]. En utilisant Crispy, on pourra facilement simuler un spectre XAS des terres rares.

Le **Chapitre 5** présente les analyses de l'échantillon d'$Er_{0.025}Pd_{0.975}$. L'erbium se présente comme Er^{3+} dans cet alliage. 2.5% d'atomes d'Er sont dilués dans Pd (structure fcc cubique à faces centrées). Avec un simple calcul, on estime que la probabilité pour un atome d'Er d'être isolé et entouré par 12 atomes de palladium est de 73.8%. Er^{3+} est paramagnétique dans la gamme de température de DICHRO50. La configuration électronique d'Er^{3+} est [Xe]$4f^{11}$ avec $S = 3/2$ et $L = 6$. Pour son état fondamental $^4I_{15/2}$, $J = L + S = 15/2$. Le moment de saturation pour un ion Er^{3+} sphérique à $T = 0\,\mathrm{K}$ est de $9\,\mu_B$ par atome d'erbium. C'est un très bon échantillon pour des mesures thermométriques à très basse température car son moment magnétique varie d'un facteur 7 pour une température entre 300 mK et 4.2 K [36]. Les mesures préliminaires de SQUID ont été réalisées pour la température entre 100 mK et 4.2 K avec un champ magnétique de 0 T à 7 T. Les mesures de SQUID montrent que à $T = 100\,\mathrm{mK}$ et $B = 8\,\mathrm{T}$, le moment magnétique d'Er^{3+} est de $6.9\,\mu_B$ par atome d'Er, ce qui est loin de $9\,\mu_B$ par atome d'Er : le moment magnétique pour un ion sphérique sans considération de l'effet du champ cristallin et de l'effet Zeeman.

Des mesures de XMCD aux seuils $M_{4,5}$ d'Er ont été réalisées sur DEIMOS à SOLEIL avec un champ magnétique extérieur à 6.5 T, 0.5 T, 0.1 T et 0 T pour des températures entre 2 K et 300 K. Les spectres XMLD peuvent être déduits de ces mesures. Deux séries de paramètres de champ cristallin ont été obtenues par des mesures de spectroscopie de neutron [132]. En utilisant Crispy et les calculs de LFM avec ces deux séries de paramètres, on arrive à comparer nos mesures de XMLD et les spectres XMLD calculés avec ces paramètres. On remarque que ces deux séries de paramètres du champ cristallin ne reproduisent pas à nos mesures (Figure 5.9).

Par la suite, dans un premier temps, on cherche une nouvelle série des paramètres du champ cristallin en ajustant nos mesures de XMLD et XMCD. On trouve

$$B_{40} = 11.3\,\mathrm{meV}, \qquad B_{60} = -3\,\mathrm{meV}. \tag{48}$$

Dans un second temps, on obtient donc pour les mesures expérimentales et pour les simulations, la variation du moment magnétique en fonction de la température et à un facteur près, la variation de $\langle J_z^2 \rangle$ en fonction de la température. La variation du moment magnétique (Figure 3 - Gauche) est à comparer à celle de l'échantillon d'$Yb_{0.005}Au_{0.995}$.

Des recherches sur la polarisation du moment magnétique de Pd sous l'influence d'Er sont discutées en comparant les mesures de XMCD et les mesures de SQUID.

L'idée est basée sur le fait que le SQUID mesure le moment magnétique total macroscopique et le XMCD donne le moment magnétique pour un atome chimiquement sélectionné. La différence entre les mesures de SQUID et les mesures de XMCD révèle la polarisation du Pd.

Le **Chapitre 6** présente les analyses de l'échantillon d'$Yb_{0.005}Au_{0.995}$. L'ytterbium se présente comme Yb^{3+} dans cet alliage. 0.5% d'atomes d'Yr sont dilués dans Au (structure fcc cubique à faces centrées). Avec un simple calcul, on estime que la probabilité pour un atome d'Yb se trouve entouré par 12 atomes d'or est de 94.16%. La configuration électronique d'Yb^{3+} est [Xe]$4f^{13}$ avec $S = 1/2$ et $L = 3$. Pour son état fondamental $^2F_{7/2}$, $J = L + S = 7/2$. Le moment de saturation pour un ion Yb^{3+} sphérique à $T = 0\,\mathrm{K}$ est de $4\,\mu_B$ alors que les mesures préliminaires de SQUID montrent qu'à $T = 2\,\mathrm{K}$ et $B = 7\,\mathrm{T}$, le moment magnétique d'Yb^{3+} est de $1.963\,\mu_B$ par atome d'ytterbium.

Sous l'effet du champ cristallin, l'état fondamental $^2F_{7/2}$ se sépare en Γ_7 (2 fois dégénéré), Γ_8 (4 fois dégénéré) et Γ_6 (2 fois dégénéré). Γ_8 et Γ_6 sont deux niveaux très proches en énergie. Avec la présence du champ magnétique extérieur sous l'effet Zeeman, la dégénérescence est levée et on a un système de 8 états. Les fonctions propres de ces 8 états sont données dans Ref.[116], et à partir de ces fonctions propres, on fait des calculs analytiques de la variation du moment magnétique et la variation de $\langle J_z^2 \rangle$ en fonction de la température.

Des mesures de XMCD aux seuils $M_{4,5}$ d'Yb ont été réalisées sur DEIMOS à SOLEIL avec un champ magnétique extérieur à 6.5 T, 0.5 T, 0.1 T et 0 T pour des températures entre 200 mK et 300 K. Les spectres XMLD sont ainsi déduits. On trace alors (Figure3-Droite) les mesures expérimentales du moment magnétique et la variation de $\langle J_z^2 \rangle$ en fonction de température.

On voit clairement les comportements différents entre les deux composés à base d'Er et d'Yb. On rappelle que les calculs de LFM ne tiennent pas compte de l'effet Kondo, ceux-ci sont en bon accord avec le système non-Kondo d'$Er_{0.025}Pd_{0.975}$. Cependant, on constate une déviation entre les calculs de LFM et les mesures pour le système Kondo d'$Yb_{0.005}Au_{0.995}$ pour $B = 0.1\,\mathrm{T}$ et $B = 0.5\,\mathrm{T}$ à une température inférieure de 1 K. Plus la température est basse, plus cette déviation est évidente. La signature Kondo est bien présente dans cette zone. Le moment magnétique de l'impureté d'Yb est couplé avec un électron de conduction pour former un singulet qui écrante le moment magnétique de l'Yb. Par conséquent, le moment magnétique détecté diminue. Pour un champ magnétique fort comme $B = 6.5\,\mathrm{T}$ ou pour une température élevée ($T \gg T_K$), l'agitation thermique ou l'énergie Zeeman détruisent le singulet et l'effet Kondo disparaît; un comportement paramagnétique réapparaît.

En utilisant une formule qui calcule l'aimantation tenant compte de l'effet Kondo

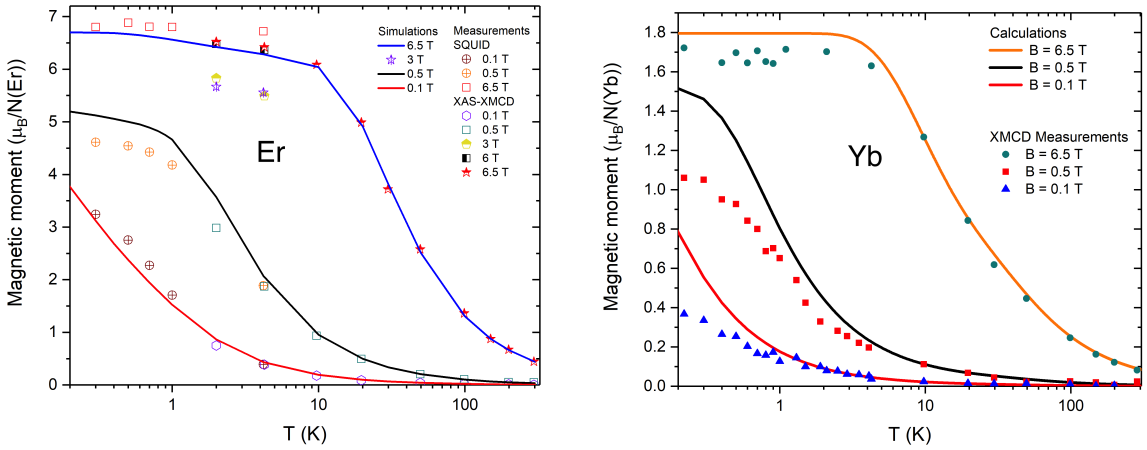

Figure 3: La comparaison de la variation du moment magnétique en fonction de température entre un système non-Kondo d'$Er_{0.025}Pd_{0.975}$ et un système Kondo d'$Yb_{0.005}Au_{0.995}$. (Gauche) Les mesures expérimentales et les simulations d'Er^{3+}. (Droite) Les mesures expérimentales et les simulations d'Yb^{3+}.

proposée par Schotte et Schotte [70], on obtient une estimation de la température de Kondo pour notre échantillon $Yb_{0.005}Au_{0.995}$: $T_K = 0.7\,\mathrm{K}$.

L'analyse des spectres de XMLD et la comparaison de la variation de $\langle J_z^2 \rangle$ en fonction de la température entre les calculs de LFM et les mesures sont également présentées.

Le **Chapitre 7** est la conclusion générale et les perspectives.

Bibliography

[1] W. C. Röntgen, "Über eine neue art von strahlen," *Sitzber. Physik. Med. Ges.*, vol. 137, pp. 132–137, 1895.

[2] A. Rogalev, F. Wilhelm, N. Jaouen, J. Goulon, and J.-P. Kappler, *X-ray Magnetic Circular Dichroism: Historical Perspective and Recent Highlights*, pp. 71–93. Berlin, Heidelberg: Springer Berlin Heidelberg, 2006.

[3] A. Rogalev and F. Wilhelm, "Magnetic circular dichroism in the hard X-ray range," *The Physics of Metals and Metallography*, vol. 116, no. 13, pp. 1285–1336, 2015.

[4] C. G. Barkla, "Polarised Röntgen radiation," *Phil. Trans A*, vol. 204, pp. 467–479, 1905.

[5] C. G. Barkla, "Polarisation in secondary Röntgen radiation," *Proceedings of the Royal Society of London. Series A*, vol. 77, no. 516, pp. 247–255, 1906.

[6] J. C. Chapman, "Some experiments on polarized Röntgen radiation," *Phil. Mag.*, vol. 25, p. 792, 1912.

[7] A. H. Forman, "The effect of magnetization on the opacity of iron to Röntgen rays," *Phys. Rev.*, vol. 3, pp. 306–313, Apr 1914.

[8] A. H. Forman, "The effect of magnetization of the opacity of iron to Röntgen rays," *Phys. Rev.*, vol. 7, pp. 119–124, Jan 1916.

[9] J. A. Becker, "The effect of the magnetic field on the absorption of X-rays," *Phys. Rev.*, vol. 20, pp. 134–147, Aug 1922.

[10] J. A. Becker, "The effect of a magnetic field on the absorption of X-rays," *Phys. Rev.*, vol. 22, pp. 320–323, Oct 1923.

[11] W. Kartschagin and E. Tschetwerikova, "Zur Frage nach der magnetischen Drehung der Polarisationsebene primärer Röntgenstrahlen," *Zeitsch. für Physik*, vol. 39, p. 886, 1926.

[12] D. K. Froman, "The faraday effect with X-rays," *Phys. Rev.*, vol. 41, pp. 693–700, Sep 1932.

[13] C. Kurylenko, "Franges au voisinage de la discontinuité K des rayons X," *J. Phys. Radium*, vol. 1, no. 4, pp. 133–145, 1940.

[14] C. Kurylenko, "Où en est la question de la discontinuité d'absorption K des rayons X et des franges qui l'accompagnent?," *Bull. Soc. R. Sci. Liège*, vol. 15, p. 236, 1946.

[15] D. Coster, "Book Reviews: *Où en est la question de la discontinuité d'absorption K des rayons X et des franges qui l'accompagnent*? by C. Kurylenko," *Acta Crystallographica*, vol. 1, p. 160, Jul 1948.

[16] J. L. Erskine and E. A. Stern, "Calculation of the M_{23} magneto-optical absorption spectrum of ferromagnetic nickel," *Phys. Rev. B*, vol. 12, pp. 5016–5024, Dec 1975.

[17] G. Schütz, E. Zech, E. Hagn, and P. Kienle, "Anisotropy of x-rays and spin depencence of the photoabsorption of circularly polarized soft x-rays in magnetized fe," *Hyperfine Interactions*, vol. 16, no. 1, pp. 1039–1042, 1983.

[18] B. T. Thole, G. van der Laan, and G. A. Sawatzky, "Strong magnetic dichroism predicted in the $M_{4,5}$ X-ray absorption spectra of magnetic rare-earth materials," *Phys. Rev. Lett.*, vol. 55, pp. 2086–2088, Nov 1985.

[19] G. van der Laan, B. T. Thole, G. A. Sawatzky, J. B. Goedkoop, J. C. Fuggle, J.-M. Esteva, R. Karnatak, J. P. Remeika, and H. A. Dabkowska, "Experimental proof of magnetic x-ray dichroism," *Phys. Rev. B*, vol. 34, pp. 6529–6531, Nov 1986.

[20] G. Schütz, W. Wagner, W. Wilhelm, P. Kienle, R. Zeller, R. Frahm, and G. Materlik, "Absorption of circularly polarized x rays in iron," *Phys. Rev. Lett.*, vol. 58, pp. 737–740, Feb 1987.

[21] P. Carra, B. T. Thole, M. Altarelli, and X. Wang, "X-ray circular dichroism and local magnetic fields," *Phys. Rev. Lett.*, vol. 70, pp. 694–697, 1993.

[22] B. T. Thole, P. Carra, F. Sette, and G. van der Laan, "X-ray circular dichroism as a probe of orbital magnetization," *Phys. Rev. Lett.*, vol. 68, pp. 1943–1946, 1992.

[23] C. T. Chen, Y. U. Idzerda, H.-J. Lin, N. V. Smith, G. Meigs, E. Chaban, G. H. Ho, E. Pellegrin, and F. Sette, "Experimental confirmation of the x-ray magnetic circular dichroism sum rules for iron and cobalt," *Phys. Rev. Lett.*, vol. 75, pp. 152–155, Jul 1995.

[24] J. P. Schillé, J. P. Kappler, Ph. Sainctavit, Ch. Cartier dit Moulin, C. Brouder, and G. Krill, "Experimental and calculated magnetic dichroism in the Ho 3*d* x-ray-absorption spectra of intermetallic $HoCo_2$," *Phys. Rev. B*, vol. 48, pp. 9491–9496, Oct 1993.

[25] F. Wilhelm, "Magnetic materials probed with polarized x-ray spectroscopies," *Synchrotron Radiation News*, vol. 26, no. 6, pp. 2–5, 2013.

[26] G. van der Laan, "Magnetic linear x-ray dichroism as a probe of the magnetocrystalline anisotropy," *Phys. Rev. Lett.*, vol. 82, pp. 640–643, Jan 1999.

[27] E. Arenholz, G. van der Laan, R. V. Chopdekar, and Y. Suzuki, "Angle-dependent Ni^{2+} X-ray magnetic linear dichroism: Interfacial coupling revisited," *Phys. Rev. Lett.*, vol. 98, p. 197201, May 2007.

[28] E. Arenholz, G. van der Laan, R. V. Chopdekar, and Y. Suzuki, "Anisotropic x-ray magnetic linear dichroism at the Fe $L_{2,3}$ edges in Fe_3O_4," *Phys. Rev. B*, vol. 74, p. 094407, Sep 2006.

[29] G. van der Laan, E. Arenholz, R. V. Chopdekar, and Y. Suzuki, "Influence of crystal field on anisotropic x-ray magnetic linear dichroism at the Co^{2+} $L_{2,3}$ edges," *Phys. Rev. B*, vol. 77, p. 064407, Feb 2008.

[30] G. van der Laan, E. Arenholz, A. Schmehl, and D. G. Schlom, "Weak anisotropic x-ray magnetic linear dichroism at the Eu $M_{4,5}$ edges of ferromagnetic EuO(001): Evidence for $4f$-state contributions," *Phys. Rev. Lett.*, vol. 100, p. 067403, Feb 2008.

[31] A. Delobbe, *Développement d'expériences de dichroïsme circulaire magnétique des rayons X dans le domaine des basses températures*. PhD thesis, Université Paris XI Orsay, 1999. PhD thesis supervised by Gérard Krill.

[32] M. Mannini, F. Pineider, Ph. Sainctavit, C. Danieli, E. Otero, C. Sciancalepore, A. Talarico, M.-A. Arrio, A. Cornia, D. Gatteschi, and R. Sessoli, "Magnetic memory of a single-molecule quantum magnet wired to a gold surface," *Nature materials*, vol. 8, pp. 194–7, 03 2009.

[33] L. Joly, J.-P. Kappler, P. Ohresser, P. Sainctavit, Y. Henry, F. Gautier, G. Schmerber, D. J. Kim, C. Goyhenex, H. Bulou, O. Bengone, J. Kavich, P. Gambardella, and F. Scheurer, "Kondo screening of the spin and orbital magnetic moments of Fe impurities in Cu," *Phys. Rev. B*, vol. 95, p. 041108, Jan 2017.

[34] T. Beeck, I. Baev, S. Gieschen, H. Meyer, S. Meyer, S. Palutke, P. Feulner, K. Uhlig, M. Martins, and W. Wurth, "New experimental perspectives for soft x-ray

absorption spectroscopies at ultra-low temperatures below 50 mK and in high magnetic fields up to 7 T," *Review of Scientific Instruments*, vol. 87, no. 4, p. 045116, 2016.

[35] I. Baev, T. Beeck, M. B. Casu, M. Martins, and W. Wurth, "XMCD going ultracold: Experiments at 100 mK and 7 T," *Journal of Physics: Conference Series*, vol. 875, p. 112005, jul 2017.

[36] J.-P. Kappler, E. Otero, W. Li, L. Joly, G. Schmerber, B. Muller, F. Scheurer, F. Leduc, B. Gobaut, L. Poggini, G. Serrano, F. Choueikani, E. Lhotel, A. Cornia, R. Sessoli, M. Mannini, M.-A. Arrio, P. Sainctavit, and P. Ohresser, "Ultralow-temperature device dedicated to soft X-ray magnetic circular dichroism experiments," *Journal of Synchrotron Radiation*, vol. 25, no. 6, pp. 1727–1735, 2018.

[37] O. Lounasmaa, *Experimental principles and methods below 1 K*. Academic Press, 1974.

[38] D. S. Betts, *Refrigeration and thermometry below one kelvin*. Graduate student series in physics, London: Chatto and Windus for Sussex University Press, 1976.

[39] R. P. Gupta, "Residual resistivity of defects in metals," *Phys. Rev. B*, vol. 35, pp. 5431–5436, Apr 1987.

[40] W. de Haas, J. de Boer, and G. van dën Berg, "The electrical resistance of gold, copper and lead at low temperatures," *Physica*, vol. 1, no. 7, pp. 1115–1124, 1934.

[41] G. Van Den Berg, "Chapter iv anomalies in dilute metallic solutions of transition elements," vol. 4 of *Progress in Low Temperature Physics*, pp. 194–264, Elsevier, 1964.

[42] B. R. Coles, "Low-temperature resistivity behaviour of molybdenum–iron, niobium–iron and palladium–iron alloys," *The Philosophical Magazine: A Journal of Theoretical Experimental and Applied Physics*, vol. 8, no. 86, pp. 335–337, 1963.

[43] M. P. Sarachik, E. Corenzwit, and L. D. Longinotti, "Resistivity of Mo-Nb and Mo-Re alloys containing 1% Fe," *Phys. Rev.*, vol. 135, pp. A1041–A1045, Aug 1964.

[44] J. Kondo, "Resistance Minimum in Dilute Magnetic Alloys," *Progress of Theoretical Physics*, vol. 32, pp. 37–49, 07 1964.

[45] J. Kondo, "Theory of dilute magnetic alloys," vol. 23 of *Solid State Physics*, pp. 183–281, Academic Press, 1970.

[46] A. C. Hewson, *Resistivity Calculations and the Resistance Minimum*, p. 29–46. Cambridge Studies in Magnetism, Cambridge University Press, 1993.

[47] K. Yamada, *s–d Hamiltonian and Kondo effect*, p. 49–71. Cambridge University Press, 2004.

[48] P. Coleman, K. Schönhammer, E. Pavarini, A. Nevidomskyy, T. Costi, K. Ingersent, F. Mila, V. Janiš, R. Frésard, A. Mielke, R. Eder, D. Sénéchal, T. Maier, E. Koch, and C. Franchini, *Many-Body Physics: From Kondo To Hubbard*. 08 2015.

[49] A. A. Abrikosov, "Electron scattering on magnetic impurities in metals and anomalous resistivity effects," *Physics Physique Fizika*, vol. 2, pp. 5–20, Sep 1965.

[50] P. W. Anderson, "Ground state of a magnetic impurity in a metal," *Phys. Rev.*, vol. 164, pp. 352–359, Dec 1967.

[51] P. W. Anderson, "A poor man's derivation of scaling laws for the kondo problem," *Journal of Physics C: Solid State Physics*, vol. 3, pp. 2436–2441, dec 1970.

[52] A. C. Hewson, *The Kondo Problem*, p. 47–70. Cambridge Studies in Magnetism, Cambridge University Press, 1993.

[53] P. W. Anderson, G. Yuval, and D. R. Hamann, "Exact results in the kondo problem. II. scaling theory, qualitatively correct solution, and some new results on one-dimensional classical statistical models," *Phys. Rev. B*, vol. 1, pp. 4464–4473, Jun 1970.

[54] K. G. Wilson, *Solution of the Spin-1/2 Kondo Hamiltonian*, pp. 68–75. Nobel Foundation, Academic Press, 1974.

[55] K. G. Wilson, "The renormalization group: Critical phenomena and the Kondo problem," *Rev. Mod. Phys.*, vol. 47, pp. 773–840, Oct 1975.

[56] H. R. Krishna-murthy, K. G. Wilson, and J. W. Wilkins, "Temperature-dependent susceptibility of the symmetric Anderson model: Connection to the Kondo model," *Phys. Rev. Lett.*, vol. 35, pp. 1101–1104, Oct 1975.

[57] H. R. Krishna-murthy, J. W. Wilkins, and K. G. Wilson, "Renormalization-group approach to the Anderson model of dilute magnetic alloys. I. Static properties for the symmetric case," *Phys. Rev. B*, vol. 21, pp. 1003–1043, Feb 1980.

[58] H. R. Krishna-murthy, J. W. Wilkins, and K. G. Wilson, "Renormalization-group approach to the Anderson model of dilute magnetic alloys. II. Static properties for the asymmetric case," *Phys. Rev. B*, vol. 21, pp. 1044–1083, Feb 1980.

[59] A. C. Hewson, *Fermi Liquid Theories*, p. 103–133. Cambridge Studies in Magnetism, Cambridge University Press, 1993.

[60] T. A. Costi, "Kondo effect in a magnetic field and the magnetoresistivity of kondo alloys," *Phys. Rev. Lett.*, vol. 85, pp. 1504–1507, Aug 2000.

[61] S. Otte, M. Ternes, K. von Bergmann, S. Loth, H. Brune, C. Lutz, C. Hirjibehedin, and A. Heinrich, "The role of magnetic anisotropy in the Kondo effect," *Nature Physics*, vol. 4, p. 847, 09 2008.

[62] Y.-S. Fu, S.-H. Ji, X. Chen, X.-C. Ma, R. Wu, C.-C. Wang, W.-H. Duan, X.-H. Qiu, B. Sun, P. Zhang, J.-F. Jia, and Q.-K. Xue, "Manipulating the Kondo resonance through quantum size effects," *Phys. Rev. Lett.*, vol. 99, p. 256601, Dec 2007.

[63] A. J. Heinrich, J. A. Gupta, C. P. Lutz, and D. M. Eigler, "Single-atom spin-flip spectroscopy," *Science*, vol. 306, no. 5695, pp. 466–469, 2004.

[64] A. F. Otte, M. Ternes, S. Loth, C. P. Lutz, C. F. Hirjibehedin, and A. J. Heinrich, "Spin excitations of a Kondo-screened atom coupled to a second magnetic atom," *Phys. Rev. Lett.*, vol. 103, p. 107203, Sep 2009.

[65] C. Praetorius and K. Fauth, "Kondo screening and beyond: An x-ray absorption and dichroism study of $CePt_5/Pt(111)$," *Phys. Rev. B*, vol. 95, p. 115113, Mar 2017.

[66] K. Chen, T.-C. Weng, G. Schmerber, V. N. Gurin, J.-P. Kappler, Q. Kong, F. Baudelet, A. Polian, and L. Nataf, "Surface- and pressure-induced bulk Kondo breakdown in SmB_6," *Phys. Rev. B*, vol. 97, p. 235153, Jun 2018.

[67] W. T. Fuhrman, J. C. Leiner, J. W. Freeland, M. van Veenendaal, S. M. Koohpayeh, W. A. Phelan, T. M. McQueen, and C. Broholm, "Magnetic dichroism in the Kondo insulator SmB_6," *Phys. Rev. B*, vol. 99, p. 020401, Jan 2019.

[68] Y. Saitoh, H. Fujiwara, A. Yasui, T. Kadono, H. Sugawara, D. Kikuchi, H. Sato, S. Suga, A. Yamasaki, A. Sekiyama, and S. Imada, "Insight into Kondo screening in the intermediate-valence compound $SmOs_4Sb_{12}$ uncovered by soft x-ray magnetic circular dichroism," *Phys. Rev. B*, vol. 102, p. 165152, Oct 2020.

[69] M. Barbier, F. Wilhelm, D. Pinek, K. Furuta, T. Ito, Y. Kim, M. Magnier, D. Braithwaite, M. Vališka, C. Opagiste, M. W. Barsoum, P. Ohresser, E. Otero, P. Le Fèvre, F. Bertran, G. Garbarino, A. Rogalev, and T. Ouisse, "$Mo_4Ce_4Al_7C_3$: A nanolamellar ferromagnetic Kondo lattice," *Phys. Rev. B*, vol. 102, p. 155121, Oct 2020.

[70] K. Schotte and U. Schotte, "Interpretation of Kondo experiments in a magnetic field," *Physics Letters A*, vol. 55, no. 1, pp. 38–40, 1975.

[71] P. Ohresser, E. Otero, F. Choueikani, K. Chen, S. Stanescu, F. Deschamps, T. Moreno, F. Polack, B. Lagarde, J.-P. Daguerre, F. Marteau, F. Scheurer, L. Joly, J.-P. Kappler, B. Muller, O. Bunau, and Ph. Sainctavit, "DEIMOS: a beamline dedicated to dichroism measurements in the 350–2500 eV energy range," *Review of Scientific Instruments*, vol. 85, no. 1, p. 013106, 2014.

[72] F. Pobell, *Matter and Methods at Low Temperatures*. Springer Berlin Heidelberg, 2007.

[73] Ph. Sainctavit and J.-P. Kappler, *X-ray Magnetic Circular Dichroism at Low Temperature*, pp. 235–253. Berlin, Heidelberg: Springer Berlin Heidelberg, 2001.

[74] N. Holden, T. B. Coplen, J. Bohlke, L. V. Tarbox, J. Benefield, J. R. de Laeter, P. Mahaffy, G. O'Connor, E. Roth, D. H. Tepper, T. Walczyk, M. Wieser, and S. Yoneda, "IUPAC periodic table of the elements and isotopes (IPTEI) for the education community (IUPAC Technical Report)," *Pure and Applied Chemistry*, vol. 90, pp. 1833–2092, 12 2018.

[75] C. F. Mate, R. Harris-Lowe, W. L. Davis, and J. G. Daunt, "^{3}He cryostat with adsorption pumping," *Review of Scientific Instruments*, vol. 36, no. 3, pp. 369–373, 1965.

[76] D. Walton, "^{3}He cryostat for operation to 0.2°K," *Review of Scientific Instruments*, vol. 37, no. 6, pp. 734–736, 1966.

[77] D. Walton, T. Timusk, and A. J. Sievers, "A compact ^{3}He cryostat using activated charcoal," *Review of Scientific Instruments*, vol. 42, no. 8, pp. 1265–1266, 1971.

[78] E. T. Swartz, "Charcoal-pumped ^{3}He cryostats for storage Dewars," *Review of Scientific Instruments*, vol. 58, no. 5, pp. 881–889, 1987.

[79] G. E. Watson, J. D. Reppy, and R. C. Richardson, "Low-temperature density and solubility of He^3 in liquid He^4 under pressure," *Phys. Rev.*, vol. 188, pp. 384–396, Dec 1969.

[80] S. Yorozu, M. Hiroi, H. Fukuyama, H. Akimoto, H. Ishimoto, and S. Ogawa, "Phase-separation curve of ^{3}He-^{4}He mixtures under pressure," *Phys. Rev. B*, vol. 45, pp. 12942–12948, Jun 1992.

[81] R. Radebaugh and J. Siegwarth, "Dilution refrigerator technology," *Cryogenics*, vol. 11, no. 5, pp. 368 – 384, 1971.

[82] C. Ebner and D. Edwards, "The low temperature thermodynamic properties of superfluid solutions of ^{3}He in ^{4}He," *Physics Reports*, vol. 2, no. 2, pp. 77 – 154, 1971.

[83] R. D. B. Ouboter, K. Taconis, C. L. Pair, and J. Beenakker, "Thermodynamic properties of liquid ^{3}He-^{4}He mixtures derived from specific heat measurements between 0.4°K and 2°K over the complete concentration range," *Physica*, vol. 26, no. 11, pp. 853 – 888, 1960.

[84] K. Taconis and R. D. B. Ouboter, "Chapter II Equilibrium Properties of Liquid and Solid Mixtures of Helium Three and Four," vol. 4 of *Progress in Low Temperature Physics*, pp. 38 – 96, Elsevier, 1964.

[85] S. G. Sydoriak and T. R. Roberts, "Vapor pressures of ^{3}He-^{4}He mixtures," *Phys. Rev.*, vol. 118, pp. 901–912, May 1960.

[86] E. H. Graf, D. M. Lee, and J. D. Reppy, "Phase separation and the superfluid transition in liquid ^{3}He-^{4}He mixtures," *Phys. Rev. Lett.*, vol. 19, pp. 417–419, Aug 1967.

[87] G. K. Walters and W. M. Fairbank, "Phase separation in ^{3}He-^{4}He solutions," *Phys. Rev.*, vol. 103, pp. 262–263, Jul 1956.

[88] D. O. Edwards, D. F. Brewer, P. Seligman, M. Skertic, and M. Yaqub, "Solubility of ^{3}He in liquid ^{4}He at 0° K," *Phys. Rev. Lett.*, vol. 15, pp. 773–775, Nov 1965.

[89] J. C. Wheatley, "Dilute solutions of ^{3}He in ^{4}He at low temperatures," *American Journal of Physics*, vol. 36, no. 3, pp. 181–210, 1968.

[90] R. Hendricks, I. Peller, A. Baron, and L. R. Center, *Joule-Thomson Inversion Curves and Related Coefficients for Several Simple Fluids*. NASA technical note, National Aeronautics and Space Administration, 1972.

[91] D. S. Greywall, "Specific heat of normal liquid ^{3}He," *Phys. Rev. B*, vol. 27, pp. 2747–2766, Mar 1983.

[92] D. S. Greywall, "^{3}He specific heat and thermometry at millikelvin temperatures," *Phys. Rev. B*, vol. 33, pp. 7520–7538, Jun 1986.

[93] V. Tadè, "La dilution de l'hélium 3 dans l'hélium 4." http://v.tade.free.fr/boulot/dilution.html, 2022.

[94] R. Goodrich, D. Hall, E. Palm, and T. Murphy, "Magnetoresistance below 1k and temperature cycling of ruthenium oxide–bismuth ruthenate cryogenic thermometers," *Cryogenics*, vol. 38, no. 2, pp. 221–225, 1998.

[95] K. S. Pedersen, M. Sigrist, M. Sørensen, A.-L. Barra, T. Weyhermüller, S. Piligkos, C. Thuesen, M. Vinum, H. Mutka, H. Weihe, R. Clérac, and J. Bendix, "$[ReF_6]^{2-}$: A robust module for the design of molecule-based magnetic materials," *Angewandte Chemie (International ed. in English)*, vol. 53, pp. 1351–4, 01 2014.

[96] CXRO - The Center for X-ray Optics, "Filter transmission." `https://henke.lbl.gov/optical_constants/filter2.html`. Accessed: 2022-01-12.

[97] L. Poggini, E. Tancini, C. Danieli, A. L. Sorrentino, G. Serrano, A. Lunghi, L. Malavolti, G. Cucinotta, A.-L. Barra, A. Juhin, M.-A. Arrio, W. Li, E. Otero, P. Ohresser, L. Joly, J. Kappler, F. Totti, Ph. Sainctavit, A. Caneschi, and M. Mannini, "Engineering chemisorption of fe4 single-molecule magnets on gold," *Advanced Materials Interfaces*, vol. 8, 11 2021.

[98] L. Zhang, M.-A. Arrio, S. Mazerat, L. Catala, W. Li, E. Otero, P. Ohresser, L. Lisnard, Ch. Cartier dit Moulin, T. Mallah, and Ph. Sainctavit, "Magnetic hysteresis in a monolayer of oriented 6 nm csnicr prussian blue analogue nanocrystals," *Inorganic Chemistry*, vol. 60, no. 21, pp. 16388–16396, 2021. PMID: 34624189.

[99] L. Zhang, Y. Tong, M. Kelai, A. Bellec, J. Lagoute, C. Chacon, Y. Girard, S. Rousset, M.-L. Boillot, E. Rivière, T. Mallah, E. Otero, Ph. Sainctavit, M.-A. Arrio, and V. Repain, "Anomalous light induced spin state switching for fe^{II} spin-crossover molecules in direct contact with metal surfaces," *Angewandte Chemie*, vol. 132, 04 2020.

[100] M. Kelai, V. Repain, A. Tauzin, W. Li, Y. Girard, J. Lagoute, S. Rousset, E. Otero, Ph. Sainctavit, M.-A. Arrio, M.-L. Boillot, T. Mallah, C. Enachescu, and A. Bellec, "Thermal bistability of an ultrathin film of iron(ii) spin-crossover molecules directly adsorbed on a metal surface," *The Journal of Physical Chemistry Letters*, vol. 12, pp. 6152–6158, 06 2021.

[101] S. Jafri, E. Koumousi, M.-A. Arrio, A. Juhin, D. Mitcov, M. Rouzieres, P. Dechambenoit, D. Li, E. Otero, F. Wilhelm, A. Rogalev, L. Joly, J.-P. Kappler, Ch. Cartier dit Moulin, C. Mathonière, R. Clérac, and Ph. Sainctavit, "Atomic scale evidence of the switching mechanism in a photomagnetic cofe dinuclear prussian blue analogue," *Journal of the American Chemical Society*, vol. 141, 12 2018.

[102] A. Balerna and S. Mobilio, *Introduction to Synchrotron Radiation*, pp. 3–28. Springer Berlin Heidelberg, 2015.

[103] F. Marteau, C. Benabderrahmane, P. Berteaud, F. Briquez, P. Brunelle, L. Chapuis, M.-E. Couprie, T. ElAjjouri, J. Filhol, C. Kitegi, and L. Nadolski, "Development and installation of insertion devices at SOLEIL," pp. 2453–2455, 01 2009.

[104] P. A. Zyla *et al.*, "Review of Particle Physics," *PTEP*, vol. 2020, no. 8, p. 083C01, 2020.

[105] Synchrotron SOLEIL, "7 étapes pour le rayonnement synchrotron :." https://www.synchrotron-soleil.fr/fr/, 2022.

[106] D. Attwood and A. Sakdinawat, *X-Rays and Extreme Ultraviolet Radiation: Principles and Applications - Chapter V Synchrotron Radiation*, p. 148–226. Cambridge University Press, 2 ed., 2017.

[107] F. de Groot and A. Kotani, *Core level spectroscopy of solids. CRC Press, Boca Raton*. 03 2008.

[108] P. Willmott, *Synchrotron Physics*, ch. 3, pp. 19–49. John Wiley & Sons, Ltd, 2019.

[109] A. F. Starace, "Potential-barrier effects in photoabsorption. I. General theory," *Phys. Rev. B*, vol. 5, pp. 1773–1784, Mar 1972.

[110] B. T. Thole and G. van der Laan, "Branching ratio in x-ray absorption spectroscopy," *Phys. Rev. B*, vol. 38, pp. 3158–3171, Aug 1988.

[111] B. T. Thole and G. van der Laan, "Linear relation between x-ray absorption branching ratio and valence-band spin-orbit expectation value," *Phys. Rev. A*, vol. 38, pp. 1943–1947, Aug 1988.

[112] B. T. Thole, G. van der Laan, and M. Fabrizio, "Magnetic ground-state properties and spectral distributions. I. X-ray-absorption spectra," *Phys. Rev. B*, vol. 50, pp. 11466–11473, Oct 1994.

[113] B. T. Thole, H. A. Dürr, and G. van der Laan, "Core hole polarization in x-ray absorption studied by magnetic circular dichroism in $2p3p3p$ resonant photoemission," *Phys. Rev. Lett.*, vol. 74, pp. 2371–2374, Mar 1995.

[114] G. van der Laan, "Applications of soft x-ray magnetic dichroism," *Journal of Physics: Conference Series*, vol. 430, p. 012127, apr 2013.

[115] G. Williams and L. L. Hirst, "Crystal-field effects in solid solutions of rare earths in noble metals," *Phys. Rev.*, vol. 185, pp. 407–415, Sep 1969.

[116] K. Lea, M. Leask, and W. Wolf, "The raising of angular momentum degeneracy of f-electron terms by cubic crystal fields," *Journal of Physics and Chemistry of Solids*, vol. 23, no. 10, pp. 1381 – 1405, 1962.

[117] K. W. H. Stevens, "Matrix elements and operator equivalents connected with the magnetic properties of rare earth ions," *Proceedings of the Physical Society. Section A*, vol. 65, pp. 209–215, mar 1952.

[118] R. Cowan, *The Theory of Atomic Structure and Spectra*, ch. 11. Los Alamos Series in Basic and Applied Sciences, University of California Press, 1981.

[119] C. Cohen-Tannoudji, B. Diu, and F. Laloë, *Mécanique quantique*, vol. I, ch. VI. EDP Sciences, September 2018.

[120] Y. Ayant, E. Belorizky, M. Guillot, and J. Rosset, "Interprétation de l'aimantation du gallate d'erbium en champ fort et à basse température," *Le Journal de Physique*, vol. 26, pp. 385–389, 07 1965.

[121] M.-A. Arrio, Ph. Sainctavit, Ch. Cartier dit Moulin, Ch. Brouder, F. M. F. de Groot, T. Mallah, and M. Verdaguer, "Measurement of magnetic moment at the atomic scale in a high T_C molecular based magnet," *J. Phys. Chem.*, vol. 100, pp. 4679–4684, 1996.

[122] M. W. Haverkort, M. Zwierzycki, and O. K. Andersen, "Multiplet ligand-field theory using wannier orbitals," *Phys. Rev. B*, vol. 85, p. 165113, Apr 2012.

[123] Y. Lu, M. Höppner, O. Gunnarsson, and M. W. Haverkort, "Efficient real-frequency solver for dynamical mean-field theory," *Phys. Rev. B*, vol. 90, p. 085102, Aug 2014.

[124] M. W. Haverkort, G. Sangiovanni, P. Hansmann, A. Toschi, Y. Lu, and S. Macke, "Bands, resonances, edge singularities and excitons in core level spectroscopy investigated within the dynamical mean-field theory," *EPL (Europhysics Letters)*, vol. 108, p. 57004, dec 2014.

[125] M. W. Haverkort, "Quanty for core level spectroscopy - excitons, resonances and band excitations in time and frequency domain," *Journal of Physics: Conference Series*, vol. 712, p. 012001, may 2016.

[126] F. M. de Groot, H. Elnaggar, F. Frati, R. pan Wang, M. U. Delgado-Jaime, M. van Veenendaal, J. Fernandez-Rodriguez, M. W. Haverkort, R. J. Green, G. van der Laan, Y. Kvashnin, A. Hariki, H. Ikeno, H. Ramanantoanina, C. Daul, B. Delley, M. Odelius, M. Lundberg, O. Kuhn, S. I. Bokarev, E. Shirley, J. Vinson, K. Gilmore, M. Stener, G. Fronzoni, P. Decleva, P. Kruger, M. Retegan, Y. Joly, C. Vorwerk, C. Draxl, J. Rehr, and A. Tanaka, "2p x-ray absorption spectroscopy of 3d transition metal systems," *Journal of Electron Spectroscopy and Related Phenomena*, vol. 249, p. 147061, 2021.

[127] M. Retegan, "Crispy: v0.7.3." https://dx.doi.org/10.5281/zenodo.1008184, 2019.

[128] P. Manfrinetti, A. Provino, N. S. Sangeetha, and S. K. Dhar, "The $R_{10}Pd_{21}$ compounds (R = Y, Pr, Nd, Sm, Gd–Lu). Crystal structure and magnetism of the 'RPd_2' phases," *J. Mater. Chem. C*, vol. 6, pp. 5250–5260, 2018.

[129] A. Provino, S. Nediadath Sathyanadhan, S. Dhar, V. Smetana, J. Gschneidner, V. Pecharsky, P. Manfrinetti, and A.-V. Mudring, "The new R_3Pd_5 compounds (R = Sc, Y, Gd-Lu): formation and stability, crystal structure and antiferromagnetism," *Crystal Growth & Design*, vol. 16, pp. 6001–6015, 09 2016.

[130] V. Dhar and A. Provino, "Ferromagnetism in the orthorhombic PrPd and SmPd," *Journal of Alloys and Compounds*, vol. 762, pp. 254–259, 2018.

[131] R. P. Guertin, H. C. Praddaude, S. Foner, E. J. McNiff, and B. Barsoumian, "Magnetic moment, susceptibility, and electrical resistivity of dilute paramagnetic palladium—rare-earth alloys," *Phys. Rev. B*, vol. 7, pp. 274–286, Jan 1973.

[132] P. Morin, J. Pierre, D. Schmitt, and W. Drexel, "Crystal field in ErMg, ErPd and related compounds," *Journal de Physique*, vol. 37, no. 5, pp. 611–616, 1976.

[133] J. Laeter, J. Bohlke, P. De Bièvre, H. Hidaka, H. Peiser, K. Rosman, and P. Taylor, "Atomic weights of the elements: Review 2000," *Pure and Applied Chemistry*, vol. 75, pp. 683–800, 01 2003.

[134] A. French and E. Taylor, *An Introduction to Quantum Physics*. M.I.T. introductory physics series, Norton, 1978.

[135] Los Alamos National Laboratory, "Periodic table of elements: Lanl - erbium." `https://periodic.lanl.gov/68.shtml`. Accessed: 2022-01-12.

[136] O. Loebich and E. Raub, "Das magnetische verhalten der legierungen des palladiums mit gadolinium, dysprosium und holmium," *Journal of the Less Common Metals*, vol. 31, no. 1, pp. 111 – 118, 1973.

[137] D. J. Newman and B. Ng, *Crystal Field Handbook - Ch. II Empirical crystal fields*, p. 26–42. Cambridge University Press, 2000.

[138] F. Gonzalez Jimenez and P. Imbert, "First observation of a Kondo anomaly on the relaxation rate: Mössbauer study of ytterbium in gold," *Solid State Communications*, vol. 13, no. 1, pp. 85–87, 1973.

[139] A. Murani, "Evidence for the negative s-f interaction in a noble metal host," *Solid State Communications*, vol. 12, no. 4, pp. 295–298, 1973.

[140] A. Benoit, J. Flouquet, and J. Sanchez, "Nuclear orientation experiments on melted or implanted auyb alloys," *Phys. Rev. B*, vol. 9, pp. 1092–1097, Feb 1974.

[141] J. M. Baker, B. Bleaney, and W. Hayes, "Paramagnetic resonance of *S*-state ions in calcium fluoride," *Proceedings of the Royal Society of London. Series A. Mathematical and Physical Sciences*, vol. 247, no. 1249, pp. 141–151, 1958.

[142] P. Rider, K. Gschneidner, and O. McMasters, "Gold-rich rare earth-gold solid solutions," *Transactions of the Metallurgical Society of AIME*, vol. 233, no. 8, p. 1488, 1965.

[143] V. Allali, P. Donzé, D. Gainon, and J. Sierro, "Magnetic behavior of ytterbium diluted in silver-gold alloys," *Journal of Applied Physics*, vol. 41, no. 3, pp. 1154–1155, 1970.

[144] H. Bethe, "Term splitting in crystals," *Annalen der Physik*, vol. 3, no. 2, pp. 133–208, 1929.

[145] W. Low, "Paramagnetic and optical spectra of ytterbium in the cubic field of calcium fluoride," *Phys. Rev.*, vol. 118, pp. 1608–1609, Jun 1960.

[146] F. Gonzalez-Jimenez, B. Cornut, and B. Coqblin, "Influence of the crystalline field and kondo effects on the relaxation rate: Application to mössbauer experiments of ytterbium diluted in gold," *Phys. Rev. B*, vol. 11, pp. 4674–4682, Jun 1975.

[147] G. Williams, "Calculated low temperature specific heats in dilute alloys of some rare-earths in noble metals," *Solid State Communications*, vol. 7, no. 21, pp. 1593–1598, 1969.

[148] M.-T. Béal-Monod and R. A. Weiner, "Negative magnetoresistivity in dilute alloys," *Phys. Rev.*, vol. 170, pp. 552–559, Jun 1968.

[149] M. T. Béal-Monod, "Kondo resistivity due to a pair of interacting impurities," *Phys. Rev.*, vol. 178, pp. 874–881, Feb 1969.

[150] M. Suzuki, N. Kawamura, H. Miyagawa, J. S. Garitaonandia, Y. Yamamoto, and H. Hori, "Measurement of a pauli and orbital paramagnetic state in bulk gold using x-ray magnetic circular dichroism spectroscopy," *Phys. Rev. Lett.*, vol. 108, p. 047201, Jan 2012.

[151] J. Bijvoet, A. van Dam, and F. van Beek, "Electric resistivities and solid solubilities of some rare-earth metals in silver," *Solid State Communications*, vol. 4, no. 9, pp. 455–458, 1966.

[152] P. Bonville, A. Ochiai, T. Suzuki, and E. Vincent, "Heterogeneous Yb^{3+}-Yb^{2+} mixed valency and unusual Kondo ground state in Yb_4As_3," *Journal de Physique I*, vol. 4, no. 4, pp. 595–603, 1994.

[153] D. Asakura, E. Hosono, Y. Nanba, H. Zhou, J. Okabayashi, C. Ban, P.-A. Glans, J. Guo, T. Mizokawa, G. Chen, A. J. Achkar, D. G. Hawthron, T. Z. Regier, and H. Wadati, "Material/element-dependent fluorescence-yield modes on soft X-ray absorption spectroscopy of cathode materials for Li-ion batteries," *AIP Advances*, vol. 6, no. 3, p. 035105, 2016.

[154] A. Di Cicco, A. Giglia, R. Gunnella, S. L. Koch, F. Mueller, F. Nobili, M. Pasqualini, S. Passerini, R. Tossici, and A. Witkowska, "SEI growth and depth profiling on ZFO electrodes by soft X-ray absorption spectroscopy," *Advanced Energy Materials*, vol. 5, p. 1500642, 07 2015.

[155] P. Steiner and S. Hüfner, "Local magnetization of Fe in Ag," *Phys. Rev. B*, vol. 12, pp. 842–846, Aug 1975.

[156] J. G. Perez-Ramirez and P. Steiner, "The magnetisation of the Kondo systems CuFe, AgFe, AuFe and MoFe," *Journal of Physics F: Metal Physics*, vol. 7, pp. 1573–1581, aug 1977.

[157] M. Abramowitz, *Handbook of Mathematical Functions, With Formulas, Graphs, and Mathematical Tables,*. USA: Dover Publications, Inc., 1974.

[158] G. E. Andrews, R. Askey, and R. Roy, *The Gamma and Beta Functions*, p. 1–60. Encyclopedia of Mathematics and its Applications, Cambridge University Press, 1999.

[159] B. Bleaney, "Lanthanide ions in metallic gold - I. crystal field and hyperfine interactions," *Proceedings of the Royal Society of London. A. Mathematical and Physical Sciences*, vol. 424, no. 1867, pp. 289–297, 1989.